Diamonds and their inclusions from Snap Lake diamond mine (Northwest Territories, Canada)

By

Kelsey Meghan Graversen

A thesis submitted in partial fulfillment of the requirements for the degree of

Master of Science

Department of Earth and Atmospheric Sciences

University of Alberta

©Kelsey Meghan Graversen, 2021

Abstract

This research was motivated by a current lack of systematic information, pairing inclusion chemistry (major, minor and trace element) to host diamond isotopic data ($\delta^{13}C$, $\delta^{15}N$, N abundance) regarding the Snap Lake kimberlite dyke. The Snap Lake kimberlite dyke is located on the southern Slave Craton, approximately 220 km northeast of Yellowknife, NWT. Previous studies (Pokhilenko et al. 2001, 2004) have inferred, through the observation of rare high-Cr majorite garnet inclusions, the presence of an unusually thick lithospheric mantle root (>200 km), which at depths corresponding to the diamond stability field was mostly harzburgitic. This thesis characterizes the various diamond substrates which make up the lithospheric mantle beneath Snap Lake, in addition to the conditions of diamond formation and mantle residence.

Based on a set of 87 inclusion-bearing diamonds it is inferred that diamond formation occurred primarily in peridotitic mantle (93%), with a more minor component forming in eclogitic mantle (6%) and a single studied diamond shows rare mixed paragenesis (1%). The peridotitic inclusion suite consists of garnet, olivine, chromite, clino- and orthopyroxene, sulphide and rare native iron-wustite, while the eclogitic inclusion suite consists of garnet, SiO_2, N-poor sulphide and potassium feldspar. From the single mixed-paragenesis diamond, a peridotitic garnet, an eclogitic coesite and an eclogitic sulphide were recovered, indicating the two sub-populations do not necessarily represent distinct environments beneath Snap Lake. Sinusoidal and weakly sinusoidal patterns of REE depletion for the majority of peridotitic (harzburgitic and lherzolitic) garnet indicate enrichment through similar styles of metasomatic fluids/melts. Geothermobarometry results indicate diamond formation occurred along a cool 36 – 38 mW/m^2 paleo-geotherm at temperatures ranging from 920 to 1230 ˚C, between 120 and at least 210 km in depth.

Overall, diamond fragments showed FTIR nitrogen abundances from below the limit of detection (< 10 at.ppm) to 1190 at.ppm with a large variation in nitrogen aggregation state ranging from 0 to 95 %B. Nitrogen-based mantle residence temperatures agree well with geothermometry results ranging from 1050 – 1280 ˚C. SIMS analysis resulted in $\delta^{13}C$ values in a tight range from – 8.0 to – 1.3 ‰ for Snap Lake diamonds, with a median of – 4.2 ‰ and an average of – 4.3 ‰. The $\delta^{13}C$ values of the peridotitic and eclogitic suites differed very little with ranges from – 8.0 to – 1.3 ‰ (median = - 4.2 ‰, average = - 4.3 ‰) and – 6.2 to – 3.9 ‰ (median = - 4.7 ‰, average = - 4.7 ‰), respectively. Snap Lake diamonds showed a wide range in $\delta^{15}N$ values ranging from – 20 to +11 ‰ reflecting a high likelihood of involvement of subducted sediments contributing to the nitrogen signature and supporting the idea of a heterogeneous nitrogen reservoir accounting for the extreme depletion in ^{15}N observed in peridotitic diamonds.

Acknowledgments

First and foremost, I would like to express my sincerest appreciation to my supervisor, Dr. Thomas Stachel. Your passion for diamonds, research and learning inspired me to explore the world of diamond geology. Without your belief in my abilities, mentorship and constant encouragement, this thesis would not have been possible.

I would also like to extend a massive thank you to my co-supervisor, Dr. D. Graham Pearson for your open-door policy and eagerness to help whenever possible. Your willingness to put students first is admirable.

Thank you to Anetta Banas for your guidance, reassurance and support in the lab, in my personal life and with internships and fieldtrips. You made my experience as a graduate student rich with extra learning and exciting experiences.

To Jeffery Harris, thank you for introducing me to diamonds with such passion, experience and wit, you made the daunting first task of describing and photographing my diamonds an absolute joy.

A special thanks goes out to Dr. Andrew Locock, for your assistance in learning about and operating the EPMA as well as your continued support afterwards by answering any questions that came up. Thank-you to Richard Stern and Robert Dokken, for teaching me the "ins and outs" SIMS analysis and keeping me involved through the project despite some challenging circumstances surrounding the pandemic situation. Thank you to Yan Luo for assistance in running the LA-ICP-MS.

I would also like to say a huge thankyou to all of my fellow team mates for always being there to answer questions, providing insight or just forget about the days worries at lunch. A special thanks to Matthew Hardman and Suzette Timmerman for your support and editing of this thesis, to Nicole Meyer for always being there to answer questions, to Jarret Hamilton and Christian Veglio for the five-minute breaks and to Mei Yan Lai for the support and laughs throughout my lab work (and for being as confused as I was once in a while).

I am grateful to Dr. Ingrid Chinn and De Beers Group for generously supplying such a beautiful set of diamonds for this study and to the Diamond Exploration Research Training School (DERTS) for providing funding for this project. I owe a depth of gratitude to my friends and family for their support and patience throughout this process.

Last but definitely not least, thank-you from the bottom of my heart to my husband Mads for your un-waivered support throughout my graduate studies. You were always there to remind me to take things one day at a time and to support me when things got really stressful.

Table of Contents

List of Tables

List of Figures

Figure 5.6: $\delta^{13}C$ histograms showing **A)** Snap Lake diamond $\delta^{13}C$ values by paragenesis (determined by inclusion chemistry), mean (-4.3 ‰) is labeled. **B**) Snap Lake $\delta^{13}C$ values in comparison to Slave craton diamond database isotope measurements from Stachel and Harris. (2008).

Figure 5.7: CL imaging of Snap Lake diamond, SN083, showing an intra-diamond $\delta^{13}C$ value difference of 3.7 ‰. SN083 shows a more negative outside (-7.9 ‰) and a less negative center (-4.2 ‰).

Figure 5.8: Bivariant plot of nitrogen content measured via FTIR versus nitrogen content measured via SIMS.

Figure 5.9: Histograms showing the distribution of $\delta^{15}N$ composition separated by paragenesis for **a)** Snap Lake Diamonds and **b)** worldwide diamonds (database of Stachel et al., 2009).

Figure 5.10: Representative photography of inclusion types observed in Snap Lake diamonds; A) Olivine (SN020), B) Diopside (SN030), C) Peridotitic garnet (SN108), D) Eclogitic garnet (SN001), E) Mg-chromite (SN046), F) Orthopyroxene (SN064), G) Sulphide (SN061), and H) K-feldspar (SN056).

Figure 5.11: CaO versus Cr2O3 of Snap Lake garnets from this study. Showing the garnet classes G10 (harzburgitic), G9 (lherzolitic), G3 (high-Ca eclogitic) and G4 (low-Ca eclogitic/pyroxenitic) after Grütter et al. (2004). Tie lines connect co-existing garnets recovered from a single diamond.

Figure 5.12: TiO_2 versus Mg# for Snap Lake garnets compared with worldwide garnet clusters from the worldwide database (Stachel & Harris, 2008). Peridotitic garnets from Snap Lake plot well within the peridotitic field defined by worldwide garnet samples, while the eclogitic also plot well within the eclogitic field defined by worldwide samples

Figure 5.13: Histogram showing the distribution of Mg# in olivine inclusions recovered from Snap Lake diamonds in this study

Figure 5.14: Plot of NiO versus Mg# ($molar\ \frac{100\,Mg}{Mg+Fe}$) of Snap Lake olivine of harzburgitic, lherzolitic, and undifferentiated peridotitic paragenesis, compared with other Slave Craton olivine inclusions and the worldwide database (Stachel & Harris, 2008).

Figure 5.15: Mg# ($molar\ \frac{100\,Mg}{Mg+Fe}$) versus Cr# ($molar\ \frac{100\,Cr}{Cr+Al}$) for Snap Lake clinopyroxene inclusions compared with peridotitic clinopyroxene inclusions and eclogitic clinopyroxene inclusions from the worldwide database (Stachel and Harris, 2008).

Figure 5.16: Na versus Cr, as cations calculated on the basis of six oxygen per formula unit, for Snap Lake clinopyroxene versus worldwide data (Stachel & Harris, 2008). The 1:1 line indicated accommodation of all Na and Cr as kosmochlor component. Inclusions plotting above the line likely contain an additional jadeite component.

Figure 5.17: Plot of TiO_2 versus Cr# for chromite inclusions from Snap Lake, versus the global database (Stachel & Harris, 2008).

Figure 5.18: Al_2O_3 versus FeO for enstatite inclusions from Snap Lake diamonds from this study, versus those from Pokhilenko et al. (2004).

Figure 5.19: CaO (wt%) versus Mg# for orthopyroxene inclusions plotted over top of the compositional fields and known orthopyroxene data. All three orthopyroxene inclusions from Snap Lake diamonds plot within the "harzburgitic only" field defined by Stachel and Harris (2008). Fields and previous data after Stachel and Harris (2008).

Figure 5.20: Sulphide compositions in weight percent (wt%) on the Fe-Ni-S quadrilateral. Ni-rich (>12 wt%) sulfides are inferred to be of peridotitic paragenesis and Ni-poor (< 8 wt%) are inferred to be of eclogitic paragenesis (Aulbach et al., 2009).

Figure 5.21: SEM images (backscattered electron images(right) and secondary electron images (left)) of the altered sulphide inclusions recovered from diamond SN008 using different contrast settings. Sulphide portion of inclusion SN008C is composed of a combination of exsolved sulphide minerals including heazelwoodite, godlevskite and pentlandite, while in SN008D the remnant sulphide is classified as peridotitic mono-sulfide solid solution. The non-sulphide material is calcite, based on quantitative EDS determination.

Figure 5.22: Photograph showing the fracture "aura" surrounding the multiple epigenetic inclusions recovered from diamond SN022. Syngenetic olivine and peridotitic garnet (lost during breakage) are also visible outside of the large fracture "aura".

Figure 5.23: **A)** Average REE_N concentrations in eclogitic garnet inclusions recovered from diamonds SN001 and SN005. **B)** Non-REE trace-element concentration in eclogitic garnet inclusions recovered from diamonds SN001 and SN005. SN001 (G3) is an average of four REE measurements from four separate inclusions recovered. Compositions are normalized to C1-Chrondite (McDonough and Sun, 1995).

Figure 5.24: A) Snap Lake peridotitic garnets showing "sinusoidal" chondrite-normalised (McDonough & Sun 1995) REE patterns. **B)** Snap Lake peridotitic garnets showing "weakly sinusoidal" chondrite-normalised REE patterns. Ranges and averages for worldwide (WW) harzburgitic and lherzolitic garnets are shown as outlined areas and dashed lines, respectively (Stachel & Harris, 2008).

Figure 5.25: Non-sinusoidal REE_N patterns of Snap Lake peridotitic garnets: **A)** humped to normal REE_N patterns and **B)** broadly V-shaped patterns with a hump at Ce-Pr and an extreme low at <0.01 times chondritic abundance at Tb.

Figure 5.26: REE_N patterns of clinopyroxene inclusions from diamond SN030 (normalized to C1 chondrite of McDonough and Sun (1995)).

Figure 5.27: Ca versus Al concentrations of Snap Lake olivine inclusions. Fields defining lherzolitic, harzburgitic and peridotitic (unclassified) are taken from De Hoog et al. (2019).

Figure 5.28: A) Na versus Al concentrations of Snap Lake olivine inclusions. **B)** Na versus Ca concentrations of Snap Lake olivine inclusions. Harzburgitic and lherzolitic fields are defined by De Hoog et al. (2019).

Figure 6.1: Paragenesis of Snap Lake diamonds based on inclusion compositions.

Figure 6.2: Comparison of the REE patterns for peridotitic garnets recovered from Snap Lake diamonds normalized to J-4 garnet (Stachel et al., 1998). **A)** Garnets with sinusoidal REE patterns when normalized to C1-chondrite. **B)** Garnets with weakly sinusoidal REE patterns when normalized to C1-chondrite.

Figure 6.3: Y versus Zr for Snap Lake harzburgitic and lherzolitic garnet inclusions. Compositional fields and trends taken from Pearson et al. (2003) adapted from Griffin and Ryan (1995).

Figure 6.4: Photographs taken of diamond SN097 pre-breakage showing the location of the three recovered inclusions within the same diamond. In addition, three more small colorless inclusions (not recovered) are visible.

Figure 6.5: Backscattered electron (BSE) image of inclusion SN088C (left) and SN088D (right) showing the native iron core rimmed by wustite.

Figure 6.6: Geothermobarometry for two clinopyroxenes (Nimis and Taylor, 2000; SN030, SN041) and one non-touching garnet-orthopyroxene pair (Nickel & Green, 1985 and Harley, 1984; SN132). P-T conditions for 50 single olivine grains were calculated using the Al-in-Ol thermometer of Bussweiler et al. (2017) projected onto a 37 mW/m^2 model geotherm. The plotted model geotherms (35 – 40 mW/m^2 surface heat flow) are from Hasterok and Chapman (2011) and the graphite-diamond transition is from Day (2012). Error bars shown are for ± 80 ˚C and ± 4 kbar

Figure 6.7: Cr_2O_3 versus CaO diagram for peridotitic garnet inclusions recovered from Snap Lake diamonds with superimposed isobars (kbar) according to the Cr-in-garnet barometer calculated for temperature conditions along a 38 mW/m^2 model geotherm (P_{38} of Grütter et al. 2004, 2006).

Figure 6.8: Nitrogen content (at.ppm) versus %B component for Snap Lake diamonds (organized by size fraction) measured with FTIR on diamond fragments. Isotherms were calculated from Leahy & Taylor (1997) and Taylor et al. (1990) for 1 and 3 Ga mantle residence time.

Figure 6.9: Histogram showing the calculated nitrogen-in-diamond based mantle residence temperatures for Snap Lake diamonds assuming a mantle residence time of 1 Ga.

Figure 6.10: Average temperatures calculated from different thermometers with standard deviation error bars, based on inclusion chemistry or host diamond nitrogen content. Peridotitic and eclogitic diamond averages were taken from Stachel & Harris (2008).

Figure 6.11: Na versus Ca (ppm) in olivine inclusions from Snap Lake (SL) compared to olivine inclusions from Akwatia (Ak; De Hoog et al., 2019).

Figure 6.12: CL images of two diamonds (SN030 & SN025) showing an inverse relationship between brightness of CL imaging and nitrogen content. Where bright sections correspond to low nitrogen content and adjacent dark sections show high nitrogen content. In diamond SN025 there is also some dramatic variation within the dark band itself showing both high and low nitrogen content (22 at.ppm and 490 at.ppm).

Figure 6.13: Total nitrogen content (at.ppm) versus $\delta^{13}C$ (‰) for Snap Lake diamonds. Each diamond represents a point analysis (3 - 5 per diamond) made by SIMS. No correlation between total nitrogen content and $\delta^{13}C$ is observed.

Figure 6.14: Plot of B' peak area (cm^{-2}) versus concentration of nitrogen in B-centers (N_B) for Snap Lake diamonds (N=244). The blue line represents the proportionality between platelet peak intensity and N_B described by Woods (1986) for ideal diamonds.

Figure 6.15: Histograms of $\delta^{13}C$ values of diamonds from Snap Lake the Slave Craton worldwide occurrences (database of Stachel & Harris, 2008) **A)** for peridotitic diamonds; **B)** for eclogitic diamonds. Typical mantle range is shaded in orange, between -8 and -2 ‰ (Cartigny et al., 2014).

List of Symbols & Abbreviations

~	Approximately
SCLM	Subcontinental lithospheric mantle
%B	Percent nitrogen aggregated into B centers
wt%	Weight percent
$\delta^{13}C$	Carbon isotope composition relative to V-PDB
$\delta^{15}N$	Nitrogen isotopic composition relative to air
CL	Cathodoluminescence
Cr#	Chromite number = [Cr/(Cr + Al)]*100
Mg#	Magnesium number = [Mg/(Mg+Fe)]*100
G3	High calcium eclogitic garnet
G4	Low calcium eclogitic garnet/pyroxenitic garnet
G10	Harzburgitic garnet
G9	Lhzerolitic garnet
Ma	Millions of years ago
Ga	Billions of years ago
GPa	Gigapascal
FTIR	Fourier transform infrared spectroscopy
REE	Rare earth element
REE_N	Rare earth element normalized to C1 chondrite
HREE	Heavy rare earth element
MREE	Middle rare earth element
LREE	Light rare earth elements

EDS	Energy dispersive spectrometry
EPMA	Electron probe microanalysis
IR	Infrared
ICP-MS	Inductively coupled plasma-mass spectrometry
SIMS	Secondary ion mass spectrometry
CCIM	Canadian Centre for Isotopic Microanalysis
Type II	Nitrogen free diamond
Type IaA	Nitrogen in diamond only aggregated in A centers
Type IaAB	Nitrogen in diamond aggregated in both A and B centers
Type IaB	Nitrogen in diamond only aggregated in B centers
Type Ib	Single substitution nitrogen in diamond
V-PDB	Vienna Pee Dee Belemite
ppm	Parts per million
at.ppm	Atomic parts per million
mW/m^2	Milliwatts per square meter
kbar	Kilobar
km	kilometer
kV	kilovolt
EV	electron volt
‰	parts per thousand or per mil
<	Less than
>	Greater than

˚C	Degree Celsius
U-type	Undifferentiated/Peridotitic
E-type	Eclogitic
LOD	Limit of detection
N	Nitrogen
n	Number
mss	Monosulfide solid solution
SL	Snap Lake
WDS	Wavelength dispersive spectrometry
µm	Micro-meter
Apfu	Atoms per formula unit
PT	Pressure-temperature
σ	Sigma or one standard deviation of the mean

1. Introduction and objectives

1.1 Introduction

Diamond is not only the hardest mineral on Earth but also one of the most valuable. It is sought after as a gemstone, for industrial uses, and in academic research. The high refractive index (~2.42 for yellow light with a wavelength of 589 nm) and its strong variation over the visible spectrum (from 2.41 for red to 2.45 for violet light) give diamond the ability to disperse light into a spectrum, aptly named "fire," making it a popular gemstone among jewelry collectors (Evans, 1976). Conversely, its extremely high heat conductivity accompanied by essentially non-existent electrical conductivity makes it an invaluable material for use in high powered electronics as a heat sink (Fromentin, 2004; Wei et al., 1993).

Geologically diamond provides us with vital information regarding fluid interactions deep within the lithospheric mantle where they were formed (Smit et al., 2016). These beautiful crystals provide the most direct evidence of conditions below the Earths' crust as other attempts to directly sample mantle via drilling have thus far been unsuccessful with current technologies. The fluids that interact to form diamond have unique and often changing isotopic signatures, which are recorded in the carbon and nitrogen isotopic signature incorporated in the diamond structure. These same fluids also precipitate/re-crystallize other minerals, which can become trapped within diamond as inclusions and protected from retrograde reactions and re-equilibration during exhumation and volcanic eruption thanks to their host diamonds' inert nature.

The isotopic signature observed in the diamond host, the inclusions recovered from within the diamond and the impurities (e.g. nitrogen, boron) in the diamond structure can all reflect

differing source chemistry, pressure and temperature conditions of the mantle during the time of formation (Tappert & Tappert, 2011).

1.2 Purpose of research

While many diamond mines have already been studied in detail, for Snap Lake on the Slave Craton in Canada only limited data exist. Previous studies of inclusions and their diamond hosts from the former Snap Lake diamond mine were completed by Pokhilenko *et al. (*2001, 2004), with samples taken during early exploration. Based on the first observation of rare high-Cr majoritic garnet inclusions, Pokhilenko *et al. (*2004) inferred the presence of an unusually thick lithospheric mantle root (>200 km), which at depths corresponding to the diamond stability field was mostly harzburgitic (Pokhilenko et al., 2001).

The purpose of this thesis is to conduct the first systematic study of Snap Lake diamonds and draw conclusions regarding the chemical environment in the lithospheric mantle underlying the southern Slave craton. I aim to determine if the diamond N content, $\delta^{13}C$, and $\delta^{15}N$, in combination with the associated inclusion chemistry, can support the conclusions of Pokhilenko *et al. (*2004).

This thesis study characterizes the various diamond substrates in the lithospheric mantle beneath Snap Lake as well as the conditions of diamond formation and mantle residence, based on a set of 147 inclusion-bearing diamonds provided by De Beers Group. For a subset of 89 diamonds, nitrogen content/aggregation state and stable isotope data of the diamond hosts will be paired with the major-element geochemistry of the accompanying mineral inclusions. In addition, garnet and clinopyroxene inclusions will be analyzed for their trace-element patterns, including rare earth elements, and olivine inclusions will be analyzed for a subset of trace-elements suitable for temperature estimates, including Al for use with the Al-in-olivine thermometer (Bussweiler et al., 2017).

The research aims to verify the presence of a super-thick lithospheric mantle beneath the southeast Slave Craton at ~ 530 Ma and provide important information regarding the paragenesis and chemical characteristics of diamond substrates underlying the southern Slave craton. Information from this study will also provide a better understanding of the diamond substrates beneath the nearby active Gahcho Kué Mine, in addition to supporting exploration work that is currently underway in the immediate area. Data obtained can also be utilized to draw conclusions about the geologic history and mantle conditions of the southern Slave.

2. General diamond background
2.1. Formation of diamonds

Natural diamonds have multiple origins including meteoritic, intra-collision zone settings, and shock metamorphism created by large impact events. Although scientifically very interesting, diamonds that have formed from these events are mostly very small, often polycrystalline, and do not form economic deposits (Bulanova, 1995; Sobolev & Shatsky, 1990). For the rest of the world's natural diamonds (~99%), formation mostly occurs within the lithospheric mantle, in a restricted area known as the diamond window, at typical depths of 140 to 200 km (Stachel & Harris, 2008, Stachel & Harris, 1997; Meyer, 1987; Boyd & Gurney, 1986). The diamond window, shown as a thin band or a triangular area as in Figure 2.1, is constrained by the graphite/diamond transition zone, the local geotherm, and the mantle adiabat (Tappert & Tappert, 2011; Stachel & Harris, 2008).

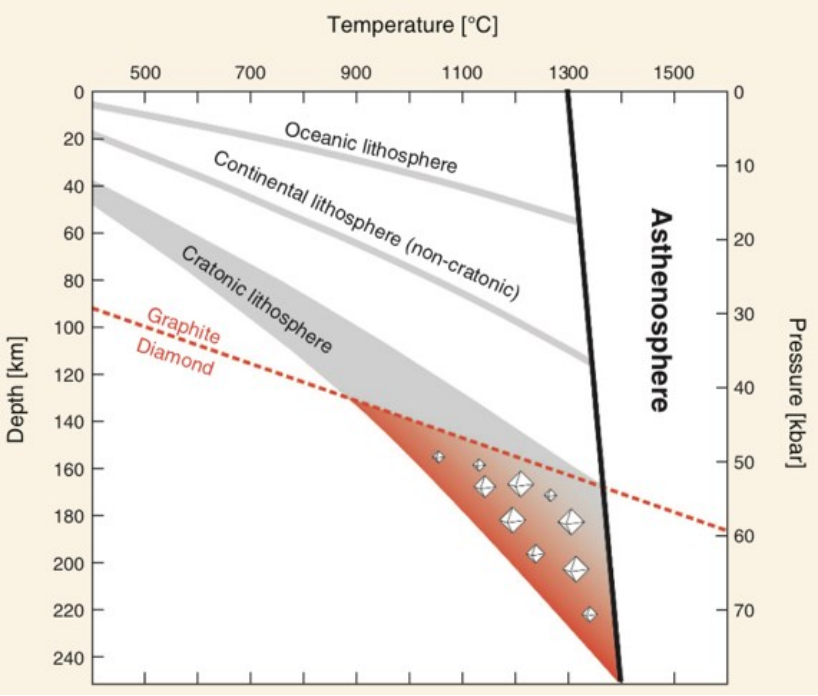

Figure 2.1: Pressure-temperature-depth diagram depicting the diamond window in comparison to typical geothermal gradients for oceanic, continental, and cratonic lithosphere. The diamond window is highlighted in red. From Tappert & Tappert (2011; their Figure. 1-03).

Primary diamond deposits have been linked to the cores of Archaean cratons older than 2.5 Ga through Clifford's rule (Janse, 1994). This rule is based on the fact that the rocks which underpin these ancient cratons to the depth of the diamond stability are much colder than asthenospheric mantle at comparable depths (Janse, 1994; Stachel, 2014). The lithospheric mantle rocks beneath these cratons have been tectonically stable for sometimes billions of years and formed as a result of major melting events producing a mantle highly depleted in Ca, Al and heat producing (radiogenic) elements such as K, Th and U (Pollack & Chapman, 1977). This depletion makes the mantle keel increasingly buoyant and cooler, resulting in a stable lithospheric mantle and favoring the formation of diamonds (Pollack & Chapman, 1977; Stachel & Harris, 2009; Pearson & Wittig, 2008)

Diamond formation is thought to occur through a number of possible mechanisms. The first of which involves the direct transformation of graphite into diamond. This mechanism appears limited to polycrystalline diamonds due to the reconstructive nature of the phase transition requiring a very high activation energy and thus happening extremely rapidly. The remaining mechanisms forming diamonds include the precipitation of diamond through redox reactions (from the reduction of CO_3^{2-} or CO_2, or the oxidation of species like CH_4), through crystallization of diamond in carbon oversaturated CHO fluids (Stachel & Luth, 2015) or during fluid-rock interactions due to a decrease in pH (Sverjensky & Huang, 2015). These three mechanisms could result in the growth zonation that is observed in gem-quality diamonds, indicating growth is episodic and slow. Diamonds are forming layer by layer often showing changing carbon isotopic composition and nitrogen concentrations, which cannot be achieved through the direct transition from graphite to diamond (Stachel & Harris, 2009).

2.1.1. Source Paragenesis

Two broad divisions of Earth's diamonds, based on the depth of formation, are subcratonic lithospheric and sublithospheric diamonds (Figure 2.2). Sublithospheric diamonds, which form between 250 and 800 km depth beneath the Earth's surface within the lower parts of the upper mantle, the transition zone, and the lower mantle, are characterized by the presence of ultra-high-pressure phases, such as majorite garnet, jeffbenite, bridgmanite, Ca-perovskite, and ferropericlase (Harte et al. 1999; Stachel et al., 2005). Sub-lithospheric diamonds are divided into metaeclogitic, metaperidotitic, and Ca-rich suites. Subcratonic lithospheric diamonds can also be divided into three suites: peridotitic (most common, accounting for 65%), eclogitic (less common, accounting for 33%), and websteritic (rare, accounting for 2%) showing a wide variety of possible mineral inclusions (Stachel & Harris, 2008).

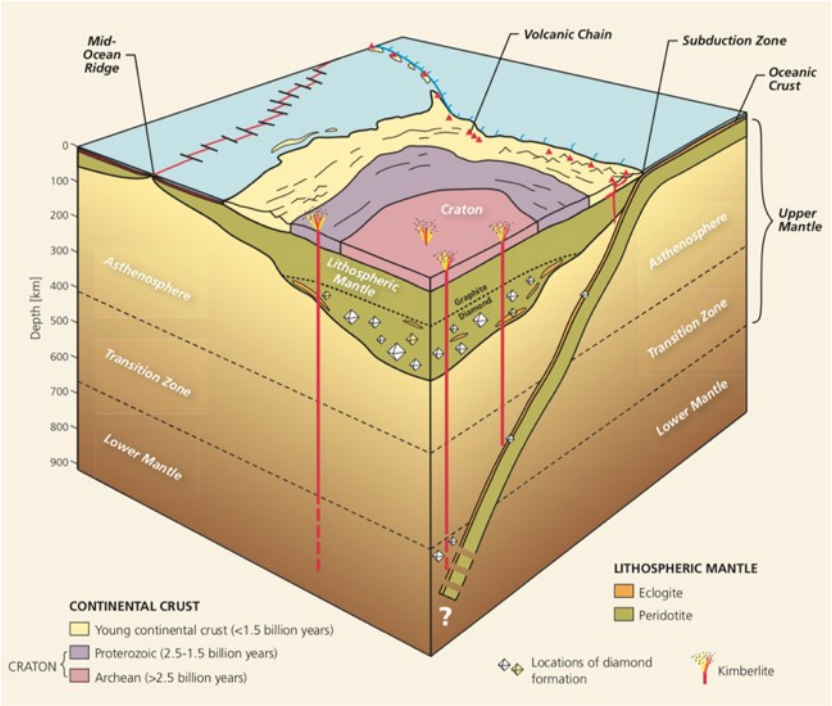

Figure 2.2: Cross-section of the Earth's crust and mantle depicting different locations of diamond formation. This diagram depicts the graphite/diamond transition within a stable Archean root, in addition to subduction-related diamond formation both within the lower mantle and transition zone. From Tappert & Tappert (2011; their Figure 1-02).

In the absence of mineral inclusions with known paragenesis, the source of the diamond-forming fluids can be further explored through carbon isotopic analysis of the host diamond. The two stable isotopes of carbon (^{12}C and ^{13}C) are both present in diamond and analysis of the ratios between them can assist in revealing the origin of that carbon. Analyses of carbon are presented as a ratio ($^{13}C/^{12}C$) which is conventionally expressed as the relative difference in ‰ $\delta^{13}C$ from the international Vienna-Pee Dee Belemnite (VPDB) standard. Globally diamonds range in $\delta^{13}C$ values from -41‰ to +3 ‰ (Cartigny et al., 2014). Despite differences in their overall range, both peridotitic and eclogitic diamonds show a dominant mode at approximately -5 ‰ (Cartigny et al., 2005), while a second mode is observed in eclogitic diamonds between ~-13 ‰ and -9 ‰ (Stachel, 2014). Lithospheric diamonds are the focus of this thesis. Hence, more detailed information regarding mineral inclusions and carbon isotope compositions of the three lithospheric suites is provided below.

2.1.1.1 Peridotitic diamonds

Peridotitic diamonds contain inclusions that have characteristically higher Mg and lower Ca and Al contents within olivine, clinopyroxene, and orthopyroxene in comparison to in the same minerals occurring as xenocrysts and within peridotite xenoliths in kimberlite (Harte et al., 1980). The peridotitic suite also includes minerals such as Mg-chromite and Cr-rich pyrope. Based on their inclusions, peridotitic diamonds can be classified further into harzburgitic, lherzolitic, and wehrlitic parageneses. Typically, these categories are assigned based on the composition of the garnets present. When dealing with high-Cr garnets (Cr_2O_3 > 1 wt%), Ca-rich garnets coexist with clinopyroxene (lherzolite) and Ca-poor garnets occur when clinopyroxene is absent (harzburgite; Sobolev et al., 1973; Gurney et al., 1984; Stachel & Harris, 2008).

Peridotitic diamonds show a range in $\delta^{13}C$ from -26.4 ‰ to +0.2 ‰ but typically (95 %) fall within the narrower range of -8 to -2 % (Stachel, 2014, Cartigny et al., 2014). This narrow range of the majority of peridotitic diamonds indicates that carbon for this paragenesis is most likely of mantle origin.

2.1.1.2 Eclogitic diamonds

In contrast to the peridotitic suite, the eclogitic inclusion suite is comprised of minerals with lower concentrations of Mg and low Cr (<1.0 wt% Cr_2O_3 in garnet), accompanied by higher concentrations of Ca, Al, and Na (Meyer, 1987; McDonough & Rudnick, 1998; Stachel, 2014). The eclogitic suite includes minerals such as Cr-poor garnet, omphacite (Na-rich clinopyroxene), and in more rare instances, kyanite, rutile, and coesite (Meyer, 1987). Eclogitic garnets can be sub-divided into containing high-Ca garnet (> 6 wt% CaO) and low-Ca garnet (<6 wt% CaO; Grütter et al., 2004).

Diamonds associated with eclogitic substrates or which contain eclogitic mineral inclusions show a wider $\delta^{13}C$ range from approximately -41.1 ‰ to 2.9 ‰ (De Stefano et al., 2009; Davies et al., 2003; Cartigny et al., 2014). The positive values correlate well with the recycling of marine carbonates, while the strongly negative values compare well with former organic matter thus indicating a possible subduction-related origin of eclogitic diamonds (Kirkley et al., 1991). The extremely ^{13}C depleted tail of the eclogitic distribution (down to -41 ‰) suggests involvement of methane in the formation of kerogen precursors for sedimentary organic carbon (Smart et al. 2011).

This idea, however, has been a major source of controversy, since the potential for the re-equilibration of carbon isotopic ratios within subducting oceanic crust is predicted to increase with temperature, thus potentially leading to a re-homogenization of the isotopic composition of subducted carbon to around the mantle value. Cartigny (2005) suggested instead that this larger range may be instead caused by fractionation in an open system. Criticism of this model focusses on the extremely high levels of Rayleigh fractionation required to achieve significant isotopic shifts and asserts that, therefore, the model cannot be used to explain the very negative values (< ~-15 ‰) seen over the eclogitic range.

2.1.1.3 Websteritic diamonds

Websteritic diamond inclusions are rarer (~2 %, see above) and not as well studied. The compositions fall in-between (often overlapping) that of peridotitic and eclogitic compositions. For instance, websteritic garnets can co-exist with both clinopyroxene and orthopyroxene (Gurney et al., 1984; Aulbach et al., 2002; Phillips et al., 2004). The $\delta^{13}C$ range of websteritic diamonds appears to be strongly associated with the locality from which they are recovered and do not appear to show any consistent pattern across multiple localities (Stachel et al., 2009). Websteritic diamonds do, however, tend to be isotopically light, showing similarities to the eclogitic isotopic range, in that the $\delta^{13}C$ range can reach as low as -41 (Stachel et al., 2009; De Stefano et al., 2009).

2.2 Morphologies of diamond

Diamonds are composed of nearly 100% carbon accompanied by some minor impurities: most commonly nitrogen, hydrogen and boron. Diamonds occur in nature as monocrystalline, fibrous, or polycrystalline crystals. Carbon forms tetrahedra within the diamond structure. The

arrangement of these tetrahedra results in an isometric (cubic) symmetry, with monocrystalline diamonds occurring in two primary geometric forms: octahedra and cuboids. Monocrystalline diamonds occur in a wide variety of appearances, all of which are a result of the modification of these two original geometric forms (Tappert & Tappert, 2011). The octahedron is the most common form, and when perfect is composed of 8 matching triangular faces. Ideal octahedral shapes, however, are not often observed in nature, instead, most natural diamonds have been distorted to some extent by favored growth directions. The amount of distortion in diamonds is variable and range from a transition of point apices to line apices, to full flattening or elongation of the octahedral shape. Regardless of the degree of distortion, the existence of octahedral habit indicates that the diamond grew in stable conditions, at a relatively slow rate (Harrison & Tolansky, 1964; Sunagawa, 1990; Tappert & Tappert, 2011). In general, octahedral diamonds form at slightly higher temperatures than their cuboid counterparts (Sunagawa, 1990).

The lowest levels of resorption of octahedral diamonds are observed as rounded corners/edges affecting the most protruded points and increases until the point at which the octahedral faces disappear completely and leave behind a rounded dodecahedron (or dodecahedroid) in its place (McCallum et al., 1994). This transition occurs in the stages shown below (Figure 2.3) where the amount of volume loss (in vol.%) increases substantially with the change in shape. In ideal scenarios, a dodecahedron is composed of 12 rhombic faces. In the case of resorbed diamonds, however, the rhombic faces are not flat but curved (i.e., are not true "faces" as they cannot be represented by a single pole point), and hence the resulting shape is referred to as a rounded dodecahedron. For this thesis, the cut off between octahedral and dodecahedral is placed at 50% surface area occupied by {111} faces and diamonds are denoted as O (<90%), OD

(50-90%), DO (10-49%) and D (<10%) based on the percentage residual octahedral faces present in the shape.

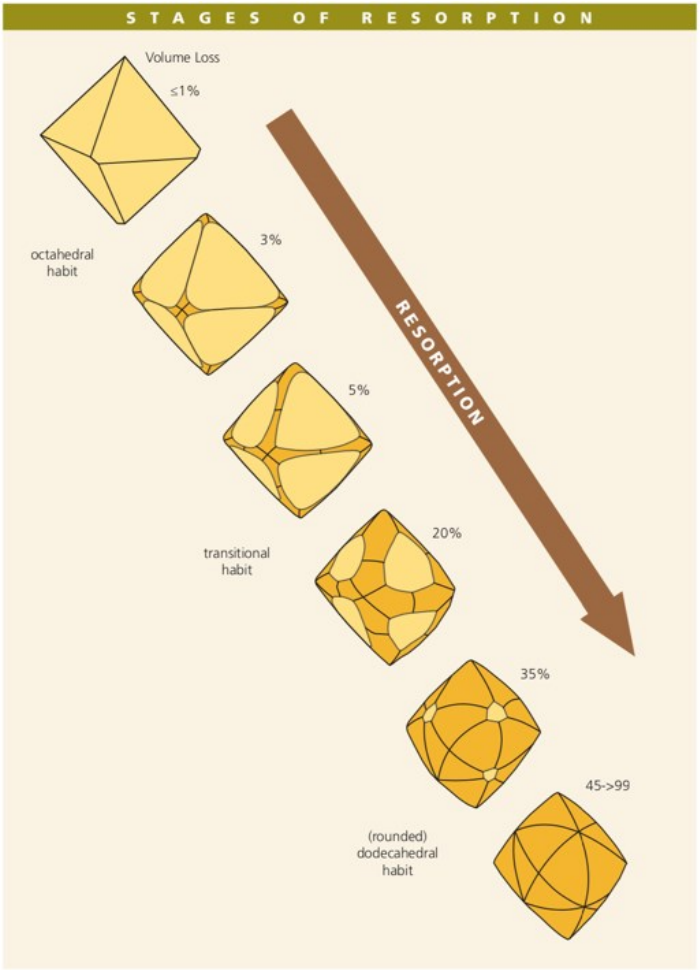

Figure 2.3: Stages of resorption of an octahedral diamond from Tappert & Tappert (2011; their Figure 2-11) which was modified from the diagram of McCallum et al. (1994).

2.2.1 Twins, parallel intergrowths and aggregates

Twins, parallel intergrowths, and aggregates are all formed by two or more intergrown diamonds. Twins are formed when two diamonds are joined together along a crystallographic plane. They can be connected along external crystal faces, termed contact twins, or along internal crystal faces, termed interpenetrant twins. Formed from the contact twinning of two flattened

octahedral diamonds, a macle is a triangular-shaped diamond that shows a twin line defining the location of the {111} compositional plane along the edge of the triangular shape. Another easily recognizable contact twin is the "Star of David" twin. This occurs when two octahedral macles, oriented in opposite directions, grow together to produce a six-pointed star. Interpenetrant twins instead consist of two diamonds that have grown within the same area, with differing orientations. These twins are most commonly seen in cubic diamonds but are sometimes observed in octahedrons as well (Tappert & Tappert, 2011; Slawson, 1950). Parallel intergrowths, often mistaken for twins, are instead the growth (and eventual adjoining) of two diamonds in a parallel orientation.

Aggregates, unlike twins or parallel intergrowths, are formed by 2 or more diamonds aggregating together with no true pattern in orientation or shape. Aggregates can be composed of diamonds with different shapes, colors, and sizes (Tappert & Tappert, 2011).

2.2.2 Irregular diamond/fragment

Diamonds that do not possess an identifiable shape are termed irregular. Apart from the lack of crystal faces these stones typically have smooth undulatory surfaces. Another type of irregular diamond is a fragment. Fragments exist when diamonds are fractured, leaving behind flat (sometime conchoidal) fracture planes which often show stepping, if breakage occurred before resorption (Tappert & Tappert, 2011). Fragmentation can occur in the mantle, during entrainment and ascent in the kimberlite, due to deposition in systems like rivers, or to damage resulting from mining processes. The presence or absence of etching and/or resorption features can indicate if the fragmentation was recent (post eruption) or occurred early (pre- or syn-eruptive) in the diamonds' life.

2.3 Colors of Diamond

Pure diamond is perceived as colorless to the naked eye, but natural diamonds exist in a wide array of colors. These colors are observed due to selective light absorption or emission influenced by the presence of color centers which affect the wavelengths which the diamond absorbs or emits. These color centers are formed from atomic or molecular impurities, such as hydrogen, nitrogen, sulphur, and boron (Figure 2.4). The color perceived is a function of both the number of color centers in the stone, as well as the size of the stone. The larger the stone, generally, the more intense the color.

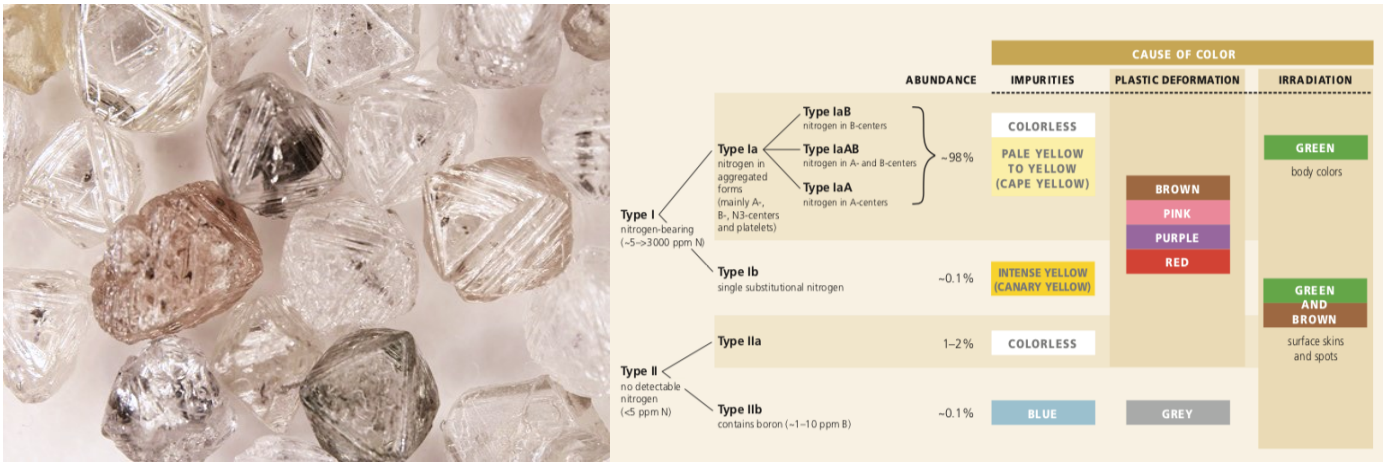

Figure 2.4: Photograph (left) showing representative colors observed in the studied Snap Lake diamond set and a flow chart (right) of possible diamond types, their potential colors and the causes of the coloration. Taken from Tappert & Tappert (2011).

Brown diamonds, which are the most common colored diamonds, are thought to get their color from plastic deformation resulting in vacancy clusters (Figure 2.4; Fisher, 2009). These vacancy clusters are understood to cause the absorption required to give the diamond a visible brown coloring (Fisher, 2009). Plastic deformation causing the brown coloration likely occurs immediately before or during kimberlite emplacement since diamonds deformed in the mantle

significantly earlier would lose the brown coloration again due to rapid annealing at high temperatures (Fisher, 2009).

Pink, red and purple diamonds, like brown, are a result of plastic deformation and usually show similar surface features as their brown counterparts. This includes the presence of deformation lines on their surfaces. These diamonds are rare and are largely produced from a few select mines, such as the Argyle mine in Western Australia (Figure 2.4; Tappert & Tappert, 2011).

Yellow diamonds are the second most common colored diamonds and, if intensely coloured, are very popular in the jewelry industry. The yellow coloring in diamond is caused by nitrogen atoms replacing carbon atoms in the crystal lattice (Figure 2.4; Evans, 1976). The intensity of the yellow coloring is dependent on the concentration of the nitrogen and the aggregation state or arrangements of the nitrogen within the diamond structure (Breeding & Shigley, 2009). Type Ib diamonds have very effective color centers (called C-centers) that form when single nitrogens replace single carbons, and even small amounts of single substitutional nitrogen will cause intense yellow coloring (termed Canary yellow). Conversely, in Type Ia diamonds, nitrogen can produce other colour centers, such as N3-centers (and associated N2-centers). N3-centers may be viewed as an intermediate stage when nitrogen aggregates from A- (pairs of nitrogen) to B-centers (aggregates of four N) in diamonds. N3 centers consist of 3 nitrogen surrounding a vacancy (physically the N3V defect), which leaves one unsaturated or “dangling” bond (Bursill & Glaisher, 1985). Transition between the first and second excited state is assumed to cause the characteristic absorption in the blue spectrum, referred to as N2 center (Babamoradi et al., 2017). This N2 center is responsible for the light-yellow color termed Cape yellow (Breeding & Shigley, 2009) but can also cause saturated yellow body colours, as in the case of diamonds

from Ellendale (Western Australia). For this reason, the absorption peaks in the visible spectrum caused by N3- and N2-centers are called “Cape lines” and located at 415 nm and 478 nm, respectively (Breeding & Shigley, 2009, Bursill & Glaisher, 1985).

More rare blue Type IIb diamonds have a single substitution of boron for carbon within a nitrogen-free crystal lattice, which is responsible for the blue color of some of these diamonds (Figure 2.4). Boron is another very effective color center and thus a very small amount (~1 ppm) can cause very intense blue body color in diamonds. Blue diamonds are the only diamonds that act as semi-conductors instead of insulators, due to the presence of boron in the crystal lattice, which acts as an acceptor (Chrenko, 1973; Custers, 1955). Blue body coloration was thought to be limited to Type IIb diamonds as the color can only develop in the absence of nitrogen (< 1 ppm; Chrenko, 1973). More recently, however, two other categories of natural blue diamonds have been described: (1) Blue to green-blue and (2) gray-blue to gray-violet (King et al., 1998 and references therein). These blue diamond’s get their color from radiation exposure and the presence of hydrogen respectively (King et al., 1998 and references therein).

Green diamonds are rare and are formed due to irradiation by radioactive elements such as uranium and thorium (Figure 2.4). Alpha-, beta- and gamma-decay of these radioactive elements in close proximity to diamonds can eject carbon atoms out of the diamond structure leaving behind vacancies, which cause the green coloration (Vance et al., 1973). Gamma-decay is thought to be the only radiation strong enough to result in extremely rare full-body coloration, as the gamma-rays can penetrate the entire diamond. More common are green coatings or surface spots, typically caused by very close proximity to particles experiencing alpha-decay; Alpha particles cannot penetrate the entire diamond and instead leaves spots along the surface of the diamond (Tappert &

Tappert, 2011) where minerals such a zircon or apatite were in contact. In the case of radioactive brines, the entire diamond surface may attain a thin green coat, as observed during early stage near-surface mining at Finsch (South Africa).

Lastly, grey/black stones are observed in many deposits worldwide. Their color is most often caused by the presence of a large proportion of tiny inclusions. Grey diamonds can be caused by the presence of graphite, whereas a black colour has been associated with inclusions of graphite, sulfides, magnetite, or hematite (Tappert & Tappert, 2011). This is generally not a desirable color and thus these diamonds can negatively affect the valuation of a mine.

2.4 Surface features of diamonds

There is large variability in surface features observed on diamonds (Figure 2.5). These surface features form at different stages during the diamond's history. Unlike octahedral diamonds, which can show both primary growth and secondary resorption features, cuboid and dodecahedral stones can only show secondary surface features.

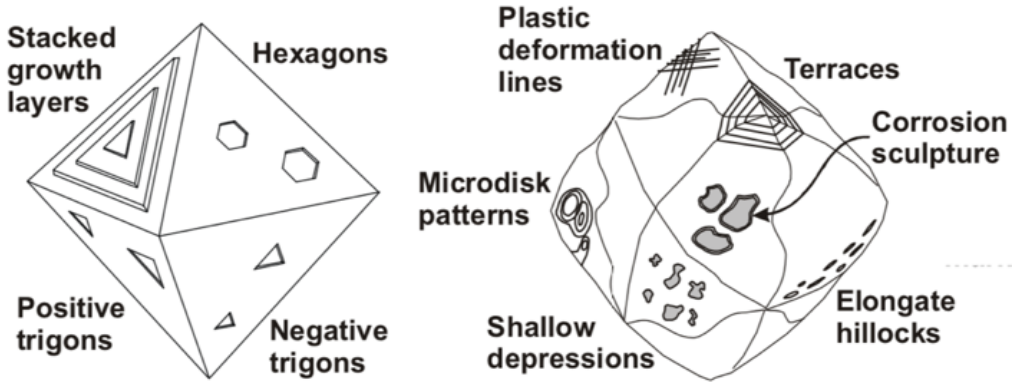

Figure 2.5: Surface feature of diamonds shown on octahedral diamonds with increasing resorption (primary octahedral and more rounded dodecahedral faces). From Stachel (2014).

2.4.1 Growth features

Primary surface features are only observed on octahedral diamonds and may be present as triangular growth plates, also called stacked growth layers (Figure 2.5). These triangular plates can overlap, creating pyramid-like stacks on the octahedral surface, or be imbricated in a more irregular pattern (Tappert & Tappert, 2011; Robinson, 1979). Immediately following development, the edges of these plates are sharp, but they are rarely observed this way on natural diamonds. Instead, most of the time resorption results in rounded edges of the growth layers (Robinson, 1979), which upon further resorption gradually take on the shape of shield-shaped laminae (see below).

2.4.2 Resorption features

2.4.2.1 Trigons and tetragons

Limited to octahedral diamond surfaces, trigons, or triangular pits are a very commonly observed secondary feature (Figure 2.5). Although positive trigons are observed on some diamonds, negative trigons are much more common. Negative trigons are present in an orientation opposite to that of the underlying crystal face (Lang, 1964). The orientation of the trigons formed on a diamond surface is thought to be dependent upon the temperature at which the etching through fluid occurs (Omar et al., 1954; Evans & Sauter, 1961). At higher temperatures, above 1000 ^{o}C, trigons form in the negative orientation, whereas etching that occurs at lower temperatures result in positively oriented trigons (Evans & Sauter, 1961). In less common situations, both positive and negative trigons have been observed on the same surface and in certain instances can combine to form hexagonal pits (Evans & Sauter, 1961; Figure 2.5).

Similar to trigons on octahedral diamonds, tetragons, or square pits are developed on cuboid faces (Evans & Sauter, 1961). Corresponding to the negative and positive orientations of trigons, tetragons can also be classified this way. Negative tetragons are rotated 45 ^{o} relative to the orientation of the cubic crystal face, while positive tetragons have sides parallel to the {100} face. Again, negative tetragons, like negative trigons, are more commonly observed and the temperature of the etching fluid is a key component in the determination of the orientation developed (Evans & Sauter, 1961).

2.4.2.2 Shield-shaped lamina

As a result of resorption of individual triangular plates, or growth layers, shield-shaped lamina have curved edges creating a shield-like appearance. These laminae are typically very thin and are distinguished from triangular growth plates based on their shape (Tappert & Tappert, 2011).

2.4.2.3 Terraces and hillocks

Terraces and hillocks are both observed on dodecahedral diamond surfaces exclusively (Figure 2.5). Terraces form as bands around the three-fold axes of dodecahedral diamond crystals and can be three- or six-sided. These bands form during the exhumation of primary growth layering during intense resorption of originally octahedral diamond as it transitions to a dodecahedral shape (Moore & Lang, 1974).

Similar to terraces, hillocks are also observed most often aligned around the three-fold axis of a dodecahedral diamond, again oriented parallel to the edges of primary growth layers (Tappert & Tappert, 2011). Hillocks appear to be longer on dodecahedral stones which show remnant

octahedral faces and shorter on those which show remnant cuboid faces. They also tend to become shorter with increased resorption, transitioning from pyramidal hillocks to drop-shape hillocks (Tappert & Tappert, 2011; Robinson, 1979).

2.4.2.4 Corrosion sculpture

Corrosion sculpture is a result of late-stage etching (Figure 2.5; Tappert & Tappert, 2011) and usually appears as elliptical or irregularly curved pits, which when deep enough can be striated at the bottom (Pandeya & Tolansky, 1961; Robinson, 1979). When the pits are shallow and un-striated, they are referred to as shallow depressions (Tappert & Tappert, 2011). Corrosion sculpture and shallow depressions appear to be more common on diamonds from deeper levels within the kimberlite, indicating that they likely result from corrosion in the root zone of kimberlites following emplacement (Robinson, 1979).

2.4.2.5 Micro-disks

Similar in appearance to corrosion sculpture, micro-discs differ from the latter in that they are raised from the diamond surface, instead of pitted. These discs are likely formed as a result of either gas or liquid micro-bubbles which preferentially protect the diamond surface beneath them from any etching fluids present (Pandeya & Tolansky, 1961).

2.4.3 Surface features not related to specific crystal faces

Surface features such as deformation lines, ruts, frosting, and graphite coating are not restricted to any specific diamond shape, or crystal face (Robinson, 1979). Deformation lines are a result of displacement and shifting of carbon atoms along octahedral planes or glide-planes

caused by plastic deformation (Tappert & Tappert, 2011, Fisher et al., 2009). These lines can be observed in multiple orientations across the same stone, which correspond to the four different orientations of octahedral planes (Tappert & Tappert, 2011). On un-resorbed octahedral faces, deformation lines are not observed as sharp ridges but instead are discernible as rows of aligned trigons (Tappert & Tappert, 2011), sometimes connected by a fine line.

Some natural diamonds have an opaque or frosted coating on them, which is thought to be a result of extremely rapid micro-etching occurring post kimberlite emplacement (Robinson, 1979).

Ruts are deep gauges in the diamond surface which do not show any relationship to the crystallographic orientation of the surfaces on which they are observed. These ruts are thought to have formed due to pre-existing areas of weakness, which are then expanded through etching and resorption (Tappert & Tappert, 2011).

3. Geological Background
3.1 Introduction

The Snap Lake kimberlite dyke is located within the Slave Craton (Figure 3.1) in Northern Canada. The Slave craton is a 210 000 km^2 Archean province which is located within the much larger North American craton, stretching from the deep southern USA to as far north as Greenland (Isachsen & Bowring, 1994; Padgham & Fyson, 1992).

The Slave Craton is structurally bound by fault zones and younger orogens (Figure 3.1). The northern edge of the Slave Craton is bound by the Bathurst fault zone. The southern border is bounded by both the Macdonald Fault, separating the Slave Craton from the Taltson magmatic zone in the Southwest, and the Great Slave Lake Shear Zone (1.98-1.93 Ga) in the southeast. The Thelon orogen (2.0-1.9 Ga) and the Wopmay Orogen (1.9-1.8 Ga) bound the Slave Craton in the East and West respectively (Hoffman et al., 1989).

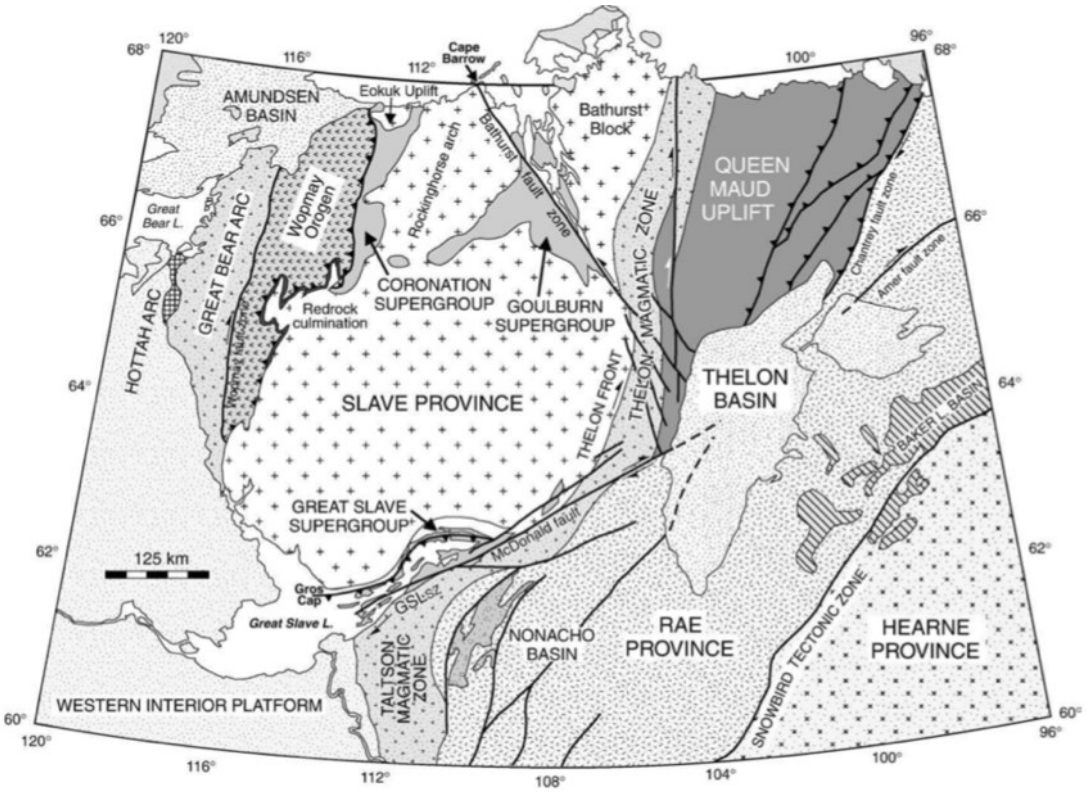

Figure 3.1: Simplified map of the Slave craton showing the bounding faults or orogens on all sides from Helmstaedt, (2009).

3.2 Geology and formation of the Slave Craton

The Slave Craton rock record extends from 4.05 Ga to 2.55 Ga and is composed mainly of gneiss, migmatite and granite as well as a large number metasedimentary (typically meta-turbiditic), metavolcanic and plutonic rocks (Bleeker et al., 1999; Padgham & Fyson, 1992; James & Mortenson, 1992). Throughout the craton, volcanic rock sequences tend to be much younger than their granite, gneiss, and metasedimentary neighbors (Reimick et al., 2014). Setting the Slave craton apart from most other Archean granite-greenstone type provinces is the high abundance of sedimentary rocks (70-80% greywacke – mudstone; Padgham & Fyson, 1992), as well its lack of ultramafic rocks and generally high abundance of deformed granites (Thompson et al., 1995; Jenner et al., 1981).

Some of the oldest terrestrial rocks known, the 4.05 to 3.40 Ga old Acasta gneiss complex, lie at the eastern edge of the Slave Craton (Reimick et al., 2014; Bowring et al., 1989, King, 1986). This complex is part of a much larger gneissic basement complex named the Central Slave Basement Complex (CSBC; Bleeker, 2002; Bleeker et al., 1999). Although the CSBC plays host to the Acasta gneiss complex, the majority of the rocks in this basement are composed of much younger (3.40 – 2.85 Ga) quartzite (Bleeker et al., 1999). The CSBC is composed of the older divisions of the Slave Craton proposed by Thompson et al. (1995; the Jolly Lake Complex (JLC)) and Henderson (1985; Sleepy Dragon Complex (SDC) and the Anton Complex (AC)).

The West Slave Terrane is almost exclusively composed of the CSBC. The granodiorite to quartz-diorite rocks of the Anton terrane dip below the Wopmay orogen in the far west of the Slave craton (Kusky, 1989; King, 1986; Henderson, 1985). Further to the east, however, the Anton terrane is present as a thick almost vertical mylonite zone (Kusky, 1989). The Anton terrane is thought to be composed of remnants of an older continent, and deformation observed has been

dated to ~2.6 Ga (Figure 3.2a; Kusky, 1989). Despite this, the origin and derivation of these rocks has not yet been well explained. To the east of the Anton terrane is the Sleepy Dragon Terrane, composed of intermediate to mafic quartzofeldspathic gneisses, banded and magmatic gneisses, and chloritic granites (Kusky, 1989; Henderson, 1985). The Sleepy Dragon Terrane may also be remnants of an ancient microcontinent, although Kusky (1988) suggests that it is more likely a piece of the Anton terrane which was uplifted and transported westward during an orogenic event (Figure 3.2c).

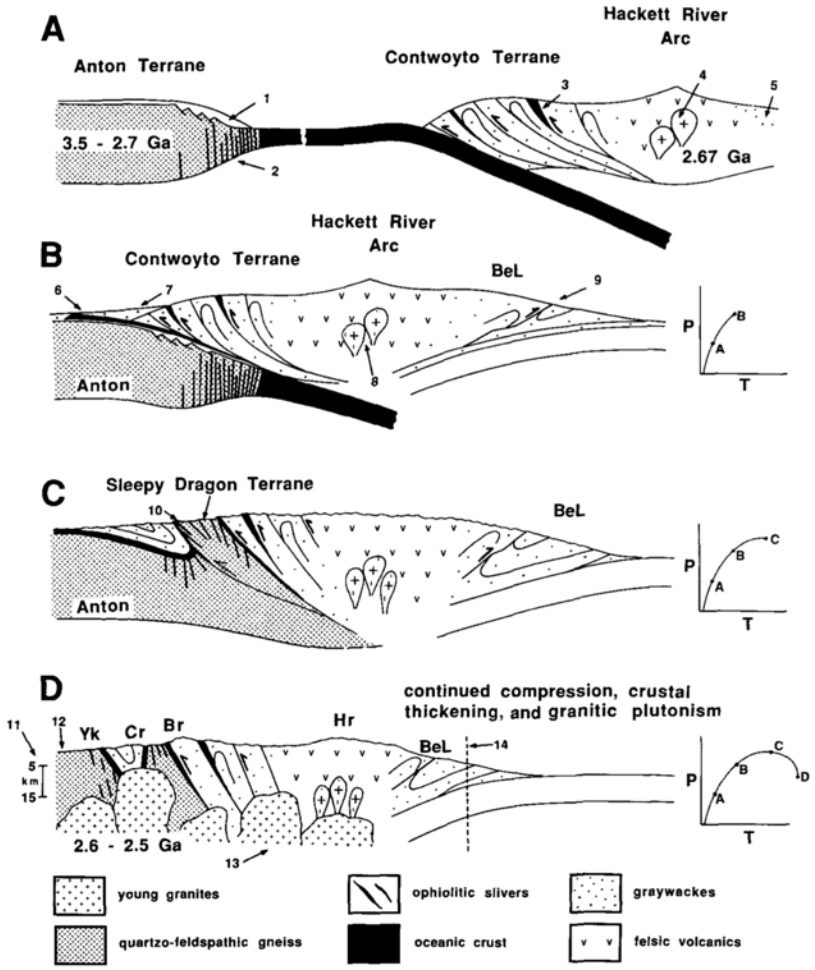

Figure 3.2: Tectonic model of accretion of the Slave craton taken from Kusky, (1989). A) Anton terrane being brought closer to the Contwotyo terrane via subduction, B) Contwoyto terrane overlying the Anton terrane, C) Sleepy Dragon terrane (remnants of the Anton terrane uplifted), D) the continuations of compression and thickening in combination with granitic plutonism creating the terrane we observe on the surface now.

The presence of the CSBC underlying the western and central terranes of the Slave Craton differentiates them from the eastern terranes where the CSBC is absent (Bleeker, 2002; Sircombe et al., 2001; Hoffman et al., 1989). This division between east and west terranes appears to roughly agree with the boundary proposed by Thorpe et al. (1992) based on Pb-isotope data from the Yellowknife Supergroup.

Terranes on the east side of the Slave craton include the Contwoyto Terrane and the Hackett River Arc. The Hackett River Arc is composed of a series of northwest-striking volcanic belts contrasted with those observed in the west due to their dominantly mafic composition (Padgham, 1985). This terrane is interpreted to be an island arc that formed above a subduction zone between 2.70-2.67 Ga (Figure 5; Kusky, 1989). The Contwoyto terrane consists mainly of laterally continuous gray-wacke to mudstone turbidites with more minor instances of allochthonous greenstone belts showing ophiolite-like stratigraphy locally (Kusky, 1989). This terrane is similar both structurally and lithologically to a forearc accretionary zone and the west-verging folds are consistent with an east-dipping subduction zone (Figure 3.2b; Kusky, 1989).

The CSBC is unconformably overlain by a discontinuous sequence of Archean Greenstone Belts, called the Yellowknife Supergroup (2.71-2.65 Ga; van Breemen et al., 1992). These greenstone belts are composed of locally deformed sequences of mafic, ultramafic, and more minor felsic volcanic rocks, conglomerate groups, quartzite, and banded iron formation (Bleeker, 1999; van Breemen et al., 1992).

3.3 Deformation and plutonism

The intrusion of granitoid plutonic rocks often marks the final stabilization of many late Archean cratons, including the Slave craton (Davies et al., 1994). This stabilization or

"cratonisation" is thought to be a result of a loss of volatiles in the subcrustal mantle lithosphere, in addition to intracrustal melting at a large scale and high-K granite production. These factors ultimately result in an elevated solidus temperature and thus give the craton new resistance to subsequent melting events (Pollack, 1986). This resistance to subsequent melting as well as the depletion of the lithospheric mantle and lower crust of heat-producing elements in turn results in a cooled and stable craton (Pollack, 1986; Kröner, 1991).

The Slave Craton experienced three distinct groups of plutonism between 2.69 - 2.58 Ga. Group one plutonism, composed of trondhjemites and high-Al diorites, was active between 2.69 – 2.65 Ga and formed the Central Belt, Gondor, Wishbone and Olga Plutonic Suites. This group of plutonism precedes deformation and peak metamorphism. Group two plutonism, composed of syn- to late-deformational massive to foliated monzodiorite to granodiorite rocks with associated trondhjemites, was intruded between 2.61 – 2.60 Ga. These rocks formed the Concession and Seige Plutonic Suites respectively. Finally, Group three plutonism, composed of post-deformational massive micaceous granites, was intruded between 2.60 – 2.58 Ga. This group of plutonism formed the Contwoyto and Yamba Plutonic Suites, which are differentiated by the occurrence of muscovite-biotite granites and solely biotite granites, respectively (van Breemen et al., 1992; Davis et al., 1994).

In general Group one and two plutons are calc-alkaline in composition and result in trace-element patterns that align well with modern subduction zone settings. Conversely, Group three plutons are more comparable to K-U-Th rich granite suites observed in many Phanerozoic post-orogenic settings (Davies et al., 1994) and have been described as the final stage in cratonisation of the Slave (Isaschsen & Bowring, 1994; Griffin et al., 1999).

In addition to these plutonic suites, several Proterozoic dyke swarms have also been documented across the Slave craton between 2.23 and 1.27 Ga (LeCheminant et al., 1996; Ernst & Buchan, 2001). The Malley dyke swarm (2.23 Ga) and slightly younger MacKay dyke swarm (2.21 Ga) trend northeast and east, respectively and are thought to be associated with rifting and break-up along the cratons southern and eastern margins (LeCheminant et al., 1996; LeCheminant & van Breemen, 1994). Younger still and with similar orientation to the MacKay dyke swarm, the ENE-striking Dogrib dyke swarm intruded the Slave craton at ~2.19 Ga (McGlynn & Irving, 1975). The Dogrib dyke swarm accompanied the Duck Lake dykes (~2.18 Ga), both of which are thought to be a result of the emplacement of a Large Igneous Province (LIP) in the southwest Slave craton (Ernst & Bleeker, 2010). Following these intrusion events and the creation of the Kilohigok sedimentary basin north of the Slave, the Lac de Gras dyke swarm (2.03-2.02 Ga) intruded from the northeast corner, likely related to the coeval Booth River intrusive complex (LeCheminant et al., 1996; Ernst & Bleeker, 2010). Thought originally to be older than the Lac de Gras dyke swarm, the Hearne dyke swarm was recently more accurately dated to approximately 1.90 Ga by Bleeker et al. (2008). These dykes are thought to be related to the collisional events along the east and south margins of the Slave craton, forming the Thelon tectonic zone, and Great Slave Lake shear zone respectively (LeCheminant et al., 1996; Ernst & Bleeker, 2010). Conversely, it has been suggested that the Hearne dykes are actually sourced from the Snowbird LIP observed in the adjacent Rae craton (Ernst & Bleeker, 2010; Buchan et al., 2009).

Collectively, the above dyke swarms appear to show a greater degree of metamorphism with increased proximity to both the Thelon Tectonic Zone on the east and the Wopmay orogen on the west. This is likely due to the collisional events occurring on either side of the Archean craton during the formation of Laurentia between 1.9-1.8 Ga (Buchan et al., 2009; Henderson et

al., 1990). In addition, all of the above-mentioned Paleoproterozoic dyke swarms are crosscut by the massive Mesoproterozoic Mackenzie dyke swarm (1.27 Ga) which can be observed across the entire Slave craton. These dykes are observed, radiating outwards for more than 2400 km along strike from their origin near Victoria Island (Buchan et al., 2009; LeCheminant et al., 1996).

3.4 Lithospheric mantle underlying the Slave Craton

Information regarding the lithospheric mantle beneath Archean cratons is typically inferred directly from studies of xenoliths and indirectly, by geophysical experiments and from the chemical composition of mantle-derived magmas (Heaman & Pearson, 2010). Xenolith geochemistry can provide great insight into the mantle composition, structure, and thermal state of the lithospheric mantle beneath a craton. However, these samples also prove to be very strongly influenced by metasomatic events directly before and during host volcanic rock activity (Pearson & Wittig, 2008; Heaman & Pearson, 2010). For instance, it has been observed that a large percentage of clinopyroxene and some garnets within these cratonic peridotites actually come from secondary events related to mantle metasomatism (Pearson & Wittig, 2008; Griffin et al., 1999). For this reason, models should combine efforts with geophysical and petrographic-geochemical-isotopic compositional data to best infer the compositional makeup of the lithospheric mantle below the Slave craton (Heaman & Pearson, 2010; Snyder et al., 2014).

3.4.1 Overview Slave Craton

In the most general sense, the dominant rock type within the Slave cratonic mantle is peridotite (Kopylova et al., 1999a; Heaman & Pearson, 2010). More recently, Griffin et al. (1999) and Kopylova & Caro (2004) showed that the uppermost ~50 km, however, are distinct in that

they consist of significantly depleted spinel peridotite, with Mg# ranging from 92-94. The minimum depth to the lithosphere-asthenosphere boundary varies across the Slave craton but generally increases in depth towards the east (Heaman & Pearson, 2010). In the northwest and southwest Slave, we see estimates of 160-190 km depth, while under Lac de Gras and Gahcho Kué it is estimated to be between 220 and 220-250 km depth, respectively (Kopylova & Russell, 2000; Griffin et al., 1999; Kopylova & Caro, 2004). Also, the observation of craton scale enhanced conductivity indicates pervasive metasomatism occurred throughout the Slave at between 150-220 km depth (Snyder et al., 2014).

The lithospheric mantle underlying the Slave craton has been divided into three eastnortheast-trending compositional domains (Grütter et al., 1999; Heaman & Pearson, 2010). These inferred domains, first based on geochemical variations within recovered garnet xenocrysts (Grütter et al., 1999), also roughly coincide with metallogenic domains suggested by Padgham (1992; Figure 3.3), the teleseismic studies of Bostock (1997) and the discovery of the central slave mantle conductor (CSMC; Jones et al., 2003; Snyder & Bruneton, 2007). The three domains have been appropriately named; Northern, Central, and Southern Slave zones (Figure 3.3).

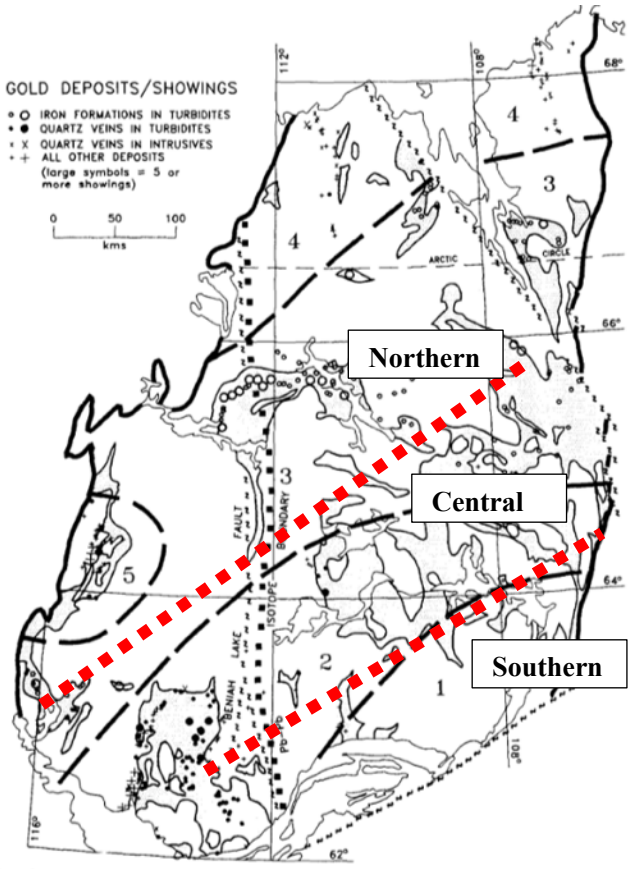

Figure 3.3: Map of Gold deposits and inferred metallogenic domains taken from Padgham (1992). Annotated with the three domains of the Slave craton (Northern, Central and Southern; Grütter et al. 1999). The four metallic domains described by Padgham (1992) roughly agree.

3.4.2 Northern Slave

The northern Slave mantle has best been characterized using xenoliths and xenocrysts recovered from the Jericho kimberlite. Kopylova et al. (1999a) described a high abundance of peridotite (~60%), a relatively high abundance of eclogitic xenoliths (~25%), and a more minor component of pyroxenite (~15%) within their large xenolith suite. These samples appear to almost completely lack harzburgitic garnets and show a notably high clinopyroxene content, which likely causes the higher CaO content observed in garnet chemistry within the northern Slave when compared to central and southern portions (Kopylova & Russell, 2000; Grütter et al., 1999). In general, the peridotite observed in the northern Slave is the least depleted and suggests the presence of a stratified-lherzolite rich domain below (Kopylova et al., 1998; Kopylova & Caro, 2004).

Utilizing Re-Os isotopes and chondrite-normalized platinum group element (PGE) patterns Kopylova et al. (1998) showed that mantle beneath the northern Slave is not only chemically stratified but also stratified with respect to age (Figure 3.4). The garnet-spinel transition zone was observed in the northern Slave craton mantle at a depth of 80-100 km. This zone separates the garnet-free mantle (spinel peridotite) from the garnet-bearing mantle below. This also represents the age boundary moving from Archean mantle towards Archean-Proterozoic ages. Below this, a fertile Proterozoic garnet peridotite lithology exists, stretching to between 190 - 200 km in depth. Finally, this "fertile" peridotite layer is underlain by a pyroxenite-rich basal layer marking the transition from the lithosphere to the asthenosphere at ~200 km depth (Kopylova & Russell, 2000).

The northern Slave craton shows a geothermal gradient (Kopylova et al. 1999b; Tappert et al., 2011), at the time of kimberlite eruption, that matches the 37 – 38 mW/m^2 surface heat flow model geotherms of Pollack & Chapman, (1977).

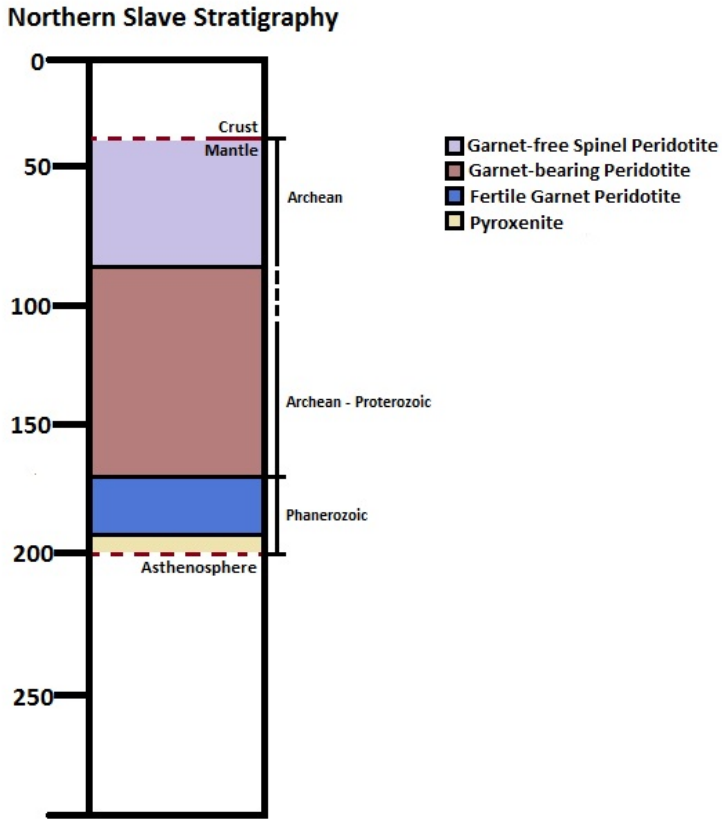

Figure 3.4: Northern Slave stratigraphic column drawn from data and interpretations made by Kopylova & Caro (2004), Kopylova & Russell (2000), O'Reilly et al. (2001), Kopylova et al. (1998, 1999b) and Jones et al. (2003).

3.4.3 Central Slave Craton

The most depleted compositions observed in the Slave mantle are from the central Slave craton (Kopylova & McCammon, 2000). Samples from Lac de Gras (mostly the Diavik and Ekati kimberlites) help to constrain the geochemical makeup of the lithospheric mantle beneath the central Slave craton (Jones et al., 2003). A bi-layered lithosphere, composed of a shallower ultra-depleted harzburgite rich layer and a deeper, less-depleted layer is observed underlying this area of the Slave (Griffin et al. 1999; O'Reilly et al., 2001). A localized region of low resistivity - beginning at ~80-110 km depth – termed the Central Slave Mantle Conductor (CSMC) appears to correlate well with the shallower half of the above described ultra-depleted layer (Figure 3.5; Jones et al., 2001, 2003; Griffin et al., 1999).

Separating the two chemical layers at approximately 140 - 150 km in depth is a fairly distinct geochemical boundary defined by olivine composition as well as the trace-element (Zr, Y, and Ti) composition of peridotitic garnet (O'Reilly et al., 2001; Figure 3.5). The thickness of these two layers appears to vary across the central Slave craton, reaching maximum thickness and depth in the central area, while closer to the margins the ultra-depleted harzburgite layer appears substantially thinned, or absent altogether (Figure 3.5; O'Reilly et al., 2001). In the upper, more Mg-rich layer, olivine forsterite content ranges from ~92-94 whereas the lower, less-depleted layer shows olivine forsterite contents ranging from ~91-92 (O'Reilly et al., 2001). In agreement, garnets sampling the uppermost layer are predominantly harzburgitic in composition (~60%), while the lower, less depleted layer reveals only 15 – 20% harzburgite and an increased abundance of "fertile" lherzolite (80-85%; Griffin et al., 1999; O'Reilly et al., 2001).

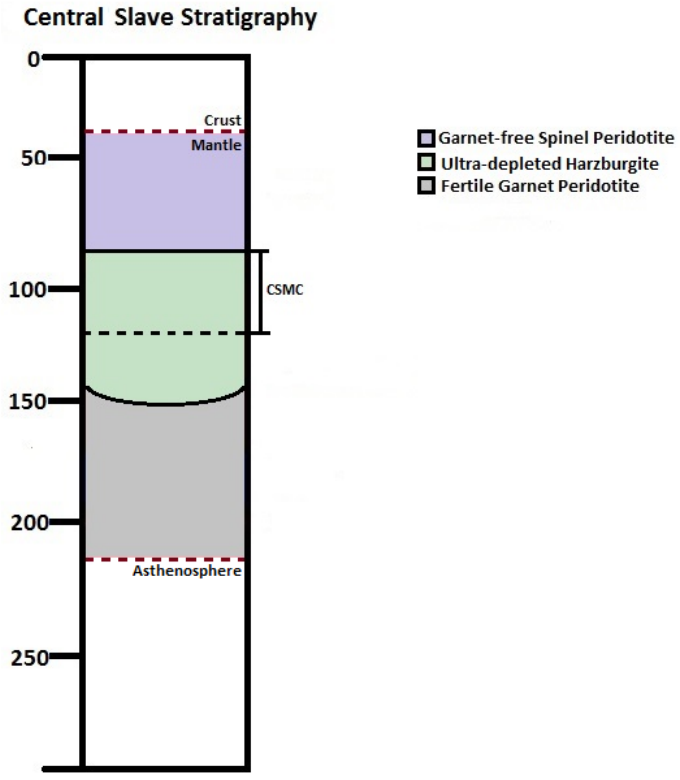

Figure 3.5: Central Slave stratigraphic column drawn based on data and interpretations taken from Kopylova & Caro (2004), Kopylova & Russell (2000), O'Reilly et al. (2001), Kopylova et al. (1998, 1999b) and Jones et al. (2003).

Pressure-temperature (P-T) studies of xenoliths from the Lac de Gras kimberlite field revealed two groups; a low temperature (<900˚C) and a high temperature (>900˚C) group. Xenoliths with low equilibrium temperatures fall close to a 35 mW/m^2 conductive geotherm, while higher temperature xenoliths fall much closer to a conductive geotherm at 40 mW/m^2 (Pearson et al., 1999; Griffin et al., 1999). The temperature estimates for eclogitic xenoliths recovered ranged from ~890-1250˚C thus indicating that these were also formed within the deeper layer (Pearson et al., 1999).

3.4.4 Southern Slave Craton

The southern Slave cratonic mantle has been separated into SE and SW domains (Carbno & Canil, 2002), using samples from the Dry Bones kimberlite in the SW and Gahcho Kué and Snap Lake in the SE. Both of these domains show WSW trending mantle anisotropy and relatively low conductivity typical of the lithospheric mantle (Jones et al., 2001; Kopylova & Caro, 2004).

The SW domain, defined based on the geochemistry of garnet xenocrysts, is composed of an ultra-depleted harzburgite at shallow depths underlain by a less depleted mantle lacking high-Cr harzburgitic garnets (Kopylova & Caro, 2004). This shallower ultra-depleted layer, extending from the central Slave craton, thins out southwest of the Drybones Bay kimberlite (Carbno & Canil, 2002). Xenocrysts from the Dry Bones kimberlites indicate that the lithospheric mantle extends to ~ 160 km in depth (Carbno & Canil, 2002).

Conversely, the SE slave mantle is dominantly lherzolite with some lesser eclogite (Grütter et al., 1999). Harzburgitic garnet xenocrysts sampled from Gahcho Kué show high Cr_2O_3 contents (> 8 wt%) but are not classified as ultra-depleted based on CaO content (Carbno & Canil, 2002; Kopylova & Caro, 2004). Despite this decrease in total depletion, similar to the rest of the Slave

craton, the shallow mantle shows greater chemical depletion than the underlying deeper sections (Kopylova & Caro, 2004). Thermobarometric data combined with mineral chemistry from both Gahcho Kué and Snap Lake indicate that the lithosphere underlying the SE Slave craton is anomalously thick and cool, extending to between 220-250 km depth and recording temperatures from 600 to 1300 ˚C (Kopylova & Caro, 2004; Pokhilenko et al., 2001, 2004).

3.5 Slave Craton Kimberlites

Since 1991, more than 300 kimberlite occurrences have been documented within the Slave craton, the majority of which are located in the central Slave province (Davis & Kjarsgaard, 1997; Heaman et al., 2003). Kimberlite emplacement in the Slave craton spans a period of almost 600 myr from the 616 Ma Artemisia kimberlite (Armstrong et al. 2012) to the 47.5 Ma Lac de Gras North Paul pipe (Davis & Kjarsgaard, 1997). Comparable to Yakutia and southern Africa, the Slave craton shows multiple kimberlite fields of various ages emplaced in a relatively small geographic area (Creaser et al., 2004). Heaman et al. (2003) subdivides the Slave craton kimberlites into 4 distinct age domains (Figure 3.6).

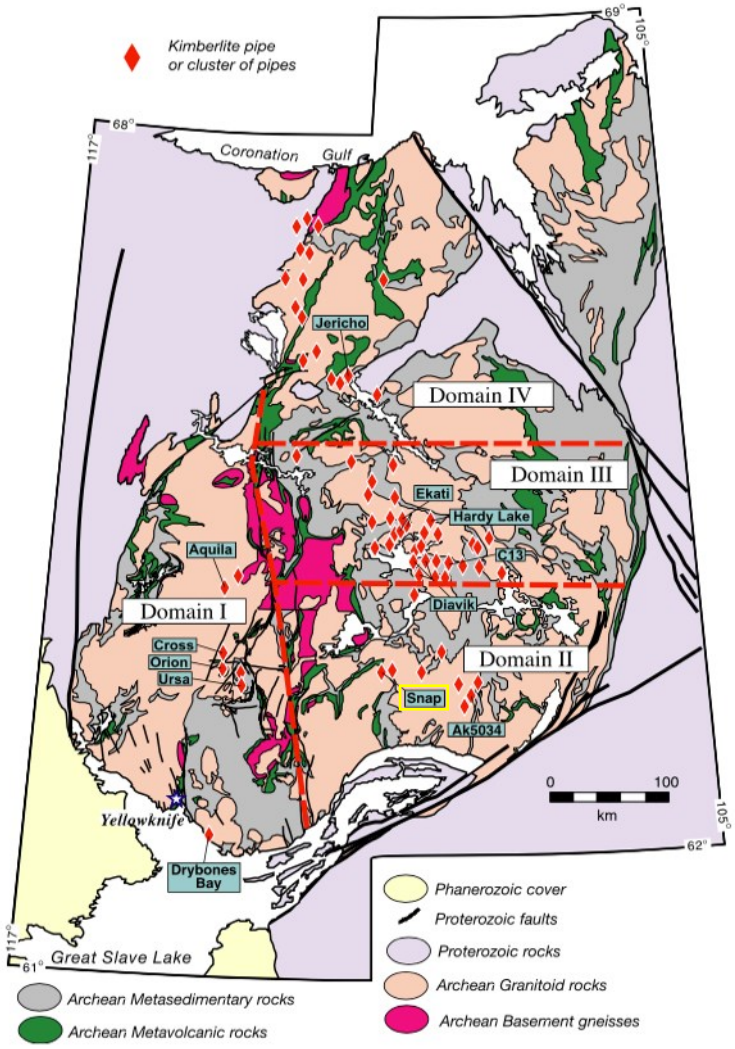

Figure 3.6: Kimberlite domains of Heaman *et al. (*2003). Snap Lake kimberlite dyke is labeled and outlined in yellow.

The southwestern Slave domain is characterized by Siluro-Ordovician (435-459 Ma) kimberlite magmatism; including Orion, Drybones Bay, Cross, and Ursa kimberlites. The southeastern Slave domain is characterized by Cambrian (523-542 Ma) kimberlite magmatism; including the AK5034 kimberlite and the Snap Lake dyke. The central Slave domain is characterized by Cretaceous and Eocene (74-48 Ma) kimberlite magmatism; including the Lac de Gras (with the Ekati and Diavik Mine properties) and Tli Kwi Cho (hosting DO27) fields. Lastly, the northern Slave domain is characterized by mixed Jurassic (173 Ma), Permian (286 Ma) and Cambrian (~616 - 520 Ma) kimberlite magmatism; including the Contwoyto field (Jericho),

Victoria Island field (Snowy Owl, Longspur, Phalarope, etc.) and the Coronation Gulf Field (Artemisiam, Potentilla, and Anuri; Armstrong et al. 2012; for a complete overview, see Heaman et al., 2003).

The majority of the Slave craton's economically significant diamondiferous pipes were emplaced in the Eocene and occur close to Lac de Gras (Pell, 1997). However, Jurassic (~172 Ma) and Cambrian (540 Ma) age pipes have also shown economic importance outside of the Lac de Gras area. This includes Snap Lake kimberlite dyke (522 - 539 Ma) in the Southeastern Slave, emplaced during a time of known widespread kimberlite magmatism across North America (Pell, 1997; Heaman et al., 2004)

3.5.1 Snap Lake Kimberlite Dyke

The Snap Lake Kimberlite Dyke is located within the Snap Lake/King Lake (SKL) area, which is approximately 220 km northeast of Yellowknife, NWT, Canada within the southern Slave craton (Figure 3.7; Pokhilenko et al., 2004, Agashev et al., 2008, Field et al., 2009). This diamondiferous dyke system is complex, comprised of hypabyssal kimberlite in a series of sub-parallel sheets (dykes) dipping between 5-30˚ to the NE and expanding under an area of 10 - 25 km^2 (Figure 3.7; Gernon et al., 2012, Agashev et al., 2008; Hammer et al., 2004; McBean et al., 2003). The main dyke, named the Northwest (NW) Dyke has a variable width of ~3 – 5 m and dips ~9-13˚ E-NE (Agashev et al., 2008, Gernon et al., 2012). Surrounding country-rock in the Snap Lake area is composed of deformed granodiorite, tonalite, and granites (2.61-2.59 Ga) as well as metavolcanics, metaturbidites and migmatites of the Yellowknife Supergroup (Gernon et al., 2012). Similar to neighboring kimberlites (the Gahcho Kué cluster; 539Ma), this dyke system has an estimated emplacement age of between 522.9 Ma (Heaman et al., 2004) and 537 Ma

(Agashev et al., 2008) representing some of the oldest kimberlite magmatism observed in the craton.

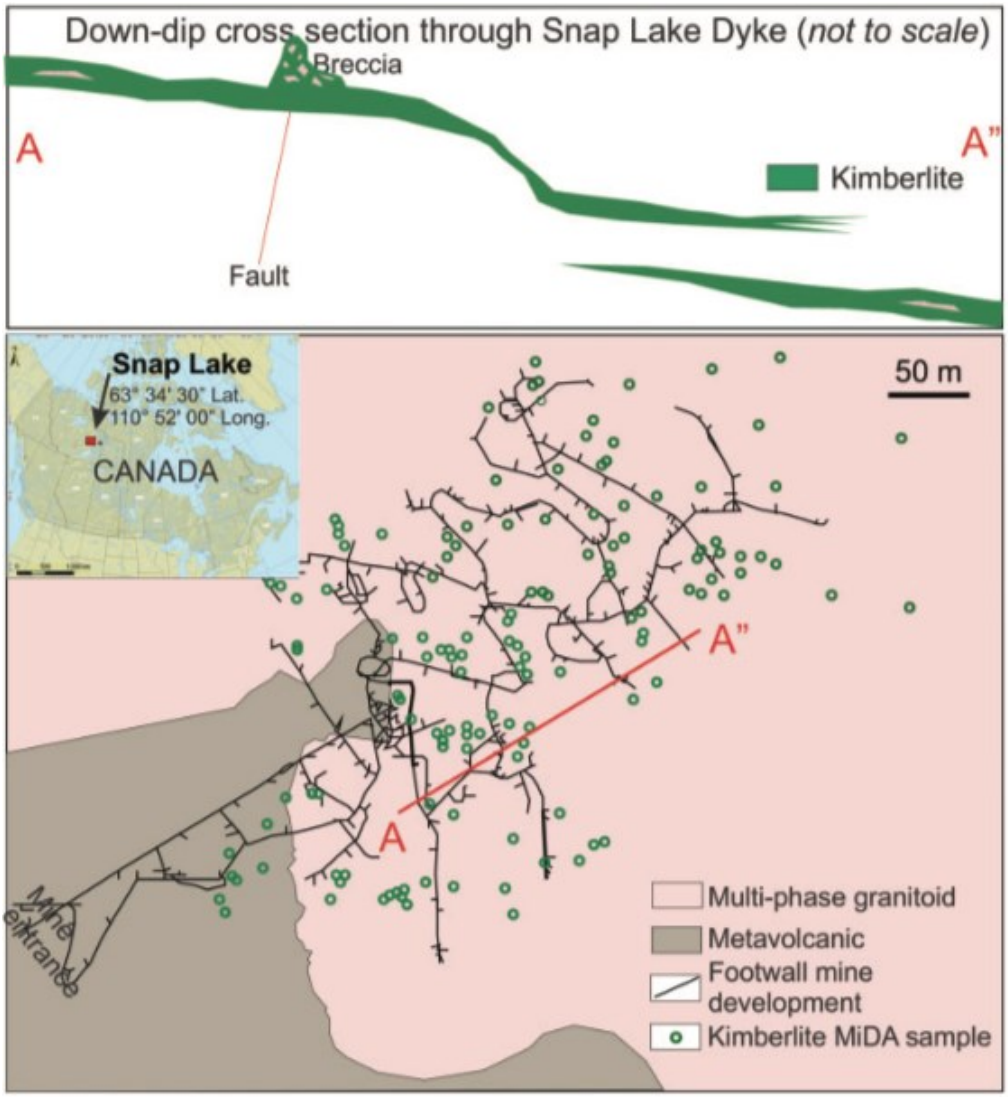

Figure 3.7: On top is a cross-section of the Snap Lake dyke system along the A-A' line designated on the plan view on the bottom, which also shows the locations of samples and the tunnel entrance for the mine. From Fulop *et al.* (2018).

In general, this dyke system is mineralogically similar to classical archetypal Group I kimberlites such as those described in Siberia and Africa (Field et al., 2009). The bulk-rock geochemical composition, however, is more similar to Group II (micaceous) kimberlite, a.k.a. orangeite or carbonate-rich olivine lamproite (see Pearson et al., 2019). This disagreement

between mineralogy and bulk rock composition is likely a result of transportation of elements (contamination) between granite xenoliths and the kimberlite (Fulop et al., 2018). The Snap Lake dyke is characterized by markedly low modal carbonate, an absence of perovskite and low amounts of Ca, P, K, Rb, Sr, Zr, and Hf (Kopylova et al., 2010).

Snap Lake dyke is composed of predominantly xenolith-poor hypabyssal kimberlites as well as two distinct types of xenolith-rich kimberlite. Xenolith-rich kimberlite can be divided based upon the type of dominant xenolith: granitoid-rich kimberlite (GRK), which includes up 50% granitoid xenoliths, and metavolcanic-rich kimberlite (MVRK), composed of up to 85% metavolcanics xenoliths (Fulop et al., 2018). These two groups of xenolith-rich kimberlite were previously thought to have been emplaced by two distinct magma batches in a multi-phased approach (Gernon et al., 2012). Fulop et al. (2018), however, suggested that due to microscopically visible gradational boundaries separating them, this cannot be the case.

3.6 Exploration history of the Slave craton

Early mapping within the Slave craton between the 1940s -1970s resulted in the discovery of multiple anomalous chemical signatures in many sediments, which did not match the surrounding environments (Pell, 1997). Chemical anomalies within garnets and pyroxenes were noted in the 1940s and 1950s, and later chromium and nickel anomalies, all of which were unexplained by the surrounding metasedimentary-granite terrains (Pell, 1997, and references therein). These anomalous findings remained unexplained, and it took until the 1980s before kimberlite exploration sharply increased took off.

When Diapros (renamed Monopros in 1981), the De Beers subsidiary in Canada, prospected for diamonds in the Mackenzie mountains west of Lac de Gras area, they noted

kimberlite indicator minerals which had been transported by glacial ice flow from the east (Pell, 1997). This finding led to many independent exploration programs in the Lac de Gras area, ~800 km east of the Mackenzie Mountains and eventually resulted in the first confirmed kimberlite in the Slave (Pell, 1997). In 1991, during the beginning of the Canadian diamond staking rush, the first diamondiferous kimberlite, named "Point Lake" pipe was drilled, and subsequently, more than 150 pipes were located in the area by late 1996 (Pell, 1997). In November 1996, the construction of Ekati Mine was approved, and in 1998 Canada's first diamond mine officially opened, including 5 pipes within the Lac de Gras area: Panda, Misery, Koala, Fox, and Sable. (Pell, 1997; Couch, 2002).

Snap Lake mine was Canada's fourth diamond mine, discovered in 1997 by Windspear Resources, a Canadian junior exploration company (Pokhilenko et al., 2004). This property was then purchased and developed into Canada's first completely underground diamond mine by De Beers Canada in 2008 (Hall, 2012). The mine operated for 7 years until 2015 when production stopped, and De Beers allowed it to flood.

4. Methodology

4.1 Diamond Cleaning, Crushing and Polishing

A set of 147 gem-quality diamonds from Snap Lake were generously supplied by DeBeers Canada. Diamonds were pre-sorted by size and range from ~2.70 – 7.43 mm (Table 4.1). Diamonds were cleaned in beakers filled partway with petroleum ether and placed in an ultrasonic bath for five minutes in the De Beers Laboratory for Diamond Research at the University of Alberta. Steps taken during the study are summarized below (Figure 4.1).

Table 4.1: Size distribution of diamonds received from De Beers Canada.

Size fraction	~ size in mm	Number of Diamonds
6 gr	7.43	3
5 gr	6.99	1
4 gr	6.49 – 6.70	5
3 gr	5.76 – 5.90	8
11+	3.10	27
9+	2.90	54
7+	2.70	49

Following cleaning, detailed descriptions of shape, distinguishing features, and inclusion content of these diamonds were made during microscopic examination and photography. Subsequently, diamonds were broken using a steel piston crusher under the microscope, and inclusions were released for mounting and analysis (Figure 4.0). Inclusions were recovered with a needle and friction mounted on glass slides until they were mounted in epoxy. Each inclusion was individually placed on two-sided tape and surrounded by a brass pip (diameter 6.25 mm or ¼ inch) and filled with West System ® 105 epoxy resin. The filled brass pips were placed on a hot plate kept at ~52 ºC for at least 24 hours to ensure the epoxy is completely hardened.

After the epoxy hardened, the pips were removed from the hot plate and left to cool. The samples were polished on 400 grit paper on the polishing wheel to expose the inclusion followed by 600, 800 and 1000 grit paper by hand. Before the final polish samples were cleaned in the ultrasonic bath with petroleum ether, water, and ethanol for 5 minutes each. The final polish was performed using a silk-screen plate and 0.25 µm Buehler blue diamond paste. Following this final polish, samples were again cleaned in the ultrasonic bath in a five-minute sequence of petroleum ether, water, and ethanol.

For sulphide inclusions, an additional polishing following cleaning was performed using Buehler MasterPrep 0.05 micron (corundum-based) polishing solution. These inclusions were then cleaned again as described above.

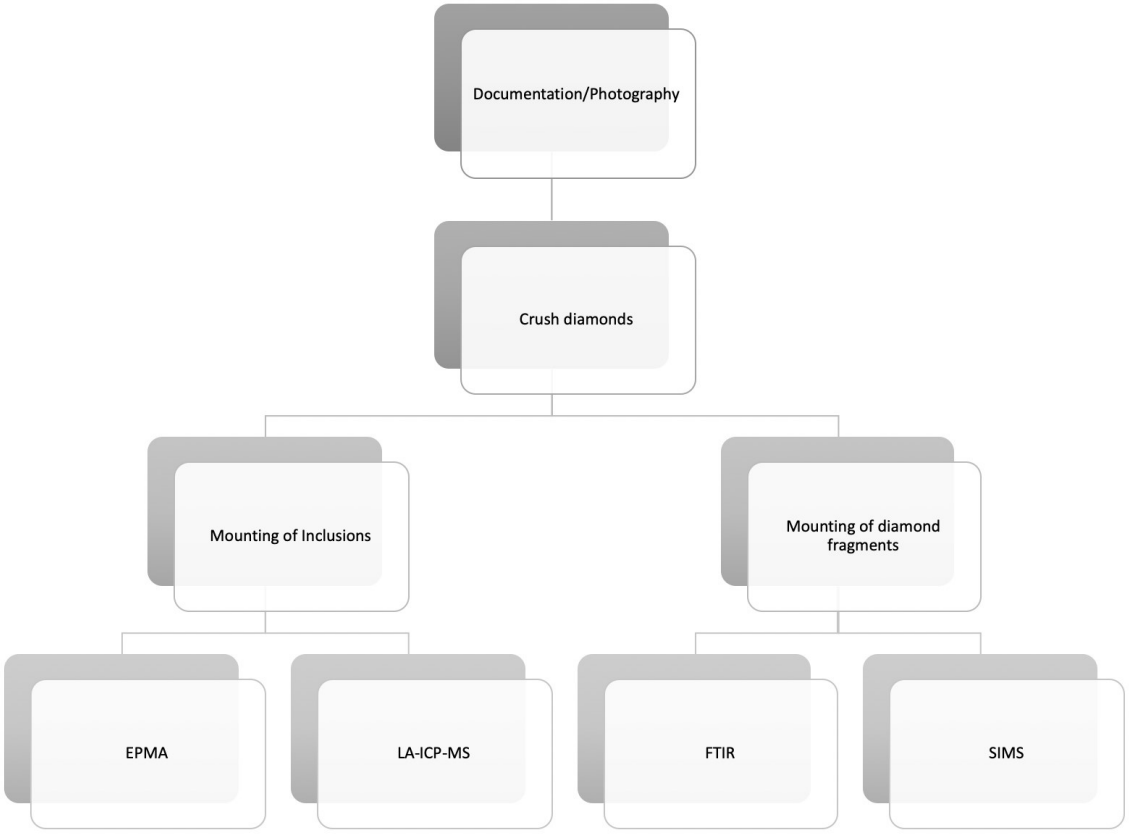

Figure 4.1: Flow chart summarizing the order of methods for this study.

4.2 Electron-Probe Microanalysis (EPMA)

4.2.1 Introduction

The major and minor element concentrations of mineral inclusions recovered from Snap Lake diamonds were quantitatively determined with electron microprobe (EPMA) techniques. EPMA works by bombarding the sample with a focused electron beam to cause the emission of characteristic X-rays.

Characteristic x-rays are produced when electrons move between shells within the atom. When the incident electron beam used impacts an electron in the inner shells of an atom it excites a stable electron to a higher, unstable state. In order to re-stabilize, an electron from one of the outer shells drops back into the effected electron shell (K or L in this case; Figure 4.2, Table 4.2a) to fill the vacancy. This downward movement between shells results in x-rays distinct to that element being released.

The intensities of characteristic x-rays, separated by wavelength (WDS or wave length-dispersive spectrometry) or by energy (EDS or energy-dispersive spectrometry), can be detected and measured. For quantitative analyses, WDS is the preferred choice. After a matrix correction, the characteristic x-ray intensities are quantified as elemental abundances through comparison with standards of known composition and thus allow to quantitatively determine the elemental make-up of the sample.

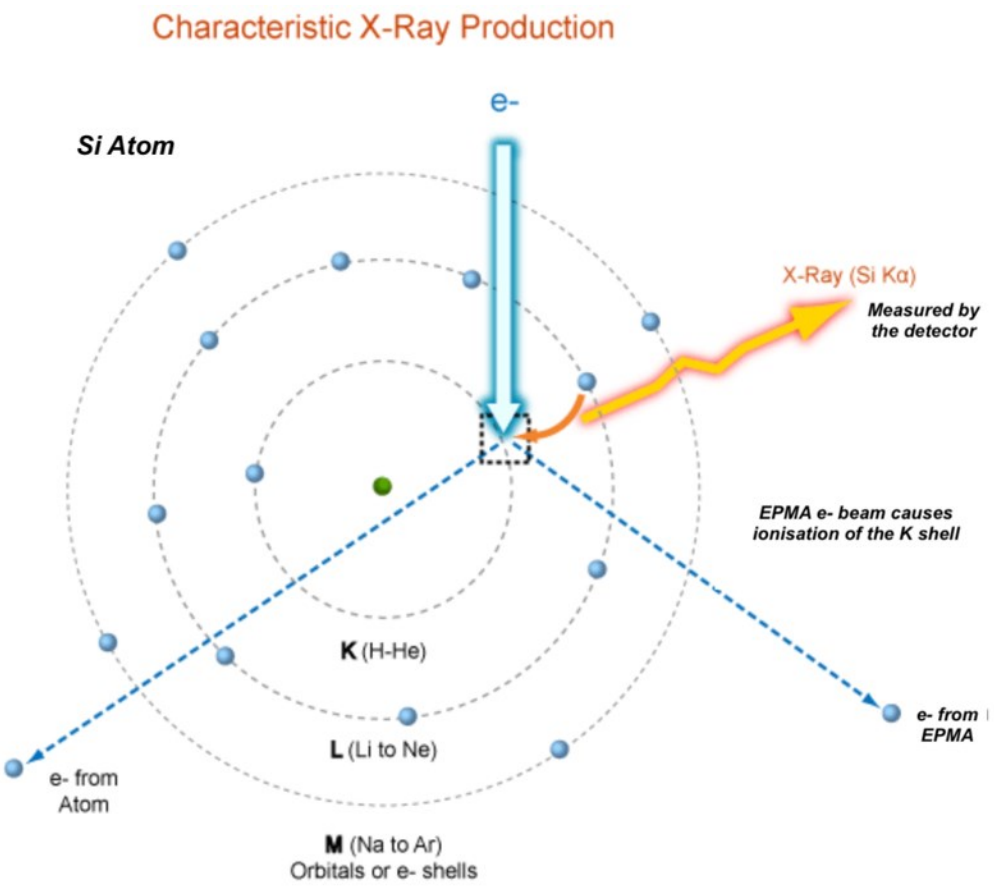

Figure 4.2: An electron beam excites and scatters an electron from the K shell of the Si atom in this particular situation. This causes the atom to regain its stability via the movement of an electron from its L shell down to fill the vacant spot in the K shell. In the process, a Si Kα characteristic x-ray is produced and can be measured by the detector. Taken and re-annotated from Microscope Australia via Myscope microscope training.

4.2.2 Major/Minor Element Analysis

Major-element compositions for garnet, olivine, orthopyroxene, clinopyroxene, chromite, SiO_2, K-feldspar, serpentine, and sulphides were determined using wavelength dispersive spectrometry (WDS) on the Cameca SX100 electron microprobe at the University of Alberta. The probe was operated with an accelerating voltage of 20 kV, a beam current of 20 nA, and a beam size of ~2 μm. Silicate, oxide, and sulphide standards were utilized for analysis and experimental

conditions are described below (Table 4.2a, b, c). On each inclusion a minimum of 2 measurements were made and the data quality was assessed based on the analysis of secondary standards bracketing each analytical session and using totals. Analyses totaling less than 99 and greater than 101 were excluded from further consideration.

Table 4.2a: Electron microprobe analysis (EPMA) settings for the quantitative analysis of major and minor elements for silicate mineral inclusions utilizing wavelength dispersive spectrometers (WDS).

Element	X-ray	Crystal	Count Times		PHA mode	Standard
			Peak (s)	Background (s)		
Si	Kα	LTAP	40	40	Integral	Frank Smith pyrope garnet or Fo90.5
Fe	Kα	LLIF	30	30	Integral	Gore garnet or Fe2SiO4 fayalite Rockport
Ca	Kα	PET	30	30	Integral	Plagioclase (labradorite) 115900 or CaMgSi2O6 diopside Wakefield
Al	Kα	TAP	40	40	Integral	Frank Smith pyrope garnet
Mg	Kα	LTAP	40	40	Integral	Frank Smith pyrope garnet or Fo90.5
Mn	Kα	LLIF	30	30	Integral	(Mn,Fe)3Al2Si3O12 spessartine, Navegadora Mine
Ni	Kα	LLIF	30	30	Integral	Ni nickel Alfa
Ti	Kα	LPET	30	30	Integral	TiO2 Rutile MTI
Cr	Kα	PET	30	30	Integral	Cr2O3 chromium oxide Alfa
Na	Kα	TAP	60	60	Integral	NaAlSi3O8 albite VA 131705
K	Kα	LPET	30	30	Integral	KAlSi3O8 sanidine Itrongay
V	Kα	PET	30	30	Integral	V vanadium Alfa
P	Kα	LPET	30	30	Integral	Ca5(PO4)3F apatite, Wilberforce

Table 4.2b: Electron microprobe analysis (EPMA) settings for the quantitative analysis of major and minor elements for chromite mineral inclusions utilizing wavelength dispersive spectrometers (WDS).

Element	X-ray	Crystal	Count Times		PHA mode	Standard
			Peak (s)	Background (s)		
Si	Kα	LTAP	40	40	Integral	Frank Smith pyrope garnet or Fo90.5
Fe	Kα	LLIF	30	30	Integral	Gore garnet or Fe2SiO4 fayalite Rockport
Ca	Kα	PET	30	30	Integral	Plagioclase (labradorite) 115900 or CaMgSi2O6 diopside Wakefield
Al	Kα	TAP	40	40	Integral	Frank Smith pyrope garnet
Mg	Kα	LTAP	40	40	Integral	Frank Smith pyrope garnet or Fo90.5
Mn	Kα	LLIF	30	30	Integral	(Mn,Fe)3Al2Si3O12 spessartine, Navegadora Mine
Ni	Kα	LLIF	30	30	Integral	Ni nickel Alfa
Ti	Kα	LPET	30	30	Integral	TiO2 Rutile MTI
Cr	Kα	PET	30	30	Integral	Cr2O3 chromium oxide Alfa
Na	Kα	TAP	60	60	Integral	NaAlSi3O8 albite VA 131705
K	Kα	LPET	30	30	Integral	KAlSi3O8 sanidine Itrongay
V	Kα	PET	30	30	Integral	V vanadium Alfa
P	Kα	LPET	30	30	Integral	Ca5(PO4)3F apatite, Wilberforce

Table 4.2c: Electron microprobe analysis (EPMA) settings for the quantitative analysis of major and minor elements for sulphide mineral inclusions utilizing wavelength dispersive spectrometers (WDS).

Element	X-ray	Crystal	Count Times		PHA mode	Standard
			Peak (s)	Background (s)		
As	lα	LTAP	30	30	Integral	Gallium arsenide GaAs
S	Kα	PET	40	40	Integral	Alabandite MnS
Fe	Kα	LLIF	30	30	Integral	Pyrrhotite Fe7S8
Cu	Kα	LLIF	30	30	Integral	Copper Cu
Co	Kα	LLIF	30	30	Integral	Cobalt Co
Zn	Kα	LLIF	30	30	Integral	Sphalerite ZnS
Ni	Kα	LLIF	30	30	Integral	Ni nickel Alfa
Mn	Kα	LLIF	30	30	Integral	Alabandite MnS
Si	Kα	LTAP	30	30	Integral	KAlSi3O8 sanidine Itrongay
Cr	Kα	PET	40	40	Integral	Cr2O3 chromium oxide Alfa
Mg	Kα	LTAP	30	30	Integral	Dolomite

Detection limits are presented at 99% confidence, exceeding three standard deviations of background. Detection limits for measured elements in silicates, chromite, and sulphides were found to be less than 350 ppm, except for P_2O_5 (up to 367 ppm, depending on matrix) in silicates and chromite and except for As (359 ppm) for sulphide analyses (Table 4.3). As reported analyses typically are averages of 2-3 individual spot measurements, the reported limits of detection represent upper limits.

Table 4.3: Limits of detection determined to 99% confidence for elements in A) silicate inclusions, B) chromite inclusions and C) sulphides inclusions recovered from Snap Lake diamonds.

A)

Element	Detection Limit (wt%)	Detection Limit (ppm)
SiO_2	0.0342	342
FeO	0.0180	180
CaO	0.0182	182
Al_2O_3	0.0340	340
MgO	0.0166	166
MnO	0.0222	222
NiO	0.0191	191
TiO_2	0.0150	150
Cr_2O_3	0.0307	307
Na_2O	0.0283	283
K_2O	0.0072	72
V_2O_3	0.0321	321
P_2O_5	0.0367	367

B)

Element	Detection Limit (wt%)	Detection Limit (ppm)
SiO2	0.0342	342
FeO	0.0180	180
CaO	0.0168	168
Al2O3	0.0340	340
MgO	0.0182	182
MnO	0.0222	222
NiO	0.0204	204
TiO2	0.0150	150
Cr2O3	0.0322	322
Na2O	0.0310	310
K2O	0.0072	72
V2O3	0.0339	339
P2O5	0.0367	367

C)

Element	Detection Limit (wt%)	Detection Limit (ppm)
Si	0.0108	108
Zn	0.0224	224
Cr	0.0110	110
Fe	0.0136	136
Co	0.0159	159
Ni	0.0202	202
Cu	0.0200	200
Mn	0.0121	121
Mg	0.0132	132
S	0.0119	119
As	0.0359	359

4.2.3 Trace Al-Ca-Cr-Na-Ti in Olivine

Trace-element analysis for olivine inclusions was run on a subset of 54 grains using wavelength dispersive spectrometry (WDS) on the Cameca SX100 electron microprobe at the University of Alberta with the same settings, except for a higher beam current (200 nA for trace-elements as opposed to 20 nA for major-elements). Trace-elements measured include Na, Cr, Ca, Al, and Ti. Synthetic and natural silicates and oxides were utilized as standards and experimental conditions are noted below (Table 4.4). Three to four analyses were performed on each olivine inclusion to examine their internal homogeneity.

Table 4.4: Electron microprobe analysis (EPMA) settings for the quantitative analysis of trace-elements Na, Cr, Ca, Al, and Ti in olivine inclusions utilizing wavelength dispersive spectrometers (WDS).

Element	X-ray	Crystal	Count Times		PHA Mode	Standard	Detection Limit (wt%)	Detection Limit (ppm)
			Peak (s)	Background (s)				
Na	Kα	LTAP	300	300	Integral	Albite	0.000875	9
Cr	Kα	PET	300	300	Integral	Synthetic Cr_2O_3	0.00156	16
Ca	Kα	LPET	300	300	Differential	Wollastonite	0.000593	6
Al	Kα	TAP	300	300	Integral	Frank Smith pyrope	0.000793	8
Ti	Kα	LPET	300	300	Integral	Synthetic Rutile	0.000516	5

4.2.4 Al-in-Ol Geothermobarometry

Using data produced by the high precision trace-element analysis of olivine grains recovered from Snap Lake diamonds, the Al-in-ol thermometer will be applied. Using the geothermometer equation derived by Bussweiler et al. (2017), Al in olivine will be used to estimate the temperature of diamond formation. The following equation was used:

$$T[^{\circ}C] = \frac{(11245 + 46.0 * P[kbar])}{(13.68 - \ln(Al[ppm])} - 273$$

Results from this thermometer were projected on a 37 mW/m^2 local paleogeotherm (model geotherm of Hasterok and Chapman, 2011), to give an estimation of the depth range for olivine-bearing diamond formation.

4.3 Laser Ablation Inductively Coupled Plasma Mass Spectrometry (LA-ICP-MS)

4.3.1 Introduction

LA-ICP-MS is routinely used for in-situ trace-element analysis from solid samples. It is a highly sensitive technique that can accurately measure concentrations from wt% to part per trillion (ppt) levels with almost no sample preparation required (Sylvester, 2008). In the laser, the sample surface is irradiated with pulsed deep-UV (193 nm) radiation, which at sufficiently high laser flux leads to the evaporation of the ablated material into a plasma of ions. The sputtered material is carried from the sample chamber to the torch of the ICP-MS via a high purity He:Ar plasma. In the torch assembly the sample is fully ionized into atomic and small polyatomic ions in a very hot (10,000 K) plasma. These ions are then accelerated and separated based on their mass-to-charge ratio and measured by detectors (Faraday cups or electron multipliers).

4.3.2 Trace-element Analyses of Garnet and Clinopyroxene

Trace-element analyses of garnet and clinopyroxene inclusions were carried out at the University of Alberta's Arctic Resources Laboratory. Analyses were done on prepared grain mounts after removal of the carbon coating used for EPMA. Data were collected by laser ablation ICP-MS, using a Resonetics (RESOlution M-50) 193 nm excimer laser system coupled to a Thermo Scientific Element XR 2 High Resolution inductively coupled plasma mass spectrometer).

Laser ablation runs were carried out in a high purity He:Ar atmosphere, with spot size ranging from 33 μm to 130 μm depending on the size of the inclusion. Individual analyses consist of ~100 seconds of measurement for background (laser off), followed by ~40 seconds of ion signal acquisition (laser on). Trace-element analyses were carried out initially with a fluence of 120 mJ and a repetition rate of 10 Hz, which was later lowered to 118 mJ at the same repetition rate for all analyses with a spot size greater than 50 μm. Data acquisition is conducted with Geostar software and data was processed and reduced with Igor Pro and Iolite software.

The mass spectrometer was operated at low-resolution mode with an M/ΔM of ~300. NIST 612 reference material was used as an external calibration and each analysis was normalized to the calcium content previously determined by EPMA, as the internal standard. Repeated measurement of both the NIST 612 reference material and PN1 and PN2 garnets throughout multiple runs showed a consistent internal error well within the range of known values. Data were processed with Iolite v3 (Paton et al., 2011), indicating detection limits between 0.2 - 16 ppb for REE, and between 300 ppb – 5 ppm for Ti and Ni. Element concentration below detection limits are indicated (<LOD) where observed.

When possible more than one spot per grain was analyzed although this was relatively rare due to the size limitations of the inclusions available. Analytical accuracy of the trace-element concentrations was verified through repeat analysis of garnet standards PN1 and PN2 (see above). These garnet grains were used because they have been fairly well characterized by many different methods including INAA, SIMS, and LA-ICP-MS in laboratories around the world (e.g. Tappert et al., 2005).

4.4 Fourier Transform Infrared (FTIR) Spectroscopy

Nitrogen concentrations and aggregation states of a subset of 89 diamond fragments were determined by FTIR. Diamond fragments were suspended, attached to a glass slide with two-sided tape, and placed on the motorized stage. Spectra were collected in transmission mode under a 15x magnification IR objective lens on a Thermo Nicolet Nexus 470 FTIR spectrometer attached to a Continuum infrared microscope with a motorized stage, in the De Beers Laboratory for Diamond Research at the University of Alberta, Canada.

Absorption spectra were collected between 650 and 4000 cm^{-1} at a resolution of 4 cm^{-1} over the course of about 2 min (200 scans that are averaged). The aperture was set to 100 μm x 100 μm. Before analysis, the detector was cooled with liquid nitrogen and left to stabilize for 30 minutes before running a background spectrum. To account for atmospheric background, a background spectrum was measured at the start of each day, and subsequently approximately every three hours. In addition, the bench and microscope assembly was continuously purged with a pure mixture of nitrogen and oxygen.

Using the OMNIC software, spectra were baseline corrected and a previously acquired pure Type II diamond spectrum was subtracted, resulting in the normalization of the spectrum to a sample thickness of 1 cm. This represents the conversion of the data from absorbance to the absorption coefficient and allows the calculation of nitrogen concentration and aggregation values. Total nitrogen content and the nitrogen aggregation was calculated using the spectral deconvolution spreadsheet CAXBD, developed by David Fisher of De Beers Technologies in Maidenhead, United Kingdom.

Spectral deconvolution was completed with the use of the normalized spectra within the nitrogen absorption region of diamonds, between 1000 and 1400 cm^{-1}. Relative abundances of nitrogen within each of the different centers (C-, A- and B-) was determined in at.ppm, using a least-squares fitting approach based on the constraints set in the solver add-in of Excel. The presence of platelet-related absorption under the nitrogen peaks was fitted as a D component but is not further quantified. Results of this spectral deconvolution are used in the classification of diamond types. Relative proportions of each center in the diamond are calculated using the equation:

$$\%B = \frac{Concentration\ in\ B\ center}{Total\ Nitrogen\ Content} * 100$$

When A-centers are present together with B-centers and if A-centers account for > 90 %, the diamond is classified as Type IaA, if B-centers are > 90 % the diamond is classified as Type IaB and if they fall somewhere in-between 10-90 %B the diamond is classified as Type IaAB. If no B-centers are present, and instead C-centers are observed together with A-centers, the diamond will be classified as Type Ib/IaA. The proportions of each center in combination with the total nitrogen content are used to estimate the mantle residence time of each diamond (Taylor et al., 1990). The limit of detection and analytical error for nitrogen content is typically 5-15 at.ppm based on previous studies from this lab.

4.5 Cathodoluminescence (CL) Imaging and Secondary Ion Mass Spectrometry (SIMS)

4.5.1. Introduction

Carbon and nitrogen isotopic compositions and total nitrogen content were measured on a subset of 89 diamonds using a Cameca IMS 1280 ion microprobe, in the Canadian Centre for Isotopic Microanalysis (CCIM) at the University of Alberta, Canada (Figure 4.3). One fragment was selected from each crushed diamond for CL and SIMS analysis. The diamond fragments were arranged in 5 mm x 5 mm arrays and then cast in epoxy for grinding and polishing. Polishing was done with the use of metal-bonded diamond pads. Following polishing the arrays were cut into blocks and then pressed into indium mount (M1601 and M1603 for this project) along with C and N reference materials (Stern et al., 2014).

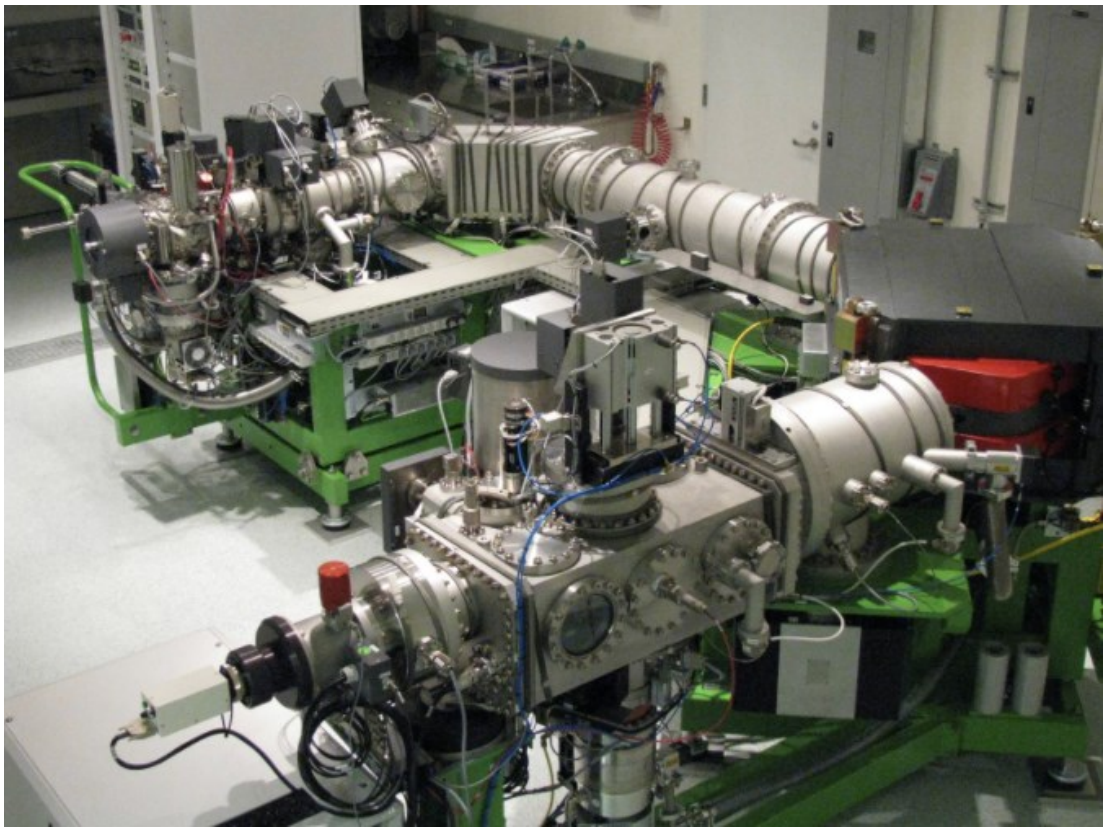

Figure 4.3: Photograph of the Cameca IMS 1280 ion microprobe, in the Canadian Centre for Isotopic Microanalysis (CCIM) at the University of Alberta, Canada. Photo taken from the CCIM website.

Reference materials diamond S0270 and vitreous carbon S0233A were used. The mounts were then coated with 25 nm Au before CL imaging, done using a Zeiss EVO MA15 scanning electron microscope (SEM) containing a CL detector, operating at 15 kV with a 3 to 5 nA beam current. The images were obtained using a parabolic mirror coupled with a high-sensitivity, broadband photomultiplier (Stern et al., 2014).

In order to accommodate the highest number of diamond fragments per mount~~,~~ diamonds were not oriented in specific orientations for imaging or analysis. Therefore, true crystal centers were not observed in many stones. For this reason, some cathodoluminescence (CL) images may appear highly-complex and do not necessarily show systematic growth zonation.

After CL imaging was completed, the mounts were coated with an additional 75 nm Au prior to SIMS analysis. C-isotopes ($^{13}C/^{12}C$), N abundances, and N-isotopes ($^{15}N/^{14}N$) were measured in three subsequent sessions using the IMS-1280 multi-collector ion microprobe utilizing slightly different methods and reference materials. The primary beam was a ~10 µm diameter beam of 20 keV $^{133}Cs^{+}$ ions, which was pre-rastered across a 20 µm X 20 µm area to clean the surface of Au and contaminants as well as implant Cs ions, stabilizing the analyzed ratios during sputtering. All three measurements were taken from identical spot locations across each diamond. Automated tuning of secondary ions in the transfer section precedes each analysis and negative secondary ions were extracted through a 10 kV potential to the grounded secondary column (Stern et al., 2014).

4.5.2. Carbon Isotopic Ratios

The primary beam used for carbon isotopic ratio determination had a current of ~2.0 nA. Secondary ions were collected through a field aperture of 5 mm by 5 mm with an entrance slit width of 110 μm, magnification of 100x, and a fully-opened energy slit. The two carbon isotopes ($^{12}C^-$ and $^{13}C^-$) were counted at mass resolutions of 2000 and 2900, respectively, in Faraday cups L2, using a 10^{10} Ω amplifier, and FC2, with a 10^{11} Ω amplifier.

Total time for each measurement (pre-raster, secondary ion tuning, and peak counting) was 240 s, with mean count rates determined over 75 s intervals, typically resulting in $1.0x10^9$ and $1.0x10^7$ counts/s for $^{12}C^-$ and $^{13}C^-$, respectively. During analysis diamond reference material S0270 ($\delta^{13}C_{VPDB}$ = -8.88 ±0.10 ‰) was measured at a 1:4 ratio interspersed with unknowns. The instrumental mass fractionation (IMF) was determined through all reference material analyses for two sessions (N = 54, 63), resulting in a standard deviation of 0.05 - 0.06‰ after correction for IMF drift. Measured uncertainties were typically ±0.13 ‰ (2 σ); ~0.05 ‰ (1 σ within-spot error and assigned between-spot error) and ~0.01 ‰ (between-session error). Results for carbon isotope ratios were reported in relation to the Vienna Pee-Dee Belemnite standard (V-PDB; Stern et al., 2014).

4.5.3. Nitrogen Abundance

For N-abundance measurements the primary beam had a current of 0.7 nA and secondary ions were collected through a field aperture of 3 mm by 3 mm with an entrance slit width of 40 μm. Collection conditions included 133x magnification and an energy slit setting at 40 eV transmitting low-energy ions. [$^{12}C^{13}C^-$] and [$^{13}C^{14}N^-$] ions were measured simultaneously through

a Faraday cup-electron multiplier combination employing L2 (using 10^{11} Ω amplifier) and the EM axial detectors. Mass resolutions were 6600 and 6000, respectively, sufficient to resolve any potential spectral interferences.

Total spot-to-spot analysis time was 210 s, and electron multiplier counts were corrected for background and deadtime (50 ns) with 50 ns utilized to correct for background and deadtime. The ratio of [$^{13}C^{14}$ N^-] / [$^{12}C^{13}C^-$] ions from unknowns were again measured in a 4:1 ratio with known diamond reference material (S0270), in identical sequence to carbon isotopes. S0270 was calibrated against diamond S0280E, which has a N abundance of 1670 at ppm. (±5 % relative, 2 σ) to determine the sensitivity factor. The error was calculated within-spot, between- spot, and between-session (Stern et al., 2014).

4.5.4. Nitrogen Isotopic Ratios

Nitrogen isotope ratios ($^{15}N/^{14}N$) were determined last on spots containing >75 ppm nitrogen with secondary ion collection conditions identical to those used for N-abundance measurements. The primary beam had a current of 2.5 – 3.0 nA. Molecular ions ($^{12}C^{14}N^-$ and $^{12}C^{15}N^-$) were analyzed simultaneously through coupled L'2 (using 10^{11} Ω amplifier) and EM axial detectors (Faraday cup-electron multiplier combination), with mass resolutions of 7000 and 6000, respectively.

Total spot-to-spot analysis time was 480 s and mean count rates ranged from $3*10^5$ to $1*10^7$ counts/s ($^{12}C^{14}N^-$), and from $1*10^3$ to $5*10^4$ counts/s ($^{12}C^{15}N^-$), determined over 300 s. Electron multiplier counts were corrected for background and deadtime (50 ns) and Faraday cup N-isotope baseline measurements were taken before each analysis.

Diamond reference material S0270 ($\delta^{15}N_{AIR}$ = -0.40 ± 0.50 ‰) was analyzed again in a 1:4 ratio with unknowns. The instrumental mass fractionation (IMF) was determined through all replicate analysis of reference material S0270 during two sessions (N = 35, 33), resulting in a standard deviation of 0.23 - 0.30 ‰ after correction for IMF drift (+0.05 ‰). Uncertainty for $\delta^{15}N_{AIR}$ averaged ±0.55 ‰ for individual analyses of diamond reference materials S0270 with 95 % confidence. For unknowns with variable nitrogen abundances, the uncertainty ranged from ± 0.5 (N abundance = 2350) to 3.6 ‰ (N abundance = 54 at.ppm). Spot uncertainties exclude the uncertainty in the composition of the reference material, which must be used to compare analyses with external data sets. Nitrogen abundances were also determined from the N-isotope data through the use of primary-beam-normalized secondary ion yields and normalized to the mean yield of S0270 (Stern et al., 2014).

5. Results

5.1 Diamond Physical Descriptions

For 147 diamonds from Snap Lake in this study, detailed information related to diamond color, morphology, surface features and inclusions is given Appendix 1a. A summary of the observations is provided below.

5.1.1 Morphology

Diamonds studied from Snap Lake are predominantly octahedral (44 %) with a relatively high proportion of macles (22 %; Figure 5.1; Appendix 1a). Octahedral and macle aggregates account for 10 and 8 % of the population respectively. Irregular stones and octahedral fragments account for ~ 6 % each and macle fragments, star twins and octahedral-dodecahedral aggregates account for ~ 1.5 % each.

Most of the fragments within the sample set have discernable shapes, with only a minor portion broken off. There are no notable differences in morphological distribution between size classes, with the exception that macle twins become more common in the smaller size classes and star twins are only noted in the smallest size class.

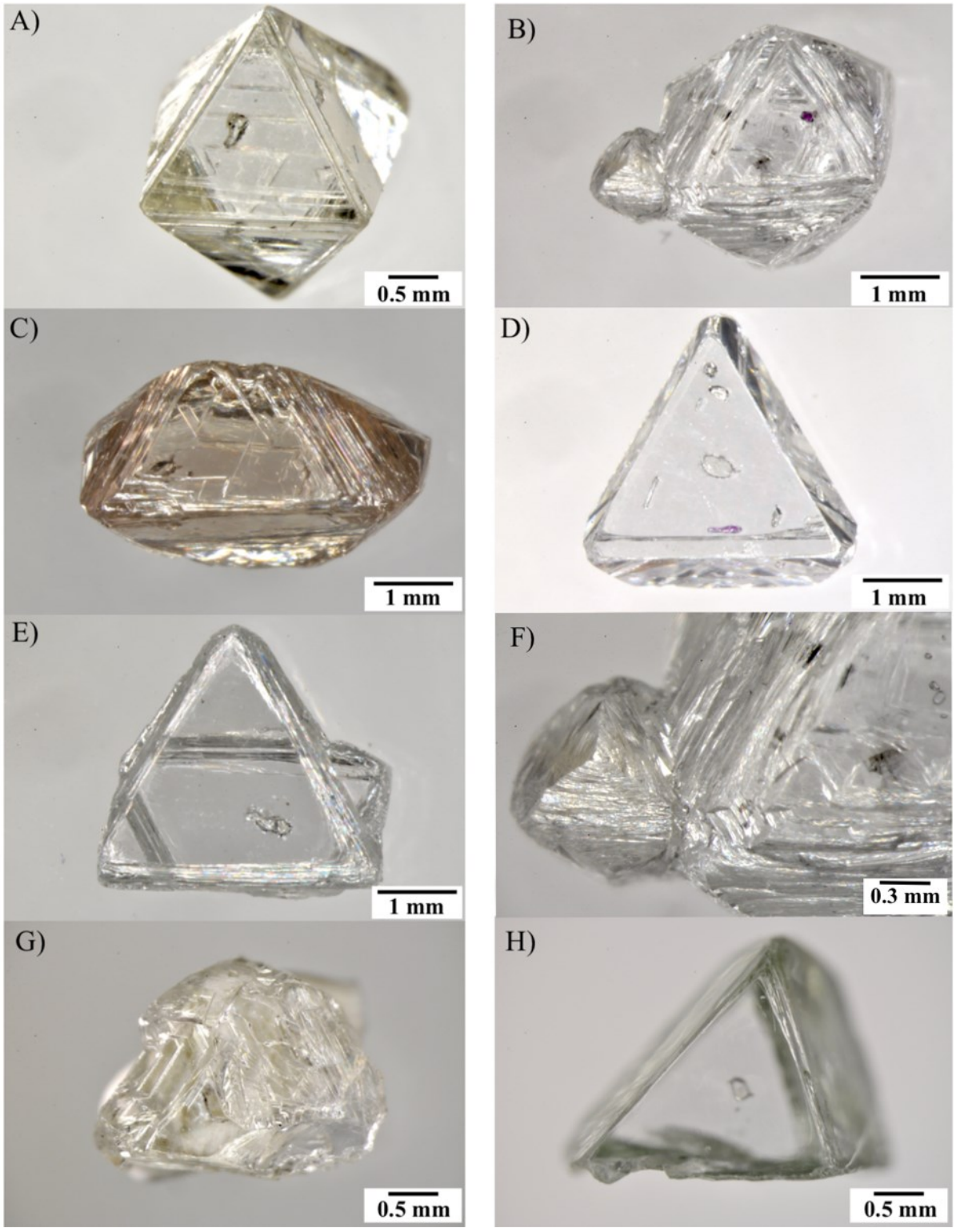

Figure 5.1: Representative photographs of morphological features of Snap Lake diamonds. **A)** Octahedron (SN107), **B)** Octahedral-aggregate (SN097), **C)** Flattened octahedron (SN090), **D)** Macle twin (SN054), **E)** Macle-aggregate (SN078), **F)** Dodecahedral (aggregated onto a larger octahedral diamond; SN097), **G)** Irregular (SN141), and **H)** Fragment (SN121).

5.1.2 Color

The majority of Snap Lake diamonds are colorless (83 %) with minor populations of yellow (8 %), brown (6 %) and pink diamonds (3 %; Figure 5.2; Appendix 1a). All diamonds in this study are transparent and have visible mineral inclusions. Some colorless stones show evidence of radioactive staining (SN018, SN083; Figure 5.2G) and on a few others, remnant kimberlite minerals are observed stuck in ruts on the surface.

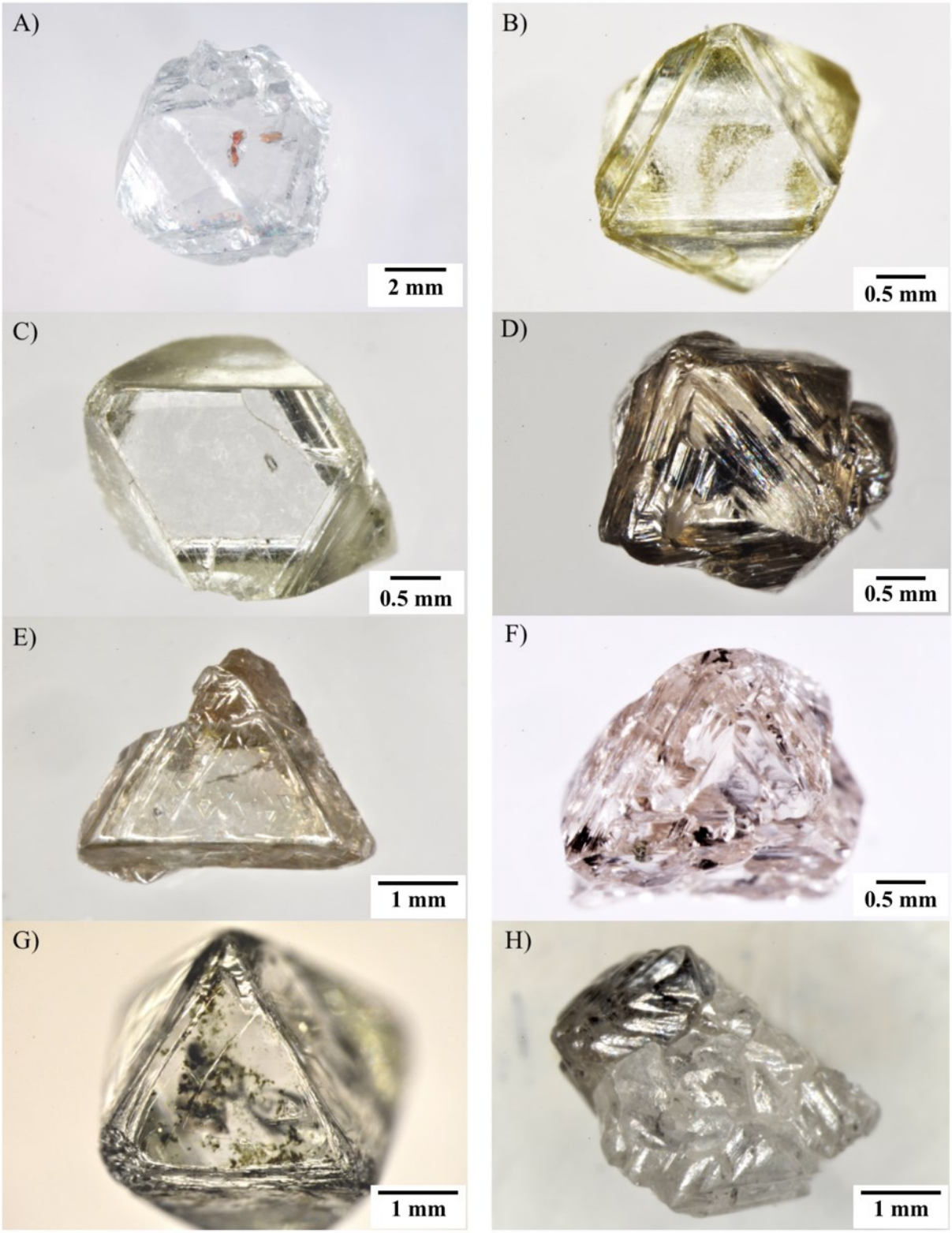

Figure 5.2: Representative photographs of Snap Lake diamond color. **A)** Colorless (SN001), **B)** Yellow (SN105), **C)** Light yellow (SN106), **D)** Dark brown (SN008), **E)** Light brown (SN112), **F)** Pink (SN055), **G)** Green spotting (SN018), and **H)** Grey inclusion coloration (SN034).

5.1.3 Surface Features

More than 90 % of diamonds from Snap Lake in this study showed some degree of stacked growth layering, 83 % showed shield-shaped laminae and negative trigons were present on 84 % of diamonds (Figure 5.3).

Both terraced and flat bottom trigons were observed, although flat bottoms were much more abundant. Deformation lines on diamond surfaces, often lined with flat bottom negative trigons, are observed on 25% of Snap Lake diamonds. Although some hillocks were observed they only appeared on 4% of diamonds (n=5). Within this sample set, tetragons appear solely on diamond SN027, on the apex of the dodecahedral aggregate (Figure 5.3c). Frosting of a diamond's surface occurred in a few instances and corrosion sculpture was also noted, but rare.

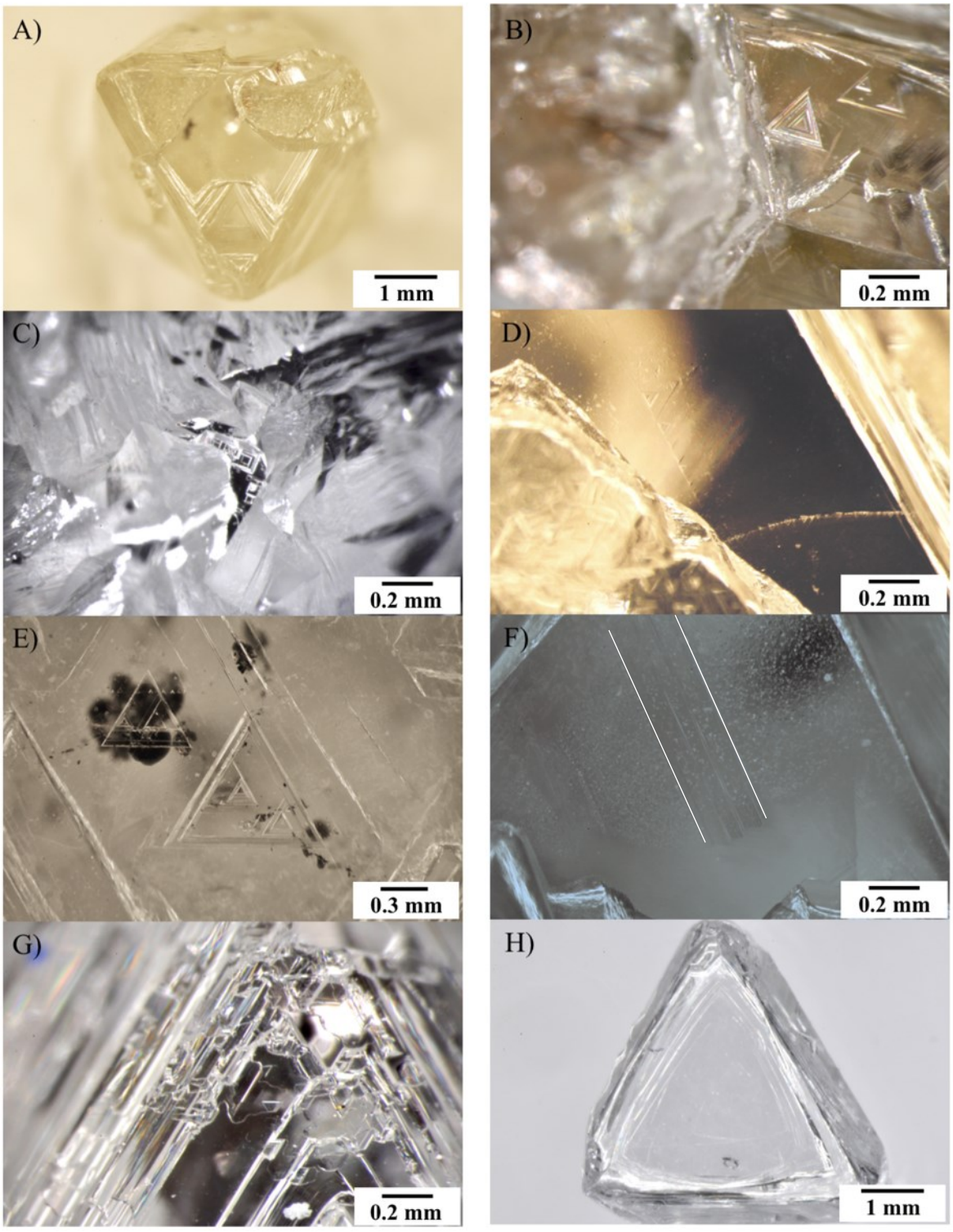

Figure 5.3: Representative photographs of surface features observed on Snap Lake diamonds. **A)** Multiple sizes of trigons (SN005), **B)** Large terraced trigon and flat-bottomed trigon (SN079), **C)** Tetragons (SN027), **D)** Deformation lines and trigons (SN005), **E)** Deformation lines (indicated by white lines) and trigons (SN009), **F)** Deformation lines and partial frosting (SN003), **G)** Corrosion sculpture (SN042), and **H)** Shield-shaped laminae (SN032).

5.2. Nitrogen Content and Aggregation State

Due to its similar size and charge, nitrogen can substitute relatively easily for carbon in the diamond crystal lattice, and is, therefore, the most common impurity in diamond (Kaiser & Bond, 1959). Diamonds are divided into two groups based on the presence (Type I) or absence (Type II) of nitrogen impurities (Breeding & Shigley, 2009; Robertson et al., 1934). Type I diamonds are further subdivided based on the degree of aggregation of the nitrogen impurities. Type Ib diamonds contain single substituted nitrogen atoms, known as C-centers. Type Ia diamonds contain only aggregated nitrogen and are termed either Type IaA (A-center; aggregates of two nitrogen atoms), or Type IaB (B-center; aggregates of four nitrogen atoms around a vacancy; Harris, 1987). Aggregation states between 10-90% in B-centers are termed Type IaAB (Evans et al., 1981).

Snap Lake diamond fragments have a wide array of nitrogen concentration, ranging from below detection (LOD; < 10 at.ppm) up to 1190 at.ppm with a mean concentration of 203 at.ppm and a median concentration of 113 at.ppm (Figure 5.4). Although 77 % of diamonds (n=68) in this set show very low nitrogen concentrations (< 250 at.ppm), three diamonds have nitrogen concentrations exceeding 1000 at.ppm (Appendix 1b). One diamond (SN136) lacks nitrogen impurities and is classified as Type II, while two additional diamonds have mixed nitrogen contents that include nitrogen-free zones (SN049 and SN134; Appendix 1b). Snap Lake diamonds have nitrogen aggregation states ranging from 0 to 95 %B with a mean value of 55 %B and a median at 58 %B.

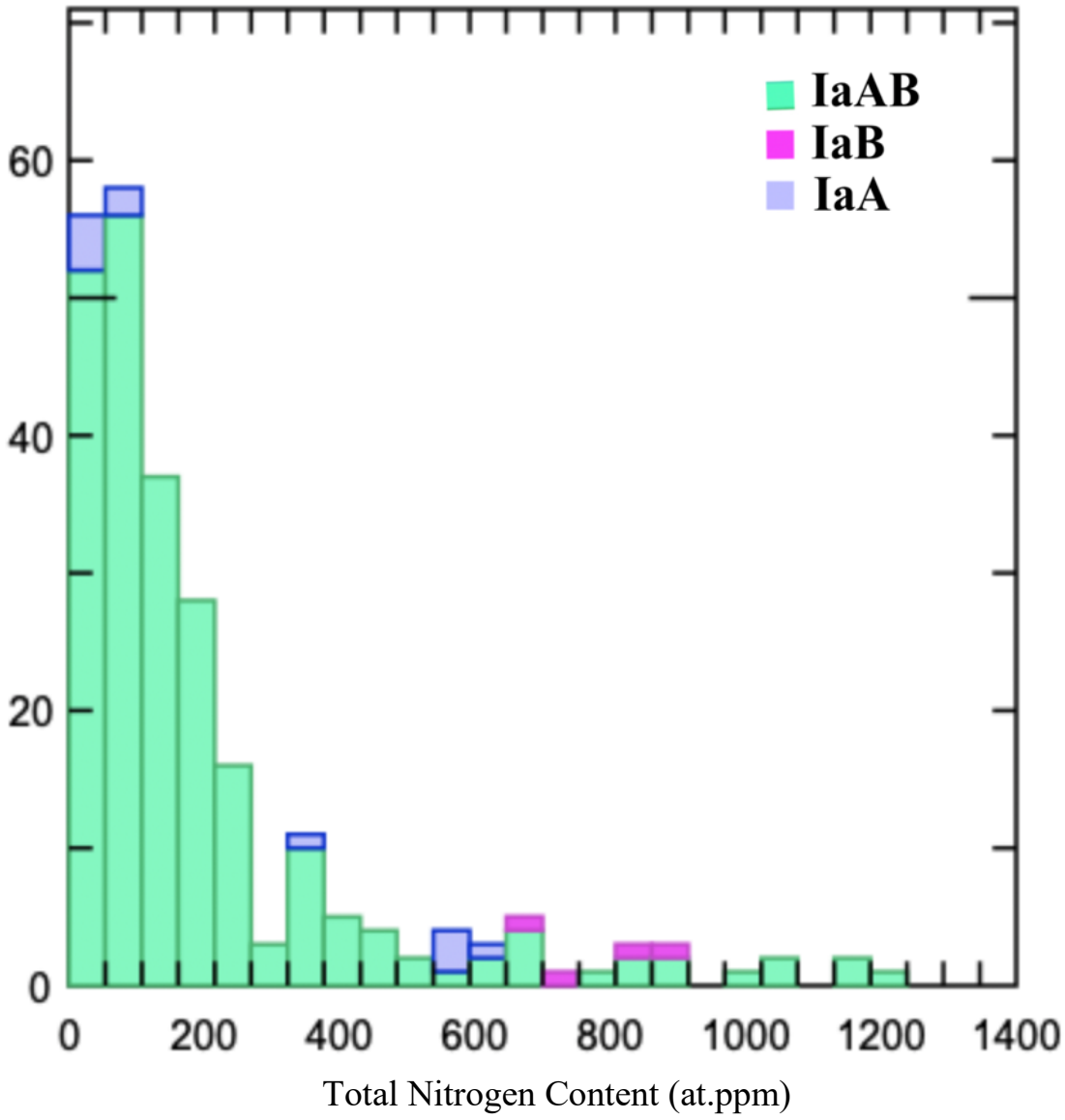

Figure 5.4: Histogram showing range in nitrogen concentration measured in Snap Lake diamond fragments.

5.2.1 Platelet Peak

Platelets are extended planar defects composed of layers of interstitial carbon in the {100} lattice plane, observed in Type IaAB and IaB diamonds (Kiflawi et al., 1998; Speich et al., 2017). Formation of platelets is thought to be a direct result of the production of B-centers containing vacancies, during nitrogen aggregation (Woods, 1986). The generation of platelets produce a sharp peak between 1358 and 1372 cm^{-1} where the exact position is dependent upon the size (nanometer

to micrometer) of the platelets (Figure 5.5; Clackson et al., 1990; Woods, 1986; Speich et al., 2017). In general, larger peaks are observed at lower wave numbers and smaller peaks at higher wave numbers (Speich et al., 2017). Platelet peak areas ranged from 0 to 90 cm^{-2} with a mean of 12 cm^{-2}.

5.2.2 Hydrogen Peak

In IR absorption spectra, hydrogen impurities generate a range of peaks between 500-3500 cm^{-1} including the major hydrogen-related peak at 3107 cm^{-1} (Figure 5.5). In Snap Lake diamonds, the 3107 cm^{-1} peak area ranges from 0 to 18.62 cm^{-2} with a mean of 2.00 cm^{-2} and a median value of 1.34 cm^{-2}. The 3107 cm^{-1} absorption peak does not appear in the Type II diamond or in the Type IaA diamond in this study, but does occur in mixed aggregation diamonds. This peak was originally thought to be associated with a stretching mode of carbon-hydrogen bonds, while the accompanying 1405 cm^{-1} was attributed to the bending mode of carbon-hydrogen bond vibrations (Woods & Collins, 1983). This idea was later challenged by Goss et al. (2014), suggesting that instead the 3107 cm^{-1} peak is actually caused by N_3VH defects.

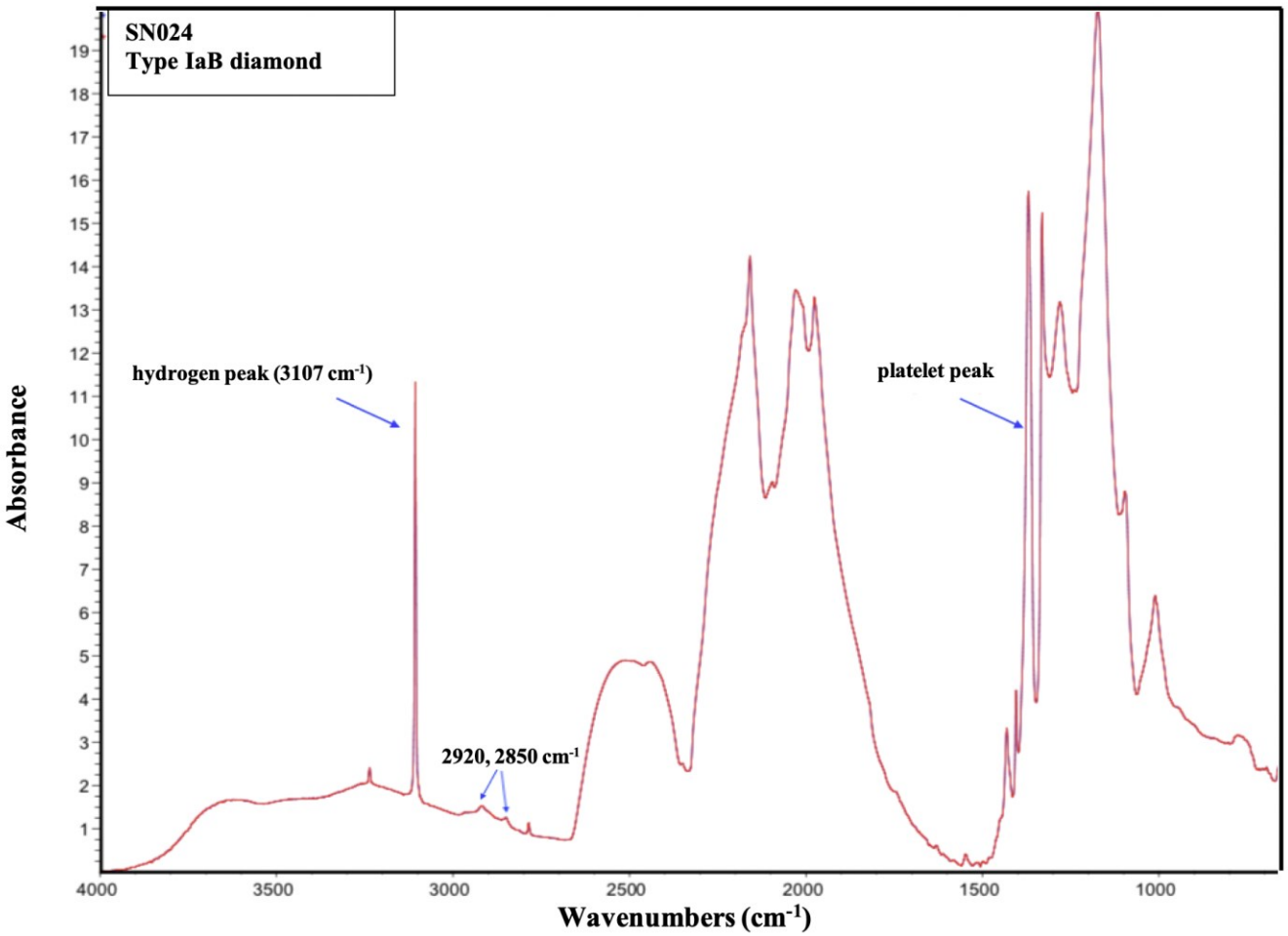

Figure 5.5: Type IaB diamond (SN024) spectrum with a clearly discernable hydrogen and platelet peak. A number of other absorption peaks are also observed (e.g. 2920. 2850 cm^{-1})

5.2.3 Other Absorbance Peaks

In addition to the platelet and hydrogen related peaks, two peaks at ~2920 cm^{-1} and ~2850 cm^{-1} are observed in many diamond spectra (Figure 5.5). These peaks are thought to relate to asymmetric stretching of CH_3^- and symmetric stretching of the CH_3^{2-} respectively (Titus et al., 2005). These peaks are unlikely to be a result of contamination as analyses were run on cleavage chips.

5.3 Cathodoluminescence Imaging and SIMS Analysis of Diamond

5.3.1 Introduction

A randomly selected subset of 87 diamonds were selected for Secondary Ion Mass Spectrometry (SIMS) analysis to determine their carbon isotope, nitrogen content, and nitrogen isotope compositions.

5.3.2 Carbon Isotopes

Snap Lake diamond fragments have carbon isotope values ($\delta^{13}C$) ranging from -8.0 to -1.3 ‰, with a mean of -4.3 ‰, median or -4.2 ‰ and mode of -4.1 ‰ (kernel density; Figure 5.4a; Appendix 1c). The carbon isotopic composition of Snap Lake diamonds in this study fall within the range of diamonds worldwide (Figure 5.6; Stachel and Harris, 2009). However, Snap Lake diamonds do not show the light isotope trail apparent in the global diamond dataset. Snap Lake diamonds show a minimum $\delta^{13}C$ value of – 8 ‰, much higher than the minimum value (-41 ‰) observed in the global database (Stachel and Harris, 2009). The average observed in $\delta^{13}C$ values for Snap Lake diamond fragments (-4.29 ‰), however, agrees relatively well with previous studies on Snap Lake diamonds by Pokhilenko et al. (2004, 2001) who found a slightly more positive $\delta^{13}C$ average at -4.0 ‰ (average of only p-type diamonds).

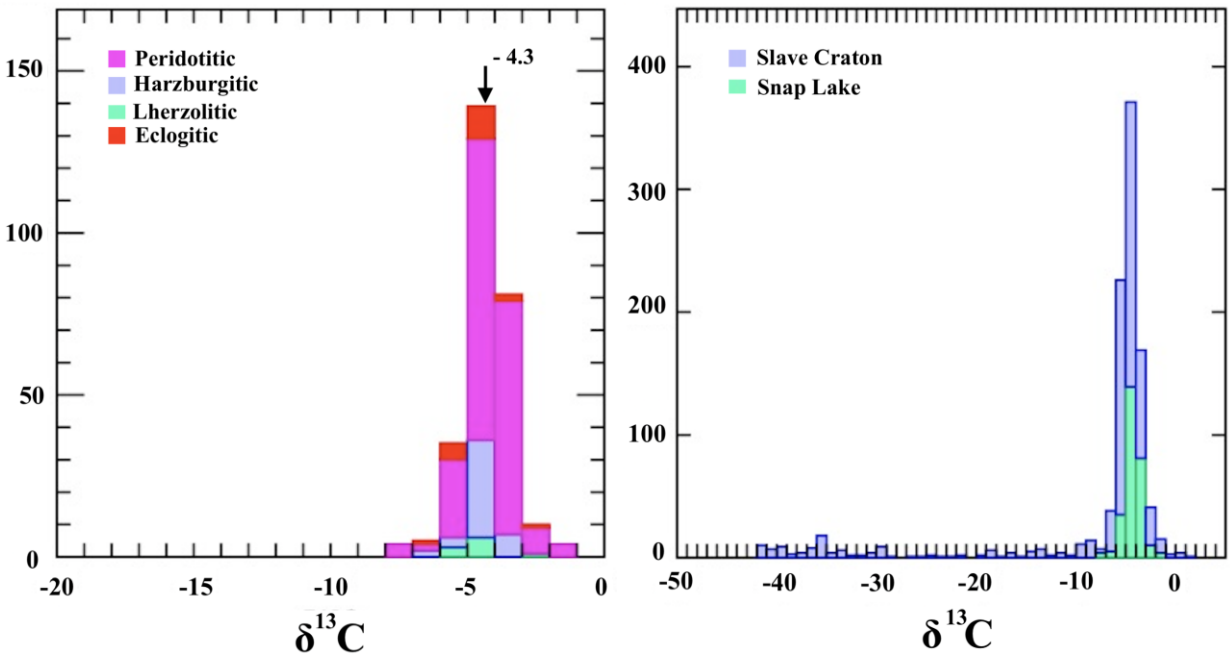

Figure 5.6: $\delta^{13}C$ histograms showing **A)** Snap Lake diamond $\delta^{13}C$ values by paragenesis (determined by inclusion chemistry), mean (-4.3 ‰) is labeled. **B**) Snap Lake $\delta^{13}C$ values in comparison to Slave craton diamond database isotope measurements from Stachel and Harris. (2008).

The majority of Snap Lake diamonds shows very little intra-diamond variation in $\delta^{13}C$ with an average standard deviation of 0.21 ‰ that is reduced to 0.16 ‰ when three diamonds showing notable internal isotopic variation (> 1 ‰) are excluded. These three diamonds (SN088, SN083, and SN030) show greater internal variation in $\delta^{13}C$, between -2.9 and -5.4 (SN088), -4.2 and -7.9 (SN083), and -3.6 and -7.8 (SN030). In addition, diamond SN083 appears to have more negative $\delta^{13}C$ values at its edges and slightly ^{13}C enriched values near its apparent centers (Figure 5.7).

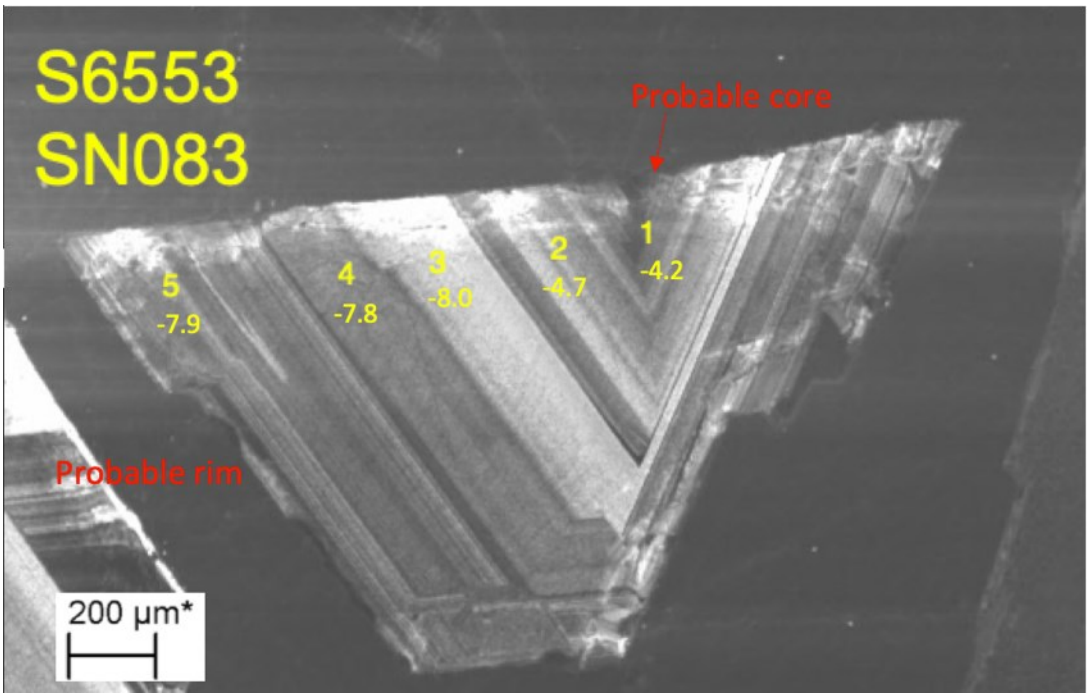

Figure 5.7: CL imaging of Snap Lake diamond, SN083, showing an intra-diamond $\delta^{13}C$ value difference of 3.7 ‰. SN083 shows a more negative outside (-7.9 ‰) and a less negative center (-4.2 ‰).

5.3.3 Nitrogen Content

SIMS and FTIR analyses of the 87 Snap Lake diamonds were conducted on different fragments of the same diamonds. SIMS and FTIR analyses agree that Snap Lake diamonds have nitrogen contents ranging from below detection (≤0.5 at.ppm for SIMS and ≤10 at.ppm for FTIR) to well over 1000 at.ppm but the upper limit is higher for SIMS (2689 at.ppm versus 1187 at.ppm with FTIR). The correlation of nitrogen content measurements via SIMS and FTIR on different fragments from the same diamond is poorly correlated ($R^2 = 0.21$; Figure 5.8).

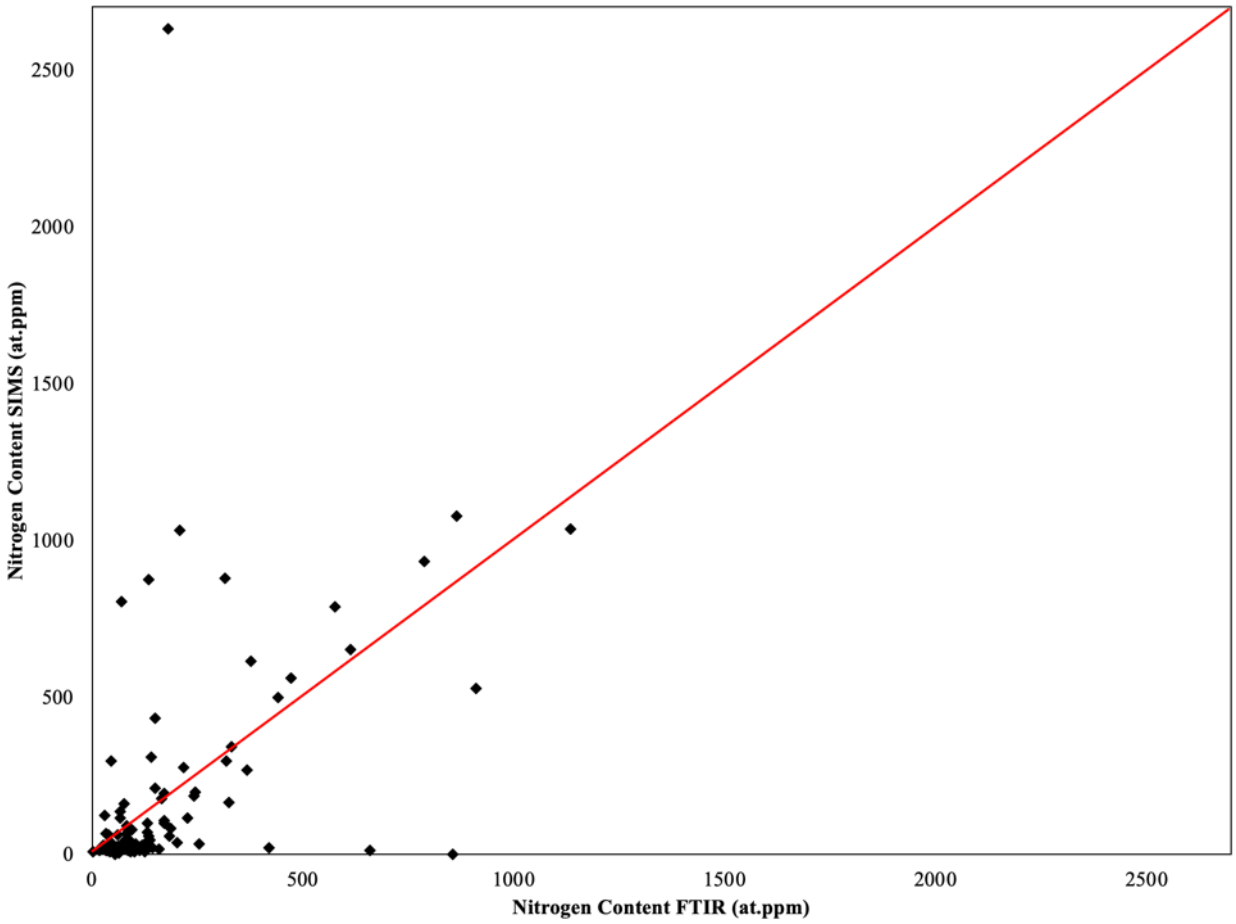

Figure 5.8: Bivariant plot of nitrogen content measured via FTIR versus nitrogen content measured via SIMS.

The SIMS and FTIR measurements differ likely due to a number of factors, including: 1) Different fragments from the same diamond were used for each method and difference may be due to possible internal heterogeneities; 2) SIMS analysis only determines nitrogen content from just below the surface (~1 µm), while FTIR measures nitrogen content through the entire diamond fragment; 3) the spot size for FTIR is ~100 x 100 µm while SIMS has a spot size diameter of ~10 µm. In addition, FTIR measures only infrared active N while SIMS measures all nitrogen present (Stern et al., 2019). This is unlikely to be the case for most of the Snap Lake diamonds as only one of the diamonds showing a larger disagreement in measurements between SIMS and FTIR is

yellow (indicating IR inactive nitrogen; N3). In general, both SIMS and FTIR analyses resulted in very similar averages for the Snap Lake diamond fragments (228 at.ppm and 203 at.ppm, respectively).

5.3.4 Nitrogen Isotopes

Nitrogen isotopes help identity the origin of the material from which the nitrogen in diamonds was sourced. Determination of nitrogen isotopic compositions was possible for 48 diamonds having N contents > 70 at.ppm.

The $\delta^{15}N$ values of mantle rocks (-5 ‰ ± 3) are generally more negative than atmospheric nitrogen (0 ‰) and crustal nitrogen (+5 ‰; Cartigny et al., 2005; Cartigny et al., 2014). Diamonds associated with peridotitic substrates are inferred to be formed from mantle-derived fluids/melts, in-part on the basis of $\delta^{15}N$ values that are within the $\delta^{15}N$ range of the mantle. Conversely, diamonds associated with eclogites have a range in $\delta^{15}N$ from positive to negative values. Positive $\delta^{15}N$ values are expected for eclogitic diamonds formed from fluids derived from the subduction of organic material associated with oceanic crust (Catigny et al., 2014). This, however, is not typically the case; worldwide, eclogitic diamonds often have negative $\delta^{15}N$ values that overlap with those of peridotitic diamonds (Figure 5.6b; Stachel et al., 2009, Cartigny et al., 2014, Palot et al., 2012).

Nitrogen isotope values ($\delta^{15}N$) of Snap Lake diamond fragments range from -19.6 to 10.9 ‰ with an average of - 3.0 ‰. While Snap Lake eclogitic and peridotitic diamonds show both negative and positive $\delta^{15}N$ values, eclogitic diamonds overall have higher $\delta^{15}N$ values with an average of 0.5 ‰ compared to peridotitic diamonds with an average of -3.6 ‰ (Figure 5.9a). In

addition, eight peridotitic diamonds from Snap Lake show extreme depletion in $\delta^{15}N$, ranging from -19.6 to -11.0 (Appendix 1b).

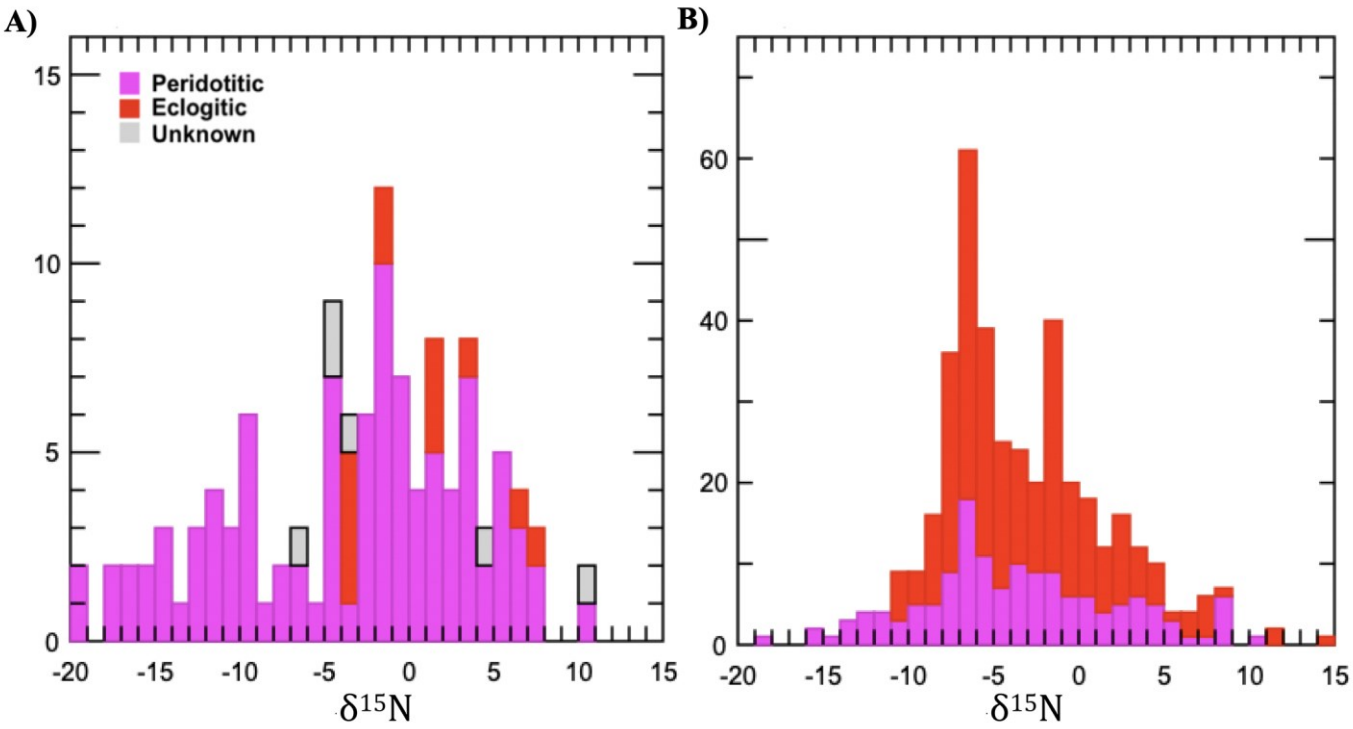

Figure 5.9: Histograms showing the distribution of $\delta^{15}N$ composition separated by paragenesis for **a)** Snap Lake Diamonds and **b)** worldwide diamonds (database of Stachel et al., 2009).

5.4 Major-element Compositions of Mineral Inclusions

Syngenetic inclusions (n=159) composed of olivine (62 %; n=98), peridotitic garnet (17 %; n=27), Mg-chromite (9 %; n=15), sulphides (3 %; n=5), eclogitic garnet (2 %; n=3), clinopyroxene (diopside; 2 %; n=3), orthopyroxene (2 %; n=3), coesite (1 %; n=2), Native Iron-Wustite (1%; n=2) and K-Feldspar (n=1; Figure 5.10) were recovered from 89 Snap Lake diamonds.

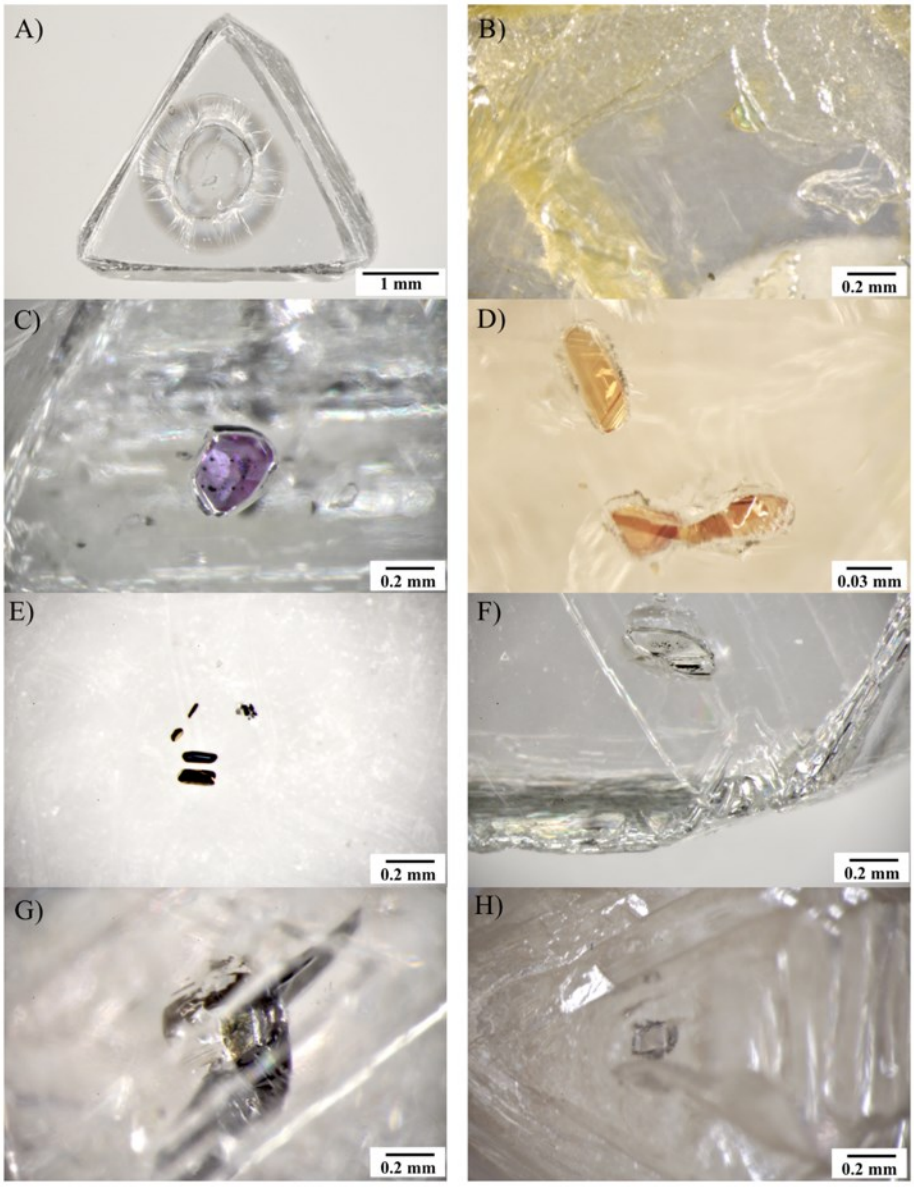

Figure 5.10: Representative photography of inclusion types observed in Snap Lake diamonds; A) Olivine (SN020), B) Diopside (SN030), C) Peridotitic garnet (SN108), D) Eclogitic garnet (SN001), E) Mg-chromite (SN046), F) Orthopyroxene (SN064), G) Sulphide (SN061), and H) K-feldspar (SN056).

5.4.1 Garnet

Garnet inclusions (n=32) were recovered from 21 diamonds. Ten diamonds contained only garnet, while 11 others contained additional phases as non-touching pairs. Bi- and tri-mineralic combinations include garnet + olivine (n=8), garnet + orthopyroxene (n=1), garnet + clinopyroxene (n=1) and garnet + coesite + mono-sulphide solid solution (mss; n=1).

Grütter et al. (2004) classifies low-Cr garnets (Cr_2O_3 < 1 wt%) as high-Ca eclogitic (G3; CaO ≥ 6 wt%) or low-Ca eclogitic/pyroxenitic (G4; CaO < 6 wt%). On this basis, four garnets in this study recovered from one diamond are high-Ca eclogitic (CaO ~12 wt%) and one is low-Ca eclogitic/pyroxenitic (Figure 5.11). With the current data, G4 garnets cannot be further sub-divided into an eclogitic versus pyroxenitic affinity.

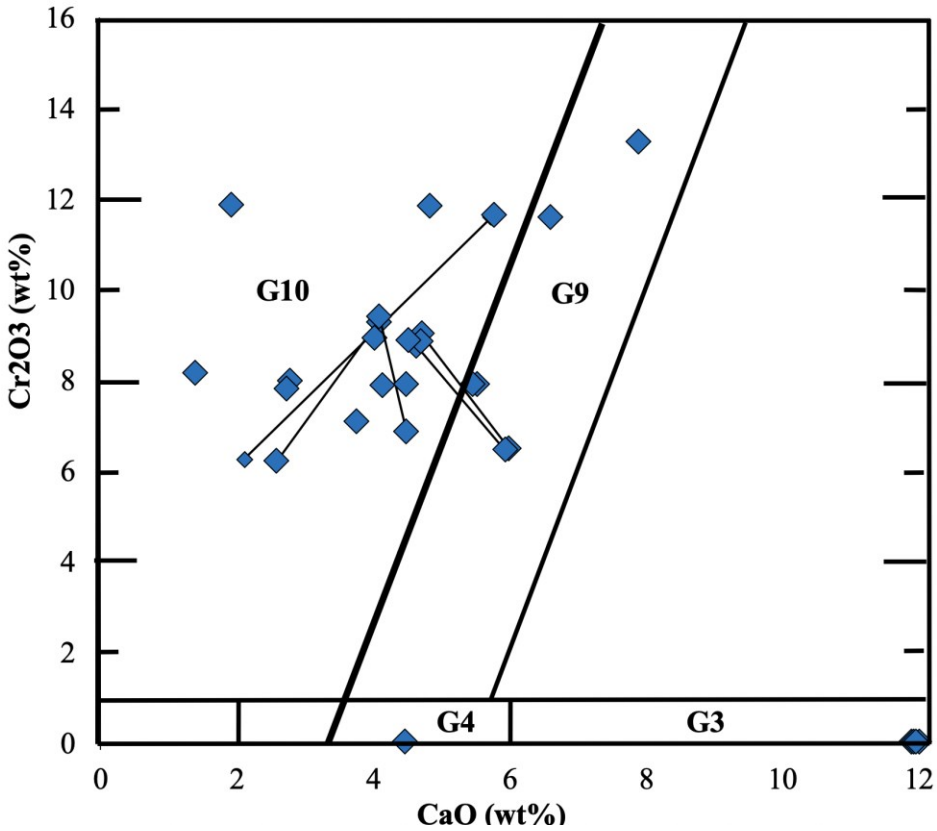

Figure 5.11: CaO versus Cr_2O_3 of Snap Lake garnets from this study. Showing the garnet classes G10 (harzburgitic), G9 (lherzolitic), G3 (high-Ca eclogitic) and G4 (low-Ca eclogitic/pyroxenitic) after Grütter et al. (2004). Tie lines connect co-existing garnets recovered from a single diamond.

Two garnet pairs, recovered from diamonds SN041 and SN118, show a distinct separation in their CaO-Cr_2O_3 chemistry between the lherzolitic field and the harzburgitic field (Figure 5.11). These garnets reflect an evolution, likely from harzburgite to lherzolite within the diamond host.

Mg# (100*Mg/[Mg+Fe]) of eclogitic garnet inclusions from diamonds in this study range from 29.4 - 52.8 and the TiO_2 contents range from 0.36 - 0.70 wt%, within the range of worldwide eclogitic garnet inclusions (Figure 5.12; Stachel & Harris, 2008). Pokhilenko et al. (2004) reported two E-type garnets, one of which showed a very low Mg# (38.8) accompanied by higher TiO_2 (1.44 wt%) while the other showed a much higher Mg# (65.5) and lower TiO_2 (0.44 wt%), both of which are within the range of compositions for Snap Lake eclogitic garnets in this study.

Of the 27 peridotitic garnets, 21 are harzburgitic and six are lherzolitic (Figure 5.8). Peridotitic garnet Mg# ranges from 72.4 - 84.5, Cr_2O_3 content ranges from 6.24 - 13.3 wt% and CaO contents range from 1.38 - 6.59 wt%. Garnet SN054D has 8.18 wt% Cr_2O_3 and 1.38 wt% CaO, with CaO contents < 1.8 wt% in harzburgitic garnets being related to derivation from ultra-depleted residual harzburgite or dunite sources (Grütter et al., 1999).

TiO_2 contents range from below detection up to 0.32 wt%. Five garnets (three harzburgitic, two lherzolitic) have enriched TiO_2 from 0.19-0.32 wt% (Appendix 1d). The Mg# of Snap Lake peridotitic garnet inclusions are within the range of worldwide peridotitic garnets (Figure 5.9; Stachel & Harris, 2008). In general, peridotitic garnets have undetectable levels of Na_2O, with the exception of one lherzolitic and one harzburgitic inclusion (SN036A and SN097A respectively) which contain 0.05 and 0.02 wt% Na_2O, respectively (Appendix 1d).

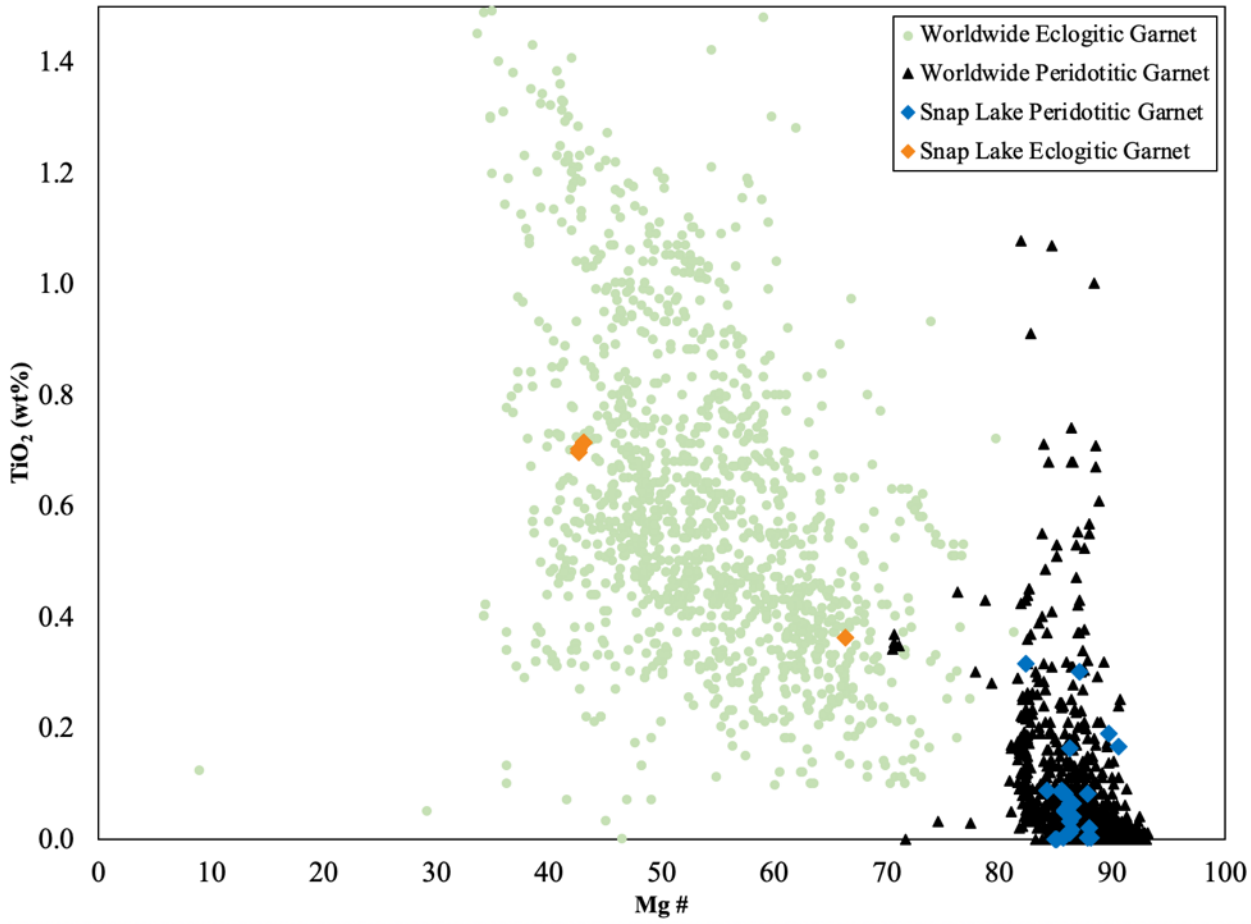

Figure 5.12: TiO_2 versus Mg# for Snap Lake garnets compared with worldwide garnet clusters from the worldwide database (Stachel & Harris, 2008). Peridotitic garnets from Snap Lake plot well within the peridotitic field defined by worldwide garnet samples, while the eclogitic also plot well within the eclogitic field defined by worldwide samples

5.4.2 Olivine

Olivine inclusions (n=98) from Snap Lake diamonds are magnesium-rich, with a narrow range of Mg# between 92.0 and 94.0, with a mean of 92.4 (Figure 5.13). Worldwide harzburgitic olivine inclusions typically fall between 92.2 and 95.4 (average = 93.2) while worldwide lherzolitic olivines typically fall between 90.0 and 93.6 (average = 92.0; Stachel & Harris, 2008). Snap Lake olivine inclusion data fall in the middle of these two populations and thus may indicate a mix of both harzburgitic and lherzolitic olivines in this dataset.

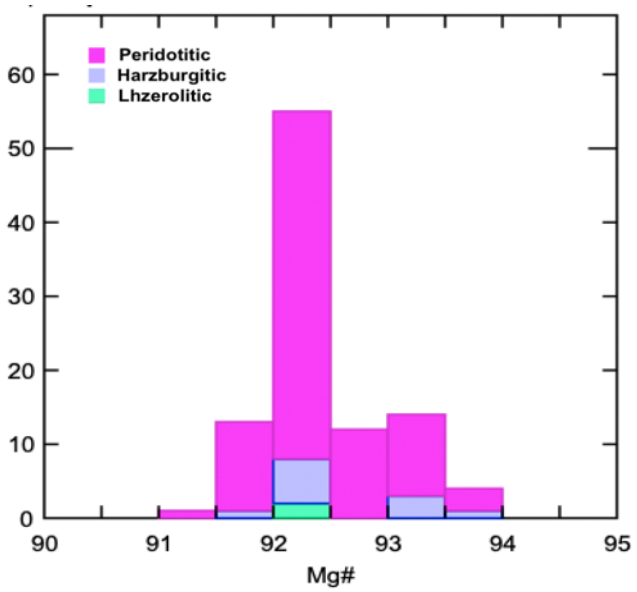

Figure 5.13: Histogram showing the distribution of Mg# in olivine inclusions recovered from Snap Lake diamonds in this study

Further classification, into harzburgitic and lherzolitic, can be accomplished for 13 of the 98 olivine inclusions recovered due co-existing garnet inclusions (11 are harzburgitic and two are lherzolitic).

Olivine inclusions (n=91) recovered from 59 diamonds have CaO < 0.04 wt%. This low CaO content is likely related to a harzburgitic paragenesis and again indicates a likely dominance of the harzburgitic over the lherzolitic paragenesis (Stachel & Harris, 2008). However, CaO contents as low as 0.01 wt% may occur during crystallization of lherzolitic olivine inclusions along a cool geothermal gradient (Stachel et al., 2009) and hence the lower cut-off at 0.04 wt% for the lherzolitic paragenesis is not well established. Consequently, in the absence of co-existing inclusions we cannot definitively classify the remaining 91 olivine inclusions as harzburgitic or lherzolitic.

Four other olivine inclusions show slight CaO enrichment with content ranging from 0.04 to 0.09 wt% and one (SN022D) shows a very enriched CaO content of 0.11 wt% (Appendix 1d).

Snap Lake olivine inclusions have compositions within the range of worldwide olivine inclusions. The very high CaO (>0.7 wt%) contents observed in select Snap Lake olivine inclusions indicate that these diamonds either formed in an orthopyroxene-free (wehrlitic) environment or experienced extreme thermal conditions (exceeding typical cratonic geotherms) (Stachel & Harris, 2008). The elevated CaO value of the olivine in diamond SN022D is among the top 5 % of CaO contents in worldwide olivine inclusions.

NiO contents range from 0.32 to 0.43 wt% and Na_2O is not detectable (<0.02 wt). A plot of NiO versus Mg# shows that Snap Lake olivine inclusions in this study have compositions within the range of the worldwide database and Slave Craton compositions in particular (Figure 5.14).

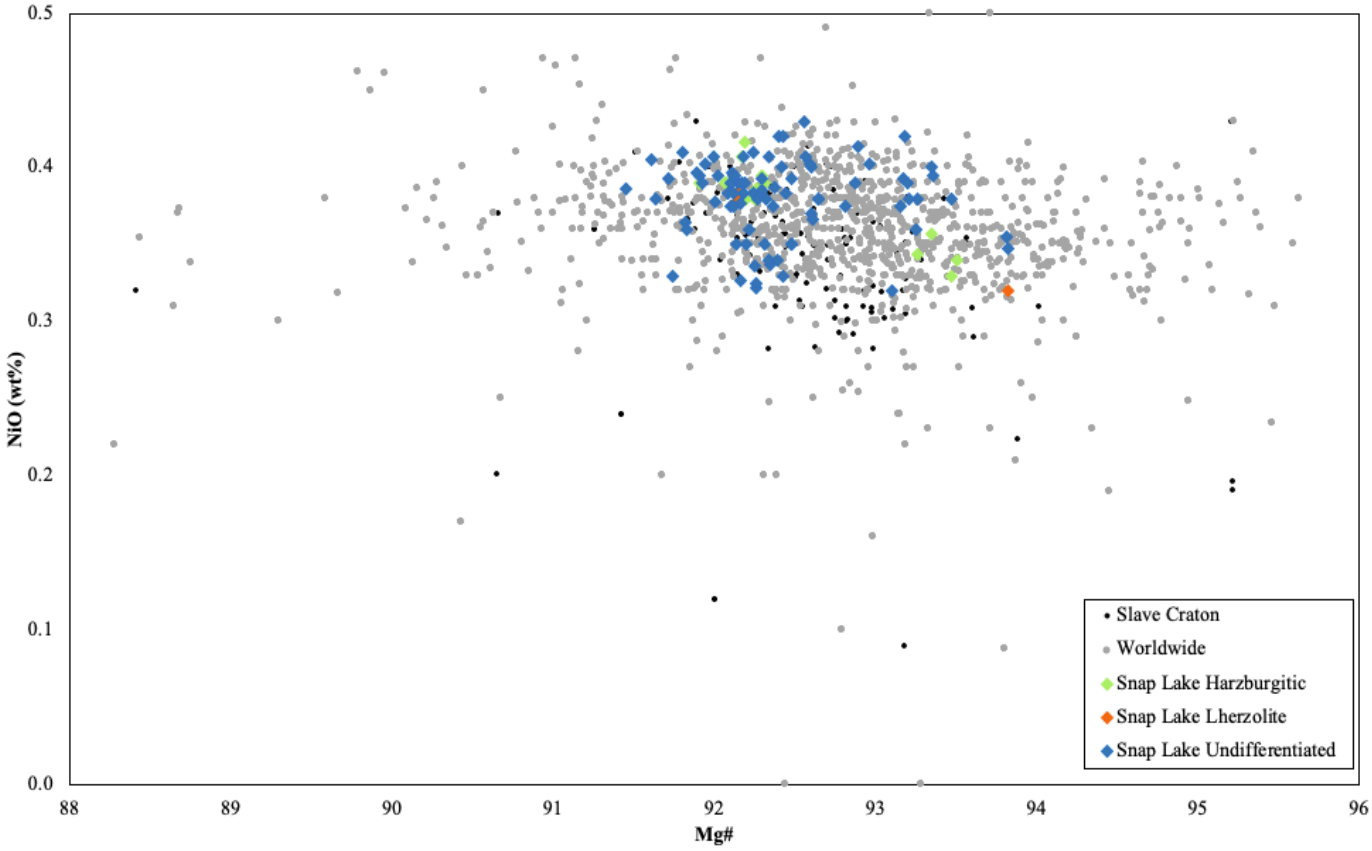

Figure 5.14: Plot of NiO versus Mg# ($molar\ \frac{100\,Mg}{Mg+Fe}$) of Snap Lake olivine of harzburgitic, lherzolitic, and undifferentiated peridotitic paragenesis, compared with other Slave Craton olivine inclusions and the worldwide database (Stachel & Harris, 2008).

5.4.3 Clinopyroxene

Three emerald-green peridotitic clinopyroxene inclusions were recovered from two diamonds. One diamond contained two clinopyroxenes, while another had a single clinopyroxene and two co-existing peridotitic garnet inclusions.

All three clinopyroxene inclusions had Cr_2O_3 content between 0.68 – 1.23 wt% and Al_2O_3 between 0.75 – 1.07 wt%. The Mg# of the three inclusions ranges from 93.4 to 93.6 and the Cr# ((100*Cr)/(Cr+Al) ranges from 47.5 to 53.4, within the center of the compositional range of peridotitic clinopyroxene from the worldwide database (Figure 5.15).

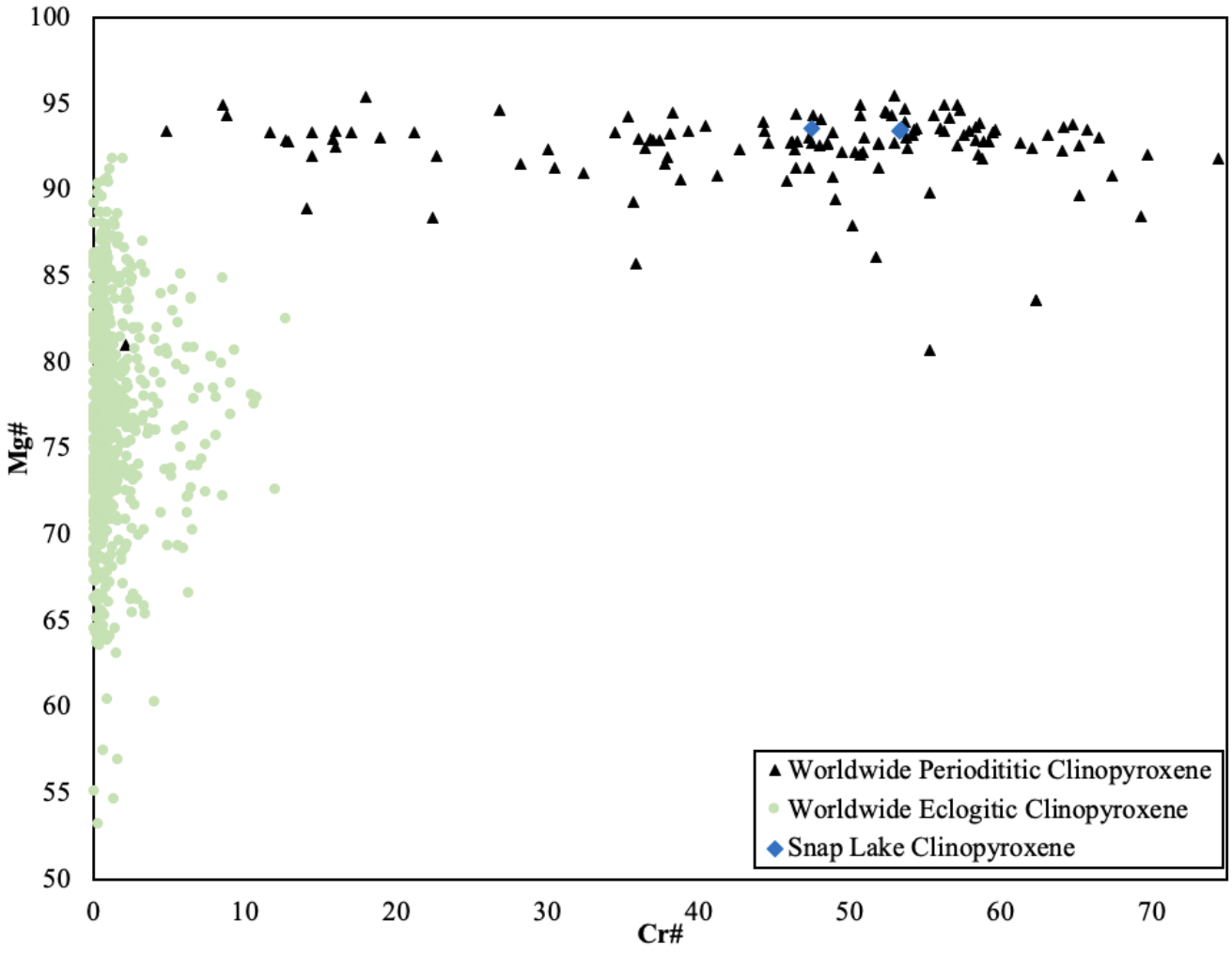

Figure 5.15: Mg# ($molar\ \frac{100\,Mg}{Mg+Fe}$) versus Cr# ($molar\ \frac{100\,Cr}{Cr+Al}$) for Snap Lake clinopyroxene inclusions compared with peridotitic clinopyroxene inclusions and eclogitic clinopyroxene inclusions from the worldwide database (Stachel and Harris, 2008).

The Na_2O content of these clinopyroxene inclusions ranges from 0.51 – 0.97 wt% and also are within the range of compositions for worldwide peridotitic clinopyroxene inclusions (Stachel & Harris, 2008).

Furthermore, Na and Cr cations on the basis of six oxygen show a weak positive correlation following the lherzolitic trend worldwide (Figure 5.16) and indicate the presence of a kosmochlor (Na-Cr) component (Stachel & Harris, 2008). When you add Al to the plot there is a slight improvement in the relationship indicating a minor jadeite component as well. The clinopyroxene from diamond SN041 occurred together with one lherzolitic and one harzburgitic garnet, documenting diamond formation in a changing compositional environment.

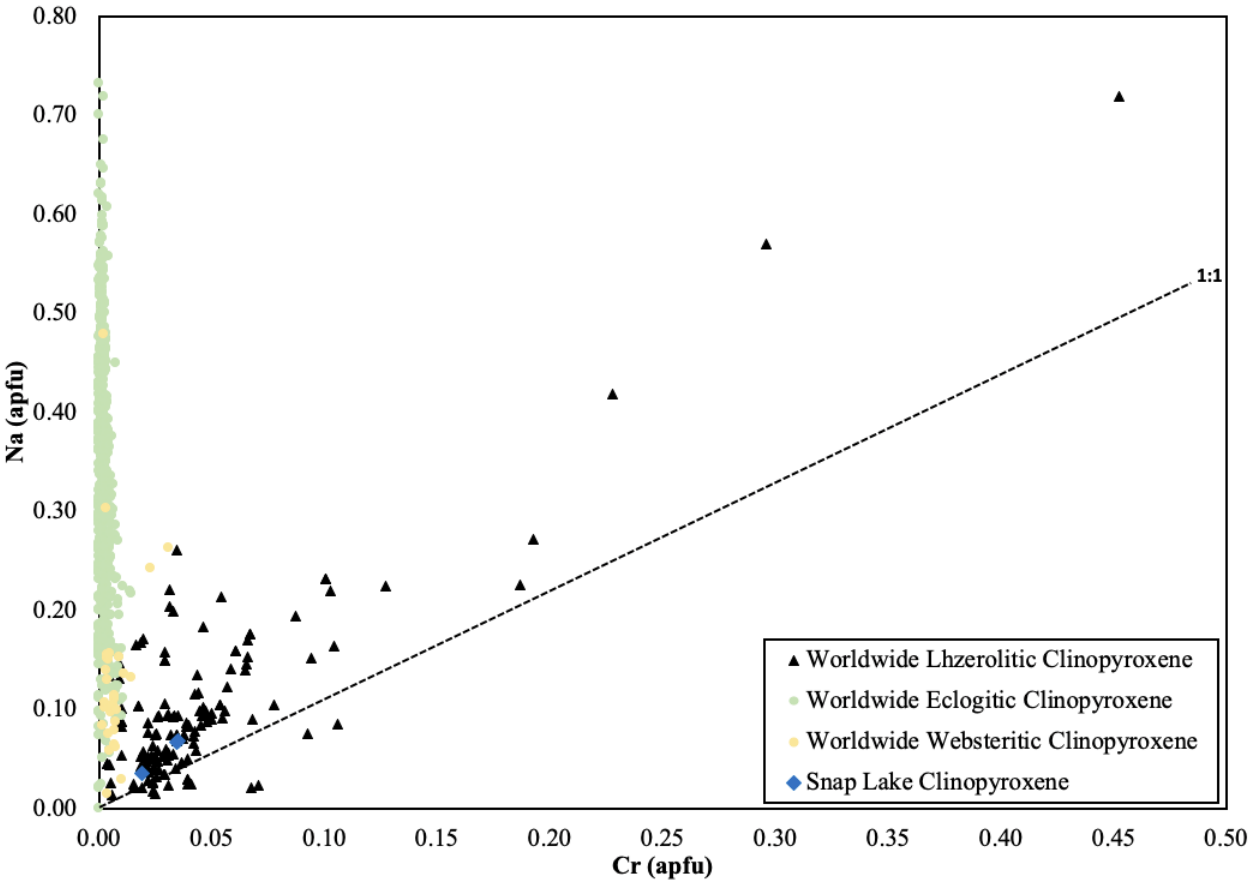

Figure 5.16: Na versus Cr, as cations calculated on the basis of six oxygen per formula unit, for Snap Lake clinopyroxene versus worldwide data (Stachel & Harris, 2008). The 1:1 line indicated accommodation of all Na and Cr as kosmochlor component. Inclusions plotting above the line likely contain an additional jadeite component.

5.4.4 Mg-Chromite

Mg-chromite inclusions (n=15) were recovered from seven Snap Lake diamonds. Six diamonds contained only Mg-chromite, while one diamond (SN134) also contained a non-touching olivine inclusion.

Mg-chromite inclusions recovered from Snap Lake diamonds have Cr_2O_3 contents ranging from 60 – 65 wt % (equivalent to a Cr# of 84 – 93), Mg# ranging from 64 – 73 and TiO_2 contents ranging from < 0.02 wt% to 0.32 wt%. All 15 inclusions show TiO_2 content and Cr# comparable with the worldwide database (Figure 5.17; Stachel & Harris, 2008). SiO_2 content ranges from 0.02 – 0.26 wt % with an average of 0.13 wt%, typical of other localities worldwide (eg. Panda; Stachel & Harris, 2008).

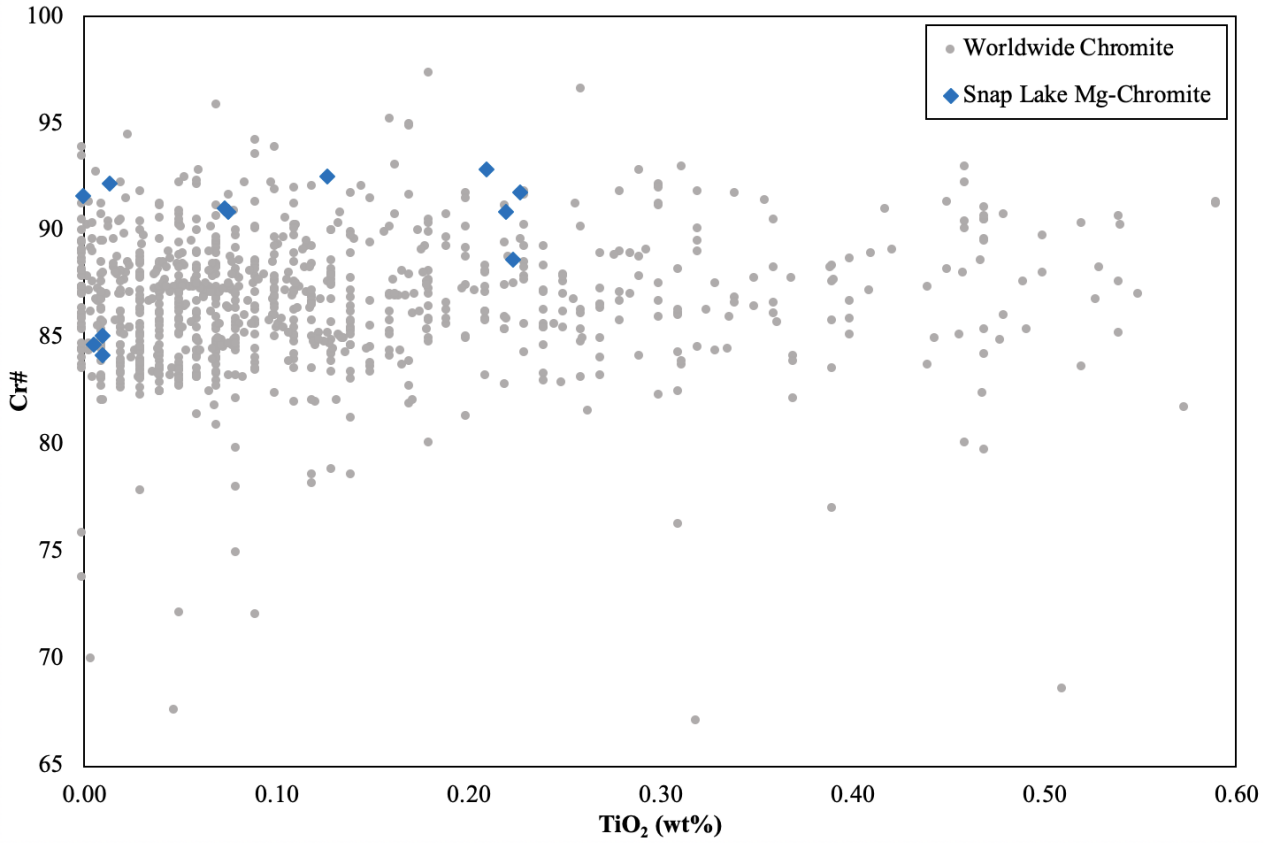

Figure 5.17: Plot of TiO_2 versus Cr# for chromite inclusions from Snap Lake, versus the global database (Stachel & Harris, 2008).

5.4.5 Orthopyroxene

Orthopyroxene inclusions (n=3) were recovered from three diamonds, two of which contained only orthopyroxene, while a third contained orthopyroxene and two non-touching garnet inclusions. The three orthopyroxene inclusions have a very narrow range in Mg# from 93.5 - 94.1, Na_2O and TiO_2 contents are below LOD (≤0.03 wt% and <0.02 wt% respectively), indicating all are of definite peridotitic paragenesis (Stachel & Harris, 2008).

FeO contents range from 4.1 - 4.5 wt % and Al_2O_3 contents range from 0.48 – 0.55 wt%, similar to diamond inclusions reported by Pokhilenko *et al. (*2004). A negative correlation between Al and Fe content is observed, similar to findings from Pokhilenko et al. (2004; Figure 5.18).

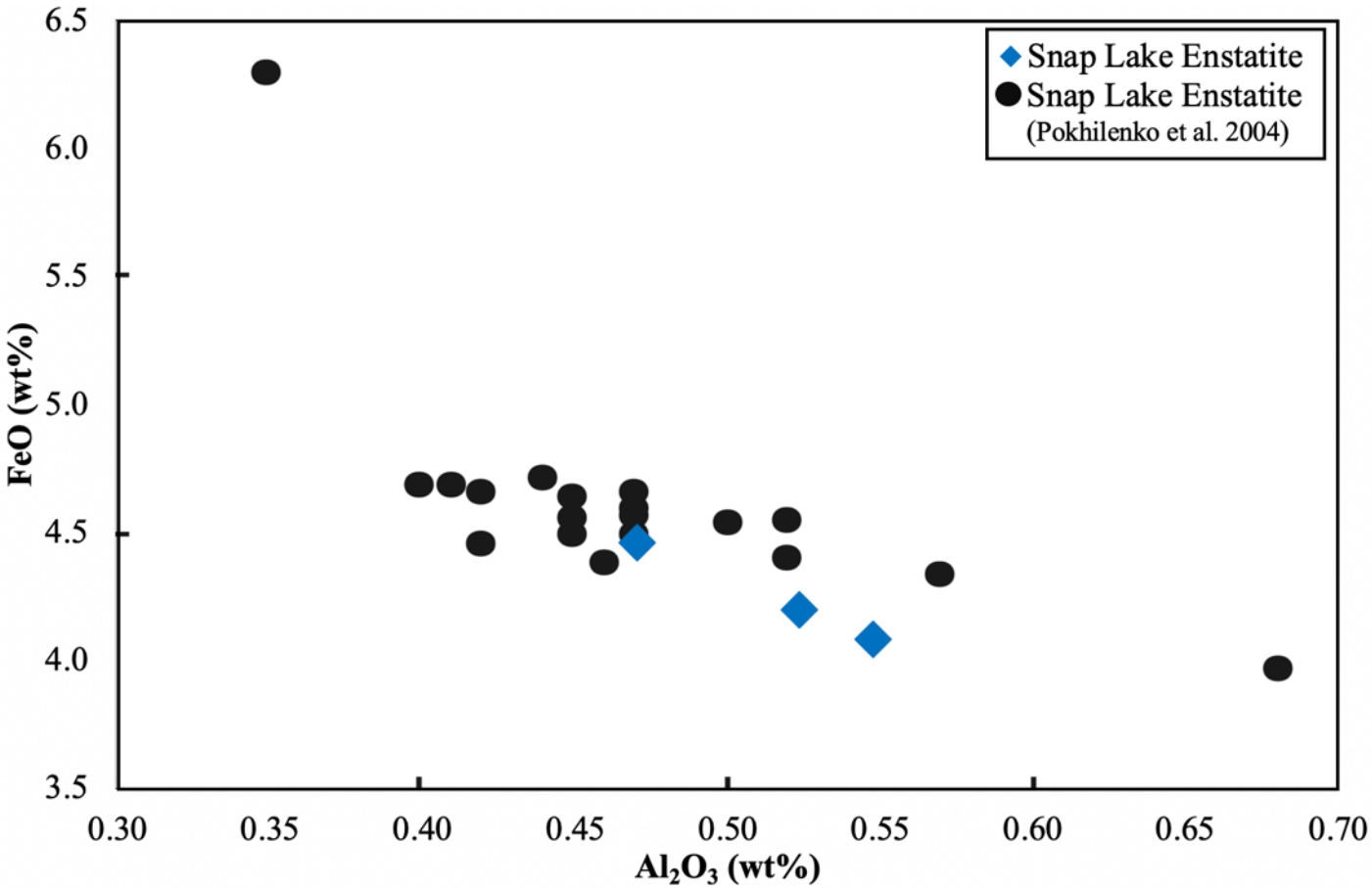

Figure 5.18: Al_2O_3 versus FeO for enstatite inclusions from Snap Lake diamonds from this study, versus those from Pokhilenko et al. (2004).

Snap Lake orthopyroxene inclusions show Cr_2O_3 and CaO contents with narrow ranges, between 0.33 – 0.43 wt % and 0.34 - 0.36 wt%, respectively. Due to co-existing G10 garnets, one inclusion (SN132C) can be classified as harzburgitic. The other two orthopyroxene inclusions are also likely harzburgitic, based on similar compositions to the fields defined by Stachel and Harris (2008) for worldwide orthopyroxene compositions (Figure 5.19).

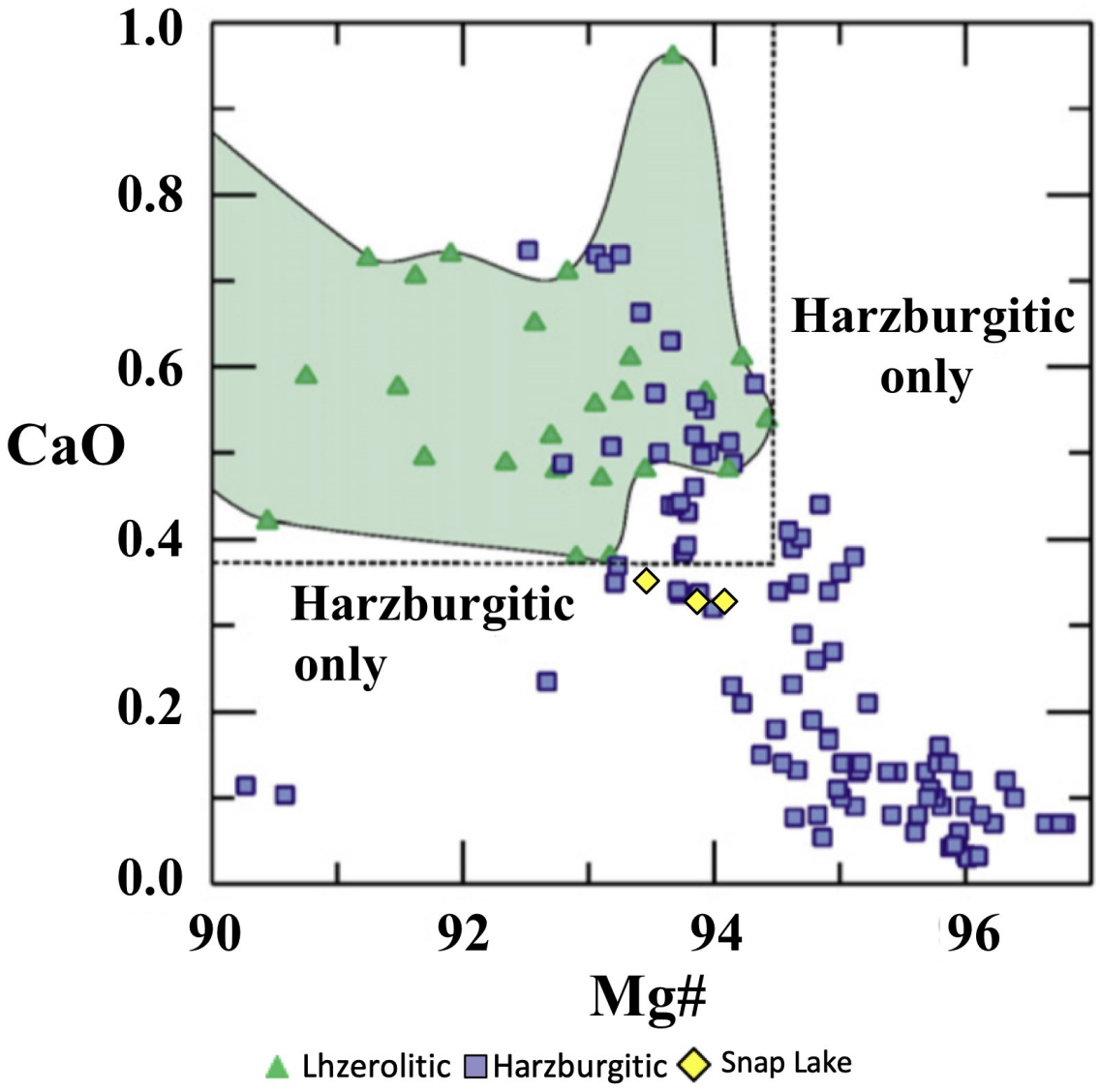

Figure 5.19: CaO (wt%) versus Mg# for orthopyroxene inclusions plotted over top of the compositional fields and known orthopyroxene data. All three orthopyroxene inclusions from Snap Lake diamonds plot within the "harzburgitic only" field defined by Stachel and Harris (2008). Fields and previous data after Stachel and Harris (2008).

5.4.6 Sulphides

Primary sulphide inclusions (n=5) were recovered from five Snap Lake diamonds; three diamonds contain solely sulphides, while one other had a co-existing olivine inclusion and a another contained a polymineralic assemblage of garnet-sulphide-coesite.

Nickel content of sulphides is typically be used to determine the paragenesis of the host diamond, with eclogitic sulphides typically having Ni < 8 wt%, peridotitic sulphides having Ni >12 wt%, and pyroxenitic sulphides having between 8-12 wt% Ni (Aulbach et al., 2009; Bulanova et al., 1996). Based on the information available, three sulphide inclusions in this study are therefore classified as peridotitic, with Ni contents ranging from 20.3 – 58.7 wt% (n=3), while two others are classified as eclogitic, with a Ni content ranging from 4.1 – 4.2 wt % (N=2; Figure 5.20).

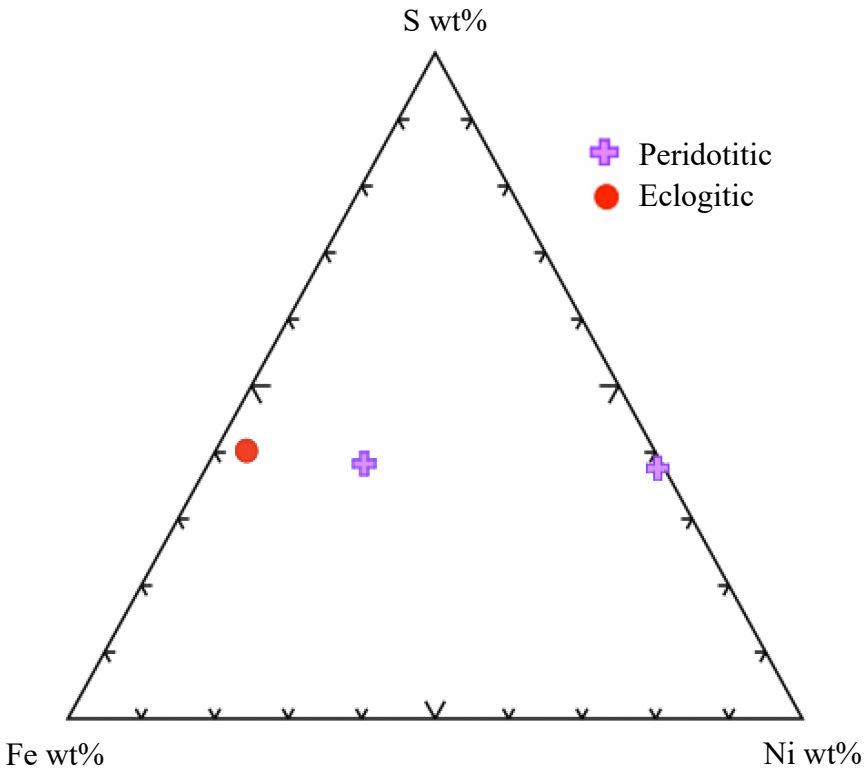

Figure 5.20: Sulphide compositions in weight percent (wt%) on the Fe-Ni-S quadrilateral. Ni-rich (>12 wt%) sulfides are inferred to be of peridotitic paragenesis and Ni-poor (< 8 wt%) are inferred to be of eclogitic paragenesis (Aulbach et al., 2009).

5.4.7 SiO_2 (Coesite)

SiO_2 inclusions (n=2) were recovered from two separate diamonds and, given their association with diamond, are assumed to be coesite. One diamond contained solely coesite (SN128), while a second diamond contained the non-touching assemblage coesite, harzburgitic garnet, and a low-Ni sulphide (mss; SN097).

Coesite in SN128 is essentially pure SiO_2. The second coesite, occurring with peridotitic garnet and low-Ni sulphide (mss), showed enrichment in Al_2O_3 (0.53 wt%), and minor amounts of FeO (0.02 wt%) and K_2O (0.09 wt%).

5.4.8 Potassium Feldspar

A single K-Feldspar inclusion was recovered from a Snap Lake diamond (SN056). The K-Feldspar inclusion has a Na_2O content of 0.52 wt% and CaO, Cr_2O_3, FeO, NiO, MnO, and MgO are all below LOD. K-Feldspar is a rare inclusion in diamond but when present it is assumed to indicate an eclogitic paragenesis.

5.4.9 Wustite-Native Iron

Two mixed metal-oxide inclusions were recovered with two co-existing olivine inclusions from one Snap Lake diamond (SN088). These were composed of a rounded core of native iron rimmed by wustite. This native iron core is nearly pure, with only trace amounts of Ni (0.18 up to 0.30 wt%), Co (0.04-0.08 wt%), Cu (0.33-0.39 wt%) and Cr (0.06-0.08 wt%).

These native iron cores were rimmed by wustite, composed of 93 – 95 wt % FeO, with minor amounts of MnO (0.67 – 0.94 wt%), Cu_2O (0.06 – 0.1 wt %), CoO (0.07 – 0.08 wt%), Cr_2O_3 (0.25 – 1.15 wt%), SiO_2 (0.40 – 3.0 wt%) and Zn (<LOD – 0.03 wt %).

5.4.10 Epigenetic Inclusions

Inclusions (n=5) recovered from two diamonds are interpreted to have an epigenetic origin. These include two secondary associations of sulphide-carbonate inclusions, one serpentine inclusion, and two talc inclusions.

SN008 contained two altered sulphide inclusions and one unaltered sulphide inclusion. The remnant sulphide minerals were composed of Ni, Fe and S, and have very high Ni content ranging from 45.3 – 70.5 wt%. Co was also present, accounting for between 1 – 10 wt%. The majority of the original sulphide-inclusion is now replaced by secondary carbonate (dominantly calcite; Figure 5.21). It appears that the sulphide has been partially dissolved and infilled with calcite, which indicates open system behavior (Figure 5.21). Although no fractures were observed connecting these inclusions to the diamond surface, it is likely that they were overlooked due to the extreme growth layering, surface features, and poor transparency of the diamond. As secondary minerals these inclusions are not further considered.

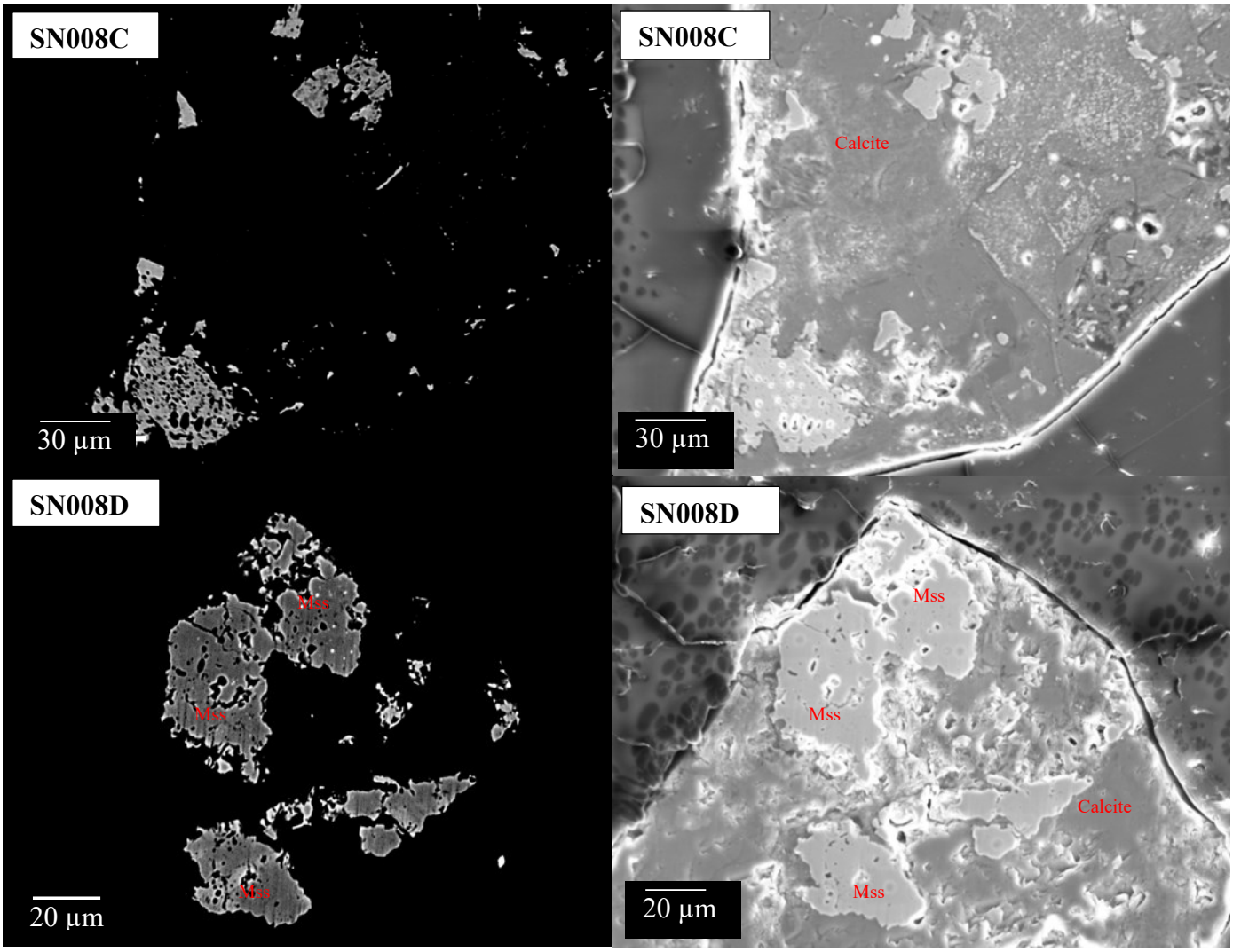

Figure 5.21: SEM images (backscattered electron images(right) and secondary electron images (left)) of the altered sulphide inclusions recovered from diamond SN008 using different contrast settings. Sulphide portion of inclusion SN008C is composed of a combination of exsolved sulphide minerals including heazelwoodite, godlevskite and pentlandite, while in SN008D the remnant sulphide is classified as peridotitic mono-sulfide solid solution. The non-sulphide material is calcite, based on quantitative EDS determination.

Diamond SN022 had a visible fracture "aura" separating the syngenetic inclusions from the altered epigenetic inclusions (Figure 5.22). From this diamond two talc and one serpentinite inclusion were recovered, along with a primary olivine recovered from outside the fracture zone.

Both talc and serpentinite minerals are not stable in the diamond stability field and are assumed to be precipitated after kimberlite emplacement. They are not further considered.

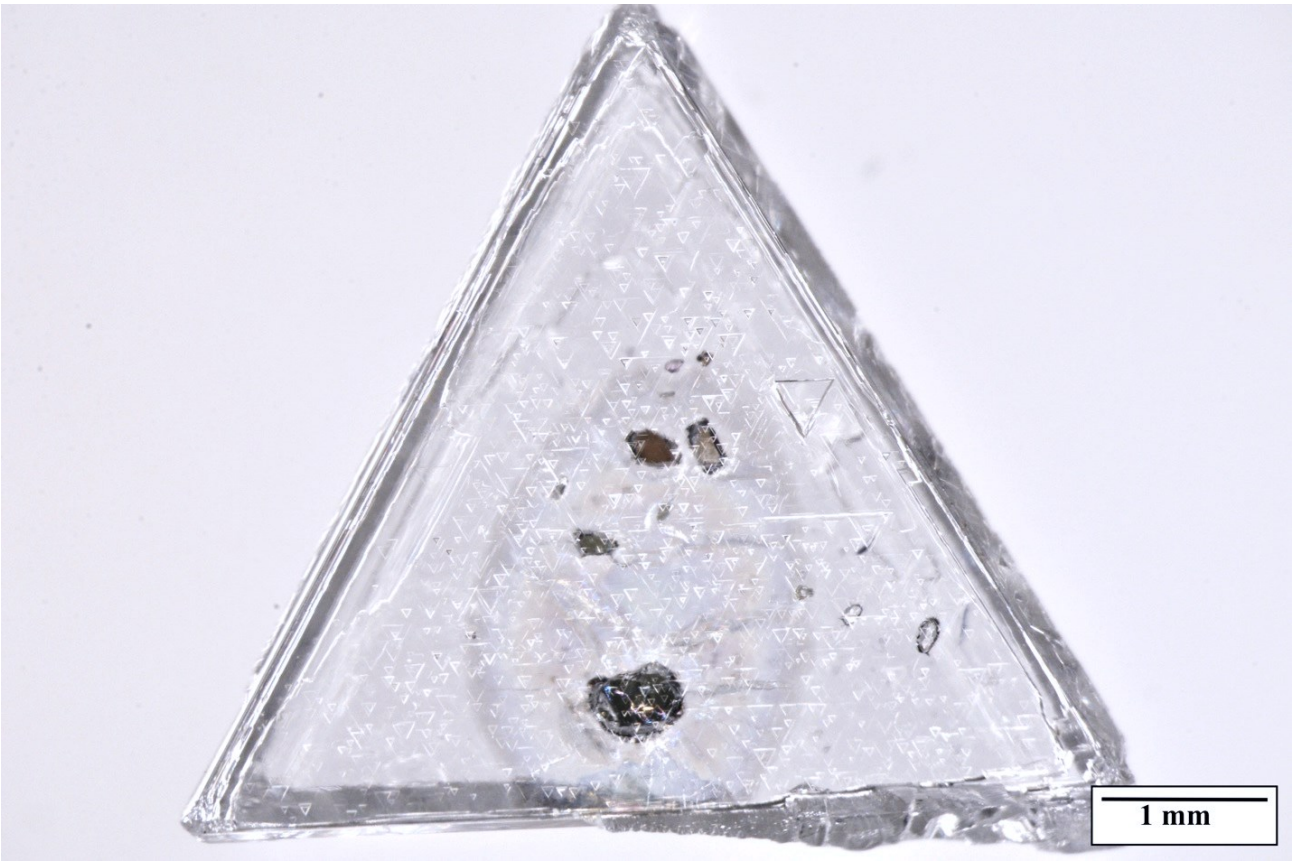

Figure 5.22: Photograph showing the fracture "aura" surrounding the multiple epigenetic inclusions recovered from diamond SN022. Syngenetic olivine and peridotitic garnet (lost during breakage) are also visible outside of the large fracture "aura".

5.5 Trace-element Compositions of Mineral Inclusions

Trace-element compositions were determined for a subset of 31 garnet and two clinopyroxene inclusions by laser-ablation ICP-MS (Appendix 1e) and on a subset of olivine inclusions, through EPMA in a high precision trace-element mode (Table 5.2). Trace-element data normalized to C1-chondrite (McDonough & Sun, 1995) are denoted with the subscript $_N$.

5.5.1 Garnet

Due to the range in size of the garnet inclusions, garnets were analysed using the maximum spot size permitted by particular grain. Spot sizes used in this study for the analysis of garnet include 30 µm (n=6), 50 µm (n=4), 75 µm (n=4), 90 µm (n=14) and 130 µm (n=3).

G3 and G4 eclogitic garnets have very similar shaped REE_N patterns, with a steep positively-sloped $LREE_N$ pattern ($Sm_N/La_N >> 1$), a decreasing positive slope through the $MREE_N$, and approximately flat $HREE_N$ similar to worldwide eclogitic garnets (Figure 5.23A; Stachel et al., 2004). High-Ca (G3) garnets have higher REE abundances than the one low-Ca (G4) garnet but with a similar pattern shape (Figure 5.23). For the high-Ca garnets, the $HREE_N$ concentrations are between 10-30 times chondrite abundance, which agrees with the worldwide average (Stachel et al., 2004). There is small positive Eu anomaly observed in the G4 garnet, but not in the G3 garnets (Figure 5.23A).

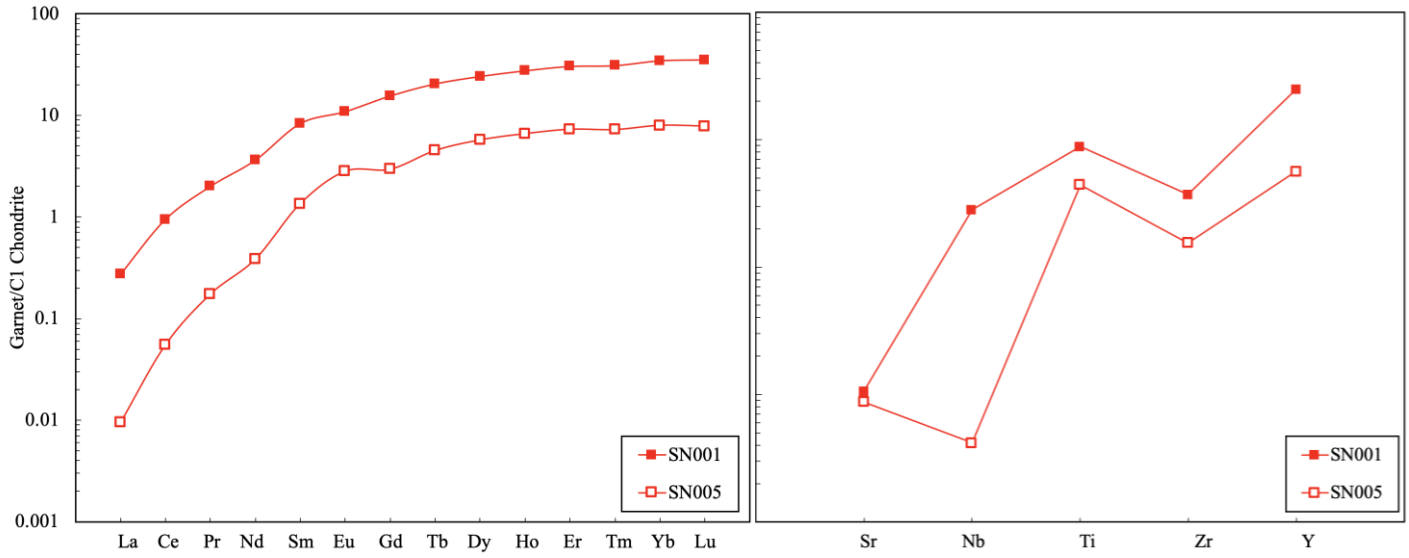

Figure 5.23: A) Average REE_N concentrations in eclogitic garnet inclusions recovered from diamonds SN001 and SN005. **B)** Non-REE trace-element concentration in eclogitic garnet inclusions recovered from diamonds SN001 and SN005. SN001 (G3) is an average of four REE measurements from four separate inclusions recovered. Compositions are normalized to C1-Chrondite (McDonough and Sun, 1995).

Trace-element compositions (Sr, Nb, Ti, Zr, Y) are similar for the G3 and G4 garnets, with the exception of a significant depletion in Nb in the G4 garnet (Figure 5.23B). Ba concentrations in all eclogitic garnets are < LOD (~ 0.02 – 0.05 ppm) and are therefore not plotted.

Peridotitic garnets have a variety of REE_N patterns and can be broadly divided into three categories: sinusoidal, weakly sinusoidal, and "normal." In addition, one diamond contained garnets with very unusual, V-shaped REE_N patterns, with a marked low at Tb (Figure 5.25B).

Ten harzburgitic garnets recovered from nine diamonds have "sinusoidal" chondrite-normalised REE_N patterns (Figure 5.24A). These garnets have a positive slope in their $LREE_N$ with a maximum at Nd, negative slopes through the $MREE_N$ with a minimum between Dy – Er, and a positive slope through the $HREE_N$ (Figure 5.24A). This group of garnets have the lowest Ti contents, with an average of 148 ppm, ranging from 35 - 285 ppm. They have an average Mg# of

87 and are the most depleted Zr and Y of the three groupings, with contents from 0.53 – 20.0 ppm (average = 3.7 ppm) and 0.19-1.2 ppm (average = 0.51 ppm) respectively (Appendix 1e). This pattern is typical of harzburgitic garnets worldwide (Stachel and Harris, 2008).

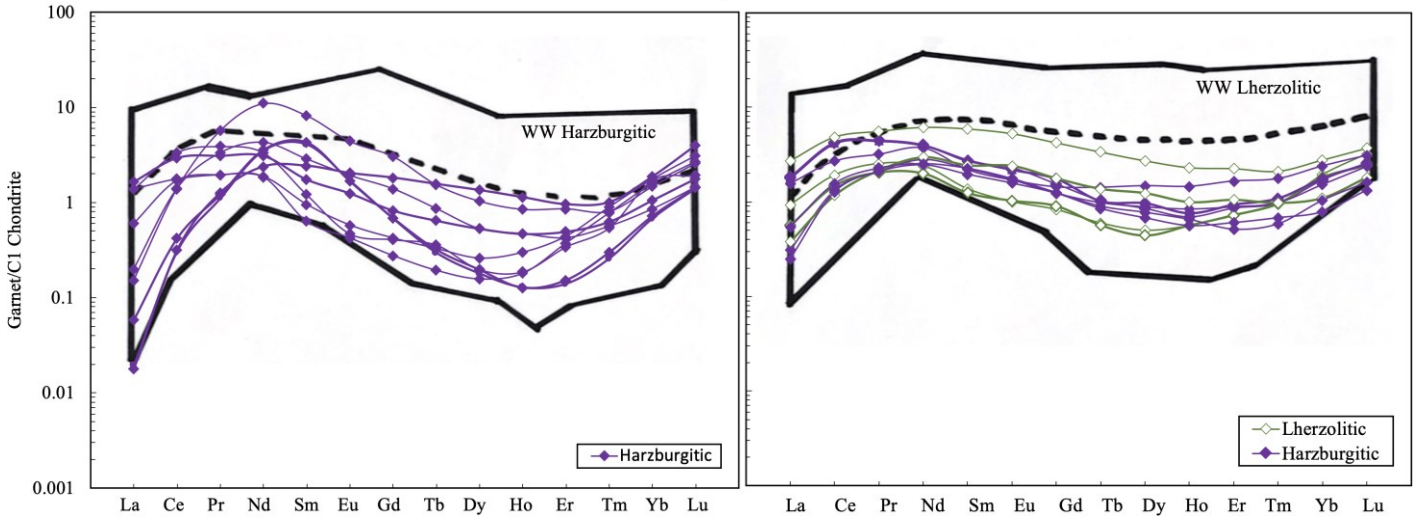

Figure 5.24: A) Snap Lake peridotitic garnets showing "sinusoidal" chondrite-normalised (McDonough & Sun 1995) REE patterns. **B)** Snap Lake peridotitic garnets showing "weakly sinusoidal" chondrite-normalised REE patterns. Ranges and averages for worldwide (WW) harzburgitic and lherzolitic garnets are shown as outlined areas and dashed lines, respectively (Stachel & Harris, 2008).

Four lherzolitic and seven harzburgitic garnets recovered from eight diamonds have weakly sinusoidal REE_N patterns. These garnets have shallow positive $LREE_N$ slopes (La to Nd), weakly negative $MREE_N$ slopes with a trough between Dy - Er, and superchondritic HREE with weak positive slopes (Figure 5.24B). These garnets show much higher Ti contents than those with sinusoidal REE patterns, ranging from 290 – 1788 ppm, with an average of 539 ppm (Appendix 1e). They have an average Mg# of 86 and moderate Zr and Y contents, ranging from 1.09 – 22.39 ppm (average = 4.98 ppm) and 0.81-3.14 ppm (average = 1.32 ppm; Appendix 1e). It is not unusual for both harzburgitic and lherzolitic garnet to show this weakly sinusoidal pattern, as the division between the two groups is transitional (Stachel and Harris, 2008).

Two harzburgitic and one lherzolitic garnet recovered from two diamonds have "humped" to "normal" chondrite-normalised REE patterns (Figure 5.25A). They have a steeply positive slope in the $LREE_N$ with a peak at Sm, and a shallow negative slope through the $MREE_N$ and $HREE_N$. The negative Tm anomaly observed in garnet SN012A is a poor result, likely caused by the less precise measurements of this smaller inclusion and is therefore not further considered. These three garnets have a Ti content ranging from 983 – 1725 ppm, with the highest average at 1242 ppm. They have an average Mg# of 88 and are enriched in both Zr and Y, ranging from 21.2 – 24.4 ppm (average = 22.8 ppm) and 1.4 – 3.9 ppm (average = 2.4 ppm) respectively.

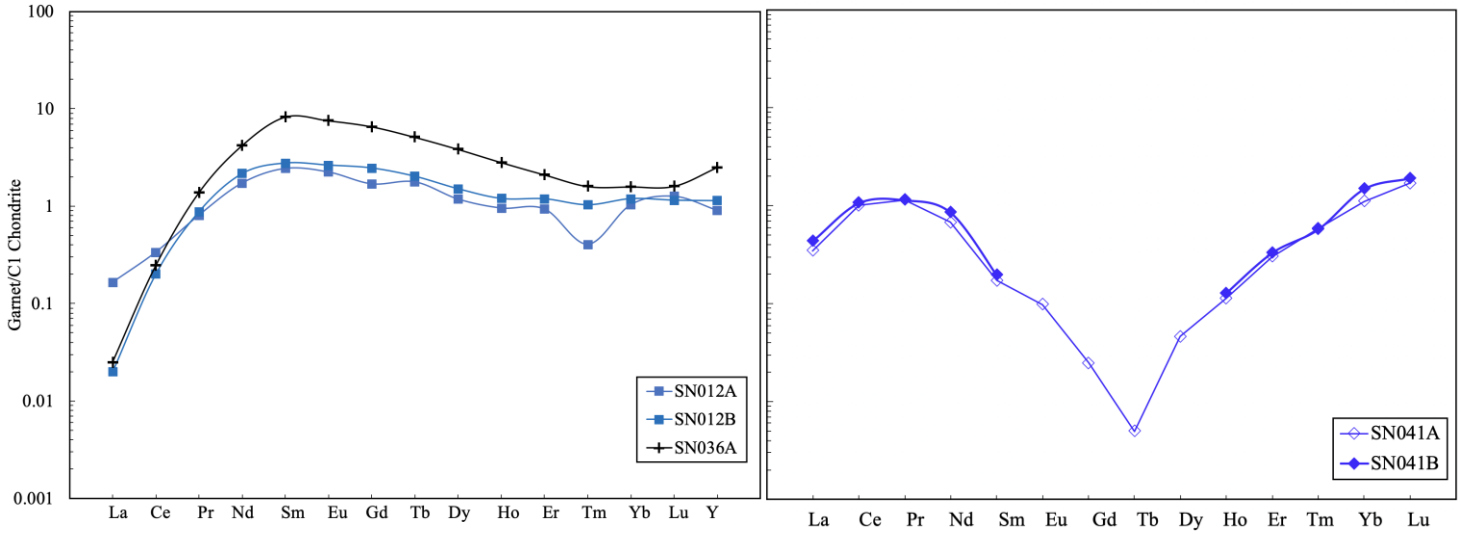

Figure 5.25: Non-sinusoidal REE_N patterns of Snap Lake peridotitic garnets: **A)** humped to normal REE_N patterns and **B)** broadly V-shaped patterns with a hump at Ce-Pr and an extreme low at <0.01 times chondritic abundance at Tb.

One lherzolitic and one harzburgitic garnet recovered from diamond SN041 have unusual, broadly V-shaped REE_N patterns, defined by a positive slope in $LREE_N$ (La_N to Ce_N), extremely steep negative slopes (decrease by over 2 orders of magnitude) from Nd_N to Tb_N, and a very steep positive slope (increasing again by over two orders of magnitude) through the $HREE_N$ (Figure 5.25B). These garnets have an average Mg# of 85, a Ti content of 11.7 and 24.1 ppm, a Zr content

of 0.03 and 0.31 ppm and a Y content of 0.23 and 0.25 ppm. They were recovered with a co-existing non-touching diopside inclusion, that is too small for trace-element analysis.

5.5.2 Clinopyroxene

Two non-touching clinopyroxene inclusions from diamond SN030 were large enough for determination of trace-element contents via LA-ICP-MS (Appendix 1e). The clinopyroxene inclusions have $LREE_N$ enriched compositions and negative slopes from La (~10 x chondrite) to Lu (~ 0.01 x chondrite; Figure 5.26). Similar to findings from Promprated et al. (2004) for Snap Lake clinopyroxene inclusions, these inclusions have high Mg# (93.5 and 93.4), high Cr (1.23 and 1.22 wt%) and low TiO_2 (0.01 and 0.01 wt%).

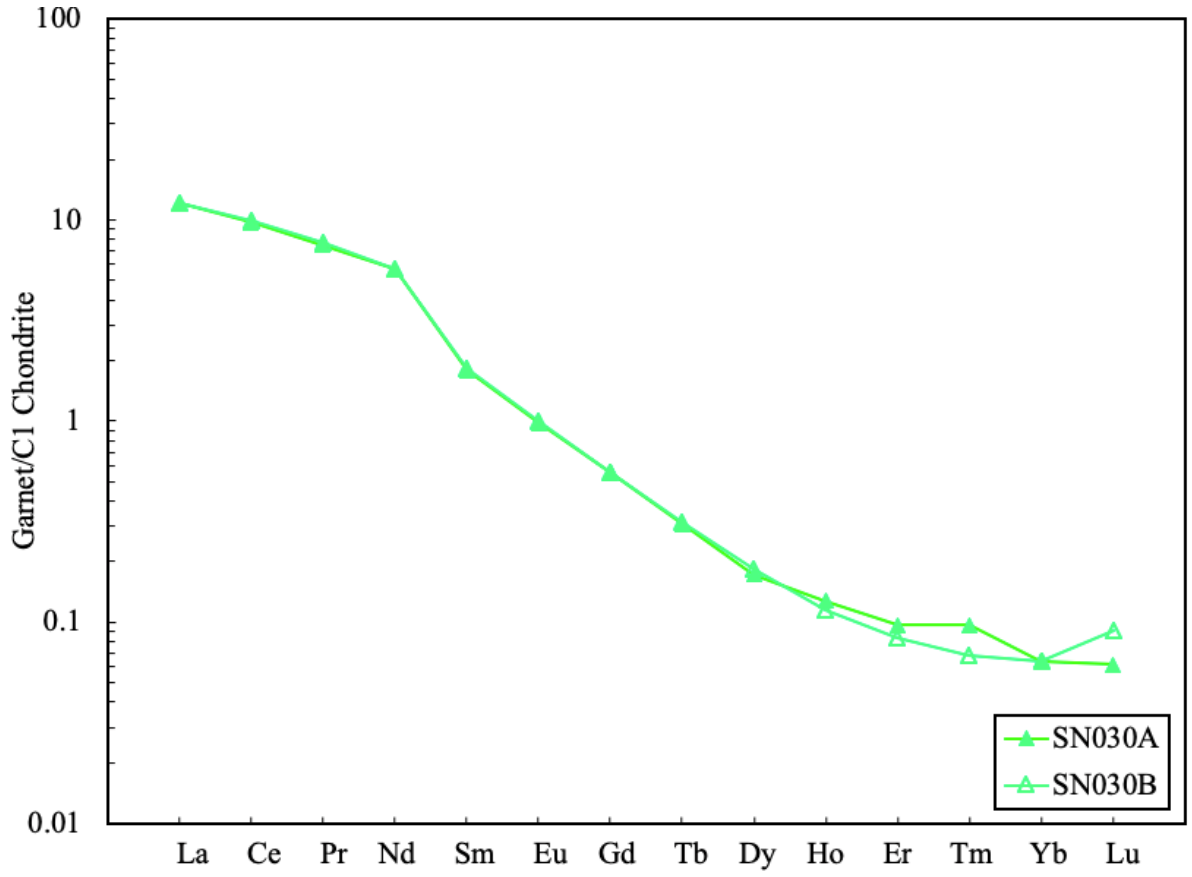

Figure 5.26: REE_N patterns of clinopyroxene inclusions from diamond SN030 (normalized to C1 chondrite of McDonough and Sun (1995)).

5.5.3 Olivine

A set of 53 olivine inclusions were chosen for trace-element analysis, including five harzburgitic, two lherzolitic and 46 unclassified peridotitic olivines.

Comparison of Ca versus Al in Snap Lake olivine inclusions shows a similar trend to that observed by De Hoog et al. (2019; Figure 5.27). There is scattered positive correlation between Ca and Al (Figure 5.27) and an apparent separation into three groups, corresponding to the lherzolitic, harzburgitic and peridotitic (unspecified paragenesis) fields of De Hoog et al. (2019). With the exception of one olivine coexisting with harzburgitic garnet, all inclusions of known lherzolitic and harzburgitic paragenesis fall into the field of peridotitic olivines with unspecified paragenesis (Figure 5.27).

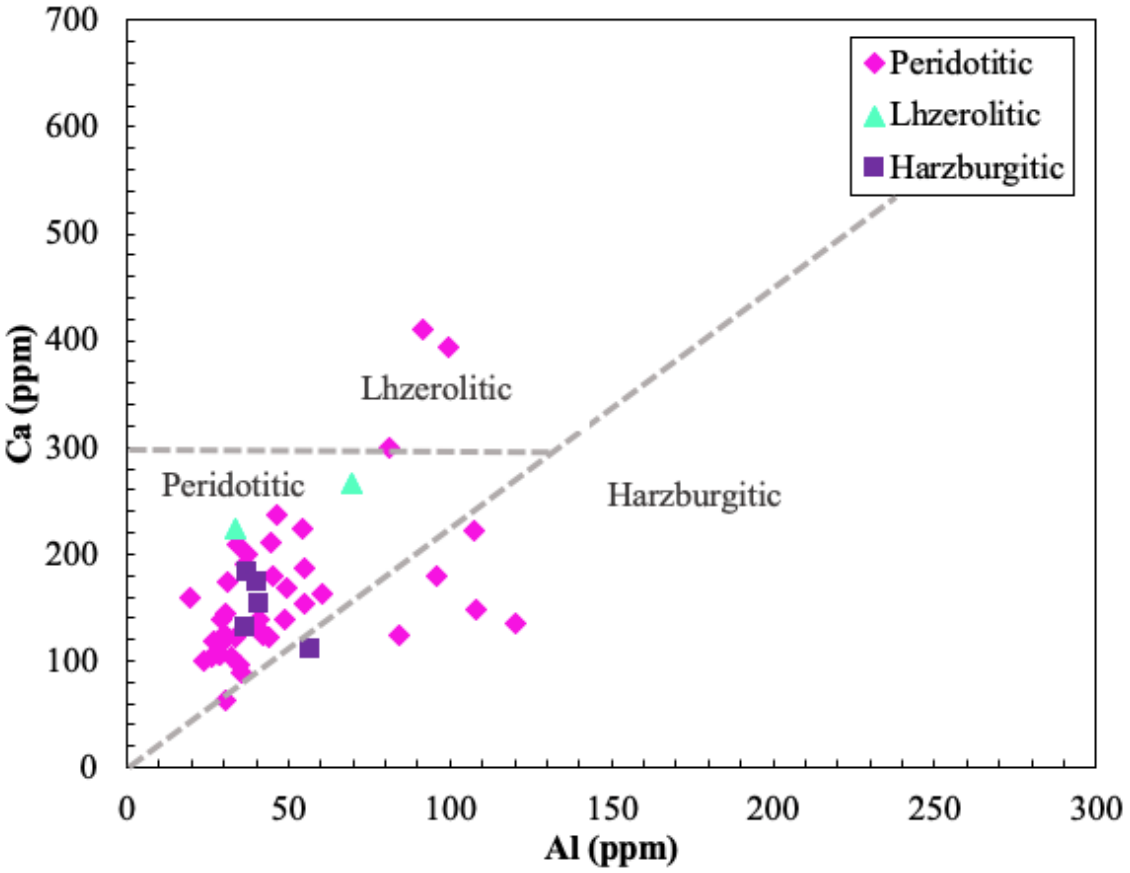

Figure 5.27: Ca versus Al concentrations of Snap Lake olivine inclusions. Fields defining lherzolitic, harzburgitic and peridotitic (unclassified) are taken from De Hoog et al. (2019).

De Hoog et al. (2019) suggests that for harzburgitic olivine inclusions which cannot be identified with the Ca/Al systematics alone, Na – Al - Ca systematics can be employed. Olivine inclusions with < 60 ppm Na and a Na/Al ratio < 0.75 (Figure 5.28A) as well as olivines with < 60 ppm Na and < 300 ppm Ca are classified as harzburgitic (Figure 5.28B; Table 5.1). By this classification method, none of the Snap Lake olivines (including the samples co-existing with harzburgitic garnet) fall within the defined harzburgitic field (Figure 5.28). Instead, all Snap Lake olivine inclusions show enrichment in Na when compared with the Akwatia olivine inclusions described by De Hoog et al. (2019).

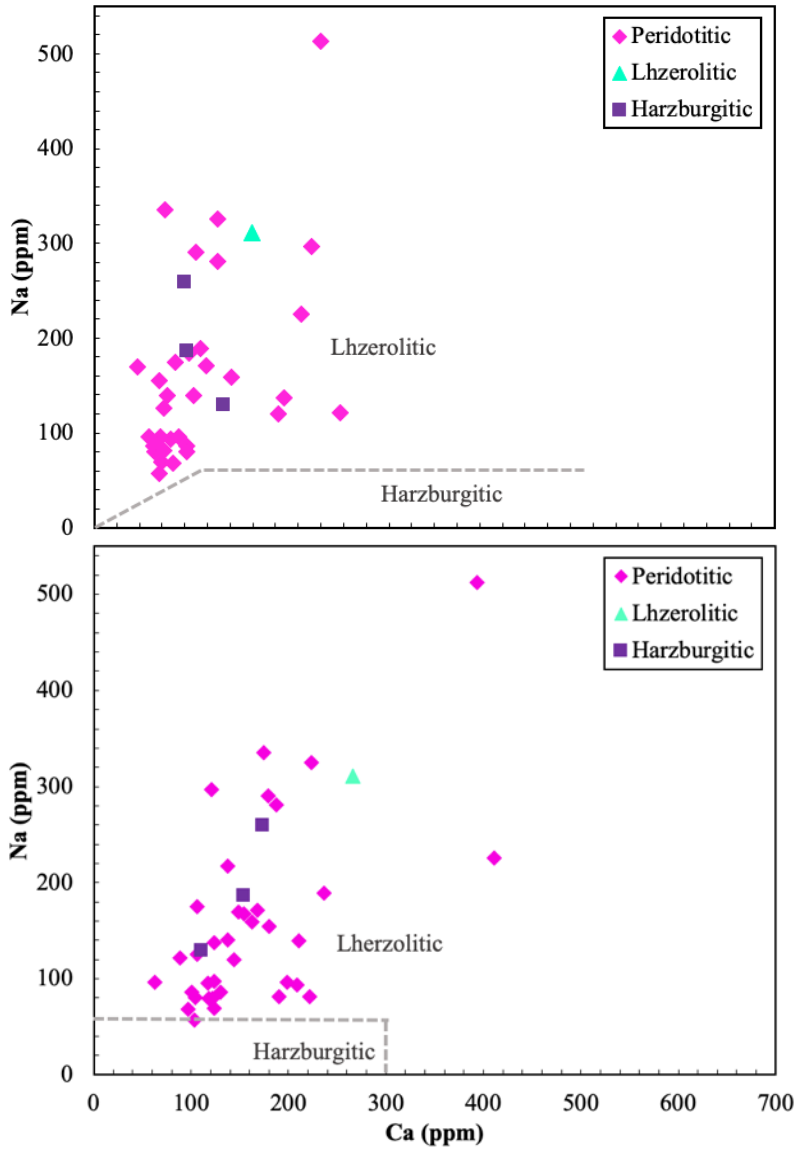

Figure 5.28: A) Na versus Al concentrations of Snap Lake olivine inclusions. **B)** Na versus Ca concentrations of Snap Lake olivine inclusions. Harzburgitic and lherzolitic fields are defined by De Hoog et al. (2019).

Table 5.1: High precision EPMA trace-element data for olivine inclusions recovered from Snap Lake diamonds.

Sample	**SN014C**	**SN020A**	**SN022D**	**SN026D**	**SN027C**	**SN033A**	**SN036B**	**SN051A**
Paragenesis	P	P	P	L	H	P	L	P
Na (ppm)	325	-	184	-	-	-	311	137
Cr (ppm)	217	175	373	145	137	120	480	212
Ca (ppm)	223	124	-	223	183	174	266	124
Al (ppm)	54	42	92	33	37	-	70	84
Ti (ppm)	<LOD	<LOD	<LOD	<LOD	<LOD	<LOD	<LOD	<LOD
Ca/Al	4.1	2.9	-	6.7	4.9	-	3.8	1.5
Na/Al	6.0	-	2.0	-	-	-	4.5	1.6

Sample	**SN052E**	**SN054A**	**SN059B**	**SN063C**	**SN065D**	**SN066B**	**SN070B**	**SN073B**
Paragenesis	H	P	P	P	P	P	P	p
Na (ppm)	130	186	189	80	69	171	336	281
Cr (ppm)	95	163	156	171	132	194	152	166
Ca (ppm)	111	154	236	118	124	168	175	188
Al (ppm)	57	41	47	27	30	49	31	55
Ti (ppm)	<LOD	<LOD	<LOD	<LOD	<LOD	<LOD	<LOD	<LOD
Ca/Al	1.9	3.8	5.1	4.4	4.2	3.4	5.6	3.4
Na/Al	2.3	4.6	4.1	3.0	2.3	3.5	10.8	5.1

Sample	**SN078B**	**SN083A**	**SN084A**	**SN085B**	**SN088A**	**SN089A**	**SN091B**	**SN094A**
Paragenesis	P	P	P	P	P	P	P	P
Na (ppm)	-	93	95	86	513	159	68	96
Cr (ppm)	-	145	181	146	330	141	174	144
Ca (ppm)	254	209	117	130	394	163	97	199
Al (ppm)	-	34	29	41	100	60	35	37
Ti (ppm)	<LOD	<LOD	<LOD	8	<LOD	<LOD	<LOD	<LOD
Ca/Al	-	6.1	4.0	3.2	3.9	2.7	2.8	5.3
Na/Al	-	2.7	3.3	2.1	5.1	2.6	2.0	2.6

- no data **<LOD** = below limit of detection **P** = peridotitic **H** = harzburgitic **L** = Lherzolitic

Sample	SN095B	SN096B	SN098A	SN099A	SN104B	SN107A	SN109A	SN111A
Paragenesis	P	H	P	P	P	P	P	P
Na (ppm)	226	259	-	169	-	122	-	-
Cr (ppm)	363	160	173	200	131	96	155	358
Ca (ppm)	411	173	159	148	177	89	138	300
Al (ppm)	91	40	19	108	-	36	41	81
Ti (ppm)	<LOD	<LOD	<LOD	<LOD	<LOD	<LOD	<LOD	<LOD
Ca/Al	4.5	4.3	8.2	1.4	-	2.5	3.4	3.7
Na/Al	2.5	6.5	-	1.6	-	3.4	-	-

Sample	SN114A	SN115C	SN116A	SN117A	SN118D	SN120A	SN121A	SN122A
Paragenesis	P	P	H	P	P	P	P	P
Na (ppm)	175	81	-	120	155	86	126	290
Cr (ppm)	214	240	137	146	163	73	114	150
Ca (ppm)	106	104	131	144	180	101	106	179
Al (ppm)	29	26	36	31	45	24	29	96
Ti (ppm)	<LOD	<LOD	<LOD	<LOD	<LOD	<LOD	<LOD	<LOD
Ca/Al	3.7	4.0	3.6	4.7	4.0	4.2	3.7	1.9
Na/Al	6.1	3.1	-	3.9	3.4	3.6	4.4	3.0

Sample	SN127A	SN129A	SN133A	SN134E	SN135A	SN136A	SN138A	SN140A
Paragenesis	P	P	P	P	P	P	P	P
Na (ppm)	96	57	297	81	139	140	-	-
Cr (ppm)	165	96	170	364	128	169	166	126
Ca (ppm)	63	104	121	222	211	138	-	135
Al (ppm)	31	32	44	107	44	49	-	120
Ti (ppm)	<LOD	<LOD	<LOD	<LOD	<LOD	<LOD	<LOD	<LOD
Ca/Al	2.0	3.2	2.8	2.1	4.8	2.8	-	1.1
Na/Al	3.1	1.8	6.8	0.8	3.1	2.9	-	-

Sample	SN142A	SN143A	SN144A	SN146B	SN147A
Paragenesis	P	P	P	P	P
Na (ppm)	97	80	81	168	217
Cr (ppm)	124	143	171	123	155
Ca (ppm)	124	122	191	154	138
Al (ppm)	31	34	37	55	29
Ti (ppm)	<LOD	<LOD	<LOD	<LOD	<LOD
Ca/Al	4.0	3.6	5.2	2.8	4.7
Na/Al	3.2	2.4	2.2	3.1	7.4

- no data **<LOD** = below limit of detection **P** = peridotitic **H** = harzburgitic **L** = Lherzolitic

5.6 Geothermobarometry

Co-existing mineral inclusions were recovered from 10 Snap Lake diamonds, permitting calculation of equilibrium temperatures and/or pressures (Table 5.2, 5.3). Accurate analyses and establishing that equilibrium existed between co-existing inclusions are both critical to calculating accurate P-T conditions. Only minerals with suitable oxide totals (99.0 – 101.0 wt%) and cation totals (olivine ≥ 2.990 apfu per 4 oxygens; orthopyroxene and clinopyroxene ≥ 3.990 apfu per 6 oxygens) were used. The PTEXL spreadsheet was used for all P-T calculations except the Ni-in-Grt thermometers of Canil (1999) and Griffin et al. (1989). Results outside of the lithospheric diamond window (900-1400 ˚C) were assumed to indicate erroneous results due to disequilibrium and were not further considered.

Using the garnet-olivine Fe-Mg exchange thermometer of O'Neill and Wood (1979; calculated at a fixes pressure of 50 Kbar), eight non-touching pairs of peridotitic garnet and olivine have equilibrium temperatures of 1110 - 1380˚C with an average of 1230˚C (Table 5.2).

The Ni-in-garnet thermometers of Griffin et al. (1989) and Canil (1999) both assume that garnet is in equilibrium with olivine (assumed to have Ni = 3000 ppm). At high temperature conditions, the Canil (1999) calibration tends to underestimate temperatures while the Griffin et al. (1989) thermometer tends to overestimate temperature (e.g., Shu et al., 2013). For this reason, as recommended by Shu et al. (2013), calculated temperatures using the two thermometers are averaged in order to get the most accurate temperature estimates for peridotitic garnet inclusions. Averaged temperature estimates range from 1050 – 1350 ˚C with an average of 1222 ˚C, agreeing relatively well with the Fe-Mg exchange thermometer of O'Neill and Wood (1979; Table 5.2, 5.3).

For lherzolitic clinopyroxene inclusions, the Nimis & Taylor (2000) single-clinopyroxene thermobarometer (PT[NT_{cpx}]) gives pressure estimates between 52 – 54 kbar (n = 3; two cpx recovered from the same diamond were average) and corresponding temperature estimates between 1090 - 1100˚C (N=3; Table 5.3). Both recovered clinopyroxene inclusions pass the Grütter (2009) and Ziberna et al. (2016) tests. The clinopyroxene based PT estimates fall between the 37-38 mW/m^2 model geotherms of Hasterok and Chapman (2011)

One non-touching harzburgitic orthopyroxene and garnet pair was recovered from diamond SN132. From this mineral pair the equilibration pressure and temperature conditions were estimated using a combination of the Harley (1984) geothermometer and Nickel & Green (1985) geobarometer. This was accomplished iteratively and resulted in a temperature estimate of 1230˚C and a pressure estimate of 68 Kbar, corresponding to a "cool" (37-36 mW/m^2) model geotherm and a depth of ~210 km (based on ~3.15 km/kbar; Figure 5.29).

The Al-in-ol thermometer of Bussweiler *et al. (*2017) was applied to 50 olivine inclusions recovered from 50 diamonds. The Al contents used for these temperature estimates were determined by high-precision analyses of these olivine inclusions via electron microprobe (Table 5.1). Assuming a pressure of 50 kbar, resultant temperatures ranged from 920 – 1130 ˚C with an average of 1020 ˚C (Table 5.3).

Table 5.2: Summary table of co-existing mineral inclusion geothermometers and geobarometers utilized with chemical data from inclusions recovered from Snap Lake diamonds.

Sample	*Assemblage*	*Grt-Ol thermometer of O'Neill & Wood (1979)*	*Grt-Opx barometer (Brey & Köhler, 1990) + T-Harley (1984) Thermometer*		*Fe/Mg exchange thermometer for cpx-gt from Krogh (1988)*
		T(˚C)	P (Kbar)	T(˚C)	T(˚C)
SN026	2 grt, 2 ol	1244			
SN027b	2 grt, ol	1288			
SN036	grt, ol	1126			
SN052	2 grt, 4 ol	1171			
SN054	1 grt, 3 ol	1380			
SN096	grt, ol	1242			
SN116	grt, 2 ol	1255			
SN118	2 grt, 3 ol	1113			
SN041	2 grt, cpx				1106
SN132	2 grt, opx		68	1232	
Average		1227			

Table 5.3: Summary table of single inclusion geothermometers and geobarometers utilized with chemical data from inclusions recovered from Snap Lake diamonds.

Sample	*Assemblage*	*Al-in-Ol Thermometer of Bussweiler et al. (2017)*	*Ni-in-gt thermometer from the averaging of Canil & Griffin*	*Single cpx thermobarometer Nimis & Taylor (2000)*	
		T(˚C)	T(˚C)	P (Kbar)	T(˚C)
SN026	2 grt, 2 ol	975	1329		
SN027a	2 grt, ol	992	1256		
SN027b	2 grt, ol	992	1324		
SN036	grt, ol	1072	1138		
SN052	2 grt, 4 ol	1045	1126		
SN054	1 grt, 3 ol	1004	1308		
SN096	grt, ol	1001	1313		
SN116	grt, 2 ol	989	1342		
SN118	2 grt, 3 ol	1016	1046		
SN041	2 grt, cpx		1296	54	1103
SN132	2 grt, opx		1302		
SN030	cpx			52	1086

SN014C	ol	1026
SN020A	ol	1007
SN022D	ol	1110
SN051A	ol	1097
SN059B	ol	1021
SN063C	ol	956
SN065D	ol	968
SN066B	ol	1026
SN070B	ol	972
SN073B	ol	1041
SN083A	ol	982
SN084A	ol	964
SN085B	ol	1004
SN088A	ol	1122
SN089A	ol	1052
SN091A	ol	986
SN093A	ol	992
SN095A	ol	1108
SN095C	ol	918
SN098A	ol	1133
SN104A	ol	1078
SN104B	ol	989
SN107A	ol	1004
SN109A	ol	1092
SN113B	ol	964
SN115B	ol	1072
SN115C	ol	972
SN117A	ol	943
SN120A	ol	964
SN121A	ol	1116
SN122A	ol	972
SN127C	ol	972
SN129A	ol	1013
SN133A	ol	1131
SN134E	ol	1013
SN135A	ol	1026
SN136B	ol	972
SN138A	ol	1094
SN140B	ol	982
SN142A	ol	982

SN143A	ol	1004			
SN146A	ol	992			
SN146C	ol	979			
SN001	grt		885		
SN005	grt		1110		
SN012	grt		1248		
SN024	grt		1253		
SN025	grt		1256		
SN049	grt		1349		
SN050	grt		1188		
SN053	grt		1304		
SN097	grt		1173		
SN108	grt		1096		
SN130	grt		1244		
Average		1017	1222	50	1095

6. Discussion

6.1 SCLM Beneath the Snap Lake Kimberlite Dyke

Based on major-element compositions of inclusions recovered from Snap Lake diamonds, the diamond-facies subcontinental lithospheric mantle (SCLM) beneath the Snap Lake kimberlite dyke is composed of predominantly peridotite with a minor component of eclogite. A peridotitic affinity is assigned to ~ 93 % (n=81) of the studied breakage population, while an eclogitic affinity is assigned to only 5.7% (n=5; Figure 6.1). A single diamond (~ 1.1 % of studied diamonds) shows a mixed paragenesis hosting a peridotitic garnet, a Ni-poor sulphide and a coesite together (Figure 6.1). This is very similar to previous studies, which estimated the diamond facies SCLM to be composed of 95 % peridotitic and 5 % eclogitic underlying Snap Lake kimberlite dyke (Pokhilenko et al., 2004, 2001).

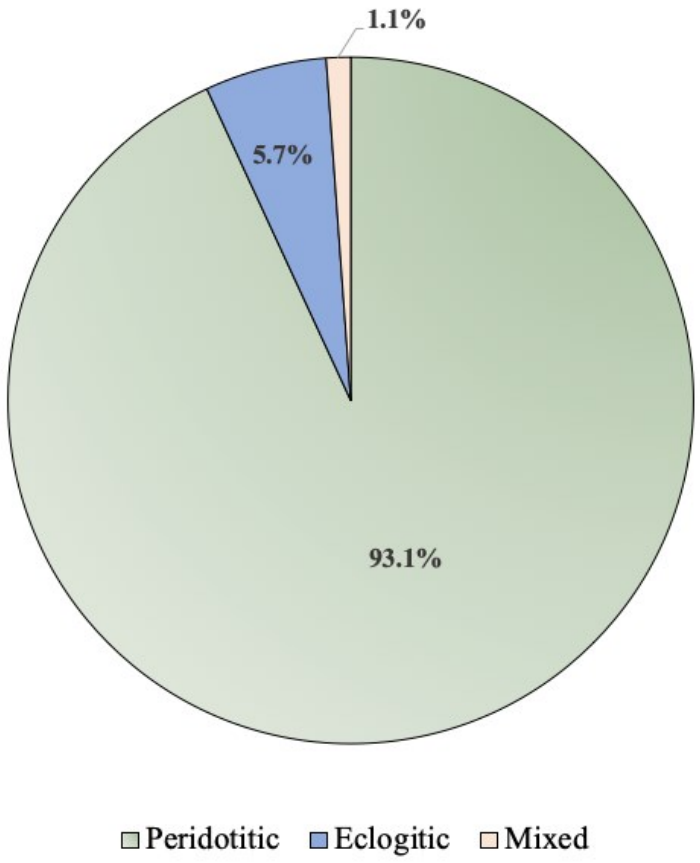

Figure 6.1: Paragenesis of Snap Lake diamonds based on inclusion compositions.

6.1.1 Peridotitic Diamond Substrate

The chemically highly depleted nature of olivine inclusions recovered from Snap Lake diamonds – inferred from Mg# ranging from 91.5 - 93.8 – indicate that the majority have a harzburgitic paragenesis (Appendix 1d). This agrees with findings which described an average Mg# of 92.6 (Pokhilenko et al., 2001, 2004) for Snap Lake olivine inclusions, as well as with worldwide xenolith data (average = 92.6; Bernstein et al., 2007). Olivine forsterite contents between 92 – 93 are only produced after extensive degrees of melting to the point of exhaustion of orthopyroxene (Bernstein et al., 2007). In addition, Snap Lake olivine inclusions largely have depleted CaO content, 63 of the 99 olivine inclusions recovered have ≤ 0.02 wt% CaO, which also suggests a dominantly harzburgitic paragenesis. Snap Lake chromite inclusions show rather low Mg# ranging from 64 – 73, which may indicate that the chromite comes from a cooler end of the observed spectrum and that chromite bearing diamonds might sit relatively shallow within the diamond sequence. Additional data is needed to verify these conclusions.

Peridotitic garnet inclusions from the Snap Lake kimberlite dyke are dominantly harzburgitic (~ 80 %; n=21) and generally low in CaO (1.4 to 7.9 wt%) content. Grütter et al. (1999) suggested that harzburgitic garnets with CaO < 1.8 wt% and Cr_2O_3 > 4 wt% may derive from ultra-depleted, likely dunitic sources (n=1 in this study), that experienced at least 50% melt extraction. The remainder of the Snap Lake garnets (CaO between 1.8 - 7.9 wt% and Cr_2O_3 < 13.3 wt%) are derived from "normal" harzburgitic substrates, indicative of melt extraction in excess of 20% but less than 50% (Grütter et al., 1999).

In contrast to the findings of Pokhilenko et al. (2001, 2004), there is a lack of majoritic garnet within the diamond population examined by me. Previous studies have estimated up to 33 %

majorite component in garnets recovered from Snap lake kimberlite dyke (Pokhilenko et al., 2001, 2004), whereas in our sample set the calculated majorite component in peridotitic garnets (0.0 to 1.6 %; calculated following Locock 2018) is not significant within analytical uncertainty.

REE_N patterns in garnet can reflect factors such as the degree of depletion and possible equilibrium with metasomatic fluids/melts (Stachel et al., 1998). The majority of Snap Lake garnets show some degree of sinuosity when normalized to C1-chondrite (McDonough & Sun, 1995), indicating a variable level of melt extraction (Figure 5.24). When normalized to J-4 garnet, thought to closely resemble garnet in equilibrium with primitive mantle, the sinuosity visible in chondrite normalized patterns is lost and instead a trough with variable depletion in MREE is observed (Figure 6.2A, B; Stachel et al., 1998). Similar to observations in Roberts Victor peridotitic garnet, the positive slope in $HREE_{J-4}$ from Ho and Lu indicates high levels of melt extraction, resulting in strongly LREE depleted patterns (very low $LREE_{J-4}/HREE_{J-4}$), suggesting a polybaric melting process starting in the garnet stability field (Stachel et al., 1998). The negative slope from the $LREE_{J-4}$ to Ho_{J-4} is interpreted as a secondary feature, caused by secondary metasomatic re-enrichment (Shimizu and Richardson 1987; Stachel et al. 1998). This type of V-shaped pattern is observed in the majority of Snap Lake garnet inclusions and points towards a depleted and then metasomatically re-enriched peridotitic SCLM beneath Snap Lake kimberlite dyke.

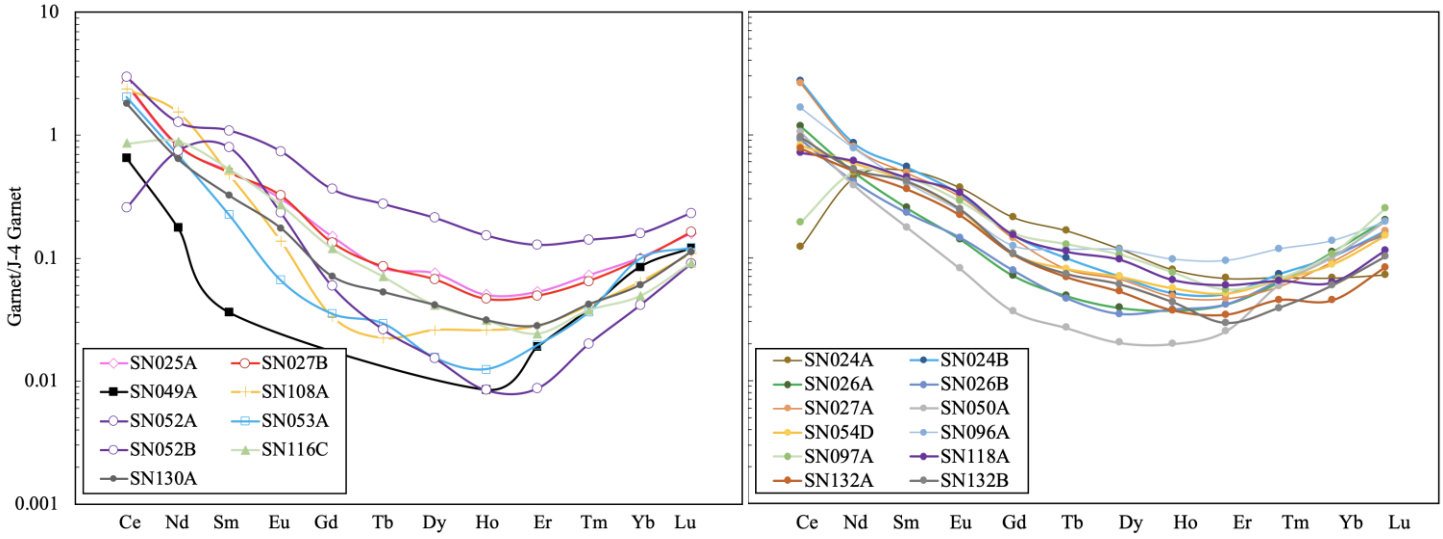

Figure 6.2: Comparison of the REE patterns for peridotitic garnets recovered from Snap Lake diamonds normalized to J-4 garnet (Stachel et al., 1998). **A)** Garnets with sinusoidal REE patterns when normalized to C1-chondrite. **B)** Garnets with weakly sinusoidal REE patterns when normalized to C1-chondrite.

REE_N patterns for both harzburgitic and lherzolitic garnets are primarily sinusoidal or weakly sinusoidal, implying that a similar style of metasomatic enrichment occurred across both harzburgitic and lherzolitic diamond substrates (Figure 5.24). This is further strengthened when comparing Y versus Zr concentrations of peridotitic garnets (Figure 6.3). All recovered Snap Lake garnet inclusions plot within the depleted field, i.e. experienced only minor metasomatic overprint. Extrapolating the overall trend shown by the inclusions indicates fluid dominated (phlogopite) type metasomatism with consistently low Y contents with increasing Zr.

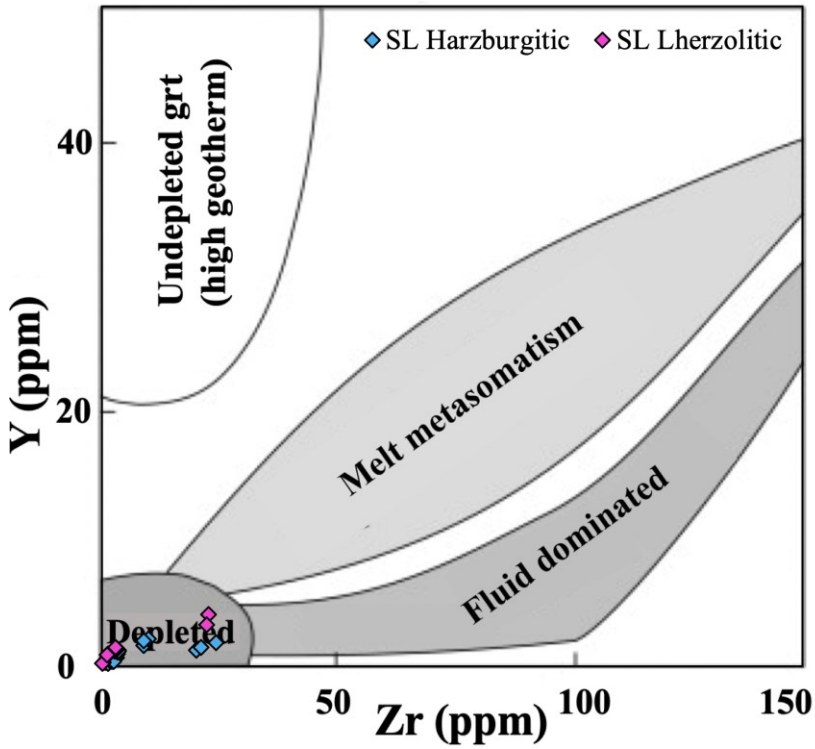

Figure 6.3: Y versus Zr for Snap Lake harzburgitic and lherzolitic garnet inclusions. Compositional fields and trends taken from Pearson et al. (2003) adapted from Griffin and Ryan (1995).

One lherzolitic and one harzburgitic garnet show "normal" (or "primitive") REE_N patterns with a much flatter $MREE_N$-$HREE_N$ (SN012A, B & SN036A in Figure 5.25; Stachel & Harris, 2008). This pattern has been previously attributed to a change in metasomatic style from fluid-dominated towards melt-dominated (Donnelly et al., 2007, Stachel et al., 2004; Stachel and Harris, 2008). The 'normal' patterns shown by these two garnets are characterized by relatively low HREE contents which fits well with them still plotting within the depleted field above (Figure 6.3).

Generally, Ti is quantitatively removed from residues of extreme melting (Prytulak & Elliott, 2007) and thus in cratonic peridotites low Ti abundances are expected. However, based on trace element data for Snap Lake inclusions, 10 of the 27 peridotitic garnets in this study have

TiO_2 > 0.04 wt%. In addition, two lherzolitic and one harzburgitic garnet show strongly elevated TiO_2 contents; SN096 - 0.16 wt%, SN036 - 0.30 wt% and SN050 - 0.32 wt%, accompanied by high Cr_2O_3 contents (8.88 - 13.3 wt%). These high Cr_2O_3 contents document high levels of melt extraction during decompression melting extending into the spinel stability field (Stachel et al. 1998; Brey & Shu 2018) and in combination with the high TiO_2 support the theory of a depleted SCLM which experienced variable degrees of metasomatic re-enrichment.

6.1.2 Eclogitic Diamond Substrate

Eclogitic inclusions recovered in this study include garnet (n = 5), sulphides (n = 4), SiO_2 (coesite; n = 2), and K-Feldspar (n = 1). Four of the recovered eclogitic garnet inclusions are classified as high-Ca (G3) while one is classified as low-Ca (G4; Grütter et al., 2004). The G3 eclogitic garnets show REE_N patterns typical of worldwide eclogitic garnet inclusions, with LREE depletion and a positive MREE-HREE slope ending at ~ 30 x chondrite (Figure 5.23). The single G4 eclogitic garnet has a similar REE_N pattern but at much lower REE concentrations than the high-Ca garnets and typical eclogitic garnet inclusions worldwide (Stachel & Harris, 2008). This pattern is very similar to that found in low-Ca garnet from previous studies on Snap Lake (Promprated et al., 2004 and references therein). The low-Ca garnet also shows a small positive Eu anomaly. The positive Eu-anomaly indicates a low-pressure igneous protolith that accumulated plagioclase, supporting a model of subducted crustal protoliths (Aulbach et al., 2002; Donnelly et al., 2007).

There appears to be a relatively high variability in the composition of the eclogitic substrate beneath the Snap Lake kimberlite dyke, indicated by the coesite and K-Feldspar inclusions

recovered. The K-feldpar recovered from Snap Lake is very similar in composition to inclusions reported by Meyer & McCallum (1986), Wang (1998) and to eclogitic xenolith data from Ater et al. (1984; Table 6.1). This feldspar inclusion has a molar K/(K+Na) ratio of 0.953, which is near the orthoclase endmember composition ($KAlSi_3O_8$).

The presence of 'evolved' phases like coesite and potassium feldspar suggest possible involvement of hydrothermal alteration of the protolith (Schulze et al., 2000; Donnelly et al., 2007 and references therein). Occurrence of primary coesite and potassium feldspar can also be an indicator of protolith composition and degree of melt extraction. During subduction of MORB tholeiite, resulting eclogite is coesite-bearing as long as potential slab melting does not exceed 20 % melt extraction (McDonough 1991; Schulze et al., 2000). For a suitable protolith composition, presence of K-feldspar in eclogite similarly indicates that extensive melting during subduction did not occur (Schulze et al., 2000). This indicates that the eclogitic protolith in the SCLM beneath Snap Lake either were not melted or underwent relatively low degrees of partial melting during subduction in order to retain free SiO_2.

Table 6.1: Major element composition of K-feldspar inclusions in diamond from Snap Lake (SN056) and the Sloan kimberlite (Meyer & McCallum, 1986), an eclogite xenolith from the Sloan kimberlite (Ater et al., 1984), and Diamond S32, Shandong, China (Wang, 1998).

Samples	*SN056*	*Sloan Diamond Inclusion*[a]	*Eclogitic Xenolith, Sloan Kimberlite*[b]	*Diamond S32*[c]
SiO_2	63.39	64.80	65.00	65.30
TiO_2	0.00	0.00	0.01	0.01
Al_2O_3	19.25	18.10	18.10	18.50
V_2O_3	0.00	-	-	-
Cr_2O_3	0.00	0.03	0.00	0.00
FeO	0.00	0.02	0.00	0.09
NiO	0.00	0.07	0.13	0.03
MnO	0.00	0.00	0.08	0.03
MgO	0.00	0.00	0.00	0.00
CaO	0.01	0.00	0.00	0.01
Na_2O	0.52	0.63	0.48	1.95
K_2O	16.24	15.80	15.50	13.50
P_2O_5	0.00	-	-	-
Total	99.41	99.40	99.80	99.40
K/(K+Na)	0.953			0.82

[a] Meyer & McCallum, (1986) [b] Ater at al. (1984) [c] Wang, (1998)

6.1.3 Mixed Paragenesis

Traditionally, mineral inclusions in diamond are divided into two principal suites, peridotitic and eclogitic (plus a minor websteritic suite). It is well accepted that both eclogitic and peridotitic mineral inclusions exist in the same diamond population, but usually do not co-exist together within single diamonds. In some rare instances, however, eclogitic and peridotitic inclusions have been documented together in a single diamond.

One diamond from Snap Lake shows a mixed paragenesis in its recovered inclusions. SN097 held a peridotitic garnet co-existing with non-touching coesite and eclogitic sulphide inclusions. The exact position of the inclusions with respect to internal growth layering is unknown but the sulphide, the coesite and the peridotitic garnet were all observed pre-breakage in the main

octahedral diamond of this aggregated sample, and not from the smaller aggregated one as described and photographed pre-breakage (Figure 6.4).

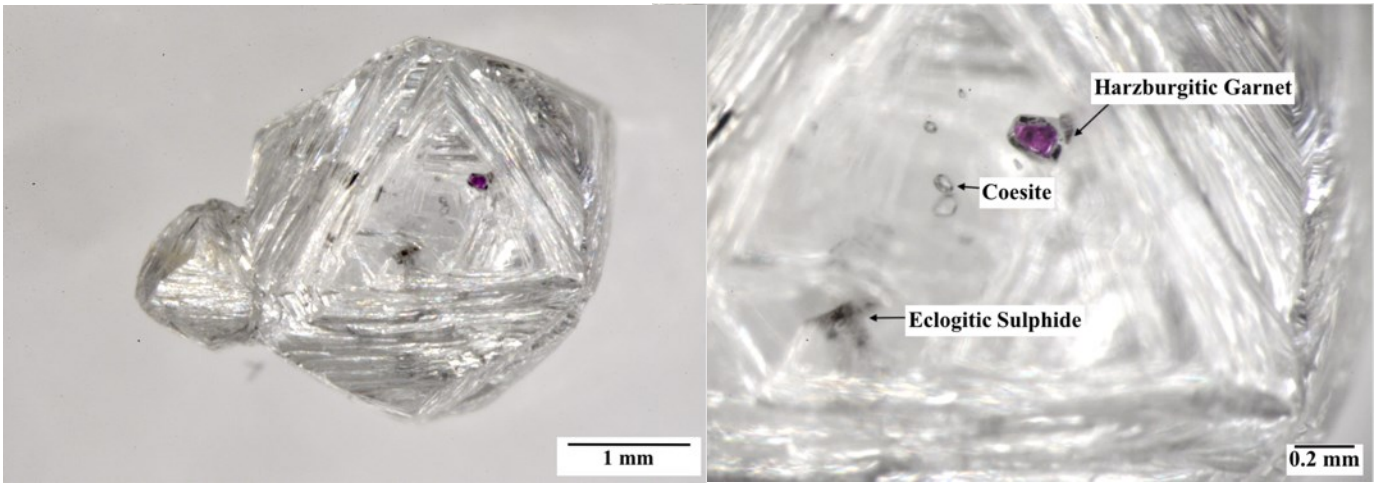

Figure 6.4: Photographs taken of diamond SN097 pre-breakage showing the location of the three recovered inclusions within the same diamond. In addition, three more small colorless inclusions (not recovered) are visible.

Researchers have suggested that coesite can also be harzburgitic in paragenesis, having been recovered previously with harzburgitic garnet from Mwadui (Stachel et al., 1998) and Namibia (Leost et al. 2003). From this association, it was suggested that coesite may form from a peridotitic bulk composition, due to sequential carbonation reactions which in turn produce SiO_2 and calcic magnesite (Stachel et al., 1998). This situation, however, is unlikely to have been the case for Snap Lake diamond SN097.

The presence of a co-existing low Ni sulphide points towards an eclogitic paragenesis. In some instances, point analysis of sulphide inclusions can be interpreted as eclogitic when in fact they are peridotitic. The exsolution of primary Ni-rich monosulfide solid solution into Ni-poor (pyrrhotite and pyrite) and Ni-rich (pentlandite) domains may occur during sufficiently slow cooling at temperatures distinctly below 1000 °C (Harris, 1992). During sample polishing, by chance only the Ni-poor portion of an exsolved Ni-rich mss may be exposed for EPMA analysis.

This, however, is doubtful to be the case for SN097. This sulphide inclusion was very small (~ 55 µm wide), the backscatter image shows very little difference in shading and four-point analyses were completed across the inclusion surface. It is unlikely that there is a hidden portion of this grain with high-Ni sulphide, which would need to account for more than half of the inclusion, as such an eclogitic paragenesis remains.

The occurrence of both eclogitic and peridotitic suite inclusions within a single diamond suggests that the two sub-populations do not necessarily represent distinct environments. Instead, at least locally, this indicates that this diamond formed in an evolving environment with both eclogitic and peridotitic substrates in close proximity to one another.

6.1.4. Mixed Oxide-metal Inclusions

One Snap Lake diamond (SN088) contained two olivine inclusions as well as two mixed oxide-metal inclusions. This mixed inclusions are composed of a core of native iron rimmed by wustite (Figure 6.5).

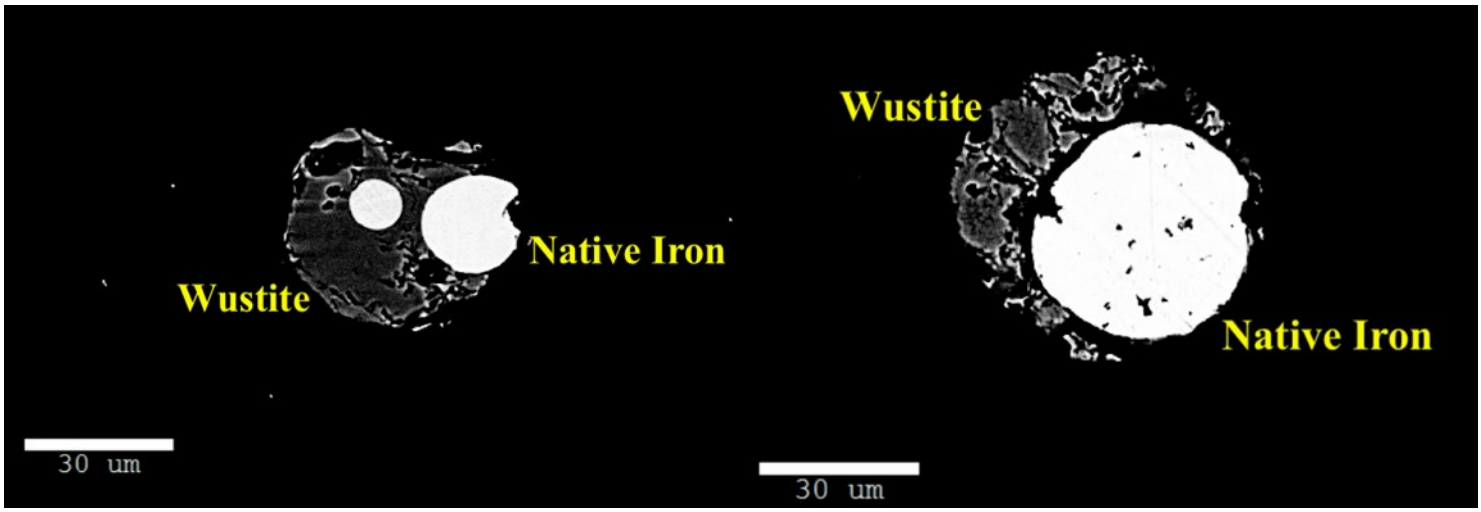

Figure 6.5: Backscattered electron (BSE) image of inclusion SN088C (left) and SN088D (right) showing the native iron core rimmed by wustite.

Similar to inclusions recovered from Mwadui (Stachel et al., 1998), Sloan (Meyer & McCallum, 1986) and Yakutia (Sobolev et al. 1981), SN088 was very pure, showing only trace amounts of Ni (0.18 wt%), Cr (0.08 wt%), Co (0.08 wt%), Cu (0.33 wt%) and Mn (0.05 wt%).

Table 6.2: Major element composition of Native Iron inclusions in diamond recovered from Snap Lake, Mwadui (Stachel et al., 1998), Sloan (Meyer & McCallum, 1986), and Yakutia (Sobolev et al., 1981).

	Snap Lake	*Mwadui*[a]	*Sloan*[b]	*Yakutia*[c]	*Yakutia*[c]
Fe	98.6	98.04	100.7	98.5	98.3
Ni	0.18	0.15	0.0	0.06	0.15
Cr	0.08	0.09	0.66	0.10	0.48
Co	0.08	0.0	-	0.10	0.14
Cu	0.33	0.24	-	-	-
Mn	0.05	0.03	0.37	-	-

[a] Stachel et al. (1998) [b] Meyer & McCallum, (1986) [c] Sobolev et al. (1981)

Comparable to Stachel et al. (1998), the wustite rim has a smooth, sharp contact with the native iron core, which suggests that secondary oxidation is likely not responsible for the boundary. In addition, analogous to previous findings, the wustite rims in this study have different minor elements than what are observed in the native iron core, mainly the presence of significant Mn (MnO = 0.67 - 0.94 wt%), Si (SiO_2 = 0.40 - 3.9 wt%), and an enrichment in Cr (Cr_2O_3 = 0.25 – 1.15 wt%) when compared with the native iron core (Cr_2O_3 = 0.09 – 0.12 wt%).

The low Ni content observed in the native iron core appears to directly contradict any suggestion of equilibrium with a typical peridotitic mantle, however, similar to Sobolev et al. (1981), they were recovered with co-existing olivine inclusions.

6.2 Geothermobarometry

Reconstruction of the paleogeotherm, using non-touching inclusions, beneath the Snap Lake kimberlite dyke at the time of diamond formation was accomplished by combining results obtained by the Nimis & Taylor (2000) single-clinopyroxene thermobarometer (PT[NT_{cpx}]; 2 diamonds) and, for garnet-orthopyroxene pairs (1 diamond), the Harley (1984) geothermometer and the Nickel & Green (1985) geobarometer (Figure 6.6).

The Nimis & Taylor (2000) single-clinopyroxene thermobarometer gives pressure estimates between 52 – 54 Kbar and corresponding temperature estimates between 1090 - 1100˚C (N=2), falling in the range of the 37-38 mW/m^2 model geotherms of Hasterok and Chapman (2011) (SN030, SN041; Table 5.3; Figure 6.6). The non-touching harzburgitic garnet and orthopyroxene pair in diamond SN132, through the iterative combination of the Harley (1984) geothermometer and Nickel & Green (1985) geobarometer, resulted in a temperature estimate of 1230˚C and a pressure estimate of 68 Kbar (SN132; Table 5.2). This corresponds to conditions falling between the 36 and 37 mW/m^2 model geotherms and document sampling down to a minimum depth of ~210 km (Figure 6.6).

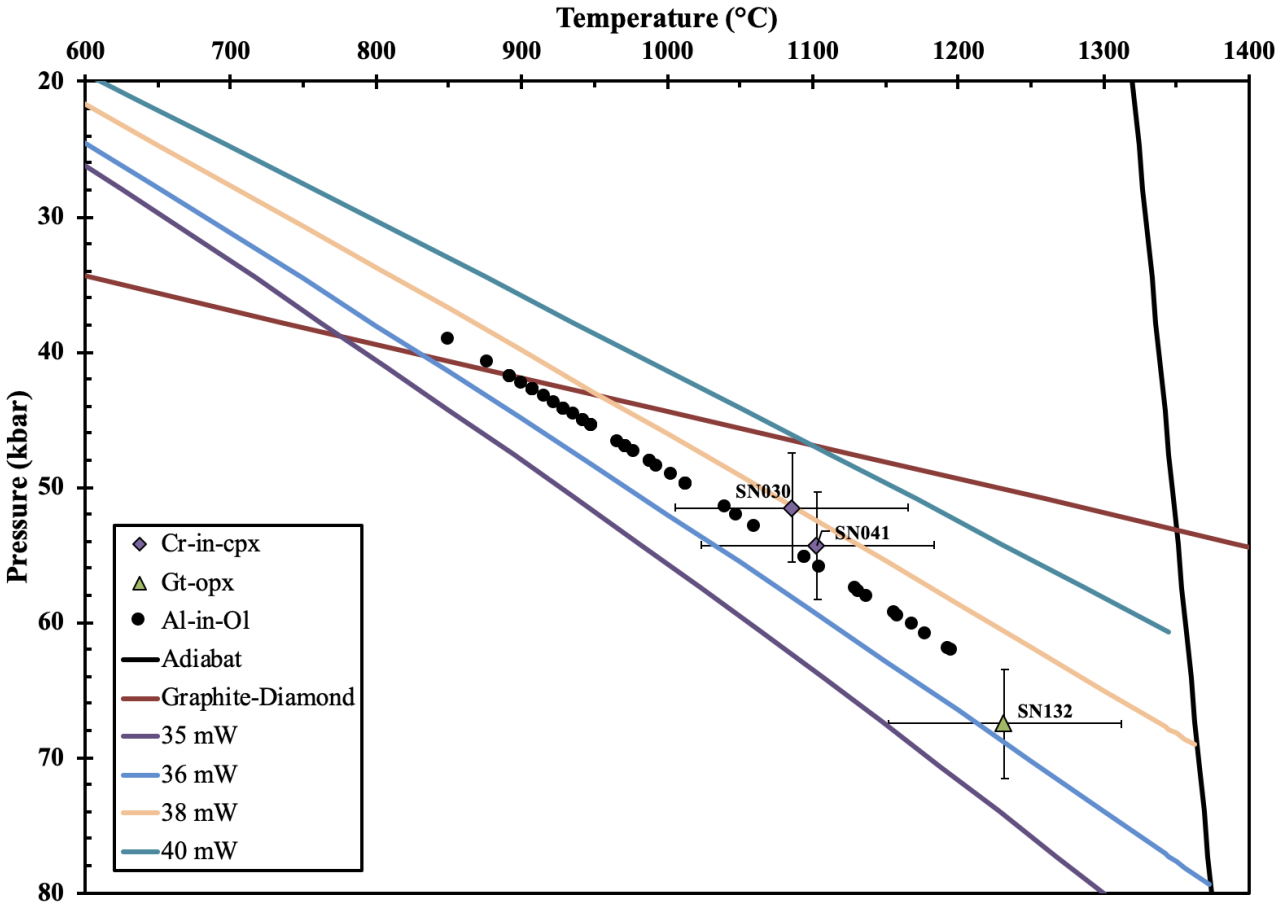

Figure 6.6: Geothermobarometry for two clinopyroxenes (Nimis and Taylor, 2000; SN030, SN041) and one non-touching garnet-orthopyroxene pair (Nickel & Green, 1985 and Harley, 1984; SN132). P-T conditions for 50 single olivine grains were calculated using the Al-in-Ol thermometer of Bussweiler et al. (2017) projected onto a 37 mW/m^2 model geotherm. The plotted model geotherms (35 – 40 mW/m^2 surface heat flow) are from Hasterok and Chapman (2011) and the graphite-diamond transition is from Day (2012). Error bars shown are for ± 80 ˚C and ± 4 kbar

In combination, the calculated temperatures and pressures match to the 36 to 38 mW/m^2 model geothermal gradients of Hasterok and Chapman (2011; Figure 6.6) and result in a paleogeotherm of 37 ±1 mW/m^2. Since the inclusions used for this estimation were all non-touching (i.e., post-entrapment re-equilibration may be excluded), this paleogeotherm applies to time of diamond formation. This new result agrees within uncertainty with geothermobarometric results reported by Stachel et al. (2003; calculated from inclusion chemistry reported in Pokhilenko

et al., 2001) for two garnet-orthopyroxene pairs from Snap Lake, which straddle a 38 mW/m^2 paleogeotherm.

Grütter et al. (2006) described the linearity of chromite saturation in harzburgite and lherzolite and demonstrated the use of the resultant arrays in Cr_2O_3 versus CaO space for garnet to derive pressure estimates (Cr-in-garnet barometry; Grütter et al., 2004). In cases where the co-existence of Mg-chromite is not established, Cr-in-garnet barometry results in minimum pressure estimates. When applied to the peridotitic garnets recovered from Snap Lake diamonds, along a 38 mW/m^2 conductive geotherm, a minimum (equilibration with Mg-chromite is not established as not present in the same diamonds) maximum thickness of the cratonic lithosphere of ~180 km (59 kbar) is estimated (Figure 6.7).

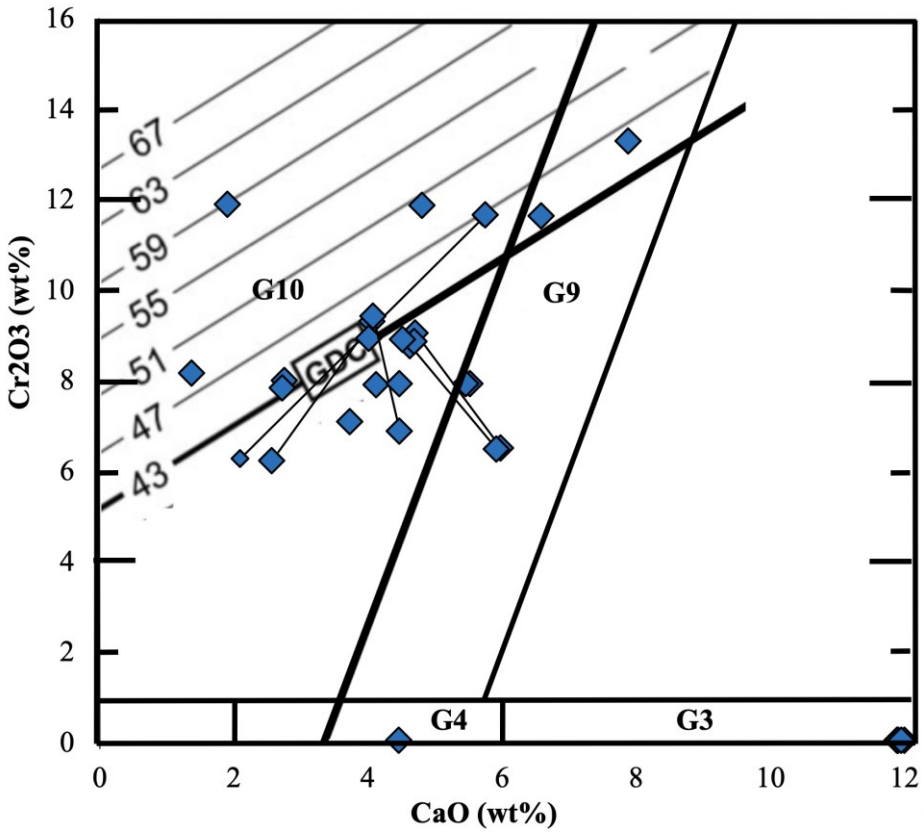

Figure 6.7: Cr_2O_3 versus CaO diagram for peridotitic garnet inclusions recovered from Snap Lake diamonds with superimposed isobars (kbar) according to the Cr-in-garnet barometer calculated for temperature conditions along a 38 mW/m^2 model geotherm (P_{38} of Grütter et al. 2004, 2006).

Using the 37 mW/m^2 paleogeotherm derived above, Al-in-ol temperatures were projected to their appropriate pressure (depth) of origin. This results in a continuous range of temperatures between 850 – 1200 ˚C and pressures from 39 – 62 Kbar, equivalent to depths between ~120 – 190 km (Figure 6.6). The general agreement, within error, of temperatures and pressures calculated from inclusions recovered from Snap Lake diamonds indicate that the diamonds were sampled from a variety of depths between 120 km and at least 210 km.

6.2.1 Nitrogen Thermometry

The aggregation state of nitrogen in diamond is dependent on the total nitrogen content, the diamond's mantle residence time and the time-averaged mantle residence temperature, where increased nitrogen concentration, residence time or temperature results in greater aggregation. Nitrogen C-centers (single substitutions) aggregate rapidly into A-centers at mantle temperatures (Taylor et al., 1996). The further aggregation from A-centers to B-centers takes a much longer time, often hundreds of millions to billions of years (Taylor et al., 1990). There is a stronger dependence of the nitrogen aggregation state on a diamonds' residence temperature, than on the residence time, thus the relationship allows the use of nitrogen and its aggregation state in diamond as a robust geothermometer (Stachel, 2014; Taylor 1990).

Snap Lake diamonds show a wide range in aggregation state, from 0 to 95 %B with an average of 55 %B (Figure 6.8). Diamonds with extremely low (< 10 at.ppm) nitrogen content were excluded, due to the difficulty in assessing the true aggregation state, while Type IaA diamonds were assumed to have 0.5 %B (the approximate detection limit for B centers) in order to calculate their maximum mantle residence temperature. A plot of nitrogen content versus %B based on FTIR data shows that Snap Lake diamonds have a wide range of time-averaged mantle

residence temperatures and thus indicates that their growth likely occurred at various depths, assuming mantle residence occurred along a steady state conductive geotherm (Taylor et al., 1990; Figure 6.8). There does not appear to be any relationship between diamond size and nitrogen aggregation state (Figure 6.8)

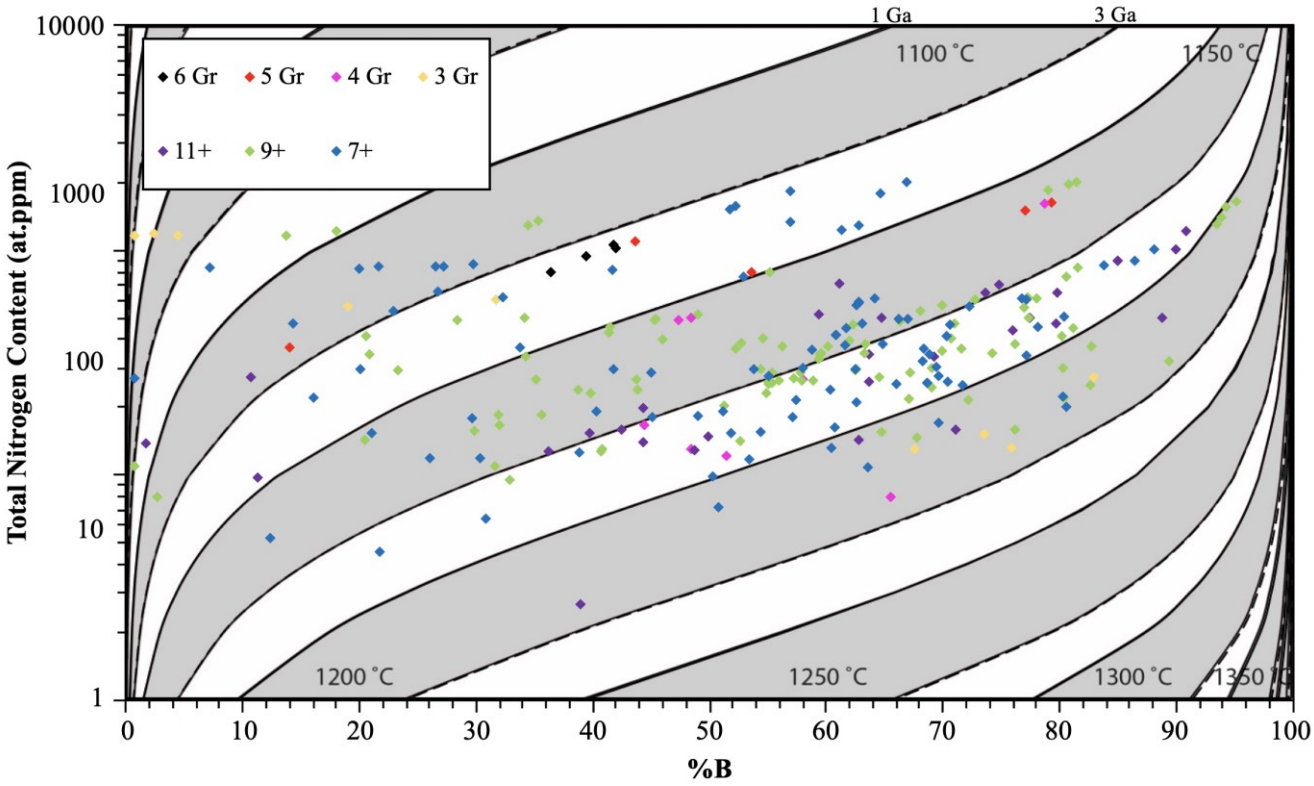

Figure 6.8: Nitrogen content (at.ppm) versus %B component for Snap Lake diamonds (organized by size fraction) measured with FTIR on diamond fragments. Isotherms were calculated from Leahy & Taylor (1997) and Taylor et al. (1990) for 1 and 3 Ga mantle residence time.

Based on an assumed 1 Ga mantle residence time, the Snap Lake diamonds range in mantle residence temperature from 1050 ˚C – 1280 ˚C, with an average mantle residence temperature of 1200 ˚C ± 36 ˚C (Figure 6.9). Increasing the assumed mantle residence time to 3 Ga would decrease the calculated residence temperatures by ~ 30 ˚C. Temperature estimates based on nitrogen thermometry agree relatively well with estimates made by inclusion

geothermobarometry. The average nitrogen-based temperature of 1200 ˚C is marginally lower than that of the Fe-Mg exchange thermometer (mean of 1230 ˚C at a fixed P of 50 kbar; O'Neill and Wood, 1979) and the Ni-in-Grt thermometer (mean of 1220 ˚C; Canil, 1999; Griffin et al., 1989) but agrees within one standard deviation (Figure 6.10).

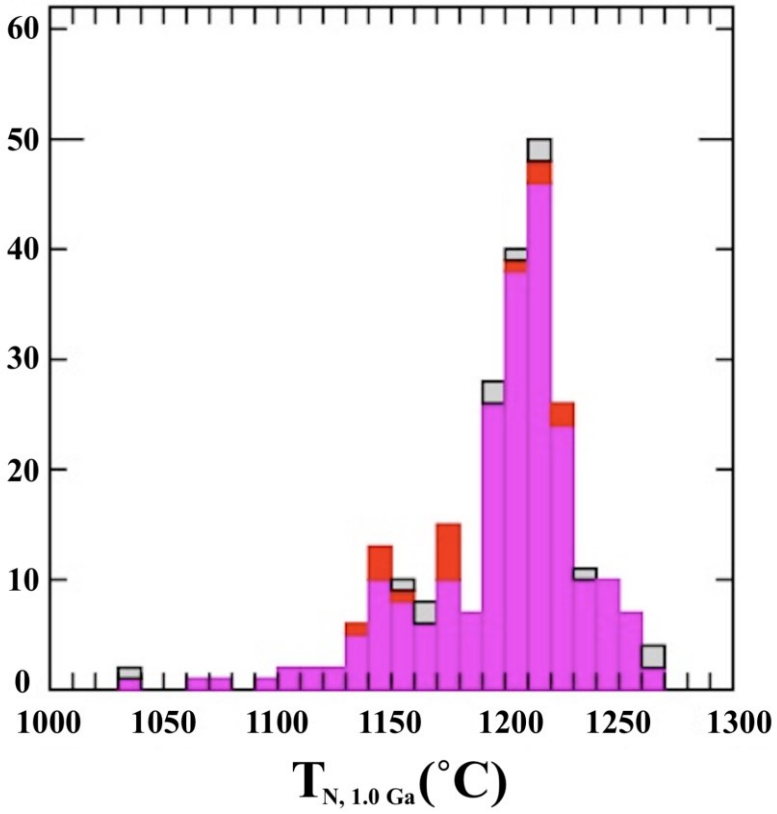

Figure 6.9: Histogram showing the calculated nitrogen-in-diamond based mantle residence temperatures for Snap Lake diamonds assuming a mantle residence time of 1 Ga.

Geothermobarometric results point towards the sampling of diamonds from a variety of depths ranging from 120 km to at least as deep at 210 km. Worldwide peridotitic diamonds have average equilibration temperatures of 1170 ± 52 ˚C, and eclogitic diamonds have average equilibrium temps of 1170 ± 50 ˚C (Stachel & Harris, 2008). These temperatures overlap with those determined for Snap Lake diamonds in this study (Figure 6.10).

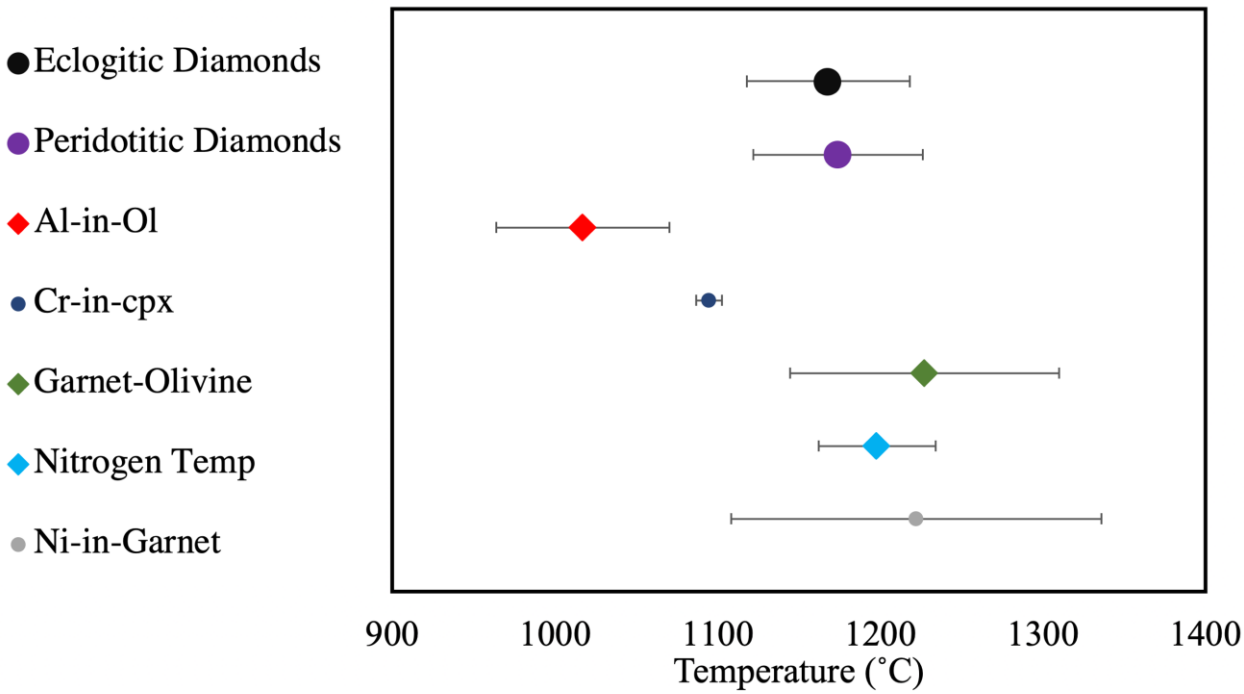

Figure 6.10: Average temperatures calculated from different thermometers with standard deviation error bars, based on inclusion chemistry or host diamond nitrogen content. Peridotitic and eclogitic diamond averages were taken from Stachel & Harris (2008).

Discrepancies between nitrogen thermometry and inclusion-based thermometry may be attributed to secular cooling or to transient heating events throughout the diamond's residence history. For example, if taken at face value, the lower temperature estimates obtained by the Al-in-olivine thermometer (representing diamond formation conditions) would suggest that the time averaged residence history of the host diamonds included one or several major transient heating events. Such heating events cannot affect isolated inclusions (protected by the diamond host) but will cause a rapid increase in the aggregation of nitrogen, thus leading to higher overall temperature estimates (e.g., Stachel and Harris, 2008).

6.3 Olivine as a Diamond Indicator Mineral

De Hoog et al. (2019) suggests that the trace element composition of olivine inclusions in diamond can be used to effectively classify the paragenesis of the host diamond. Based on a study of diamonds from Akwatia, De Hoog et al. (2019) described elemental cut-offs separating lherzolitic olivine from harzburgitic olivine. Olivine inclusions are lherzolitic when they have Ca > 300 ppm, Ca/Al > 2.2, and Na < 60 ppm or harzburgitic when they have Ca < 100 ppm or Ca/Al < 2.2, Na ≤ 60 ppm and Na/Al ≤ 0.75. This application of trace-element data appears to be less effective for the classification of Snap Lake diamonds, as none of the olivines of known harzburgitic and lherzolitic paragenesis (established based on co-existing garnet inclusions) were classified correctly (Table 5.1). Snap Lake olivines appear to be generally enriched in Na when compared to the Akwatia diamonds from De Hoog et al. (2019; Figure 6.8). Additionally, due to the dependence of Ca content on both pressure and temperature this classification system may not work well for different deposits which formed along warmer/cooler paleo geotherms.

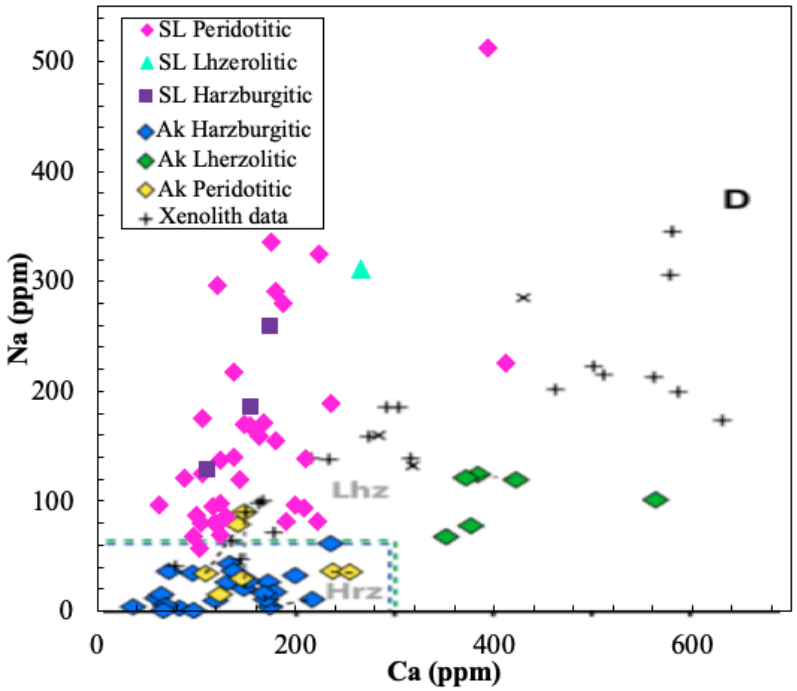

Figure 6.11: Na versus Ca (ppm) in olivine inclusions from Snap Lake (SL) compared to olivine inclusions from Akwatia (Ak; De Hoog et al., 2019).

6.4 Sources of Diamond-Forming Fluids

6.4.1 CL brightness versus Nitrogen Content

In previous studies a strong relationship between the CL brightness of diamond and the nitrogen content has been demonstrated (Hauri et al., 2002, Harte et al., 1999). Typically, regions of diamonds which are brightest in CL imaging are also characterized by the higher total nitrogen contents (Hauri et al., 2002). In general, Snap Lake diamonds follow this relationship and show the highest nitrogen contents within the brightest areas of the CL images, however, for two diamonds the reverse is observed.

SN030 and SN025 both show extremely dark zones with very high nitrogen content (2400 at.ppm and 490 at.ppm respectively), accompanied by drastically lighter zones, showing low nitrogen content (39 at.ppm & 275 at.ppm respectively; Figure 6.12). The common blue luminescence in natural diamonds generally increases with increasing nitrogen in C centers, whereas nitrogen in A centers appears to quench luminescence, which in some instances can explain low luminescence in nitrogen rich diamonds. This relationship, however, cannot explain the observation made in SN025 (Fig. 6.12), where the dark inner band shows both higher and lower nitrogen contents than neighbouring growth bands with bright CL response.

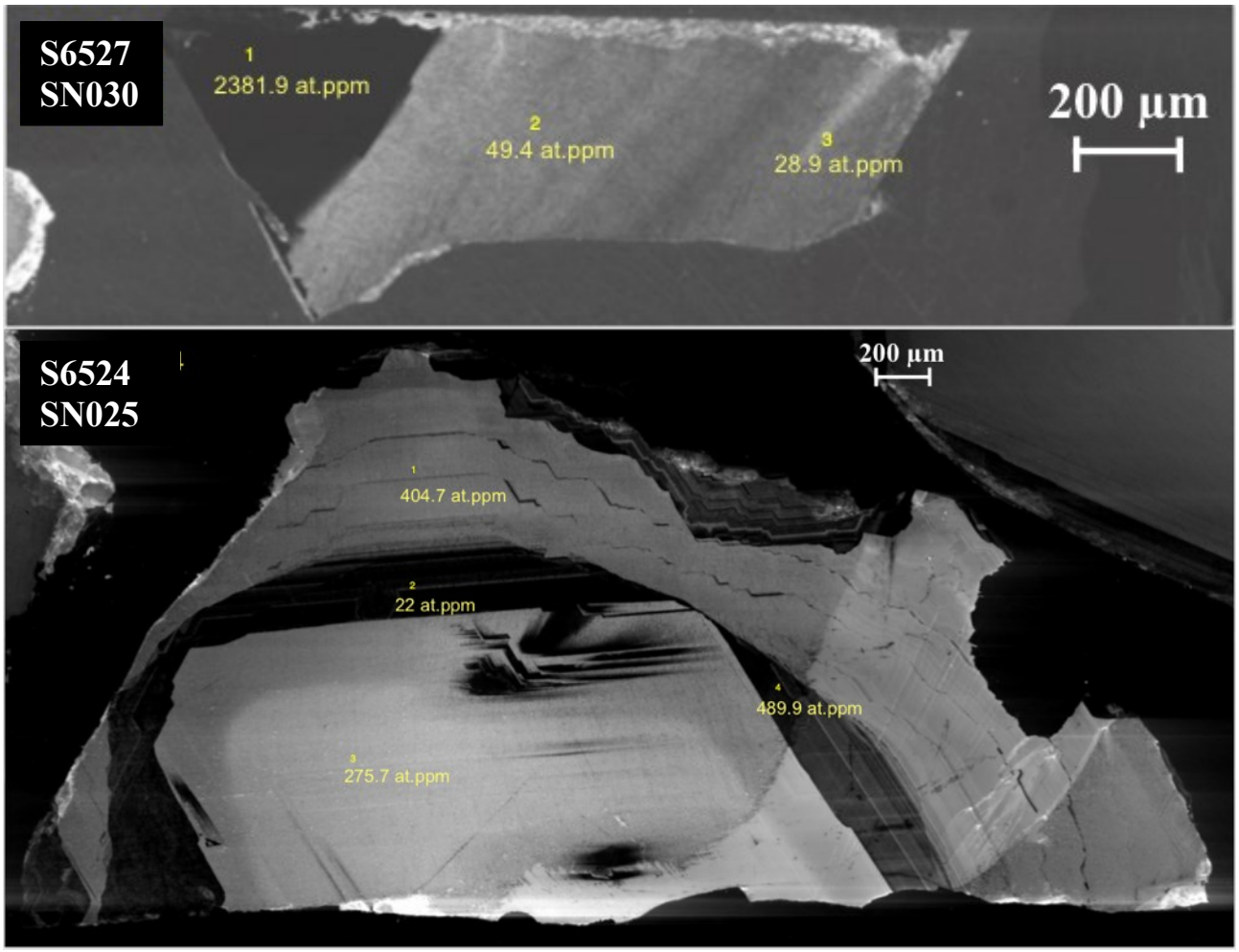

Figure 6.12: CL images of two diamonds (SN030 & SN025) showing an inverse relationship between brightness of CL imaging and nitrogen content. Where bright sections correspond to low nitrogen content and adjacent dark sections show high nitrogen content. In diamond SN025 there is also some dramatic variation within the dark band itself showing both high and low nitrogen content (22 at.ppm and 490 at.ppm).

6.4.2 Relationship between Carbon and Nitrogen

A plot of total nitrogen content (at.ppm; SIMS) compared with $\delta^{13}C$ (‰) for Snap Lake diamonds indicates a decoupled behaviour. A narrow range in $\delta^{13}C$ (‰) is accompanied by large variations in nitrogen content (0-2900 at.ppm). This suggests that Rayleigh fractionation during diamond precipitation was not a dominant process and that there was likely the involvement of multiple pulses of fluids derived from different sources during diamond formation (Figure 6.13).

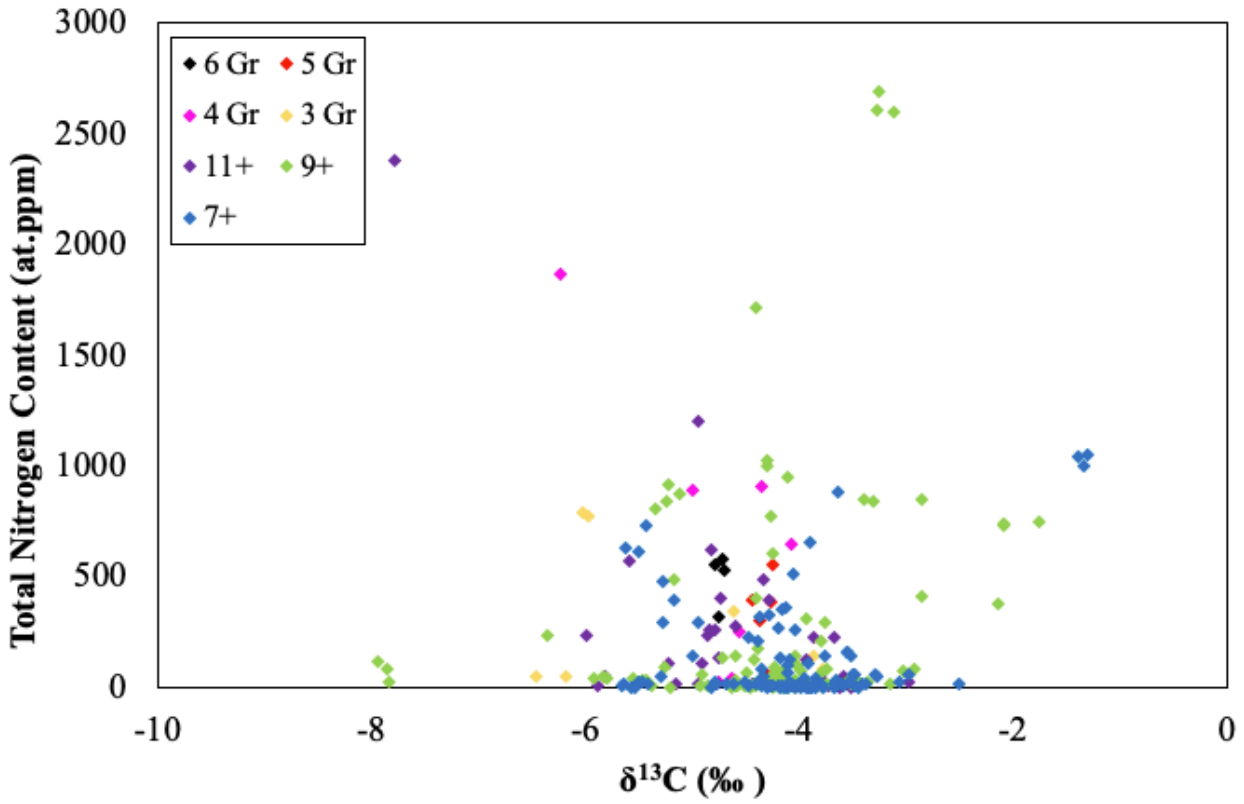

Figure 6.13: Total nitrogen content (at.ppm) versus $\delta^{13}C$ (‰) for Snap Lake diamonds. Each diamond represents a point analysis (3 - 5 per diamond) made by SIMS. No correlation between total nitrogen content and $\delta^{13}C$ is observed.

6.4.3 Platelet Peak and Evidence of Thermal Events

Woods (1986) suggested that there is a genetic relationship between B-centers and the formation of platelets, which is apparent in a linear relationship between the two. On the basis of this relationship diamonds can be classified as "regular" or "irregular", based on whether they share a linear relationship or not. The breakdown of this linear relationship in "irregular diamonds" is thought to be a result of platelet degradation. Since the width of B'-centers related absorption peak is not constant, the baseline-corrected peak area (integrated absorption) is utilized in place of peak height to measure of the strength of the B'-center (Woods, 1986). The observed relationship between the B' peak area and the amount of nitrogen in B centers indicates that although some of

the Snap Lake diamonds can be termed as "regular" the majority may be considered mildly "irregular" and experienced a minor degree of platelet degradation (Figure 6.14). A few samples, plotting along the X-axis in Figure 6.14, document complete platelet degradation.

Speich et al. (2018) described a third category termed "subregular" where low mantle residence temperatures (≤ 1120 ^{o}C) cause the formation of platelet peaks that are smaller than expected. Although some Snap Lake diamonds document residence temperatures below ≤ 1120 ^{o}C and thus may fit into this sub-regular category, the majority experienced mantle residence temperatures in excess of 1120˚C.

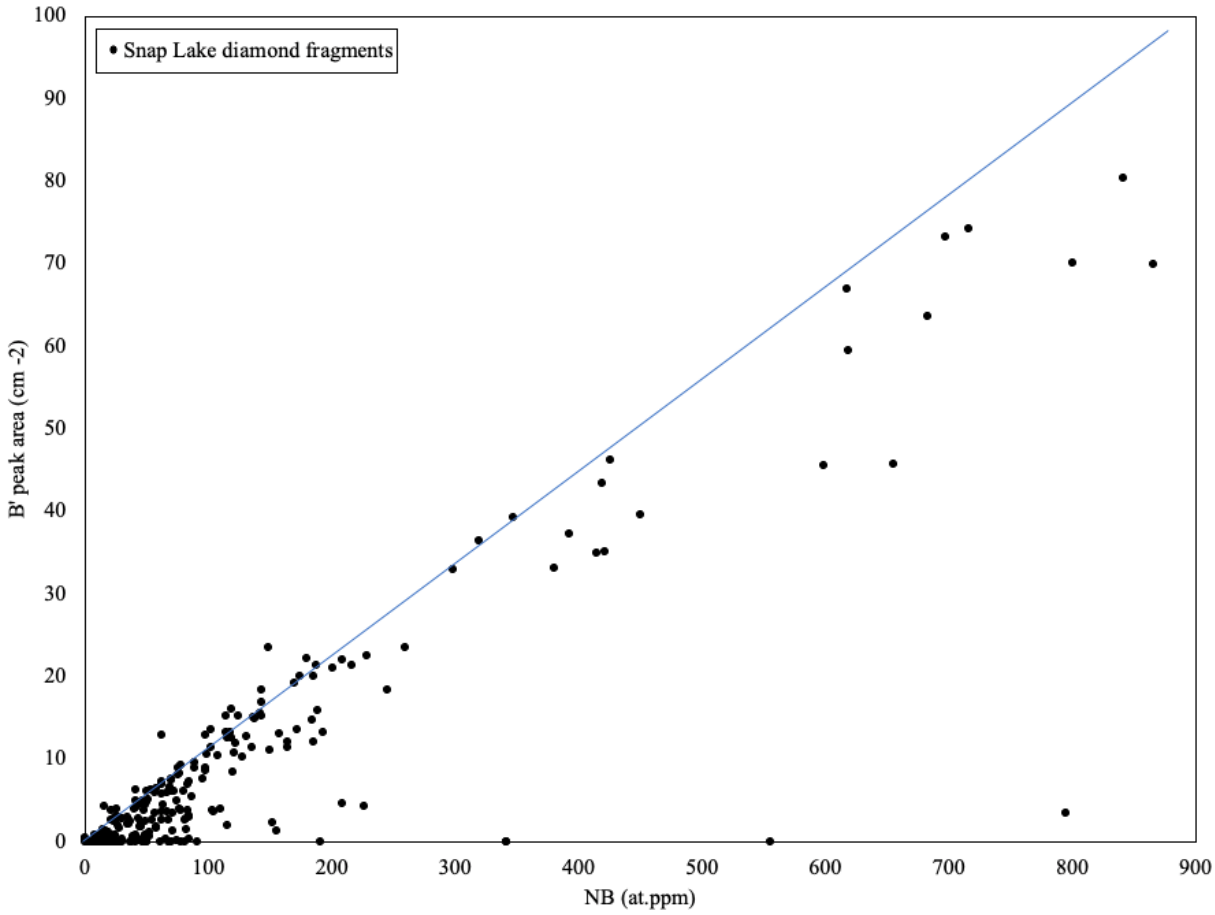

Figure 6.14: Plot of B' peak area (cm^{-2}) versus concentration of nitrogen in B-centers (N_B) for Snap Lake diamonds (N=244). The blue line represents the proportionality between platelet peak intensity and N_B described by Woods (1986) for ideal diamonds.

With an increase in B-centers, the Snap Lake diamonds show increasing deviation from the linear relationship proposed by Wood (1986; Figure 6.14). Allowing for some scatter, the data overall fall on a linear trend through the origin but with a somewhat lower slope than predicted by Wood (1986), consistent with mild degradation over time for the majority of samples. Strong platelet degradation, as indicated by the samples with elevated N_B and B' peak areas < 10 cm^{-2}, typically occurs in response to intense short-term heating (thermal pulses) and/or deformation events in the lithospheric mantle (Evans et al., 1995; Woods, 1986). This indicates that Snap Lake diamonds may actually comprise of multiple subsets of diamonds, of which only some were exposed to an intense thermal perturbation or deformation event while others were not.

6.4.4 $\delta^{13}C$ Signature of Snap Lake Diamonds

The 89 Snap Lake diamonds analyzed via SIMS have $\delta^{13}C$ values ranging from -7.9 to - 1.3 ‰, with a median $\delta^{13}C$ of – 4.17 and an average $\delta^{13}C$ of -4.29 ‰. This is consistent with the dominantly peridotitic suite identified through inclusion chemistry. The mean $\delta^{13}C$ values for peridotitic and eclogitic diamonds are very similar, -4.26 and -4.70 ‰ respectively, indicating that the carbon may have been sourced from a similar or related fluids/melts.

Snap Lake peridotitic diamonds overlap but have a higher $\delta^{13}C$ mean and mode, than both Slave Craton diamonds and the worldwide peridotitic database (Figure 6.15A; Stachel et al., 2009; Stachel & Harris, 2008). According to Welch's t-test (unequal variances t-test), $t(460) = 8.2$, $p < 0.05$, Snap Lake peridotitic diamond $\delta^{13}C$ values ($M = -4.26$, $SD = 0.84$) are more positive than worldwide peridotitic diamond $\delta^{13}C$ values ($M = -4.80$, $SD = 2.60$). There was also a significant difference in the mean $\delta^{13}C$ values of Snap Lake peridotitic diamonds ($M = -4.26$, $SD = 0.84$) and

Slave craton peridotitic diamonds (M = - 5.09, SD = 0.99), t (539) = 10.0, p <0.05. This difference might equate to the existence of a heterogenous $\delta^{13}C$ source for peridotitic Snap Lake diamonds.

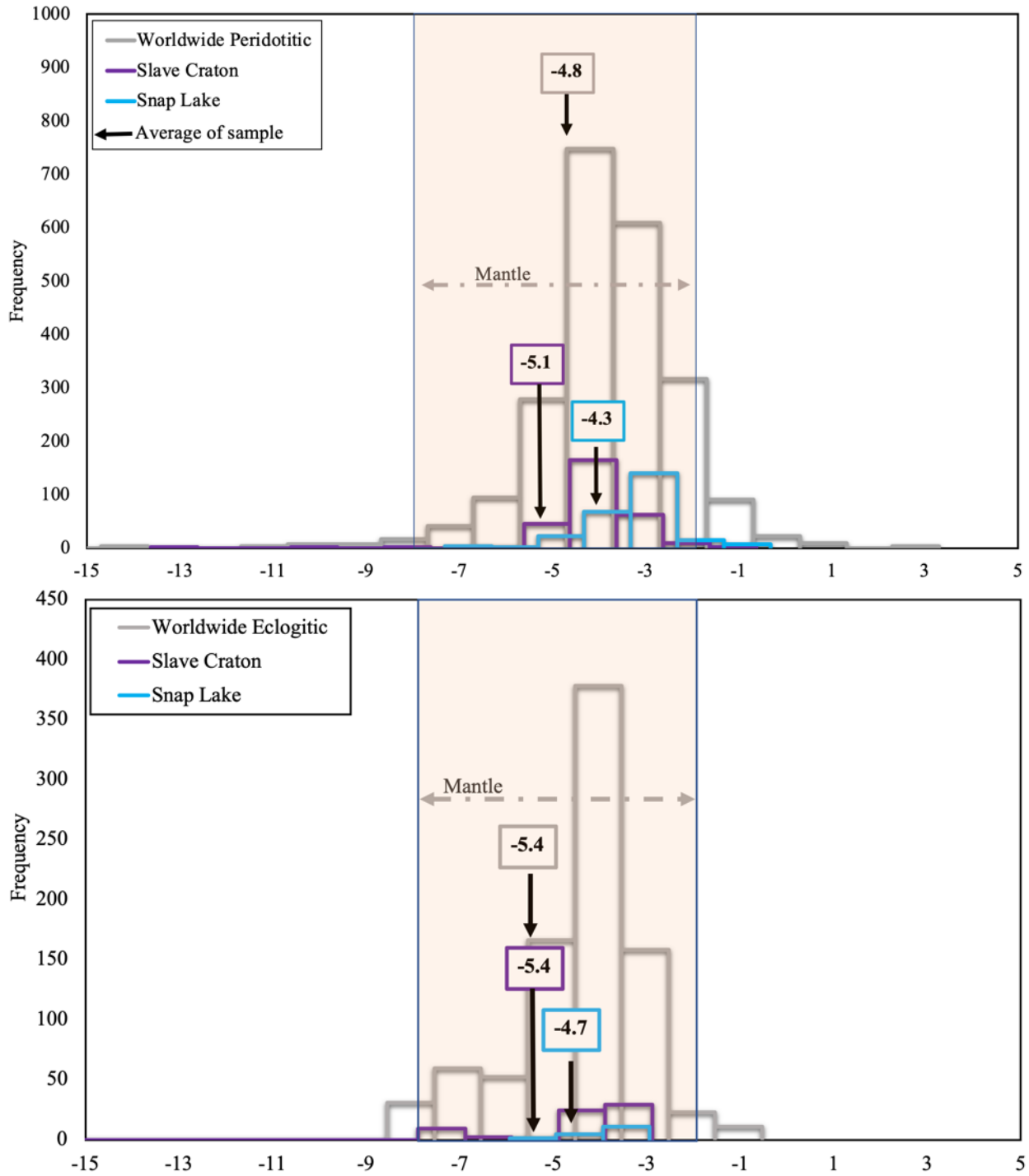

Figure 6.15: Histograms of $\delta^{13}C$ values of diamonds from Snap Lake the Slave Craton worldwide occurrences (database of Stachel & Harris, 2008) **A)** for peridotitic diamonds; **B)** for eclogitic diamonds. Typical mantle range is shaded in orange, between -8 and -2 ‰ (Cartigny et al., 2014).

The worldwide database of eclogitic values and Slave Craton eclogitic values are non-normal and skewed to low $\delta^{13}C$, with a large range (Figure 6.15). Snap Lake diamonds appear to lack the highly depleted values comprising of the depleted end of this wide range observed in other localities. Based on the assumption that strongly depleted and more enriched eclogitic diamonds are independent populations, data below -9 ‰ and above -1 ‰ have been removed to compare the means of the enriched populations. Eclogitic diamonds from Snap Lake have a higher average $\delta^{13}C$ value for enriched eclogitic diamonds than both the worldwide database and Slave Craton (Figure 6.15).

The comparatively small range of the peridotitic diamond $\delta^{13}C$ values are compatible with an origin from a mantle "reservoir," given that most of the values fall within the mantle range (-8 to -2 ‰; Figure 6.15A). The eclogitic diamond $\delta^{13}C$ values also fall in a tight range around the typical mantle value of - 5 ‰ (Figure 6.15B). CH_4-bearing fluids may originate in the asthenosphere or can be remobilized from within the lithosphere and consequently have $\delta^{13}C$ values within the typical mantle range. On the more oxidizing side, carbonatite melts have a range in $\delta^{13}C$ compositions between -8 and -1 ‰ (Deines & Gold, 1973), which could account for $\delta^{13}C$ values observed in Snap Lake diamonds.

The agreement between the peridotitic and eclogitic distributions and means and the accepted mantle range, however, is not conclusive in establishing a mantle origin of carbon for the entirety of the sample set. The isotopic composition of subducted marine carbonates or of average altered oceanic crust (AOC) also fall within the range of observed compositions (Li et al., 2019, Shilobreeva et al., 2011). Subducted AOC can have an average $\delta^{13}C$ value indistinguishable from the mantle average (~ -4.7 ‰; Shilobreeva et al., 2011; Li et al., 2019). Marine carbonates have

an average $\delta^{13}C$ value of ~ 0 ‰ (Schidlowski, 2001; Li et al., 2019). When these carbonates are subducted into the upper mantle, devolatilization and associated isotopic fractionation deplete the residual carbonates in ^{13}C, creating mantle-like $\delta^{13}C$ values that may then be imprinted on diamond as isotopic signatures (Li et al., 2019; Kirkley et al., 1991, and references therein).

Through observation of the CL images of Snap Lake diamonds, it may be deduced that these diamonds experienced multiple growth events from distinct melts/fluids that may have tapped a number of the different carbon sources described above.

6.4.5 Source of Nitrogen

Nitrogen isotopic signatures resulting from (meta)sediments or mantle sources are isotopically distinct from one another: (meta)sediment derived nitrogen is consistently more positive in its isotopic composition than mantle derived nitrogen (Cartigny et al., 2005). Nitrogen in sediments is accumulated as ammonium ions within clays and during metamorphism transferred into micas (e.g. Illite, phengite, Cartigny, 2005; Li et al., 2019). Most sediments have positive $\delta^{15}N$ (average +6 ‰), and when subducted, the devolatilization results in a further increase in this value (Haendel et al., 1986; Cartigny, 2005). Conversely, the Earth's upper mantle appears to be quite heterogeneous, with reported $\delta^{15}N$ values ranging from -25 to +15 ‰, with a mean of -5 ± 3 ‰ (Cartigny, 2005).

Nitrogen isotopic compositions of Snap Lake diamonds span a very wide range from -19.6 to +10.9 ‰ with an average of -3 ‰. This suggests that formation of Snap Lake diamonds involved a number of different nitrogen sources. Due to the vast majority of diamonds recovered from Snap Lake being of peridotitic paragenesis, it is not surprising that most $\delta^{15}N$ values are negative. The internal growth zones observed through CL imaging in combination with the extreme range in

$\delta^{15}N$ indicates that multiple growth events, which likely involved isotopically distinct fluids/melts, occurred.

6.4.5.1 Highly depleted $\delta^{15}N$ values

A subset of eight diamonds from Snap Lake show substantially ^{15}N-depleted isotopic signatures ranging, from -20 to -11 ‰. Mantle fractionation processes have been used to explain $\delta^{15}N$ values between -10 and +7 ‰ (Cartigny et al., 1997). This extreme depletion, however, cannot be explained by mantle fractionation processes, as known fractionation factors are generally negative (e.g. for diamond-N2, diamond NH3 or diamond NH_4^+; Petts et al., 2015) and thus the nitrogen isotopic signature would only be able to fractionate to more positive values (Li et al., 2007, Cartigny et al., 2007).

Li et al. (2019) suggested that in some localities clay minerals forming in altered oceanic crust (AOC) at high temperature conditions (>250˚C) can assimilate ammonium, resulting in $\delta^{15}N$ values as low as -16 ‰. Since both carbon and nitrogen are introduced by different minerals in AOC, they are decoupled during both alteration and introduction to the mantle and thus can result in differences in isotopic signatures in diamond-forming fluids (Li, et al., 2019). This theory, however, only applies to diamonds with a proposed subduction component and therefore cannot be readily used to explain the highly negative $\delta^{15}N$ values observed in Snap Lake peridotitic diamonds, unless the origins of nitrogen and carbon are completely decoupled (AOC origin for nitrogen and mantle origin for carbon).

The ^{15}N depleted peridotitic diamonds from Snap Lake are very similar to diamonds described by Cartigny et al. (1997) from Pipe 50 in Fuxian, China, which also had very depleted $\delta^{15}N$ values, reaching as low as -25 ‰ accompanied by broadly mantle-like $\delta^{13}C$ (-6.2 to +0.8 ‰, with a mean of -3.5 ‰). Cartigny et al. (1997) suggested that the most likely interpretation for

these depleted values are remnant signatures from early Earth, showing nitrogen isotopic compositions approaching that of enstatite chondrites. These Snap Lake diamonds could then be used to support the idea of a heterogeneous accretion model for Earth, as proposed by Javoy et al. (1986) and Palot et al. (2012). This proposal was revisited by Cartigny et al. (2014), who suggested that the extremely depleted values may imply a secular change in mantle $\delta^{15}N$. This suggestion has yet to be confirmed through concrete observations.

7. Conclusions:

Major element chemistry of mineral inclusions recovered from Snap Lake diamonds, indicate a predominantly peridotitic source mantle with a much more minor eclogitic component. The presence of a mixed-paragenesis diamond (hosting peridotitic garnet, coesite and eclogitic sulphide), as well as a number of chemically distinct lherzolitic-harzburgitic garnet pairs recovered from single diamonds indicates an evolving chemical environment with different substrates in close proximity to one another. The high Mg# and depleted CaO content of olivine inclusions implies a predominantly harzburgitic paragenesis, thus indicating a largely depleted peridotitic mantle source. REE_N patterns for both harzburgitic and lherzolitic garnets are primarily sinusoidal or weakly sinusoidal suggesting a similar style of metasomatic enrichment across both substrates. There is a notable absence of majorite garnet in this study, which were observed in previous studies on Snap Lake diamonds (Pokhilenko et al., 2001, 2004). The presence of K-feldspar and coesite within the eclogitic suite of inclusions recovered indicates that the protolith of the eclogitic SCLM beneath Snap Lake kimberlite dyke was either not melted or underwent very low degrees of partial melting during subduction in order to retain these 'evolved' phases (Schulze et al., 2000).

Geothermobarometry results indicate that diamond formation occurred along a cool 36 – 38 mW/m^2 paleo-geotherm at temperatures ranging from 850 to 1200 ˚C. Projecting Al-in-ol temperatures onto an estimated 37 mW/m^2 paleo-geotherm, results in depths of formation estimates between 120 and at least 210 km. Nitrogen-based mantle residence temperatures, calculated for 1 Ga mantle residence time, ranged from 1050 – 1280 ˚C, which agrees well with geothermobarometric results. Nitrogen abundance determined through FTIR spectroscopy ranged from below the limit of detection (<10 at.ppm) to 1190 at.ppm with a large variation in nitrogen aggregation state (0-95 %B).

The carbon isotopic compositions of Snap Lake diamonds ranges from – 8.0 to - 1.3 ‰ with a median $\delta^{13}C$ value of – 4.17 ‰ and an average of – 4.29 ‰. Peridotitic and eclogitic suites differed only slightly, ranging from – 8.0 to – 1.3 ‰ (median = - 4.15 ‰, average = - 4.26 ‰) and – 6.2 to – 3.9 ‰ (median = - 4.71 ‰, average – 4.70 ‰), respectively. The agreement between the peridotitic and eclogitic distributions, medians and means and the accepted mantle range, however, is not conclusive in establishing a mantle origin of carbon for the entirety of the sample set. It is likely that both diamond suites experienced multiple growth events from distinct melts/fluids which may have tapped a number of different carbon sources including remobilized CH_4-fluids, carbonatite melts, and subduction related AOC, and marine carbonates all of which can have $\delta^{13}C$ values indistinguishable from the mantle average.

Snap Lake diamonds showed a wide range in $\delta^{15}N$ values from – 20 to +11 ‰ reflecting a high likelihood of involvement of subducted sediments contributing to the nitrogen signature and supporting the idea of a heterogeneous nitrogen reservoir accounting for the extreme depletion observed in peridotitic diamonds.

Bibliography

Agashev, A.M., Pokhilenko, N.P., Takazawa, E., McDonald, J.A., Vavilov, M.A., Watanabe, T. & Sobolev, N.V. (2008) Primary melting sequence of deep (>250 km) lithospheric mantle as recorded in the geochemistry of kimberlite-carbonatite assemblages, Snap Lake dyke system, Canada. *Chemical Geology* 255: 317-328

Armstrong, J. P., Fitzgerald, C. E., Kjarsgaard, B. A., Heaman, L., & Tappe, S. (2012, February). Kimberlites of the Coronation Gulf Field, Northern Slave Craton, Nunavut Canada. *In International Kimberlite Conference: Extended Abstracts* (Vol. 10).

Ater, P.C., Eggler, D.H. & McCallum, M.E. (1984) Petrology and geochemistry of mantle eclogite xenoliths from Colorado-Wyoming kimberlites: recycled ocean crust? *Developments in Petrology; Elsevier* 11(2): 309-318

Aulbach, S., Stachel, T., Viljoen, K.S., Brey, G.P. & Harris, J.W. (2002) Eclogitic and websteritic diamond sources beneath the Limpopo Belt - is slab-melting the link*? Contributions to Mineralogy and Petrology* 143: 56-70

Aulbach, S., Stachel, T., Creaser, R.A., Heaman, L.M., Shirey, S.B., Muehlenbachs, K., Eichenberg, D. & Harris, J.W. (2009) Sulphide survival and diamond genesis during formation and evolution of Archaean subcontinental lithosphere: A comparison between the Slave and Kaapvaal cratons. *Lithos* 112S: 747-757

Aulbach, S. & Viljoen, K.S. (2011) Eclogite xenoliths from the Lace kimberlite, Kaapvaal craton: From convecting mantle source to palaeo-ocean floor and back. *Earth and Planetary Science Letters* 431: 274-286

Babamordi, M., Liyai, M.R., Azimirad, R. & Salehi, H. (2017) Electronic structure and optical properties of the single crystal and two-dimensional structure of CdWO4 from first principles. *Physica B: Condensed Matter* 511: 103-10

Bernstein, S., Kelemen, P.B. & Hanghøj, K. (2007) Consistent olivine Mg# in cratonic mantle reflects Archean mantle melting to the exhaustion of orthopyroxene. *Geology* 35(5): 459-462

Bleeker, W. (2002) Archean tectonics: a review, with illustrations from the Slave craton. *Geological Society, London, Special Publications* 199(1): 151-181

Bleeker, W., Hamilton, M., Söderlund, U. & Ernst, R.E. (2008) Towards a complete magmatic event "barcode" for the Slave craton, I: A precise U-Pb baddeleyite age for the Hearne swarm with

implications for a newly recognized Paleoproterozoic LIP across the western Canadian Shield. *In Annual Meeting, Abstracts* 33: 23

Bleeker, W., Ketchum, J.W.F., Jackson, V.A. & Villeneuve, M.E. (1999a) The Central Slave Basement Complex, Part I: its structural topology and autochthonous cover. *Canadian Journal of Earth Sciences* 36: 1083-1109

Bleeker, W., Ketchum, J.W.F. & Davis, W.J. (1999b) The Central Slave Basement Complex, Part II: age and tectonic significance of high-strain zones along the basement-cover contact. *Canadian Journal of Earth Sciences* 36: 1111-1130

Bleeker, W., Ketchum, J.W.F., Jackson, V.A. & Villeneuve, M.E. (1999) The Central Slave Basement Complex, Part I: its structural topology and autochthonous cover. *Canadian Journal of Earth Science* 36(7): 1083-1109

Bostock, M.G. (1997) Anisotropic upper-mantle stratigraphy and architecture of the Slave craton. *Nature* 390: 392-395

Bowring, S.A., Williams, I.S., & Compston, W. (1989) 3.96 Ga gneiss from the Slave province, Northwest Territories, Canada. *Geology* 17(11): 971-975

Boyd, F.R. & Gurney, J.J. (1986) Diamonds and the African Lithosphere. *Science* 232(4749): 472-477

Breeding, C.M., & Shigley, J.E. (2009) The "Type" Classification System of Diamonds and Its Importance in Gemology. *Gems and Gemology* 45: 96-111

Brey, G.P. & Kohler, T. (1990) Geothermobarometry in Four-phase Lherzolites II. New Thermobarometers, and Practical Assessment of Existing Thermobarometers. *Journal of Petrology* 31(6): 1353-1378

Brey, G.P. & Shu, Q. (2018) The birth, growth and ageing of the Kaapvaal subcratonic mantle. *Mineralogy and Petrology* 112: 23-41

Buchan, K.L., LeCheminant, A.N. & van Breemen, O. (2009) Paleomagnetism and U-Pb geochronology of the Lac de Gras diabase dyke swarm, Slave Province, Canada: implications for relative drift of Slave and Superior provinces in the Paleoproterozoic. *Canadian Journal of Earth Science* 46:361-379

Bulanova, G. P. (1995). The formation of diamond. *Journal of Geochemical Exploration* 53(1-3): 1-23.

Bulanova, G.P., Griffin, W.L., Ryan, C.G., Shestakova, O.Ye. & Barnes, S.J. (1996) Trace elements in sulfide inclusions from Yakutian diamonds. *Contributions to Mineralogy and Petrology* 124: 11-125

Bursill, L.A. & Glaisher, R.W. (1985) Aggregation and dissolution of small and extended defect structures in Type Ia diamond. *American Mineralogist* 75(5-6): 608-618

Bussweiler, Y., Brey, G.P., Pearson, D.G., Stachel, T., Stern, R.A., Hardman, M.F., Kjarsgaard, B.A. & Jackson, S.E. (2017). The aluminum-in-olivine thermometer for mantle peridotites - Experimental versus empirical calibration and potential applications. *Lithos* 272: 301-314

Canil, D. (1999) The Ni-in-garnet geothermometer: calibration at natural abundances. *Contributions to Mineralogy and Petrology* 136: 240-246

Carbno, G.B. & Canil, D. (2002) Mantle Structure Beneath the SW Slave Craton, Canada: Constraints from Garnet Geochemistry in the Drybones Bay Kimberlite. *Journal of Petrology* 43(1): 129-142

Cartigny, P. (2005) Stable Isotopes and the origin of Diamond. *Elements* 1: 79-84

Cartigny, P., Boyd, S.R., Harris, J.W. & Javoy, M. (1997) Nitrogen isotopes in peridotitic diamonds from Fuxian, China: the mantle signature *Terra Nova* 9: 175-179

Cartigny, P., Palot, M., Thomassot, E. & Harris, J.W. (2014) Diamond Formation: A Stable Isotope Perspective. *Annual Reviews of Earth and Planetary Sciences* 42:699-732

Chrenko, R.M. (1973) Boron, the Dominant Acceptors in Semiconducting Diamond. *Physical Review B* 7(10): 4560-4567

Clackson, S.G., Moore, M., Walmsley, J.c., Woods, G.S. (1990) The relationship between platelet size and the frequency of the B' infrared absorption peak in Type Ia diamond. *Philosophical Magazine B* 62(2): 115-128

Couch, W.J. (2002) Strategic resolution of policy, environmental and socio-economic impacts in Canadian Arctic diamond mining: BHP's NWT diamond project. *Impact Assessment and Project Appraisal* 20(4): 265-278

Creaser, R.A., Grütter, H., Carlson, J. & Crawford, B. (2004) Macrocrystal phlogopite Rb-Sr dates for the Ekati property kimberlites, Slave Province, Canada: evidence for multiple intrusive episodes in the Paleocene and Eocene. *Lithos* 76: 399-414

Custers, J.F.H. (1955) Semiconductivity of a Type IIb Diamond. *Nature* 176(4472), 173-174

Davies, R.M., Griffin, W.L., O'Reilly, S.Y. & Andrew, A.S. (2003) Unusual mineral inclusions and carbon isotopes of alluvial diamonds from Bingara, eastern Australia. *Lithos* 69:51-66

Davis, W.J., Fryer, B.J. & King, J.E. (1994) Geochemistry and evolution of Late Archean plutonism and its significance to the tectonic development of the Slave craton. *Precambrian Research* 67(3-4): 207-241

Davis, W.J. & Kjarsgaard, B.A. (1997) A Rb-Sr Isochron Age for A Kimberlite from the recently Discovered Lac De Gras Field, Slave Province, Northwest Canada. *The Journal of Geology* 105(4): 503-510

Day, H.W. (2012) A revised diamond-graphite transition curve. *American Mineralogist* 97(1): 52-62

De Hoog, J.C.M., Stachel, T. & Harris, J.W. (2019) Trace-element geochemistry of diamond-hosted olivine inclusions from the Akwatia Mine, West African Craton: implications for diamond paragenesis and geothermobarometry. *Contributions to Mineralogy and Petrology* 174: 100-128

Deines, P. & Gold, D.P. (1973) The isotopic composition of carbonatite and kimberlite carbonates and their bearing on the isotopic composition of deep-seated carbon. *Geochimica et Cosmochimica Acta* 37: 1709-1733

De Stefano, A., Kopylova, M.G., Cartigny, P. & Afanasiev, V. (2009) Diamonds and eclogites of the Jericho kimberlites (Northern Canada). *Contributions to Mineralogy and Petrology* 158: 295-315

Donnelly, C.L., Stachel, T., Creighton, S., Muehlensbachs, K. & Whiteford, S. (2007) Diamonds and their mineral inclusions from the A154 South pipe, Diavik Diamond Mine, Northwest territories, Canada. *Lithos* 98: 160-176

Ernst, R.E. & Bleeker, W. (2010) Large igneous provinces (LIPs), giant dyke swarms and mantle plumes: significance for breakup events within Canada and adjacent regions from 2.5 Ga to the Present. *Canadian Journal of Earth Science* 47: 695-739

Ernst, R.E. & Buchan, K.L. (2001) Large mafic magmatic events through time and links to mantle-plume heads, *in Ernst, R.E., & Buchan, K.L., eds., Mantle Plumes: Their Identification Through Time: Boulder, Colorado, Geological Society of America, Special Paper* 352: 483-575

Evans, T. (1976) Diamonds. *Contemporary Physics* 17(1): 45-70

Evans, T., Kiflawi, I., Luyten, W., van Tendeloo, G. & Woods, G.S. (1995) Conversion of platelets into dislocation loops and voidite dormation in type IaB diamonds. *Proceedings of the Royal Society of London A* 449: 295-313

Evans, T. & Sauter, D.H. (1961) Etching of diamond surfaces with gases. *Philosophical Magazine* 6(63): 429-440

Evans, T., Zengdu, Qi., Maguire, J. (1981) The stages of nitrogen aggregation in diamond. *Journal of physics C: solid state physics* 14(12): L379-L384

Field, M., Gernon, T.M., Mock, A., Walters, A., Sparks, R.S.J. & Jerra, D.A. (2009) Variations of olivine abundance and grain size in the Snap Lake kimberlite intrusion, Northwest Territories, Canada: A possible proxy for diamonds. *Lithos* 112S: 23-35

Fisher, D. (2009) Brown diamonds and high pressure high temperature treatment. *Lithos* 112: 619-624

Fromentin, S. (2004). "Resistivity of Carbon, Diamond". *The Physics Factbook*. *Glenn Elert (ed.)* Retrieved 13 September 2020

Fulop, A., Kopylova, M., Kurszlaukis, S., Hilchie, L., Ellemers, P. & Squibb, C. (2018) Petrography of Snap Lake Kimberlite Dyke (Northwest Territories, Canada) and its Interaction with Country Rock Granitoids. *Journal of Petrology* 59(12): 2493-2518

Gernon, T.M., Field, M. & Sparks, R.S.J. (2012) Geology of Snap Lake Kimberlite intrusion, Northwest Territories, Canada: field observations and their interpretation. *Journal of the Geological Society, London* 169: 1-16

Goss, J.P., Briddon, P.R., Hill, V., Jones, R., Rayson, M.J. (2014) Identification of the structure of the 3107 cm^{-1} H-related defect in diamond. *Journal of physics: Condensed matter* 26(14) 145801

Griffin, W.L., Cousens, D.R., Ryan, C.G., Sie, S.H. & Suter, G.F. (1989) Ni in chrome pyrope garnets: a new geothermometer. *Contributions to Mineralogy and Petrology* 103: 199-202

Griffin, W.L., Doyle, B.J., Ryan, C.G., Pearson, N.J., O'Reilly, S.Y., Davies, R., Kivi, K., Van Achterbergh, E. & Natapov, L.M. (1999) Layered Mantle Lithosphere in the Lac de Gras Area, Slave Craton: Composition, Structure and Origin. *Journal of Petrology* 40(5): 705-727

Griffin, W.L. & Ryan, C.G. (1995) Trace elements in indicator minerals: area selection and target evaluation in diamond exploration. *Journal of Geochemical Exploration* 53: 311-337

Grütter, H.S. (2009) Pyroxene xenocrysts geotherms: Techniques and applications. *Lithos* 112S: 1167-1178

Grütter, H.S., Apter, D.B. & Kong, J. (1999) Crust-mantle coupling: Evidence from Mantle-Derived xenocrystic garnets. *In Proceedings of the 7th International Kimberlite Conference, Red Roof Design Cape Town* 1: 307-313

Grütter, H.S., Gurney, J.J., Menzies, A.H. & Winter, F. (2004) An updated classification scheme for mantle-derived garnet, for use by diamond explorers. *Lithos* 77: 814-857

Grütter, H., Latti, D. & Menzies, A. (2006) Cr-saturation Arrays in Concentrate Garnet Compositions from Kimberlite and their Use in Mantle Barometry. *Journal of Petrology* 47(4): 801-820

Gurney, J.J., Harris, J.W., Ricard, R.S. (1984) Silicate and oxide inclusions in diamonds from Orapa Mine, Botswana. Komprobst, J. (Ed.), Kimberlites II: the mantle and crust-mantle relationship. *Elsevier, Amsterdam*, 3-9

Haendel, D., Mühle, K., Nitzche, H.M., Stiehl, G. & Wand, U. (1986) Isotopic variations of the fixed nitrogen in metamorphic rocks. *Geochimica et Cosmochimica Acta* 50: 749-758

Hammer, P.T.C., Clowes, R.M. & Ramachandran, K. (2004) Seismic reflection imaging of thin, kimberlite dykes and sills: exploration and deposit characterization of the Snap Lake dyke, Canada. *Lithos* 76: 359-367

Harley, S.L. (1984) Comparison of the Garnet-Orthopyroxene Geobaromater with Recent Experimental Studies, and Applications to Natural Assemblages. *Journal of Petrology* 25(3): 697-712

Harris, J.W. (1987) Recent physical, chemical, and isotopic research of diamond. 477-500

Harrison, E.R. & Tolansky, S. (1964) Growth history of a natural octahedral diamond. *Proceedings of the Royal Society of London A. Mathematical and Physical Sciences* 279: 490-496

Harte, B., Fitzsimons, W., Harris, J.W. & Otter, M.L. (1999) Carbon isotope ratios and nitrogen abundances in relation to cathodoluminescence characteristics for some diamonds from the Kaapvaal Province, S. Africa. *Mineralogical Magazine* 63(6): 829-856

Harte, B., Gurney, J.J. & Harris, J.W. (1980) The formation of peridotitic suite inclusions in diamonds. *Contributions to mineralogy and petrology* 72: 181-190

Harte, B., Harris, J.W., Hutchison, M.T., Watt, G.R. & Wilding, M.C. (1999) Lower mantle mineral associations in diamonds from Sao Luiz, Brazil. *In: Mantle Petrology: Field Observations and High Pressure Experimentation: A tribute to Francis R (Joe) Boyd. Vol Special Publication No. 6. Fei Y, Bertka CM, Mysen BO, (eds). The Geochemical Society, Houston* 125-153

Hasterok, D. & Chapman, D.S. (2011) Heat production and geotherms for the continental lithosphere. *Earth and Planetary Science Letters.* 307: 59-70

Hauf, M.V., Grotz, B., Naydenov, B., Dankerl, M., Pezzagna, S., Meijer, J., Jelezko, F., Wrachtrup, J., Stutzmann, M. Reinhard F. & Garrido, J.A. (2011) Chemical control of the charge state of nitrogen-vacancy centers in diamond. *American Physical Society* 83: 081304-1

Hauri, E.H., Wang, J., Pearson, D.G. & Bulanova, G.P. (2002) Microanalysis of $\delta^{13}C$, $\delta^{15}N$ and N abundances in diamonds by secondary ion mass spectrometry. *Chemical Geology* 185: 149-163

Heaman, L.M., Kjarsgaard, B.A. & Creaser, R.A. (2003) The timing of kimberlite magmatism in North America: implications for global kimberlite genesis and diamond exploration. *Lithos* 71: 153-184

Heaman, L.M., Kjarsgaard, B.A. & Creaser, R.A. (2004) The temporal evolution of North American kimberlites. *Lithos* 76: 377-397

Heaman, L.M. & Pearson, D.G. (2010) Nature and evolution of the Slave Province subcontinental lithospheric mantle. *Canadian Journal of Earth Sciences* 47: 369-388

Helmstaedt, H. (2009) Crust-mantle coupling revisited: The Archean Slave craton, NWT, Canada. Lithos 112S: 1055-1068

Henderson, J.B. (1985) Geology of the Yellowknife-Hearne Lake area, District of Mackenzie: a segment across an Archean basin. Geological Survey of Canada

Henderson, J.B., McGrath, P.H., Theriault, R.J. & van Breemen, O. (1990) Intracratonic indentation of the Archean Slave Province into the Early Proterozoic Thelon Tectonic Zone of the Churchill Province, northwestern Canadian Shield. *Canadian Journal of Earth Sciences* 27(12): 1699-1713

Hoffman, P.F., Bally, A.W & Palmer, A.R. (1989) Precambrian geology and tectonic history of North America. *The geology of North America - an overview* 447-512

Isachsen, C.E. & Bowring, S.A. (1994) Evolution of the Slave Craton. *Geology* 22: 917-920

James, D.T. & Mortensen, J.K. (1992) An Archean metamorphic core complex in the southern Slave Province: basement-cover structural relations between the Sleep Dragon Complex and the Yellowknife Supergroup. *Canadian Journal of Earth Science* 29: 2133-2145

Janse, A.J.A. (1994) Is Clifford's rule still valid? Affirmative examples from around the world. *In Diamonds: Characterization, Genesis and Exploration (ed. H.O.A. Meyer & O.H. Leonardos), CPRM Special Publication Jan/94, Brasilia*, 215-235

Javoy, M., Pineau, F. & Delorme, H. (1986) Carbon and Nitrogen isotopes in the mantle. *Chemical Geology* 57: 41-62

Jenner, G.A., Fryer, B.J., & McLennan, S.M. (1981) Geochemistry of the Archean Yellowknife Supergroup. *Geochimica et Cosmochimica Acta* 45(7): 111-1129

Jones, W.G., Ferguson, I.J., Chave, A.D., Evans, R.L. & McNeice, G.W. (2001) Electric lithosphere of the Slave craton. *Geology* 29(5): 423-426

Jones, A.G., Lezaeta, P., Ferguson, I.J., Chave, A.D., Evans, R.L., Garcia, X. & Spratt, J. (2003). The electrical structure of the Slave craton. *Lithos* 71: 505-527

Kaiser, W. & Bond, W.L. (1959) Nitrogen, A major impurity in common Type I diamond. *Physical Review* 115(4): 857-863

Kiflawi, I., Bruley, J., Luyten, W., Van Tendeloo, G. (1998) 'Natural' and 'man-made' platelets in type-Ia Diamonds. *Philosophical Magazine B* 78(3): 299-314

King, J.E. (1986) The metamorphic internal zone of Wopmay orogen (Early Proterozoic), Canada: 30 km of structural relief in a composite section based on plunge projection. *Tectonics* 5(7): 973-994

King, J.M., Moses, T.M., Shigley, J.E., Welbourn, C.M., Lawson, S.C., Cooper, M. (1998) Characterizing natural-color type IIb blue diamonds. *Gems & Gemology* 34(4): 246-268

Kirkley, M.B., Gurney, J.J., Otter, M.L., Hill, S.J. & Daniels, L.R. (1991) The application of C isotope measurements to the identification of the sources of C in diamonds: a review. *Applied Geochemistry* 6: 477-494

Kopylova, M.G. & Caro, G. (2004) Mantle xenoliths from the Southeastern Slave Craton: Evidence for Chemical zonation in a thick, Cold lithosphere. *Journal of Petrology* 45(5): 1045-1067

Kopylova, M.G. & McCamman, C. (2000) Composition and the redox state of the Slave peridotitic mantle. *In International Kimberlite Conference: Extended Abstracts* 8: 1-5

Kopylova, M.G. & Russell, J.K. (2000) Chemical stratification of cratonic lithosphere: constraints from the Northern Slave craton, Canada. *Earth and Planetary Science Letters* 181: 71-87

Kopylova, M.G., Mogg, T. & Scott Smith, B. (2010) Mineralogy of the Snap Lake Kimberlite, Northwest Territories, Canada, and compositions of phlogopite as records of its crystallization. *The Canadian Mineralogist* 48: 549-570

Kopylova, M.G., Russell, J.K. & Cookenboo (1998) Upper-mantle stratigraphy of the Slave craton, Canada: Insights into a new kimberlite province. *Geology* 26(4): 315-318

Kopylova, M.G., Russell, J.K. & Cookenboo, H. (1999) Petrology of Peridotite and Pyroxenite Xenoliths from the Jericho Kimberlite: Implications for the Thermal State of the Mantle beneath the Slave Craton, Northern Canada. *Journal of Petrology* 40(1): 79-104

Kopylova, M.G., Russell, J.K. & Cookenboo, H. (1999b) Mapping the Lithosphere beneath the North Central Slave Craton. *In Proceedings of the VIIth International Kimberlite Conference* 1: 468-479

Kröner, A. (1991) Tectonic evolution of the Archaean and Proterozoic. *Tectonophysics* 187(4): 393-410

Kusky, T.M. (1989) Accretion of the Archean Slave province. *Geology* 17: 63-67

Lang, A.R. (1964) Dislocations in diamond and the origin of trigons. Proceedings of the Royal Society of London, Series A. Mathematical and Physical Sciences 78(1373): 234-242

LeCheminant, A.N., Heaman, L.M., van Breemen, O., Ernt, R.E., Baragar, W.R.A & Buchan, K.L. (1996) Mafic magnetism, mantle roots and kimberlites in the Slave craton. *Searching for diamonds in*

Canada. Edited by AN LeCheminant et al. Geological Survey of Canada, Open-File 3228: 161-169

Leost, I., Stachel, T., Brey, G.P., Harris, J.W. & Ryabchikov, I.D. (2003) Diamond formation and source carbonation: mineral associations in diamonds from Namibia. *Contributions to Mineralogy and Petrology* 145: 15-24

Li, K., Li., L., Pearson, D.G. & Stachel, T. (2019) Diamond isotope compositions indicate altered igneous oceanic crust dominates deep carbon recycling. *Earth and Planetary Science Letters* 516: 190-201

Li, L., Bebout, G.E. & Idleman, B.D. (2007) Nitrogen concentration and $\delta^{15}N$ of altered oceanic crust obtained on ODP Legs 129 and 185: Insights into alteration-related nitrogen enrichment and the nitrogen subduction budget. *Geochimica et Cosmochimica Acta* 71: 2344-2360

Locock, A.J. (2018) An excel spreadsheet to recast analyses of garnet into end-member components, and a synopsis of the crystal chemistry of natural silicate garnets. *Computers & Geosciences* 34: 1769-1780

McBean, D., Kirkley, M. & Revering, C. (2003) Structural controls on the Morphology of the Snap Lake Kimberlite dyke. *In International Kimberlite Conference: Extended Abstracts* 8: 1-5

McCallum, M.E., Huntley, P.M., Falk, R.W. & Otter, M.L. (1994) Morphological, resorption and etch feature trends of diamonds from kimberlites within the Colorado-Wyoming State line district, USA *In 5th International Kimberlite Conference: Extended Abstracts* 2: 32-50

McDonough, W.F. (1991) Partial melting of subducted oceanic crust and isolation of its residual eclogitic lithology. *Philosophical Transactions of the Royal Society of London. Series A: Physical and Engineering Sciences* 335(1638): 407-418

McDonough, W.F. & Rudnick, R.L. (1998) Mineralogy and Composition of the upper mantle. *Reviews in Mineralogy* 37: 139-164

McGlynn, J.C. & Irving, E. (1975) Paleomagnetism of early Aphebian diabase dykes from the Slave structural province, Canada. *Tectonophysics* 26: 23-38

Meyer, H.O.A. (1987) Inclusions in Diamond. Mantle Xenoliths

Meyer, H.O.A. & McCallum, M.E. (1986) Mineral inclusions in diamonds from the Sloan Kimberlite, Colorado. *The Journal of Geology* 94(4): 600-612

Moore, M. & Lang, A.R. (1974) On the origin of the rounded dodecahedral habit of natural diamond. *Journal of Crystal Growth* 26(1): 133-139

Morphological, resorption and etch feature trends of diamonds from kimberlites within the Colorado-Wyoming state line district, USA. *In Proceedings of the 5th International Kimberlite Conference* 2: 32-50

Nickel, K.G. & Green, D.H. (1985) Empirical geothermobarometry for garnet peridotites and implications for the nature of the lithosphere, kimberlites and diamonds. *Earth and Planetary Science Letters* 73: 158-170

Nimis, P. & Taylor, W.R. (2000) Single clinopyroxene thermobarometry for garnet peridotites. Part I. Calibration and testing of a Cr-in-Cpx barometer and an enstatite-in Cpx thermometer. *Contributions to Mineralogy and Petrology.* 139: 541-554

O'Reilly, S.Y., Griffin, W.L., Djomani, Y.P., Natapov, L.M., Pearson, N.J., Davies, R.M., Doyle, B.J. & Kivi, K. (2001) The mantle beneath the Slave Craton (Canada): Composition and Architecture. *In Slave-Kaapvaal Workshop, Merrickville, Ontario, Canada* 5-9

Omar, M., Pandya, N.S., & Tolansky, S. (1954) The etching of diamond I. Octahedron faces. *Proceedings of the Royal Society of London. Series A. Mathematical and Physical Sciences* 225(1160): 33-40

O'Neill, H.St.C. & Wood, B.J. (1979) An Experimental Study of Fe-Mg Partitioning Between Garnet and Olivine and Its Calibration as a Geothermometer. *Contributions to Mineralogy and Petrology.* 70: 59-70

Orlov, I. L. (1977). The mineralogy of the diamond. *John Wiley & Sons*.

Padgham, W.A. (1985) Observations and speculations on supracrustal successions in the Slave Structural Province. Evolution of Archean Sequences. *Geological Association of Canada, Special Paper* 28: 133-151

Padgham, W.A. (1992) Mineral deposits in the Archean Slave Structural Province; lithological and tectoic setting. *Precambrian Research* 58: 1-24

Padgham, W.A., & Fyson, W.K. (1992) The Slave Province: a distinct Archean craton. *Canadian Journal of Earth Science* 29: 2072-2086

Palot, M., Cartigny, P., Harris, J.W., Kaminsky, F.V. & Stachel, T. (2012) Evidence for deep mantle convection and primordial heterogeneity from nitrogen and carbon stable isotopes in diamond. *Earth and Planetary Science Letters* 357-358: 179-193

Pandeya, D.C. & Tolansky, S. (1961) Micro-disk patterns on diamond dodecahedra. *Proceedings of the Physical Society* 78(1): 12

Pearson, N.J., Griffin, W.L., Doyle, B.J., O'Reilly, S.Y., Van Achterbergh, E. & Kivi, K. (1998) Xenoliths from kimberlite pipes of the Lac de Gras area, Slave craton, Canada. *In International Kimberlite Conference: Extended Abstracts* 7: 670-672

Pearson, D.G. & Wittig, N. (2008) Formation of Archaean continental lithosphere and its diamonds: the root of the problem. *Journal of the Geological Society, London* 165: 895-914

Pearson DG, Woodhead J, Janney PE (2019) Kimberlites as Geochemical Probes of Earth's Mantle. Elements 15:387-392, doi:10.2138/gselements.15.6.387

Petts DC, Chacko T, Stachel T, Stern RA, Heaman LM (2015) A nitrogen isotope fractionation factor between diamond and its parental fluid derived from detailed SIMS analysis of a gem diamond and theoretical calculations. Chemical Geology 410:188-200

Pell, J.A. (1997) Kimberlites in the Slave Craton, Northwest Territories, Canada. *Geoscience Canada* 24(2): 77-90

Phillips, D., Harris, J.W. & Viljoen, K.S. (2004) Mineral chemistry and thermobarometry of inclusions from De Beers Pool diamonds, Kimberley, South Africa. *Lithos* 77: 155-179

Pokhilenko, N.P., Sobolev, N.V., McDonald, J.A., Hall, A.E., Yefimova, E.S., Zedgenizov, D.A., Logvinova, & Reimers, L.F. (2001). Crystalline Inclusions in Diamonds from Kimberlites of the Snap Lake Area (Slave Craton, Canada): New evidences for the Anomalous Lithospheric Structure. *Doklady Earth Sciences C/C of Doklady - Akademiia Nauk* 380: 806-811

Pokhilenko, N.P., Sobolev, N.V., Reutsky, V.N., Hall, A.E. & Taylor, L.A. (2004) Crystalline inclusions and C isotope ratios in diamonds from the Snap Lake/King Lake kimberlite dyke system: evidence of ultradeep and enriched lithospheric mantle. *Lithos* 77(1-4): 57-67

Pollack, H.N. (1991) Cratonization and thermal evolution of the mantle. *Earth and Planetary Science Letters* 80: 175-182

Pollack, H.N. & Chapman, D.S. (1977) Mantle heat flow. *Earth and Planetary Science Letters* 34(2): 174-184

Promprated, P., Taylor, L.A, Floss, C., Malkovets, V., Anand, M., Griffin, W., Pokhilenko, N., Sobolev, N. (2003) Diamond inclusions from Snap Lake, NWT, Canada. *In International Kimberlite Conference: Extended Abstracts* 8: 1-5

Promprated, P., Taylor, L.A., Anand, M., Floss, C., Sobolev, N.V. & Pokhilenko, N.P. (2004) Multiple-mineral inclusions in diamonds from the Snap Lake/King Lake kimberlite dyke, Slave craton, Canada: a trace-element perspective. *Lithos* 77: 69-81

Prytulak, J. & Elliott, T. (2007) TiO_2 enrichment in ocean island basalts. *Earth and Planetary Science Letters* 263: 388-403

Reimink, J.R., Chacko, T., Stern, R.A. & Heaman, L. (2014) Earth's earliest evolved crust generated in an Iceland-like setting. *Nature Geoscience* 7(7), 529-533

Robertson, R., Fox, J.J., Martin, A.E. (1934) Two types of diamond. *Philosophical transactions of the royal society of London A* 232: 463-535

Robinson, D.N. (1979) Surface textures and other features of diamonds (Doctoral dissertation, University of Cape Town)

Schulze, D.J., Valley, J.W. & Spicuzza, M.J. (2000) Coesite eclogites from the Roberts Victor kimberlite, South Africa. *Lithos* 54: 23-32

Schidlowski, M. (2001) Carbon isotopes as biogeochemical recorders of life over 3.8 Ga of Earth history: evolution of a concept. *Precambrian Research* 106: 117-134

Shilobreeva, S., Martinez, I., Busigny, V., Agrinier, P. & Laverne, C. (2011) Insights into C and H storage in thee altered oceanic crust: Results from ODP/IODP Hole 1256D. *Geochimica et Cosmochimica Acta* 75: 2237-2255

Shimizu, N. & Richardson, S.H. (1987) Trace element abundance patterns of garnet inclusions in peridotite-suite diamonds. *Geochimica et Cosmochimica Acta* 51(3): 755-758

Shu, Q., Brey, G.P., Gerdes, A. & Hoefer, H.E. (2013) Geochronological and geochemical constraints on the formation and evolution of the mantle underneath the Kaapvaal craton: Lu-Hf and Sm-Nd systematics. *Geochimica et Cosmochimica Acta* 113: 1-20

Sircombe, K.N., Bleeker, W., Stern, R.A. (2001) Detrital zircon geochronology and grain-size analysis of a ~2800 Ma Mesoarchean proto-cratonic cover succession, Slave Province, Canada. *Earth and Planetary Science Letters* 189(3-4): 207-220

Slawson, C.B. (1950) Twinning in the diamond. *American Mineralogist: Journal of earth and planetary materials* 35(3-4): 193-206

Smart, K.A., Chacko, T., Stachel, T., Muehlenbachs, K., Stern, R.A. & Heaman, L.M. (2011) Diamond growth from oxidized carbon sources beneath the Northern Slave Craton, Canada: A $d^{13}C$-N study of eclogite-hosted diamonds from the Jericho kimberlite. *Geochimica et Cosmochimica Acta* 75: 6027-6047

Smit, K.V., Shirey, S.B., & Wang, W. (2016) Type Ib diamond formation and preservation in the West African lithospheric mantle: Re-Os age constraints from sulphide inclusions in Zimmi diamonds. *Precambrian Research* 286: 152-166

Snyder, D. & Bruneton, M. (2007) Seismic anisotropy of the Slave craton, NW Canada, from joint interpretation of SKS and Rayleigh waves. *Geophysical Journal International* 169(1): 170-188

Snyder, D.B., Hillier, M.J., Kjarsgaard, B.A., de Kemp, E.A. & Craven, J.A. (2014) Lithospheric architecture of the Slave craton, northwest Canada, as determined from an interdisciplinary 3-D model. *Geochemistry, Geophysics, Geosystems* 15: 1895-1910

Sobolev, N.V. (1981) Native Iron in Yakutian diamonds, its paragenesis. *Geologiya I geofizika* 22: 25-29

Sobolev, N. V., & Shatsky, V. S. (1990). Diamond inclusions in garnets from metamorphic rocks: a new environment for diamond formation. *Nature* 343(6260): 742-746

Sobolev, N.V., Lavrent'ev, Y.G., Pokhilenko, N.P. & Usova, L.V. (1973) Chrome-rich garnets from the kimberlites of Yakutia and their parageneses. *Contributions to Mineralogy and Petrology* 40: 39-52

Speich, L., Kohn, S.C., Bulanova, G.P. & Smith, C.B. (2018) The behavior of platelets in natural diamonds and the development of a new mantle thermometer. *Contributions to Mineralogy and Petrology* 173: 39-60

Speich, L., Kohn, S.C., Wirth, R., Bulanova, G.P., Smith, C.B. (2017) The relationship between platelet size and the B' infrared peak of diamonds revisited. *Lithos* 278: 419-426

Stachel, T. (2014) Diamonds. *Geology of Gem Deposits Edition* 2: 1-28

Stachel, T., Brey, G.P. & Harris, J.W. (2005) Inclusions in Sublithospheric Diamonds: Glimpses of Deep Earth. *Elements* 1(2): 73-78

Stachel, T. & Harris, J.W. (1997) Syngenetic inclusions in diamond from the Birim field (Ghana) - a deep peridotitic profile with a history of depletion and re-enrichment. *Contributions to Mineralogy and Petrology* 127(4): 336-352

Stachel, T., & Harris, J. W. (2008). The origin of cratonic diamonds—constraints from mineral inclusions. *Ore Geology Reviews* 34(1-2): 5-32

Stachel, T. & Harris, J.W. (2009) Formation of diamond in the Earth's mantle. *Journal of Physics: Condensed Matter* 21(36): 364206

Stachel, T., Harris, J.W. & Brey, G.P. (1998) Rare and unusual mineral inclusions in diamonds from Mwadui, Tanzania. *Contributions to Mineralogy and Petrology* 132: 34-47

Stachel, T., Harris, J.W., Tappert, R. & Brey, G.P. (2003) Peridotitic diamonds from the Slave and the Kaapvaal cratons – similarities and differences based on a preliminary data set. *Lithos* 71: 489-503

Stachel, T., Harris, J.W. & Muehlenbachs, K. (2009) Sources of carbon in inclusion bearing diamonds. *Lithos* 112S: 625-637

Stachel, T., & Luth, R.W. (2015) Diamond formation - Where. When and how? *Lithos* 220-223: 200-220

Stachel, T., Viljoen, K.S., McDade, P. & Harris, J.W. (2004) Diamondiferous lithospheric roots along the western margin of the Kalahari Carton – the peridotitic inclusion suite in diamonds from Orapa and Jwaneng. *Contributions to Mineralogy and Petrology* 147: 32-47

Stern, R.A., Howell, D., Stachel, T., Pearson, D.G., Cartigny, P., Oh, A. (2014) Methods and reference materials for SIMS diamond C- and N-isotope analysis. *Canadian Centre for Isotopic Microanalysis, Research Report 14-01. University of Alberta, Education and Research Archive*

Sunagawa, I. (1990) Growth and morphology of diamond crystals under stable and metastable conditions. *Journal of Crystal Growth* 99(1-4), 1156-1161

Sverjensky, D.A. & Huang, F. (2015) Diamond formation due to a pH drop during fluid-rock interactions. *Nature Communications* 6: 8702

Sylvester, P.J. (2008) LA-(MC)-ICP-MS Trends in 2006 and 2007 with Particular Emphasis on Measurement Uncertainties. *Geostandards and Geoanalytical Research* 32(4): 469-488

Tappert, R. & Tappert, M.C. (2011) Diamonds in nature: a guide to rough diamonds. *Springer Science and Business Media*

Tappert, R., Stachel, T., Harris, J.W., Muehlenbachs, K., Ludwig, T. & Brey, G.P. (2005) Diamonds from Jagersfontein (South Africa): messengers from the sublithospheric mantle. *Contributions to Mineralogy and Petrology* 150: 505-522

Taylor, W.R., Canil, D. & Milledge, H.J. (1996) Kinetics of Ib to IaA nitrogen aggregation in diamond. *Geochimica et Cosmochimica Acta* 60(23): 4725-4733

Taylor, W.R., Jaques, A.L., Ridd, M. (1990) Nitrogen-defect aggregation characteristics of some Australian diamonds: Time-temperature constraints on the source regions of pipe and alluvial diamonds. *American Mineralogist* 75: 1290-1310

Thompson, P.H., Judge, A.S. & Lewis, T.J. (1996) Thermal evolution of the lithosphere in the central Slave province: Implications for diamond genesis. *In Searching for Diamonds in Canada. Geological Survey of Canada, Open File*, 3228: 151-160

Thorpe, R.I., Hickman, A.H., Davis, D.W., Mortenson, J.K. & Trendall, A.F. (1992) U-Pb zircon geochronology of Archaean felsic units in the Marble Bar region, Pilbara Craton, Western Australia. *Precambrian Research* 56(3-4): 169-189

Titus, E., Misra, D.S., Sikder, A.K., Tyagi, P.K., Singh, M.K., Misra, A., Ali, N., Cabral, G., Neto, V.F. & Gracio, J. (2005) Quantitative analysis of hydrogen in chemical vapour deposited diamond films. *Diamond & Related Materials* 14: 476-481

van Breemen, O., Davis, W.J. & King, J.E. (1992) Temporal distribution of granitoid plutonic rocks in the Archean Slave Province, northwest Canadian Shield. *Canadian Journal of Earth Science* 29: 2186-2199

Vance, E.R., Harris, J.W., & Milledge, H.J. (1973) Possible origins of α-damage in diamonds from kimberlite and alluvial sources. *Mineralogical Magazine* 39(303): 349-360

Wagner, P.A. (1914) The diamond fields of southern Africa. The Transvall Leader. Johannesburg, South Africa

Wang, W. (1998) Formation of diamond with mineral inclusions of "mixed" eclogite and peridotite paragenesis. *Earth and Planetary Science Letters* 160: 831-843

Wei, L., Kuo, P.K. & Thomas, R.L. (1993) Thermal Conductivity of Isotopically Modified single crystal diamond. *Physical Review Letters* 70(24): 3764-2767

Woods, G.S. (1986) Platelets and the infrared absorption of Type Ia diamonds. *Proceedings of the Royal Society of London A. Mathematical and Physical Sciences* 407: 219-238

Woods, G.S. & Collins, A.T. (1983) Infrared absorption spectra of hydrogen complexes in Type I diamonds. *Journal of Physics and Chemistry of Solid* 44(5): 471-475

Ziberna, L., Nimis, P., Kuzmin, D. & Malkovets, V.G. (2016) Error sources in single-clinopyroxene thermobarometry and a mantle geotherm for the Novinka kimberlite, Yakutia. *American Mineralogist* 101: 2222-2232

Appendixes

Appendix A

Diamond Physical Characteristics

Sample	Sieve Size	Morphology	Color	Surface Textures										Inclusion Suite
				Stacked growth layers	Shield-shaped laminae	Trigons	Tetragons	Hillocks	Terraces	Pitting	Late-Stage Etching	Deformation Lines	Resorption	
SN001	6 gr	of	colorless			y-							weak	Grt
SN002	6 gr	od	light brown	y	y	y-							weak	
SN003	6 gr	od-agg	light brown	y	y	y-						y	weak	
SN004	5 gr	o	colorless	y		y-						y		Chr
SN005	4 gr	o	yellow	y	y	y-						y	moderate	Grt
SN006	4 gr	o	colorless	y	y	y-								
SN007	4 gr	f	colorless										weak	
SN008	4 gr	od	brown	y	y	y-							weak	Sul
SN009	4 gr	o	colorless	y		y-						y	weak	
SN010	3 gr	od	colorless	y	y	y-							weak	Chr
SN011	3 gr	m	pink			y							strong	
SN012	3 gr	f	colorless	y									weak	Grt
SN013	3 gr	of	colorless	y	y	y-						y	weak-moderate	
SN014	3 gr	of	colorless	y	y	y-						y	weak	Ol
SN015	3 gr	od	light yellow	y		y-					y		moderate-strong	
SN016	3 gr	f	light brown									y	weak	
SN017	3 gr	o	colorless	y	y							y	moderate	
SN018	11+	o	colorless	y	y	y-							moderate	
SN019	11+	o	colorless	y	y	y-							moderate	Sul
SN020	11+	m	colorless	y		y-							weak	Ol
SN021	11+	o (fl)	colorless	y	y	y-							moderate	Ol

				Surface Textures										
Sample	**Sieve Size**	**Morphology**	**Color**	**Stacked growth layers**	**Shield-shaped laminae**	**Trigons**	**Tetragons**	**Hillocks**	**Terraces**	**Pitting**	**Late-Stage Etching**	**Deformation Lines**	**Resorption**	**Inclusion Suite**
SN022	11+	m	colorless	y		y-								Ol-Epi
SN023	11+	of	colorless	y	y	y-							weak	
SN024	11+	m	colorless	y	y	y-						y	moderate	Grt
SN025	11+	od	colorless	y	y						y		weak	Grt
SN026	11+	m-agg	colorless	y	y	y-					y		weak-moderate	Grt-Ol
SN027	11+	od-agg	colorless	y	y	y-	y	y	y				strong	Grt-Ol
SN028	11+	o	colorless	y	y	y-					y	y	weak	
SN029	11+	do-agg	colorless	y	y	y-							strong	
SN030	11+	od-agg	yellow	y	y	y-			y		y		strong	Cpx
SN031	11+	o	colorless	y	y	y-							moderate	
SN032	11+	m	colorless	y	y	y-							moderate	
SN033	11+	of	colorless	y	y						y		weak	Ol-Sul
SN034	11+	of-agg	colorless	y	y					y			moderate	
SN035	11+	of	colorless	y	y	y-							moderate	
SN036	11+	o	colorless	y	y	y-						y	weak	Grt-Ol
SN037	11+	od	colorless	y	y					y	y		moderate	
SN038	11+	o	pink	y	y	y-								
SN039	11+	od	colorless	y	y								weak	
SN040	11+	of-agg	pink/brown	y	y	y-					y	y	weak	
SN041	11+	f	colorless	y		y-						y	weak	Grt-Cpx
SN042	11+	o	colorless	y		y-							weak	

				Surface Textures										
Sample	**Sieve Size**	**Morphology**	**Color**	**Stacked growth layers**	**Shield-shaped laminae**	**Trigons**	**Tetragons**	**Hillocks**	**Terraces**	**Pitting**	**Late-Stage Etching**	**Deformation Lines**	**Resorption**	**Inclusion Suite**
SN043	11+	od	colorless	y	y								moderate	
SN044	11+	o	colorless	y	y	y-						y	weak-moderate	
SN045	9+	mf	colorless	y	y	y							weak	Chr
SN046	9+	m	colorless			y-								Chr
SN047	9+	o	colorless	y		y-							weak	Chr
SN048	9+	o	colorless	y	y	y-							weak-moderate	Chr
SN049	9+	m	colorless	y	y								moderate	Grt
SN050	9+	m	colorless	y	y	y-							moderate	Grt
SN051	9+	o-agg (fl)	colorless	y	y	y-						y	weak-moderate	Ol
SN052	9+	o	colorless	y	y	y-							moderate	Grt-Ol
SN053	9+	m	colorless	y	y			y					Strong	Grt
SN054	9+	m	colorless			y-							weak-moderate	Grt-Ol
SN055	9+	od-f	pink	y	y	y-							weak	
SN056	9+	do	light yellow	y	y								moderate	K-Spar
SN057	9+	o	colorless	y	y								weak-moderate	
SN058	9+	do	brown	y	y								strong	
SN059	9+	I	colorless	y	y						y		moderate	Ol
SN060	9+	o-agg	colorless	y	y	y-		y					moderate	
SN061	9+	o	yellow			y-						y		
SN062	9+	o	colorless	y	y	y-							weak	
SN063	9+	m	colorless		y	y-						y	weak	Ol

				Surface Textures										
Sample	**Sieve Size**	**Morphology**	**Color**	**Stacked growth layers**	**Shield-shaped laminae**	**Trigons**	**Tetragons**	**Hillocks**	**Terraces**	**Pitting**	**Late-Stage Etching**	**Deformation Lines**	**Resorption**	**Inclusion Suite**
SN064	9+	o (fl)	colorless	y	y	y-						y	weak	Opx
SN065	9+	o	colorless	y	y	y-								Ol
SN066	9+	m	colorless	y		y-						y	weak-moderate	Ol
SN067	9+	m-agg	yellow	y	y	y-							weak-moderate	
SN068	9+	od	colorless	y	y	y-							weak-moderate	
SN069	9+	od-f	colorless	y	y	y-							moderate	
SN070	9+	m	colorless	y	y	y-							weak	Ol
SN071	9+	o-agg	colorless	y	y	y-							weak	
SN072	9+	o	colorless	y	y								weak	
SN073	9+	m-agg	colorless	y		y-								Ol
SN074	9+	m	colorless	y	y								weak-moderate	Ol
SN075	9+	m	colorless	y	y	y-						y		Ol
SN076	9+	o	colorless	y	y								weak-moderate	
SN077	9+	o	colorless	y	y	y-						y	weak	
SN078	9+	m-agg	colorless	y		y-						y	weak	Ol
SN079	9+	mf	light brown	y	y	y-							weak	
SN080	9+	of	colorless	y		y-							moderate	
SN081	9+	o	colorless	y	y	y-							weak-moderate	
SN082	9+	m	colorless	y	y	y-							weak	
SN083	9+	o (fl)	colorless	y	y	y-								Ol
SN084	9+	I	colorless		y	y-								Ol

				Surface Textures										
Sample	**Sieve Size**	**Morphology**	**Color**	**Stacked growth layers**	**Shield-shaped laminae**	**Trigons**	**Tetragons**	**Hillocks**	**Terraces**	**Pitting**	**Late-Stage Etching**	**Deformation Lines**	**Resorption**	**Inclusion Suite**
SN085	9+	o-agg	colorless	y	y	y-						y		Ol
SN086	9+	of	brown	y	y	y-							weak	Sul
SN087	9+	o (fl)	colorless	y	y	y-						y	weak	
SN088	9+	f	colorless		y	y-					y		weak	Ol-Sul
SN089	9+	mf	colorless	y		y-							weak	Ol
SN090	9+	od (fl)	pink/brown	y	y	y-							weak-moderate	
SN091	9+	m-agg	colorless	y	y	y-							weak	Ol
SN092	9+	o	colorless	y	y	y-							weak-moderate	
SN093	9+	f	colorless		y	y-							moderate	Ol
SN094	9+	m-agg	colorless	y	y	y-						y	weak-moderate	Ol
SN095	9+	odf	colorless	y	y	y-							moderate	Ol
SN096	9+	od	colorless	y	y	y-		y					moderate-strong	Grt-Ol
SN097	9+	o-agg	colorless	y	y								weak	Grt-Co-Sul
SN098	9+	mf	colorless	y	y	y-							weak	Ol
SN099	7+	m	colorless	y	y	y-								Ol
SN100	7+	m	colorless	y		y-							weak	Opx
SN101	7+	m	pink	y		y-					y		moderate	
SN102	7+	m	colorless	y	y	y-								Ol
SN103	7+	m	colorless	y	y	y-							weak	
SN104	7+	m	yellow	y		y-							weak-moderate	Ol
SN105	7+	o	yellow	y	y	y-						y	weak-moderate	

				Surface Textures										
Sample	**Sieve Size**	**Morphology**	**Color**	**Stacked growth layers**	**Shield-shaped laminae**	**Trigons**	**Tetragons**	**Hillocks**	**Terraces**	**Pitting**	**Late-Stage Etching**	**Deformation Lines**	**Resorption**	**Inclusion Suite**
SN106	7+	o	light yellow	y	y	y-							weak	
SN107	7+	o	light yellow	y	y	y-								Ol
SN108	7+	o	colorless		y	y-								Grt
SN109	7+	m-agg	colorless	y	y	y-						y	weak	Ol
SN110	7+	m	colorless	y	y	y-						y	weak	
SN111	7+	m-agg	colorless			y-								Ol
SN112	7+	do-agg	brown	y	y	y-+							moderate	
SN113	7+	o	colorless	y	y	y-						y		Ol
SN114	7+	om-agg	colorless	y	y	y-							moderate	Ol
SN115	7+	o	colorless	y	y	y-						y	weak	Ol
SN116	7+	o	colorless	y	y	y-							weak	Grt-Ol
SN117	7+	m	colorless	y	y	y-							weak-moderate	Ol
SN118	7+	mf	colorless	y	y	y-						y	weak	Grt-Ol
SN119	7+	o (fl)	colorless	y	y	y-							weak	
SN120	7+	o	colorless	y	y	y-						y	weak	Ol
SN121	7+	mf	colorless	y	y	y-							weak	Ol
SN122	7+	f	colorless		y	y-							weak	Ol
SN123	7+	m (twin)	colorless	y	y	y-							weak	
SN124	7+	m-agg	colorless	y	y	y-							weak	
SN125	7+	od	colorless	y	y	y-						y	weak	
SN126	7+	o	colorless	y	y	y-							weak	

				Surface Textures										
Sample	**Sieve Size**	**Morphology**	**Color**	**Stacked growth layers**	**Shield-shaped laminae**	**Trigons**	**Tetragons**	**Hillocks**	**Terraces**	**Pitting**	**Late-Stage Etching**	**Deformation Lines**	**Resorption**	**Inclusion Suite**
SN127	7+	o	colorless	y	y	y-						y		Ol
SN128	7+	m	colorless	y	y	y-							weak-moderate	Co
SN129	7+	o	colorless	y	y	y-							weak	Ol
SN130	7+	m	colorless	y	y	y-							moderate	Grt
SN131	7+	I	colorless	y	y	y-							weak	
SN132	7+	m-agg	colorless	y	y	y-						y	weak-moderate	Grt-Opx
SN133	7+	om-agg	colorless	y	y	y-							weak	Ol
SN134	7+	o	pink	y	y	y-							weak	Ol-Chr
SN135	7+	mf	colorless	y	y	y-						y	weak-moderate	Ol
SN136	7+	m	colorless	y	y								weak-moderate	Ol
SN137	7+	I	colorless	y	y			y					moderate-strong	
SN138	7+	o-agg	colorless	y	y	y-								Ol
SN139	7+	om-agg	colorless	y	y	y-							weak	
SN140	7+	f	colorless	y	y	y-							weak-moderate	Ol
SN141	7+	I-agg	colorless	y	y	y-							weak	
SN142	7+	o-agg	colorless	y	y								weak-moderate	Ol
SN143	7+	f	colorless		y	y-							weak	Ol
SN144	7+	o	colorless	y	y	y-						y	weak-moderate	Ol
SN145	7+	f	colorless	y	y	y-								
SN146	7+	m-agg	colorless	y	y	y-						y	weak	Ol
SN147	7+	I	colorless	y	y	y-							weak-moderate	Ol

o=octahedral, d=dodecahedron, m=macle, agg=aggregate, f=fragment, I=irregular, fl=flattened

Appendix B

FTIR results on Snap Lake diamond fragments

Sample	Type	Total nitrogen (at.ppm)	%B	T[N,1Ga]	Platelet Peak Area (cm-2)	3107 Peak Area (cm-2)
SN001_1	IaAB	500.4	41.8	1148	22.00	-
SN001_2	IaAB	432.1	39.4	1149	19.22	-
SN001_3	IaAB	479.9	41.9	1149	20.94	-
SN001_4	IaAB	342.8	36.3	1151	15.30	-
SN004_1	IaAB	122.5	13.9	1145	1.27	-
SN004_2	IaAB	345.8	53.6	1169	12.13	0.85
SN004_3	IaAB	522.9	43.6	1148	22.47	-
SN005_1	IaAB	800.5	77.2	1175	66.91	1.51
SN005_2	IaAB	902.9	79.3	1175	74.24	1.65
SN005_3	IaAB	884.7	78.8	1175	73.24	1.49
SN008_1	IaAB	184.7	48.4	1180	8.85	1.05
SN008_2	IaAB	177.9	47.3	1180	7.25	2.44
SN008_3	IaAB	78.9	58.0	1213	1.73	0.91
SN010_1	IaAB	27.6	51.4	1234	0.05	0.80
SN010_2	IaAB	30.6	48.4	1228	1.50	0.53
SN010_3	IaAB	42.6	44.4	1214	1.12	0.73
SN012_1	IaAB	15.7	65.6	1267	0.06	1.17
SN012_2	IaAB	37.1	73.6	1253	-	3.00
SN012_3	IaAB	30.8	76.0	1262	-	1.14
SN014_1	IaA	588.3	2.2	1063	-	1.48
SN014_2	IaA	568	0.0	1031	-	1.39
SN014_3	IaA	569.1	4.3	1079	-	1.34
SN019_1	IaAB	235.2	31.6	1155	5.01	0.93
SN019_2	IaAB	214.3	18.9	1141	4.01	0.84
SN019_3	IaAB	60.9	67.2	1231	4.92	0.95

Sample	Type	Total nitrogen (at.ppm)	%B	T[N,1Ga]	Platelet Peak Area (cm-2)	3107 Peak Area (cm-2)
SN001_1	IaAB	500.4	41.8	1148	22.00	-
SN001_2	IaAB	432.1	39.4	1149	19.22	-
SN001_3	IaAB	479.9	41.9	1149	20.94	-
SN001_4	IaAB	342.8	36.3	1151	15.30	-
SN004_1	IaAB	122.5	13.9	1145	1.27	-
SN004_2	IaAB	345.8	53.6	1169	12.13	0.85
SN004_3	IaAB	522.9	43.6	1148	22.47	-
SN005_1	IaAB	800.5	77.2	1175	66.91	1.51
SN005_2	IaAB	902.9	79.3	1175	74.24	1.65
SN005_3	IaAB	884.7	78.8	1175	73.24	1.49
SN008_1	IaAB	184.7	48.4	1180	8.85	1.05
SN008_2	IaAB	177.9	47.3	1180	7.25	2.44
SN008_3	IaAB	78.9	58.0	1213	1.73	0.91
SN010_1	IaAB	27.6	51.4	1234	0.05	0.80
SN010_2	IaAB	30.6	48.4	1228	1.50	0.53
SN010_3	IaAB	42.6	44.4	1214	1.12	0.73
SN012_1	IaAB	15.7	65.6	1267	0.06	1.17
SN012_2	IaAB	37.1	73.6	1253	-	3.00
SN012_3	IaAB	30.8	76.0	1262	-	1.14
SN014_1	IaA	588.3	2.2	1063	-	1.48
SN014_2	IaA	568	0.0	1031	-	1.39
SN014_3	IaA	569.1	4.3	1079	-	1.34
SN019_1	IaAB	235.2	31.6	1155	5.01	0.93
SN019_2	IaAB	214.3	18.9	1141	4.01	0.84
SN019_3	IaAB	60.9	67.2	1231	4.92	0.95

Sample	Type	Total nitrogen (at.ppm)	%B	T[N,1Ga]	Platelet Peak Area (cm-2)	3107 Peak Area (cm-2)
SN033_2	IaAB	111.4	63.7	1210	1.31	1.40
SN033_3	IaAB	192.8	59.4	1190	15.14	8.55
SN036_1	IaAB	184.3	77.5	1214	18.36	0.89
SN036_2	IaAB	169.5	79.8	1220	11.39	1.77
SN036_3	IaAB	156.4	76.0	1217	16.05	1.60
SN041_1	IaAB	53.3	44.3	1208	2.49	1.03
SN041_2	IaAB	260.9	79.9	1209	4.55	-
SN045_1	IaAB	66	54.8	1214	2.11	1.43
SN045_2	IaAB	77.8	58.9	1214	2.21	0.76
SN045_3	IaAB	213.1	77.0	1210	11.42	2.69
SN046_1	IaAB	29.5	40.7	1220	-	-
SN046_2	IaAB	49	31.8	1196	4.35	2.88
SN046_3	IaAB	24.1	31.5	1215	-	-
SN047_1	IaAB	657.6	34.4	1133	4.25	0.78
SN047_2	IaAB	569.6	13.6	1108	3.96	0.80
SN047_3	IaAB	609.9	17.9	1114	3.96	0.83
SN048_1	IaB	909	95.3	1219	69.88	4.92
SN048_2	IaB	727.1	94.0	1218	63.67	3.91
SN048_3	IaB	661	93.6	1219	59.45	5.23
SN048_4	IaB	849	94.3	1216	70.07	4.77
SN049_1	IaAB	71.1	69.1	1229	2.46	2.01
SN049_2	IaAB	138.4	70.7	1213	8.99	4.05
SN049_3	II	0	-	-	-	0.31
SN050_1	IaAB	60.1	72.2	1238	0.22	0.17
SN050_2	IaAB	38.6	64.8	1240	0.19	-

Sample	Type	Total nitrogen (at.ppm)	%B	T[N,1Ga]	Platelet Peak Area (cm-2)	3107 Peak Area (cm-2)
SN050_3	IaA	15.7	2.5	1151	0.20	-
SN051_1	IaAB	129.9	52.7	1193	6.57	1.59
SN051_2	IaAB	125	56.2	1198	6.02	1.59
SN051_3	IaAB	139.9	54.5	1193	8.26	1.29
SN052_1	IaAB	345.3	55.1	1171	-	-
SN052_2	IaAB	178.6	45.3	1177	-	-
SN052_3	IaAB	79	35.1	1187	-	-
SN053_1	IaAB	125.2	82.8	1234	3.77	1.92
SN054_1	IaAB	73.5	82.7	1249	-	-
SN054_2	IaAB	120.3	71.7	1218	5.37	2.56
SN054_3	IaAB	90.1	62.5	1214	3.40	1.69
SN054_4	IaAB	114	74.3	1223	2.94	1.08
SN056_1	IaAB	108.5	34.2	1178	2.44	1.22
SN056_2	IaAB	151.6	41.3	1177	2.62	-
SN059_1	IaAB	19.8	32.8	1222	0.15	0.27
SN063_1	IaAB	86.4	55.3	1207	3.73	3.00
SN063_2	IaAB	78.3	55.9	1211	2.84	2.63
SN063_3	IaAB	170.1	71.1	1207	10.74	6.48
SN064_1	IaAB	90.5	54.4	1205	4.41	3.63
SN064_2	IaAB	68.8	43.8	1201	2.73	1.67
SN064_3	IaAB	65.4	39.8	1198	0.09	0.03
SN064_4	IaAB	125.2	60.1	1203	8.94	3.00
SN065_1	IaAB	174.6	66.3	1201	12.64	3.91
SN065_2	IaAB	365.9	81.7	1203	32.96	2.50
SN065_3	IaAB	104.4	59.4	1207	12.98	3.48

Sample	Type	Total nitrogen (at.ppm)	%B	T[N,1Ga]	Platelet Peak Area (cm-2)	3107 Peak Area (cm-2)
SN066_1	IaAB	111.8	20.8	1160	-	-
SN066_2	IaAB	143.1	20.5	1153	-	0.49
SN066_3	IaAB	62.1	80.5	1250	-	-
SN070_1	IaAB	42	31.9	1200	0.93	0.52
SN070_2	IaAB	49	35.5	1201	0.96	0.55
SN070_3	IaAB	218.2	69.9	1199	2.27	1.25
SN071_1	IaAB	101.7	89.5	1256	-	-
SN071_2	IaAB	35.4	67.8	1247	-	-
SN073_1	IaAB	160.8	81.2	1224	12.68	4.08
SN073_2	IaAB	128.5	76.3	1222	8.52	4.64
SN073_3	IaAB	91.9	69.1	1222	4.37	3.06
SN074_1	IaAB	75.3	55.4	1211	4.14	2.23
SN074_2	IaAB	86.6	57.9	1210	4.73	3.30
SN074_3	IaAB	39.6	76.3	1256	-	-
SN075_1	IaAB	194.7	48.9	1179	7.64	4.33
SN075_2	IaAB	162.3	41.4	1176	3.62	2.67
SN075_3	IaAB	182.8	45.4	1177	3.81	2.67
SN078_1	IaAB	92.5	80.3	1238	0.14	0.15
SN078_2	IaAB	30.4	40.8	1220	0.16	0.79
SN078_3	IaAB	60.9	67.2	1231	0.19	0.22
SN083_1	IaAB	79.5	43.6	1197	2.20	0.71
SN083_2	IaAB	68.7	38.7	1195	1.91	0.67
SN083_3	IaAB	136	46.0	1185	7.29	1.76
SN084_1	IaAB	104.4	59.4	1207	6.89	2.01
SN084_2	IaAB	243	77.4	1207	21.28	1.82

Sample	Type	Total nitrogen (at.ppm)	%B	T[N,1Ga]	Platelet Peak Area (cm-2)	3107 Peak Area (cm-2)
SN084_3	IaAB	77	55.1	1210	4.35	1.53
SN085_1	IaA	23.9	0.0	1101.3	-	-
SN085_2	IaAB	39.3	29.8	1200	-	0.43
SN085_3	IaAB	34.4	20.3	1190	-	0.44
SN086_1	IaAB	695.6	35.3	1133	18.37	1.83
SN086_2	IaAB	117.6	70.0	1216	2.80	4.17
SN086_3	IaAB	128.2	63.4	1206	2.54	3.14
SN088_1	IaAB	81.7	64.6	1219	1.10	0.99
SN088_2	IaAB	77.4	57.9	1213	1.76	-
SN088_3	IaAB	33.8	52.7	1230	1.01	0.78
SN088_4	IaAB	111.3	59.5	1205	5.96	2.17
SN089_1	IaAB	167.8	62.3	1197	3.61	3.67
SN089_2	IaAB	120.3	52.2	1195	3.65	3.97
SN089_3	IaAB	113	59.6	1205	2.57	3.25
SN091_1	IaAB	86.6	67.2	1221	1.61	0.97
SN091_2	IaAB	112.9	63.3	1209	3.50	3.93
SN091_3	IaAB	54.8	51.3	1215	1.57	0.74
SN093_1	IaAB	1179.9	81.5	1172	90.77	-
SN093_2	IaAB	1160	80.9	1171	89.54	-
SN093_3	IaAB	1063.4	79.1	1171	80.43	-
SN094_1	IaAB	134.4	62.1	1203	6.86	2.87
SN094_2	IaAB	184.6	77.5	1214	16.90	5.09
SN094_3	IaAB	241.7	78.1	1208	15.82	2.77
SN095_1	IaAB	144.1	80.2	1226	2.04	0.54
SN096_1	IaAB	74.3	55.0	1211	6.29	1.14

Sample	Type	Total nitrogen (at.ppm)	%B	T[N,1Ga]	Platelet Peak Area (cm-2)	3107 Peak Area (cm-2)
SN096_2	IaAB	91.7	62.6	1214	6.46	1.29
SN096_3	IaAB	80.8	57.2	1211	4.94	0.92
SN097_1	IaAB	89.7	23.2	1169	2.67	0.91
SN097_2	IaAB	183	34.0	1165	5.74	1.54
SN097_3	IaAB	177.5	28.3	1159	6.07	1.60
SN098_1	IaAB	238.5	72.8	1201	19.99	1.89
SN098_2	IaAB	201.2	68.1	1199	15.03	1.84
SN098_3	IaAB	321.9	80.7	1205	23.50	1.79
SN099_1	IaAB	109.7	77.2	1228	0.29	-
SN099_2	IaAB	38	51.8	1226	0.30	-
SN099_3	IaAB	58.1	62.7	1226	-	-
SN100_1	IaAB	72.9	71.7	1232	0.56	-
SN100_2	IaAB	87.2	45.0	1196	0.71	0.43
SN102_1	IaAB	83.6	55.0	1208	4.65	2.10
SN102_2	IaAB	92.1	58.0	1208	6.20	1.98
SN102_3	IaAB	47.6	48.9	1216	2.71	1.22
SN104_1	IaAB	170.2	14.2	1138	-	0.68
SN104_2	IaAB	203.7	22.8	1148	-	0.55
SN104_3	IaAB	242.7	32.2	1155	-	0.44
SN107_1	IaAB	1187.6	67.0	1152	3.51	1.05
SN107_2	IaAB	1014.2	64.7	1153	45.74	1.30
SN107_3	IaAB	357.1	41.6	1156	23.45	1.83
SN108_1	IaAB	1051.8	56.9	1144	45.55	-
SN108_2	IaAB	814.9	51.8	1145	35.16	-
SN108_3	IaAB	861.4	52.2	1144	39.55	-

Sample	Type	Total nitrogen (at.ppm)	%B	T[N,1Ga]	Platelet Peak Area (cm-2)	3107 Peak Area (cm-2)
SN109_1	IaAB	11.7	30.8	1234	-	-
SN109_2	IaAB	23.6	63.6	1253	-	-
SN109_3	IaAB	13.6	50.7	1254	-	-
SN111_1	IaAB	26.6	53.4	1237	0.22	-
SN111_2	IaAB	54.7	80.6	1254	0.18	-
SN113_1	IaAB	689.3	57.0	1155	37.30	0.45
SN113_2	IaAB	660.5	62.9	1162	34.90	0.43
SN113_3	IaAB	620.6	61.3	1162	33.18	0.53
SN114_1	IaAB	240.9	76.8	1206	19.98	1.92
SN114_2	IaAB	238.4	77.3	1207	14.78	3.49
SN115_1	IaAB	41	60.7	1234	0.85	-
SN115_2	IaAB	38.4	54.4	1228	0.86	-
SN116_1	IaAB	381	83.9	1206	36.39	4.21
SN116_2	IaAB	474.8	88.2	1210	43.33	3.26
SN116_3	IaAB	400.9	86.5	1210	39.17	2.76
SN117_1	IaAB	219.6	62.6	1190	14.91	2.83
SN117_2	IaAB	226.8	62.8	1190	15.58	2.79
SN117_3	IaAB	228	62.9	1190	15.23	2.66
SN118_1	IaAB	37.7	21.0	1188	0.76	0.76
SN118_2	IaAB	50.7	40.2	1205	0.79	0.82
SN120_1	IaAB	385.6	29.6	1141	13.18	0.38
SN120_2	IaAB	370.3	26.4	1138	12.86	0.34
SN120_3	IaAB	374.7	27.1	1138	13.54	0.40
SN121_1	IaAB	46.6	29.6	1195	-	-
SN121_2	IaAB	62.1	15.9	1167	-	-

Sample	Type	Total nitrogen (at.ppm)	%B	T[N,1Ga]	Platelet Peak Area (cm-2)	3107 Peak Area (cm-2)
SN121_3	IaAB	26.8	30.2	1210	-	-
SN122_1	IaAB	119.7	58.8	1202	7.58	1.30
SN122_2	IaAB	167.2	70.6	1207	13.21	1.16
SN122_3	IaAB	126.4	61.6	1204	9.24	1.14
SN125_1	IaAB	324.9	52.9	1170	13.56	6.15
SN127_1	IaAB	91.3	53.8	1204	0.71	-
SN127_2	IaAB	241.9	64.2	1190	1.35	-
SN128_1	IaAB	51	51.2	1217	3.92	2.30
SN128_2	IaAB	94.3	69.5	1221	0.25	0.08
SN128_3	IaAB	47.4	57.2	1226	3.02	1.76
SN129_1	IaA	364.8	7.0	1101	3.06	0.67
SN129_2	IaAB	364.3	19.8	1129	6.13	0.63
SN129_3	IaAB	373.1	21.5	1131	6.13	0.55
SN130_1	IaAB	186.4	80.5	1219	11.08	4.27
SN130_2	IaAB	144.6	70.4	1211	11.33	4.42
SN130_3	IaAB	162.6	78.2	1219	10.18	4.56
SN131_1	IaAB	43.8	69.6	1243	0.36	0.27
SN131_2	IaAB	20.9	50.2	1241	0.16	-
SN131_3	IaAB	31.1	60.5	1241	0.14	-
SN132_1	IaAB	123.5	33.7	1174	-	-
SN132_2	IaAB	9	12.2	1209	-	-
SN132_3	IaAB	263.1	26.6	1147	-	2.08
SN133_1	IaAB	169.9	63.2	1198	10.41	0.86
SN133_2	IaAB	181.5	66.2	1200	8.43	1.00
SN133_3	IaAB	160.4	61.8	1198	10.61	0.83

Sample	Type	Total nitrogen (at.ppm)	%B	T[N,1Ga]	Platelet Peak Area (cm-2)	3107 Peak Area (cm-2)
SN134_1	IaAB	101.7	68.3	1218	7.44	4.67
SN134_2	IaAB	75.3	68.7	1227	5.14	2.78
SN134_3	II	0	-	-	-	-
SN135_1	IaAB	217.3	72.3	1202	13.05	4.08
SN135_2	IaAB	182.1	67.1	1201	11.96	3.48
SN135_3	IaAB	145.2	60.9	1199	9.62	3.20
SN136_1	II	0	-	-	-	-
SN136_2	II	0	-	-	-	-
SN138_1	IaAB	27	25.9	1204	-	1.27
SN138_2	IaAB	29.1	38.8	1219	-	1.82
SN138_3	IaAB	62.8	80.4	1249	-	3.21
SN140_1	IaAB	69.1	60.3	1219	0.84	0.45
SN140_2	IaAB	120.2	68.4	1213	1.50	0.80
SN140_3	IaAB	74.3	66.1	1224	0.85	0.86
SN142_1	IaAB	76.9	70.5	1228	2.63	1.22
SN142_2	IaAB	91.2	62.5	1214	6.00	1.63
SN143_1	IaAB	90.6	41.7	1191	-	-
SN144_1	IaAB	112.6	68.9	1216	3.83	1.22
SN144_2	IaAB	129.6	64.9	1207	3.17	0.97
SN144_3	IaAB	60.1	57.4	1219	3.02	0.86
SN146_1	IaAB	90.5	20.0	1164	-	-
SN146_2	IaA	79.8	0.0	1074	-	0.60
SN146_3	IaAB	7.4	21.6	1233	-	-
SN147_1	IaAB	83	69.6	1225	1.73	1.00
SN147_2	IaAB	47	45.1	1213	3.85	2.32

Appendix C

SIMS results on Snap Lake diamond fragments

Spot Name	$\delta^{13}C$ (VPDB)	[N] at ppm	$\delta^{15}N$ (air)
SN001@1	-4.73	583.0	-3.69
SN001@2	-4.76	323.8	-3.79
SN001@3	-4.80	555.8	-3.54
SN001@4	-4.71	529.5	-3.40
SN004@1	-4.31	64.2	1.64
SN004@2	-4.44	395.7	-4.26
SN004@3	-4.25	555.8	-4.48
SN004@4	-4.26	389.2	-4.66
SN004@5	-4.37	306.7	-1.70
SN005@1	-6.23	1866.9	-1.44
SN005@2	-4.08	647.1	6.53
SN005@3	-4.36	910.8	1.68
SN005@4	-5.00	889.9	-1.49
SN008@1	-4.57	254.5	
SN008@2	-4.63	47.4	
SN008@3	-4.75	24.2	
SN008@4		517.1	-0.58
SN010@1	-3.87	147.1	0.97
SN010@2	-3.78	82.5	1.88
SN010@3	-4.26	7.5	
SN010@4	-3.98	20.8	
SN012@1	-6.46	52.2	
SN012@2	-6.18	52.0	
SN012@3	-4.27	41.7	
SN012@4	-4.62	345.3	4.63
SN014@1	-5.97	778.1	-4.19
SN014@2	-6.03	796.3	-4.96
SN019@1	-4.79	264.9	3.79
SN019@2	-4.85	260.4	3.51
SN019@3	-4.91	109.3	5.98
SN019@4	-4.75	136.4	3.27
SN020@1	-3.52	4.7	
SN020@2	-3.63	5.4	
SN020@3	-3.74	7.4	
SN021@1	-3.69	230.0	-12.81
SN021@2	-3.88	232.6	-14.53
SN021@3	-3.94	125.1	-11.34
SN022@1	-3.81	46.3	
SN022@2	-4.05	16.0	
SN022@3	-4.10	16.1	
SN024@1	-4.29	397.2	-10.16
SN024@2	-4.45	22.0	
SN024@3	-4.94	1200.6	-11.61
SN024@4	-4.83	620.8	-11.14
SN025@1	-4.73	404.7	2.43
SN025@2	-5.15	20.1	
SN025@3	-4.61	275.7	-0.79
SN025@4	-4.34	489.9	2.14

Spot Name	$\delta^{13}C$ (VPDB)	[N] at ppm	$\delta^{15}N$ (air)
SN026@1	-4.96	16.4	
SN026@2	-4.05	21.6	
SN026@3	-2.98	26.4	
SN030@1	-7.78	2381.9	-1.51
SN030@2	-3.59	49.4	
SN030@3	-4.23	28.9	
SN033@1	-5.23	114.0	10.89
SN033@2	-4.86	234.8	3.71
SN033@3	-5.59	576.1	6.12
SN036@1	-5.82	53.6	
SN036@2	-5.90	7.2	
SN036@3	-6.00	233.9	0.98
SN041@1	-3.77	13.2	
SN041@2	-4.05	22.5	
SN041@3	-3.60	16.0	
SN045@1	-4.12	28.7	
SN045@2	-3.87	26.0	
SN045@3	-3.83	31.2	
SN045@4	-4.05	32.4	
SN046@1	-3.99	13.0	
SN046@2	-4.14	11.0	
SN046@3	-4.16	11.7	
SN047@1	-1.76	753.3	-4.55
SN047@2	-2.14	376.8	-2.00
SN047@3	-2.10	733.9	-3.94
SN047@4	-2.09	744.1	-4.04
SN048@1	-4.30	999.6	-7.78
SN048@2	-4.30	1026.9	-6.97
SN048@3	-4.27	773.1	-7.63
SN049@1	-4.42	14.9	
SN049@2	-4.60	15.7	
SN049@3	-4.52	12.8	
SN050@1	-4.34	20.6	
SN050@2	-4.60	7.5	
SN050@3	-4.41	12.4	
SN050@4	-4.46	5.2	
SN051@1	-4.49	67.6	-1.63
SN051@2	-4.60	141.7	-9.32
SN051@3	-4.63	2.6	
SN052@1	-4.17	38.7	
SN052@2	-4.11	39.3	
SN052@3	-4.21	37.2	
SN053@1	-4.04	10.2	
SN053@2	-4.05	4.3	
SN053@3	-4.14	4.2	
SN054@1	-4.52	9.9	
SN054@2	-4.45	10.3	
SN054@3	-4.58	12.3	

Spot Name	$\delta^{13}C$ (VPDB)	[N] at ppm	$\delta^{15}N$ (air)
SN056@1	-4.39	179.1	7.44
SN056@2	-4.19	70.1	1.57
SN056@3	-4.36	41.5	
SN059@1	-3.16	22.1	
SN059@2	-3.36	24.7	
SN059@3	-3.87	19.0	
SN063@1	-3.84	10.5	
SN063@2	-3.76	10.2	
SN063@3	-3.95	9.5	
SN064@1	-5.83	50.9	
SN064@2	-5.80	41.9	
SN064@3	-5.93	44.9	
SN065@1	-3.79	212.3	-1.85
SN065@2	-3.94	312.1	-1.81
SN065@3	-3.77	298.6	-1.52
SN066@1	-3.86	17.9	
SN066@2	-4.06	16.6	
SN066@3	-3.80	12.4	
SN070@1	-4.87	10.2	
SN070@2	-4.93	9.9	
SN070@3	-4.64	11.7	
SN071@1	-4.25	609.2	-4.47
SN071@2	-4.40	1716.7	-6.89
SN071@3	-4.14	86.5	4.39
SN073@1	-4.23	92.2	-13.13
SN073@2	-4.25	3.0	
SN073@3	-4.04	10.1	
SN074@1	-6.35	239.8	
SN074@2	-5.56	45.7	
SN074@3	-4.92	60.2	-1.89
SN075@1	-3.26	2689.2	-2.42
SN075@2	-3.27	2607.0	-2.15
SN075@3	-3.12	2601.4	-2.19
SN078@1	-3.99	74.3	5.01
SN078@2	-3.80	69.2	6.08
SN078@3	-3.81	15.0	
SN078@4	-3.75	84.2	6.68
SN083@1	-4.19	24.5	
SN083@2	-4.72	135.6	-1.05
SN083@3	-7.95	120.3	7.17
SN083@4	-7.83	27.3	
SN083@5	-7.86	84.5	5.87
SN084@1	-3.75	18.9	
SN084@2	-3.52	18.7	
SN084@3	-3.65	18.5	
SN085@1	-3.98	10.0	
SN085@2	-4.09	12.0	
SN086@1	-5.17	485.5	3.12

Spot Name	$\delta^{13}C$ (VPDB)	[N] at ppm	$\delta^{15}N$ (air)
SN086@2	-5.24	915.8	1.61
SN086@3	-5.25	843.3	3.97
SN088@1	-5.43	33.9	
SN088@2	-5.48	33.0	
SN088@3	-2.86	415.4	10.76
SN089@1	-4.12	953.5	-9.81
SN089@2	-2.87	848.9	-12.92
SN089@3	-3.32	843.5	-14.88
SN089@4	-3.39	855.2	-15.36
SN091@1	-3.04	74.5	7.25
SN091@2	-2.97	72.6	3.71
SN091@3	-2.93	83.4	5.31
SN093@1	-5.22	0.7	
SN093@2		2203.2	-0.72
SN093@3	-5.27	91.0	1.85
SN093@4	-5.36	813.4	-1.11
SN094@1	-4.18	3.1	
SN094@2	-4.03	99.0	-9.28
SN094@3	-4.05	142.5	-11.80
SN095@1		28.7	
SN095@2	-3.45	24.6	
SN095@3	-3.54	39.6	
SN096@1	-4.60	32.7	
SN096@2	-4.42	126.1	-10.59
SN096@3	-4.26	40.0	
SN097@1	-5.12	874.0	-4.19
SN097@2	-4.41	409.8	-3.10
SN097@3	-5.39	13.8	
SN098@1	-4.15	23.2	
SN098@2	-4.24	69.5	
SN098@3	-4.45	9.2	
SN099@1	-4.08	15.6	
SN099@2	-4.41	15.5	
SN099@3	-4.33	20.9	
SN100@1	-4.80	26.6	
SN100@2	-4.34	28.6	
SN100@3	-4.39	215.7	-16.22
SN102@1	-4.05	5.5	
SN102@2	-4.01	21.1	
SN102@3	-4.10	130.5	-19.57
SN102@4	-4.08	9.8	
SN104@1	-1.35	1001.4	-10.33
SN104@2	-1.40	1047.3	-9.57
SN104@3	-1.32	1051.3	-9.98
SN108@1	-3.64	882.9	-2.94
SN108@2	-3.91	661.0	-2.73
SN108@3	-3.66	36.0	
SN109@1	-4.26	7.4	

Spot Name	$\delta^{13}C$ (VPDB)	[N] at ppm	$\delta^{15}N$ (air)
SN109@2	-4.48	8.2	
SN109@3	-4.62	15.9	
SN111@1	-3.91	6.0	
SN111@2	-3.95	7.2	
SN111@3	-4.27	8.4	
SN113@1	-4.82	4.9	
SN113@2	-4.78	15.6	
SN113@3	-4.69	19.9	
SN114@1	-4.38	323.4	0.57
SN114@2	-4.11	102.5	1.23
SN114@3	-4.18	134.6	0.98
SN115@1	-3.80	15.4	
SN115@2	-3.55	157.9	-0.91
SN115@3	-3.49	14.0	
SN116@1	-3.84	45.0	
SN116@2	-4.01	7.6	
SN116@3	-4.12	5.1	
SN117@1	-4.39	30.9	
SN117@2	-4.36	85.6	-2.95
SN117@3	-4.47	225.0	-5.41
SN118@1	-4.11	3.5	
SN118@2	-4.13	367.0	-8.48
SN118@3	-4.06	515.6	-9.10
SN120@1	-5.28	480.1	2.83
SN120@2	-5.44	735.3	3.66
SN120@3	-5.50	616.9	2.62
SN120@4	-5.63	634.7	3.71
SN121@1	-4.52	26.9	
SN121@2	-4.34	52.1	
SN121@3	-3.06	29.6	
SN122@1	-4.03	10.9	
SN122@2	-3.92	109.8	5.52
SN122@3	-3.96	10.9	
SN125@1	-5.31	53.0	
SN125@2	-5.00	147.7	1.49
SN125@3	-5.29	294.7	-0.31
SN127@1	-3.69	18.1	
SN127@2	-3.96	11.7	
SN127@3	-3.88	15.2	
SN128@1	-3.99	4.5	
SN128@2	-3.94	0.7	
SN129@1	-4.16	358.9	-0.03
SN129@2	-5.18	393.6	4.41
SN129@3	-5.65	20.2	
SN129@4	-4.94	296.6	-0.02
SN130@1	-4.20	270.4	-14.91
SN130@2	-4.04	261.0	-16.47
SN130@3	-4.16	1.0	

Spot Name	$\delta^{13}C$ (VPDB)	[N] at ppm	$\delta^{15}N$ (air)
SN131@1	-3.42	15.0	
SN131@2	-2.50	14.7	
SN131@3	-3.61	19.0	
SN132@1	-3.78	4.0	
SN132@2	-3.77	143.1	-6.09
SN132@3	-3.38	19.1	
SN133@1	-3.55	165.9	-17.99
SN133@2	-3.52	145.1	-17.99
SN133@3	-3.48	61.7	-19.04
SN133@4	-3.50	57.6	-15.75
SN134@1	-5.58	1.2	
SN134@2	-5.54	3.6	
SN134@3	-5.50	24.5	
SN135@1	-2.98	58.7	
SN135@2	-3.29	59.2	
SN135@3	-3.27	53.0	
SN136@1	-3.85	5.6	
SN136@2	-3.94	8.2	
SN136@3	-3.93	5.6	
SN138@1	-3.59	10.8	
SN138@2	-3.54	30.1	
SN138@3	-3.68	4.7	
SN140@1	-5.66	10.7	
SN140@2	-5.42	19.2	
SN140@3	-5.47	24.5	
SN142@1	-4.03	11.7	
SN142@2	-4.09	10.1	
SN142@3	-4.17	9.0	
SN143@1	-4.36	12.9	
SN143@2	-3.88	4.1	
SN143@3	-3.45	0.7	
SN144@1	-4.31	5.6	
SN144@2	-4.27	7.1	
SN144@3	-4.18	4.1	
SN146@1	-4.11	65.5	
SN146@2	-4.20	7.6	
SN146@3	-3.90	3.7	
SN146@4	-4.27	12.0	
SN147@1	-3.95	41.8	
SN147@2	-4.09	27.7	
SN147@3	-4.29	331.3	-12.73

Appendix D

Major element chemistry for inclusions recovered from Snap Lake diamonds

Mineral	Garnet															
Sample	SN001A	SN001B	SN001C	SN001D	SN005A	SN012A	SN012B	SN024A	SN024B	SN025A	SN026A	SN026B	SN027A	SN027B	SN036A	SN041A
Paragenesis	E	E	E	E	E	H	H	H	H	H	L	L	H	H	L	L
Assemblage	Grt	Grt	Grt	Grt	Grt	Grt	Grt	Grt	Grt	Grt	Grt, Ol	Grt, Ol	Grt, Ol	Grt, Ol	Grt, Ol	Grt, Cpx
SiO_2	39.12	39.31	39.84	39.28	41.61	41.93	42.37	41.33	40.60	41.48	41.53	41.55	42.61	41.06	40.91	41.42
TiO_2	0.71	0.70	0.71	0.70	0.36	0.06	0.19	0.08	0.09	0.02	0.05	0.05	0.17	0.08	0.30	0.00
Al_2O_3	21.11	20.97	21.23	21.04	22.93	16.71	19.44	14.99	14.85	15.10	17.33	17.52	19.59	14.92	14.95	18.73
V_2O_3	0.06	0.06	0.06	0.06	0.02	0.06	0.04	0.05	0.05	0.03	0.04	0.06	0.01	0.05	0.05	0.06
Cr_2O_3	0.05	0.05	0.06	0.05	0.06	9.32	6.24	11.59	11.62	11.90	7.94	7.94	6.27	11.66	11.62	6.51
FeO	18.23	18.45	18.41	18.40	14.55	6.02	4.85	5.96	5.94	5.59	6.06	6.11	4.54	5.96	5.21	6.30
NiO	0.00	0.00	0.00	0.00	0.00	0.01	0.00	0.01	0.01	0.00	0.02	0.01	0.01	0.01	0.00	0.02
MnO	0.45	0.45	0.45	0.45	0.32	0.28	0.21	0.30	0.30	0.29	0.27	0.28	0.19	0.30	0.28	0.28
MgO	7.75	7.74	7.86	7.68	16.26	21.84	23.98	20.33	19.83	23.29	20.68	20.84	24.68	20.18	19.98	20.14
CaO	11.89	12.01	11.91	11.95	4.46	4.07	2.57	5.74	5.71	1.91	5.52	5.46	2.10	5.76	6.59	5.99
Na_2O	0.17	0.17	0.19	0.15	0.10	0.00	0.00	0.00	0.00	0.00	0.00	0.00	0.00	0.00	0.05	0.00
K_2O	0.00	0.00	0.01	0.00	0.00	0.00	0.00	0.00	0.00	0.00	0.00	0.00	0.00	0.00	0.01	0.00
P_2O_5	0.02	0.02	0.03	0.03	0.03	0.01	0.02	0.02	0.01	0.00	0.01	0.01	0.00	0.03	0.04	0.01
Total	99.56	99.94	100.76	99.80	100.67	100.30	99.90	100.41	99.01	99.62	99.46	99.83	100.17	100.00	99.99	99.46
Si	2.98	2.99	3.00	2.99	3.01	3.01	3.00	3.01	3.00	3.01	3.01	3.00	3.00	3.00	2.99	2.99
Ti	0.04	0.04	0.04	0.04	0.02	0.00	0.01	0.00	0.00	0.00	0.00	0.00	0.01	0.00	0.02	0.00
Al	1.90	1.88	1.89	1.89	1.95	1.42	1.62	1.29	1.29	1.29	1.48	1.49	1.62	1.28	1.29	1.60
V	0.00	0.00	0.00	0.00	0.00	0.00	0.00	0.00	0.00	0.00	0.00	0.00	0.00	0.00	0.00	0.00
Cr	0.00	0.00	0.00	0.00	0.00	0.53	0.35	0.67	0.68	0.68	0.46	0.45	0.35	0.67	0.67	0.37
Fe2+	1.16	1.17	1.16	1.17	0.89	0.36	0.29	0.36	0.37	0.34	0.37	0.37	0.27	0.36	0.32	0.38
Ni	0.00	0.00	0.00	0.00	0.00	0.00	0.00	0.00	0.00	0.00	0.00	0.00	0.00	0.00	0.00	0.00
Mn	0.03	0.03	0.03	0.03	0.02	0.02	0.01	0.02	0.02	0.02	0.02	0.02	0.01	0.02	0.02	0.02
Mg	0.88	0.88	0.88	0.87	1.75	2.34	2.53	2.20	2.18	2.52	2.23	2.24	2.59	2.20	2.17	2.17
Ca	0.97	0.98	0.96	0.98	0.35	0.31	0.20	0.45	0.45	0.15	0.43	0.42	0.16	0.45	0.52	0.46
Na	0.02	0.03	0.03	0.02	0.01	0.00	0.00	0.00	0.00	0.00	0.00	0.00	0.00	0.00	0.01	0.00
K	0.00	0.00	0.00	0.00	0.00	0.00	0.00	0.00	0.00	0.00	0.00	0.00	0.00	0.00	0.00	0.00
P	0.00	0.00	0.00	0.00	0.00	0.00	0.00	0.00	0.00	0.00	0.00	0.00	0.00	0.00	0.00	0.00
Total Cations	8.0	8.0	8.0	8.0	8.0	8.0	8.0	8.0	8.0	8.0	8.0	8.0	8.0	8.0	8.0	8.0
Oxygen	12.0	12.0	12.0	12.0	12.0	12.0	12.0	12.0	12.0	12.0	12.0	12.0	12.0	12.0	12.0	12.0
Mg#	43.1	42.8	43.2	42.7	66.4	86.6	89.8	85.9	85.6	88.1	85.9	85.9	90.7	85.8	87.2	85.1

Mineral	Garnet															
Sample	SN041C	SN049A	SN050A	SN052A	SN052B	SN053	SN054D	SN096A	SN097A	SN108A	SN116C	SN118A	SN118B	SN130A	SN132A	SN132B
Paragenesis	H	H	L	H	H	H	H	H	H	H	H	L	H	H	H	H
Assemblage	Grt, Cpx	Grt	Grt	Grt, Ol	Grt, Ol	Grt	Grt, Ol	Grt, Ol	Sul, Grt, Co	Grt	Grt, Ol	Grt, Ol	Grt, Ol	Grt	Grt, Opx	Grt, Opx
SiO_2	41.24	42.15	40.39	41.95	42.08	42.06	41.64	41.68	41.31	40.67	41.41	41.87	41.43	41.49	41.50	41.26
TiO_2	0.08	0.04	0.32	0.00	0.00	0.03	0.08	0.16	0.06	0.00	0.02	0.00	0.09	0.05	0.01	0.06
Al_2O_3	17.24	18.27	13.15	18.66	18.42	17.65	17.82	17.06	16.76	15.07	16.85	18.92	16.64	18.00	18.34	16.48
V_2O_3	0.05	0.04	0.06	0.04	0.05	0.05	0.04	0.05	0.08	0.06	0.06	0.06	0.05	0.05	0.04	0.07
Cr_2O_3	9.05	7.11	13.29	8.01	7.84	7.91	8.18	8.88	8.91	11.88	8.95	6.49	8.77	7.94	6.89	9.42
FeO	6.26	6.15	6.79	5.64	5.56	6.18	5.80	6.05	6.11	6.01	6.06	6.30	6.88	6.15	6.08	6.11
NiO	0.00	0.01	0.00	0.00	0.01	0.00	0.00	0.00	0.01	0.00	0.00	0.01	0.01	0.01	0.00	0.01
MnO	0.29	0.29	0.35	0.28	0.29	0.28	0.30	0.29	0.29	0.33	0.28	0.29	0.31	0.28	0.28	0.29
MgO	20.84	22.34	17.83	23.06	23.27	21.94	23.80	21.35	21.25	20.41	21.68	20.42	20.77	21.39	21.44	21.55
CaO	4.70	3.74	7.88	2.76	2.72	4.13	1.38	4.69	4.51	4.82	4.02	5.92	4.63	4.47	4.48	4.08
Na_2O	0.00	0.00	0.00	0.00	0.00	0.00	0.00	0.00	0.02	0.00	0.00	0.00	0.00	0.00	0.00	0.00
K_2O	0.00	0.00	0.00	0.00	0.00	0.00	0.00	0.00	0.01	0.00	0.00	0.00	0.00	0.00	0.00	0.00
P_2O_5	0.02	0.01	0.02	0.00	0.00	0.01	0.00	0.02	0.03	0.00	0.03	0.01	0.01	0.02	0.00	0.00
Total	99.78	100.14	100.07	100.41	100.23	100.24	99.01	100.23	99.34	99.25	99.35	100.29	99.58	99.86	99.03	99.32
Si	2.99	3.01	3.00	2.98	2.99	3.01	2.99	3.00	3.00	2.99	3.00	3.00	3.01	2.99	3.00	3.00
Ti	0.00	0.00	0.02	0.00	0.00	0.00	0.01	0.01	0.00	0.00	0.00	0.00	0.00	0.00	0.00	0.00
Al	1.47	1.54	1.15	1.56	1.54	1.49	1.51	1.45	1.43	1.31	1.44	1.60	1.43	1.53	1.56	1.41
V	0.00	0.00	0.00	0.00	0.00	0.00	0.00	0.00	0.00	0.00	0.00	0.00	0.00	0.00	0.00	0.00
Cr	0.52	0.40	0.78	0.45	0.44	0.45	0.47	0.51	0.51	0.69	0.51	0.37	0.50	0.45	0.39	0.54
Fe2+	0.38	0.37	0.42	0.34	0.33	0.37	0.35	0.36	0.37	0.37	0.37	0.38	0.42	0.37	0.37	0.37
Ni	0.00	0.00	0.00	0.00	0.00	0.00	0.00	0.00	0.00	0.00	0.00	0.00	0.00	0.00	0.00	0.00
Mn	0.02	0.02	0.02	0.02	0.02	0.02	0.02	0.02	0.02	0.02	0.02	0.02	0.02	0.02	0.02	0.02
Mg	2.25	2.38	1.97	2.44	2.47	2.34	2.55	2.29	2.30	2.24	2.34	2.18	2.25	2.30	2.31	2.33
Ca	0.37	0.29	0.63	0.21	0.21	0.32	0.11	0.36	0.35	0.38	0.31	0.45	0.36	0.34	0.35	0.32
Na	0.00	0.00	0.00	0.00	0.00	0.00	0.00	0.00	0.00	0.00	0.00	0.00	0.00	0.00	0.00	0.00
K	0.00	0.00	0.00	0.00	0.00	0.00	0.00	0.00	0.00	0.00	0.00	0.00	0.00	0.00	0.00	0.00
P	0.00	0.00	0.00	0.00	0.00	0.00	0.00	0.00	0.00	0.00	0.00	0.00	0.00	0.00	0.00	0.00
Total Cations	8.0	8.0	8.0	8.0	8.0	8.0	8.0	8.0	8.0	8.0	8.0	8.0	8.0	8.0	8.0	8.0
Oxygen	12.0	12.0	12.0	12.0	12.0	12.0	12.0	12.0	12.0	12.0	12.0	12.0	12.0	12.0	12.0	12.0
Mg#	85.6	86.6	82.4	87.9	88.2	86.3	88.0	86.3	86.1	85.8	86.5	85.2	84.3	86.1	86.3	86.3

Mineral	Olivine															
Sample	SN014B	SN014C	SN020A	SN021A	SN022D	SN026C	SN026D	SN027C	SN033A	SN036B	SN051A	SN052D	SN052E	SN052F	SN052G	SN054A
Paragenesis	P	P	P	P	P	L	L	H	P	L	P	H	H	H	H	H
Assemblage	Ol	Ol	Ol	Ol	Ol, Epi	Grt, Ol	Grt, Ol	Grt, Ol	Sul, Ol	Grt, Ol	Ol	Grt, Ol	Grt, Ol	Grt, Ol	Grt, Ol	Grt, Ol
SiO_2	41.41	41.36	41.14	41.29	41.04	41.02	41.22	40.81	41.00	41.41	40.94	41.14	40.91	41.21	41.44	41.12
TiO_2	0.00	0.00	0.00	0.00	0.00	0.00	0.00	0.00	0.00	0.00	0.00	0.00	0.00	0.00	0.00	0.00
Al_2O_3	0.00	0.00	0.00	0.00	0.00	0.00	0.00	0.00	0.00	0.00	0.00	0.00	0.00	0.00	0.00	0.00
V_2O_3	0.00	0.01	0.00	0.00	0.00	0.00	0.00	0.00	0.00	0.00	0.01	0.00	0.00	0.00	0.00	0.00
Cr_2O_3	0.03	0.04	0.02	0.03	0.07	0.01	0.02	0.01	0.00	0.08	0.03	0.02	0.01	0.00	0.01	0.03
FeO	6.55	6.69	7.70	8.22	7.55	7.64	7.71	7.88	7.17	6.10	7.39	6.54	6.61	6.41	6.40	7.73
NiO	0.32	0.32	0.39	0.39	0.40	0.38	0.38	0.39	0.38	0.32	0.39	0.36	0.34	0.33	0.34	0.39
MnO	0.09	0.09	0.11	0.11	0.10	0.11	0.11	0.11	0.10	0.09	0.11	0.08	0.10	0.10	0.09	0.10
MgO	51.59	51.21	50.80	50.34	50.42	50.32	50.66	50.23	50.43	52.03	50.47	51.50	51.26	51.54	51.80	50.36
CaO	0.03	0.02	0.02	0.03	0.11	0.03	0.02	0.03	0.02	0.02	0.01	0.00	0.00	0.01	0.02	0.02
Na_2O	0.00	0.00	0.00	0.00	0.00	0.00	0.00	0.00	0.00	0.00	0.00	0.00	0.00	0.00	0.00	0.00
K_2O	0.00	0.00	0.00	0.00	0.00	0.00	0.00	0.00	0.01	0.00	0.00	0.00	0.00	0.00	0.00	0.01
P_2O_5	0.01	0.00	0.00	0.00	0.00	0.00	0.00	0.00	0.00	0.00	0.00	0.00	0.00	0.00	0.00	0.00
Total	100.02	99.72	100.17	100.42	99.68	99.52	100.11	99.46	99.11	100.06	99.34	99.63	99.24	99.59	100.10	99.75
Si	1.00	1.00	1.00	1.00	1.00	1.00	1.00	1.00	1.00	1.00	1.00	1.00	1.00	1.00	1.00	1.00
Ti	0.00	0.00	0.00	0.00	0.00	0.00	0.00	0.00	0.00	0.00	0.00	0.00	0.00	0.00	0.00	0.00
Al	0.00	0.00	0.00	0.00	0.00	0.00	0.00	0.00	0.00	0.00	0.00	0.00	0.00	0.00	0.00	0.00
V	0.00	0.00	0.00	0.00	0.00	0.00	0.00	0.00	0.00	0.00	0.00	0.00	0.00	0.00	0.00	0.00
Cr	0.00	0.00	0.00	0.00	0.00	0.00	0.00	0.00	0.00	0.00	0.00	0.00	0.00	0.00	0.00	0.00
Fe2+	0.13	0.14	0.16	0.17	0.15	0.16	0.16	0.16	0.15	0.12	0.15	0.13	0.13	0.13	0.13	0.16
Ni	0.01	0.01	0.01	0.01	0.01	0.01	0.01	0.01	0.01	0.01	0.01	0.01	0.01	0.01	0.01	0.01
Mn	0.00	0.00	0.00	0.00	0.00	0.00	0.00	0.00	0.00	0.00	0.00	0.00	0.00	0.00	0.00	0.00
Mg	1.86	1.85	1.84	1.82	1.83	1.83	1.83	1.83	1.84	1.87	1.84	1.86	1.86	1.86	1.86	1.83
Ca	0.00	0.00	0.00	0.00	0.00	0.00	0.00	0.00	0.00	0.00	0.00	0.00	0.00	0.00	0.00	0.00
Na	0.00	0.00	0.00	0.00	0.00	0.00	0.00	0.00	0.00	0.00	0.00	0.00	0.00	0.00	0.00	0.00
K	0.00	0.00	0.00	0.00	0.00	0.00	0.00	0.00	0.00	0.00	0.00	0.00	0.00	0.00	0.00	0.00
P	0.00	0.00	0.00	0.00	0.00	0.00	0.00	0.00	0.00	0.00	0.00	0.00	0.00	0.00	0.00	0.00
Total Cations	3.0	3.0	3.0	3.0	3.0	3.0	3.0	3.0	3.0	3.0	3.0	3.0	3.0	3.0	3.0	3.0
Oxygen	4.0	4.0	4.0	4.0	4.0	4.0	4.0	4.0	4.0	4.0	4.0	4.0	4.0	4.0	4.0	4.0
Mg#	93.4	93.2	92.2	91.6	92.2	92.2	92.1	91.9	92.6	93.8	92.4	93.3	93.3	93.5	93.5	92.1

Mineral	Olivine															
Sample	SN054B	SN054C	SN059B	SN059C	SN063A	SN063B	SN063C	SN065A	SN065D	SN066A	SN066B	SN066D	SN070A	SN070B	SN070C	SN070D
Paragenesis	H	H	P	P	P	P	P	P	P	P	P	P	P	P	P	P
Assemblage	Grt, Ol	Grt, Ol	Ol	Ol	Ol	Ol	Ol	Ol	Ol	Ol	Ol	Ol	Ol	Ol	Ol	Ol
SiO_2	41.14	41.16	40.97	40.80	40.94	41.32	41.35	41.49	41.49	41.23	41.47	41.30	41.15	41.00	41.30	41.03
TiO_2	0.00	0.00	0.00	0.00	0.00	0.00	0.00	0.00	0.00	0.00	0.00	0.00	0.00	0.00	0.00	0.00
Al_2O_3	0.00	0.00	0.00	0.00	0.00	0.00	0.00	0.00	0.00	0.00	0.00	0.00	0.00	0.00	0.00	0.00
V_2O_3	0.00	0.00	0.00	0.00	0.00	0.00	0.01	0.00	0.00	0.00	0.00	0.00	0.00	0.00	0.00	0.00
Cr_2O_3	0.02	0.03	0.00	0.01	0.04	0.02	0.01	0.02	0.02	0.03	0.01	0.00	0.02	0.00	0.03	0.02
FeO	7.50	7.76	7.74	7.64	7.30	7.32	7.29	7.21	7.21	7.05	7.02	6.93	7.93	8.00	7.96	7.82
NiO	0.40	0.39	0.41	0.38	0.39	0.39	0.38	0.38	0.38	0.36	0.35	0.35	0.38	0.40	0.38	0.39
MnO	0.10	0.11	0.10	0.11	0.10	0.11	0.10	0.10	0.10	0.09	0.10	0.09	0.11	0.11	0.11	0.11
MgO	50.40	50.60	50.59	50.31	50.38	51.14	51.29	51.02	51.02	51.12	51.41	51.27	50.60	50.40	50.68	50.13
CaO	0.03	0.03	0.03	0.04	0.03	0.01	0.01	0.02	0.02	0.03	0.02	0.03	0.02	0.03	0.02	0.03
Na_2O	0.00	0.00	0.00	0.00	0.00	0.00	0.00	0.00	0.00	0.00	0.00	0.00	0.00	0.00	0.00	0.00
K_2O	0.01	0.00	0.01	0.00	0.01	0.00	0.00	0.00	0.00	0.00	0.00	0.00	0.00	0.00	0.00	0.01
P_2O_5	0.00	0.00	0.00	0.00	0.00	0.00	0.00	0.00	0.00	0.00	0.00	0.00	0.00	0.01	0.00	0.00
Total	99.58	100.08	99.85	99.27	99.17	100.30	100.45	100.23	100.23	99.91	100.38	99.97	100.20	99.93	100.47	99.54
Si	1.00	1.00	1.00	1.00	1.00	1.00	1.00	1.00	1.00	1.00	1.00	1.00	1.00	1.00	1.00	1.00
Ti	0.00	0.00	0.00	0.00	0.00	0.00	0.00	0.00	0.00	0.00	0.00	0.00	0.00	0.00	0.00	0.00
Al	0.00	0.00	0.00	0.00	0.00	0.00	0.00	0.00	0.00	0.00	0.00	0.00	0.00	0.00	0.00	0.00
V	0.00	0.00	0.00	0.00	0.00	0.00	0.00	0.00	0.00	0.00	0.00	0.00	0.00	0.00	0.00	0.00
Cr	0.00	0.00	0.00	0.00	0.00	0.00	0.00	0.00	0.00	0.00	0.00	0.00	0.00	0.00	0.00	0.00
Fe2+	0.15	0.16	0.16	0.16	0.15	0.15	0.15	0.15	0.15	0.14	0.14	0.14	0.16	0.16	0.16	0.16
Ni	0.01	0.01	0.01	0.01	0.01	0.01	0.01	0.01	0.01	0.01	0.01	0.01	0.01	0.01	0.01	0.01
Mn	0.00	0.00	0.00	0.00	0.00	0.00	0.00	0.00	0.00	0.00	0.00	0.00	0.00	0.00	0.00	0.00
Mg	1.83	1.83	1.83	1.83	1.84	1.84	1.85	1.84	1.84	1.85	1.85	1.85	1.83	1.83	1.83	1.83
Ca	0.00	0.00	0.00	0.00	0.00	0.00	0.00	0.00	0.00	0.00	0.00	0.00	0.00	0.00	0.00	0.00
Na	0.00	0.00	0.00	0.00	0.00	0.00	0.00	0.00	0.00	0.00	0.00	0.00	0.00	0.00	0.00	0.00
K	0.00	0.00	0.00	0.00	0.00	0.00	0.00	0.00	0.00	0.00	0.00	0.00	0.00	0.00	0.00	0.00
P	0.00	0.00	0.00	0.00	0.00	0.00	0.00	0.00	0.00	0.00	0.00	0.00	0.00	0.00	0.00	0.00
Total Cations	3.0	3.0	3.0	3.0	3.0	3.0	3.0	3.0	3.0	3.0	3.0	3.0	3.0	3.0	3.0	3.0
Oxygen	4.0	4.0	4.0	4.0	4.0	4.0	4.0	4.0	4.0	4.0	4.0	4.0	4.0	4.0	4.0	4.0
Mg#	92.3	92.1	92.1	92.2	92.5	92.6	92.6	92.6	92.6	92.8	92.9	93.0	91.9	91.8	91.9	91.9

Mineral	Olivine															
Sample	SN073A	SN073B	SN074A	SN075A	SN078B	SN078A	SN083A	SN084A	SN084B	SN085A	SN085B	SN088A	SN088B	SN089A	SN091A	SN091B
Paragenesis	P	P	P	P	P	P	P	P	P	P	P	P	P	P	P	P
Assemblage	Ol	Ol	Ol	Ol	Ol	Ol	Ol	Ol	Ol	Ol	Ol	Ol, W-NI	Ol, W-NI	Ol	Ol	Ol
SiO_2	40.80	40.83	40.87	41.23	41.03	41.19	41.39	40.85	40.89	41.37	41.17	41.00	41.22	41.31	40.86	41.05
TiO_2	0.00	0.00	0.00	0.00	0.00	0.00	0.00	0.00	0.00	0.00	0.00	0.01	0.00	0.00	0.00	0.00
Al_2O_3	0.00	0.00	0.00	0.00	0.00	0.00	0.00	0.00	0.00	0.00	0.00	0.00	0.00	0.00	0.00	0.00
V_2O_3	0.00	0.00	0.00	0.01	0.00	0.00	0.00	0.00	0.00	0.00	0.00	0.00	0.00	0.00	0.00	0.00
Cr_2O_3	0.02	0.01	0.00	0.02	0.02	0.02	0.00	0.03	0.03	0.02	0.01	0.05	0.05	0.02	0.02	0.03
FeO	7.47	7.40	6.97	8.09	7.58	7.42	7.80	7.44	7.17	7.39	7.29	7.69	7.72	7.63	7.34	7.44
NiO	0.40	0.38	0.37	0.38	0.39	0.38	0.36	0.39	0.38	0.39	0.38	0.36	0.35	0.38	0.38	0.38
MnO	0.11	0.10	0.10	0.12	0.10	0.11	0.12	0.10	0.10	0.11	0.11	0.10	0.10	0.10	0.10	0.10
MgO	50.52	50.45	50.96	50.48	50.54	50.70	51.08	50.36	50.32	50.97	50.86	50.39	50.74	50.97	50.21	50.55
CaO	0.02	0.01	0.02	0.02	0.03	0.03	0.02	0.02	0.03	0.02	0.02	0.05	0.05	0.02	0.03	0.00
Na_2O	0.00	0.00	0.00	0.00	0.00	0.00	0.00	0.00	0.00	0.00	0.00	0.00	0.00	0.00	0.00	0.00
K_2O	0.01	0.00	0.00	0.00	0.00	0.01	0.00	0.00	0.00	0.00	0.00	0.01	0.00	0.00	0.01	0.00
P_2O_5	0.00	0.01	0.00	0.00	0.00	0.00	0.00	0.01	0.00	0.00	0.00	0.00	0.00	0.00	0.00	0.00
Total	99.33	99.19	99.27	100.35	99.68	99.84	100.77	99.20	98.90	100.26	99.84	99.63	100.23	100.42	98.93	99.55
Si	1.00	1.00	1.00	1.00	1.00	1.00	1.00	1.00	1.00	1.00	1.00	1.00	1.00	1.00	1.00	1.00
Ti	0.00	0.00	0.00	0.00	0.00	0.00	0.00	0.00	0.00	0.00	0.00	0.00	0.00	0.00	0.00	0.00
Al	0.00	0.00	0.00	0.00	0.00	0.00	0.00	0.00	0.00	0.00	0.00	0.00	0.00	0.00	0.00	0.00
V	0.00	0.00	0.00	0.00	0.00	0.00	0.00	0.00	0.00	0.00	0.00	0.00	0.00	0.00	0.00	0.00
Cr	0.00	0.00	0.00	0.00	0.00	0.00	0.00	0.00	0.00	0.00	0.00	0.00	0.00	0.00	0.00	0.00
Fe2+	0.15	0.15	0.14	0.16	0.15	0.15	0.16	0.15	0.15	0.15	0.15	0.16	0.16	0.15	0.15	0.15
Ni	0.01	0.01	0.01	0.01	0.01	0.01	0.01	0.01	0.01	0.01	0.01	0.01	0.01	0.01	0.01	0.01
Mn	0.00	0.00	0.00	0.00	0.00	0.00	0.00	0.00	0.00	0.00	0.00	0.00	0.00	0.00	0.00	0.00
Mg	1.84	1.84	1.85	1.83	1.84	1.84	1.84	1.84	1.84	1.84	1.84	1.83	1.83	1.84	1.84	1.84
Ca	0.00	0.00	0.00	0.00	0.00	0.00	0.00	0.00	0.00	0.00	0.00	0.00	0.00	0.00	0.00	0.00
Na	0.00	0.00	0.00	0.00	0.00	0.00	0.00	0.00	0.00	0.00	0.00	0.00	0.00	0.00	0.00	0.00
K	0.00	0.00	0.00	0.00	0.00	0.00	0.00	0.00	0.00	0.00	0.00	0.00	0.00	0.00	0.00	0.00
P	0.00	0.00	0.00	0.00	0.00	0.00	0.00	0.00	0.00	0.00	0.00	0.00	0.00	0.00	0.00	0.00
Total Cations	3.0	3.0	3.0	3.0	3.0	3.0	3.0	3.0	3.0	3.0	3.0	3.0	3.0	3.0	3.0	3.0
Oxygen	4.0	4.0	4.0	4.0	4.0	4.0	4.0	4.0	4.0	4.0	4.0	4.0	4.0	4.0	4.0	4.0
Mg#	92.3	92.4	92.9	91.7	92.3	92.4	92.1	92.3	92.6	92.5	92.6	92.1	92.1	92.2	92.4	92.4

Mineral	Olivine															
Sample	SN091C	SN093A	SN094A	SN094B	SN094C	SN095A	SN095B	SN095C	SN096B	SN098A	SN099A	SN099B	SN102B	SN104A	SN104B	SN107A
Paragenesis	P	P	P	P	P	P	P	P	H	P	P	P	P	P	P	P
Assemblage	Ol	Ol	Ol	Ol	Ol	Ol	Ol	Ol	Grt, Ol	Ol	Ol	Ol	Ol	Ol	Ol	Ol
SiO_2	41.23	42.62	41.18	40.89	41.03	41.09	41.32	41.16	40.91	40.85	41.21	41.45	40.42	41.13	40.93	41.16
TiO_2	0.00	0.00	0.00	0.00	0.00	0.00	0.00	0.00	0.00	0.00	0.00	0.00	0.00	0.00	0.00	0.00
Al_2O_3	0.00	0.00	0.00	0.00	0.00	0.00	0.00	0.00	0.00	0.00	0.00	0.00	0.00	0.00	0.00	0.00
V_2O_3	0.00	0.00	0.00	0.01	0.01	0.00	0.00	0.00	0.00	0.00	0.00	0.02	0.00	0.00	0.00	0.00
Cr_2O_3	0.03	0.06	0.04	0.01	0.02	0.06	0.06	0.03	0.02	0.02	0.01	0.03	0.04	0.01	0.01	0.02
FeO	7.36	7.49	7.90	8.05	8.00	7.48	7.56	7.54	7.54	7.96	7.82	7.69	7.50	7.64	7.64	6.71
NiO	0.38	0.33	0.39	0.41	0.40	0.38	0.38	0.38	0.39	0.41	0.40	0.39	0.36	0.40	0.40	0.34
MnO	0.10	0.10	0.10	0.11	0.11	0.09	0.11	0.11	0.11	0.11	0.11	0.10	0.11	0.11	0.11	0.11
MgO	50.79	52.68	50.25	49.95	50.22	50.97	51.09	50.73	50.43	50.13	50.50	50.82	49.19	50.75	50.54	51.17
CaO	0.02	0.05	0.03	0.02	0.02	0.05	0.05	0.04	0.01	0.01	0.01	0.02	0.09	0.02	0.03	0.01
Na_2O	0.00	0.00	0.00	0.00	0.00	0.00	0.00	0.00	0.00	0.00	0.00	0.00	0.00	0.00	0.00	0.00
K_2O	0.00	0.00	0.00	0.00	0.00	0.01	0.00	0.01	0.00	0.00	0.00	0.00	0.03	0.00	0.00	0.00
P_2O_5	0.00	0.00	0.00	0.00	0.00	0.00	0.00	0.01	0.00	0.01	0.00	0.00	0.04	0.00	0.00	0.00
Total	99.91	103.33	99.90	99.44	99.79	100.13	100.56	99.98	99.41	99.50	100.05	100.50	97.78	100.04	99.65	99.50
Si	1.00	1.00	1.00	1.00	1.00	1.00	1.00	1.00	1.00	1.00	1.00	1.00	1.01	1.00	1.00	1.00
Ti	0.00	0.00	0.00	0.00	0.00	0.00	0.00	0.00	0.00	0.00	0.00	0.00	0.00	0.00	0.00	0.00
Al	0.00	0.00	0.00	0.00	0.00	0.00	0.00	0.00	0.00	0.00	0.00	0.00	0.00	0.00	0.00	0.00
V	0.00	0.00	0.00	0.00	0.00	0.00	0.00	0.00	0.00	0.00	0.00	0.00	0.00	0.00	0.00	0.00
Cr	0.00	0.00	0.00	0.00	0.00	0.00	0.00	0.00	0.00	0.00	0.00	0.00	0.00	0.00	0.00	0.00
Fe2+	0.15	0.15	0.16	0.16	0.16	0.15	0.15	0.15	0.15	0.16	0.16	0.16	0.16	0.16	0.16	0.14
Ni	0.01	0.01	0.01	0.01	0.01	0.01	0.01	0.01	0.01	0.01	0.01	0.01	0.01	0.01	0.01	0.01
Mn	0.00	0.00	0.00	0.00	0.00	0.00	0.00	0.00	0.00	0.00	0.00	0.00	0.00	0.00	0.00	0.00
Mg	1.84	1.84	1.82	1.82	1.83	1.84	1.84	1.84	1.84	1.83	1.83	1.83	1.82	1.84	1.84	1.85
Ca	0.00	0.00	0.00	0.00	0.00	0.00	0.00	0.00	0.00	0.00	0.00	0.00	0.00	0.00	0.00	0.00
Na	0.00	0.00	0.00	0.00	0.00	0.00	0.00	0.00	0.00	0.00	0.00	0.00	0.00	0.00	0.00	0.00
K	0.00	0.00	0.00	0.00	0.00	0.00	0.00	0.00	0.00	0.00	0.00	0.00	0.00	0.00	0.00	0.00
P	0.00	0.00	0.00	0.00	0.00	0.00	0.00	0.00	0.00	0.00	0.00	0.00	0.00	0.00	0.00	0.00
Total Cations	3.0	3.0	3.0	3.0	3.0	3.0	3.0	3.0	3.0	3.0	3.0	3.0	3.0	3.0	3.0	3.0
Oxygen	4.0	4.0	4.0	4.0	4.0	4.0	4.0	4.0	4.0	4.0	4.0	4.0	4.0	4.0	4.0	4.0
Mg#	92.4	92.6	91.9	91.7	91.8	92.4	92.3	92.3	92.3	91.8	92.0	92.2	92.1	92.2	92.2	93.2

Mineral	Olivine															
Sample	SN109A	SN111A	SN113A	SN113B	SN114A	SN115B	SN115C	SN116A	SN116B	SN117A	SN118C	SN118D	SN118E	SN120A	SN121A	SN122A
Paragenesis	P	P	P	P	P	P	P	H	H	P	P	P	P	P	P	P
Assemblage	Ol	Ol	Ol	Ol	Ol	Ol	Ol	Grt, Ol	Grt, Ol	Ol	Grt, Ol	Grt, Ol	Grt, Ol	Ol	Ol	Ol
SiO_2	41.10	41.32	41.79	41.07	41.00	41.04	40.46	41.04	41.06	40.85	41.39	41.02	40.90	41.07	40.97	41.13
TiO_2	0.00	0.00	0.00	0.00	0.00	0.00	0.00	0.00	0.00	0.00	0.00	0.00	0.00	0.00	0.00	0.00
Al_2O_3	0.00	0.00	0.00	0.00	0.00	0.00	0.00	0.00	0.00	0.00	0.00	0.00	0.00	0.00	0.00	0.00
V_2O_3	0.00	0.00	0.00	0.00	0.00	0.00	0.00	0.00	0.00	0.01	0.00	0.00	0.00	0.01	0.00	0.00
Cr_2O_3	0.02	0.05	0.00	0.01	0.02	0.04	0.03	0.01	0.02	0.03	0.03	0.02	0.00	0.01	0.00	0.01
FeO	7.53	7.64	6.11	6.06	7.64	7.47	7.49	7.64	7.65	7.63	7.58	7.65	7.53	6.76	7.60	7.56
NiO	0.42	0.39	0.33	0.33	0.42	0.40	0.41	0.42	0.41	0.37	0.39	0.38	0.38	0.35	0.43	0.40
MnO	0.09	0.11	0.08	0.09	0.11	0.10	0.10	0.11	0.10	0.10	0.10	0.10	0.11	0.10	0.09	0.11
MgO	50.61	50.99	52.12	51.59	50.60	50.76	50.04	50.53	50.59	50.38	51.04	50.68	50.31	51.21	50.78	50.83
CaO	0.01	0.03	0.02	0.02	0.02	0.01	0.00	0.01	0.02	0.02	0.02	0.02	0.02	0.01	0.01	0.02
Na_2O	0.00	0.00	0.00	0.00	0.00	0.00	0.00	0.00	0.00	0.00	0.00	0.00	0.00	0.00	0.00	0.00
K_2O	0.00	0.00	0.00	0.00	0.00	0.00	0.00	0.00	0.00	0.00	0.00	0.00	0.00	0.00	0.00	0.00
P_2O_5	0.02	0.00	0.00	0.00	0.00	0.00	0.00	0.00	0.00	0.00	0.00	0.00	0.00	0.00	0.00	0.00
Total	99.79	100.53	100.45	99.15	99.81	99.81	98.52	99.75	99.85	99.39	100.55	99.87	99.25	99.51	99.89	100.05
Si	1.00	1.00	1.00	1.00	1.00	1.00	1.00	1.00	1.00	1.00	1.00	1.00	1.00	1.00	1.00	1.00
Ti	0.00	0.00	0.00	0.00	0.00	0.00	0.00	0.00	0.00	0.00	0.00	0.00	0.00	0.00	0.00	0.00
Al	0.00	0.00	0.00	0.00	0.00	0.00	0.00	0.00	0.00	0.00	0.00	0.00	0.00	0.00	0.00	0.00
V	0.00	0.00	0.00	0.00	0.00	0.00	0.00	0.00	0.00	0.00	0.00	0.00	0.00	0.00	0.00	0.00
Cr	0.00	0.00	0.00	0.00	0.00	0.00	0.00	0.00	0.00	0.00	0.00	0.00	0.00	0.00	0.00	0.00
Fe2+	0.15	0.15	0.12	0.12	0.16	0.15	0.15	0.16	0.16	0.16	0.15	0.16	0.15	0.14	0.15	0.15
Ni	0.01	0.01	0.01	0.01	0.01	0.01	0.01	0.01	0.01	0.01	0.01	0.01	0.01	0.01	0.01	0.01
Mn	0.00	0.00	0.00	0.00	0.00	0.00	0.00	0.00	0.00	0.00	0.00	0.00	0.00	0.00	0.00	0.00
Mg	1.84	1.84	1.87	1.87	1.84	1.84	1.84	1.83	1.83	1.84	1.84	1.84	1.83	1.86	1.84	1.84
Ca	0.00	0.00	0.00	0.00	0.00	0.00	0.00	0.00	0.00	0.00	0.00	0.00	0.00	0.00	0.00	0.00
Na	0.00	0.00	0.00	0.00	0.00	0.00	0.00	0.00	0.00	0.00	0.00	0.00	0.00	0.00	0.00	0.00
K	0.00	0.00	0.00	0.00	0.00	0.00	0.00	0.00	0.00	0.00	0.00	0.00	0.00	0.00	0.00	0.00
P	0.00	0.00	0.00	0.00	0.00	0.00	0.00	0.00	0.00	0.00	0.00	0.00	0.00	0.00	0.00	0.00
Total Cations	3.0	3.0	3.0	3.0	3.0	3.0	3.0	3.0	3.0	3.0	3.0	3.0	3.0	3.0	3.0	3.0
Oxygen	4.0	4.0	4.0	4.0	4.0	4.0	4.0	4.0	4.0	4.0	4.0	4.0	4.0	4.0	4.0	4.0
Mg#	92.3	92.2	93.8	93.8	92.2	92.4	92.3	92.2	92.2	92.2	92.3	92.2	92.3	93.1	92.3	92.3

Mineral	Olivine															
Sample	SN127A	SN127B	SN127C	SN129A	SN133A	SN134E	SN135A	SN136A	SN136B	SN138A	SN140A	SN140B	SN142A	SN143A	SN144A	SN146A
Paragenesis	P	P	P	P	P	P	P	P	P	P	P	P	P	P	P	P
Assemblage	Ol	Ol	Ol	Ol	Ol	Ol, Chr	Ol	Ol	Ol	Ol	Ol	Ol	Ol	Ol	Ol	Ol
SiO_2	40.52	41.13	41.51	40.95	41.02	41.08	40.94	41.10	41.35	41.06	41.85	41.60	41.05	40.88	41.06	41.37
TiO_2	0.00	0.00	0.00	0.00	0.00	0.00	0.00	0.00	0.00	0.00	0.00	0.00	0.00	0.00	0.00	0.00
Al_2O_3	0.00	0.00	0.00	0.00	0.00	0.00	0.00	0.00	0.00	0.00	0.00	0.00	0.00	0.00	0.00	0.00
V_2O_3	0.00	0.00	0.02	0.00	0.00	0.00	0.00	0.01	0.00	0.01	0.00	0.00	0.00	0.00	0.00	0.00
Cr_2O_3	0.01	0.00	0.00	0.00	0.03	0.05	0.01	0.02	0.04	0.01	0.02	0.02	0.00	0.02	0.02	0.03
FeO	6.60	6.51	6.46	6.64	7.83	6.60	7.65	8.36	8.23	7.49	6.74	6.64	7.35	7.60	7.78	7.79
NiO	0.35	0.34	0.33	0.34	0.38	0.37	0.40	0.39	0.41	0.39	0.34	0.35	0.40	0.40	0.40	0.42
MnO	0.10	0.10	0.09	0.09	0.11	0.09	0.09	0.10	0.11	0.11	0.09	0.09	0.10	0.10	0.10	0.11
MgO	50.55	51.43	51.86	51.14	50.42	51.21	50.40	50.22	50.62	50.60	51.95	51.54	50.79	50.32	50.64	51.00
CaO	0.01	0.00	0.02	0.02	0.01	0.02	0.03	0.02	0.02	0.01	0.00	0.02	0.01	0.02	0.03	0.02
Na_2O	0.00	0.00	0.00	0.00	0.00	0.00	0.00	0.00	0.00	0.00	0.00	0.00	0.00	0.00	0.00	0.00
K_2O	0.01	0.00	0.00	0.01	0.00	0.00	0.00	0.00	0.01	0.00	0.00	0.00	0.00	0.00	0.00	0.00
P_2O_5	0.00	0.01	0.00	0.01	0.01	0.03	0.00	0.01	0.00	0.00	0.00	0.00	0.00	0.00	0.00	0.01
Total	98.15	99.52	100.29	99.19	99.82	99.45	99.51	100.24	100.78	99.67	100.98	100.25	99.71	99.34	100.03	100.74
Si	1.00	1.00	1.00	1.00	1.00	1.00	1.00	1.00	1.00	1.00	1.00	1.00	1.00	1.00	1.00	1.00
Ti	0.00	0.00	0.00	0.00	0.00	0.00	0.00	0.00	0.00	0.00	0.00	0.00	0.00	0.00	0.00	0.00
Al	0.00	0.00	0.00	0.00	0.00	0.00	0.00	0.00	0.00	0.00	0.00	0.00	0.00	0.00	0.00	0.00
V	0.00	0.00	0.00	0.00	0.00	0.00	0.00	0.00	0.00	0.00	0.00	0.00	0.00	0.00	0.00	0.00
Cr	0.00	0.00	0.00	0.00	0.00	0.00	0.00	0.00	0.00	0.00	0.00	0.00	0.00	0.00	0.00	0.00
Fe2+	0.14	0.13	0.13	0.14	0.16	0.13	0.16	0.17	0.17	0.15	0.14	0.13	0.15	0.16	0.16	0.16
Ni	0.01	0.01	0.01	0.01	0.01	0.01	0.01	0.01	0.01	0.01	0.01	0.01	0.01	0.01	0.01	0.01
Mn	0.00	0.00	0.00	0.00	0.00	0.00	0.00	0.00	0.00	0.00	0.00	0.00	0.00	0.00	0.00	0.00
Mg	1.86	1.86	1.86	1.86	1.83	1.86	1.83	1.82	1.82	1.84	1.85	1.85	1.84	1.83	1.83	1.83
Ca	0.00	0.00	0.00	0.00	0.00	0.00	0.00	0.00	0.00	0.00	0.00	0.00	0.00	0.00	0.00	0.00
Na	0.00	0.00	0.00	0.00	0.00	0.00	0.00	0.00	0.00	0.00	0.00	0.00	0.00	0.00	0.00	0.00
K	0.00	0.00	0.00	0.00	0.00	0.00	0.00	0.00	0.00	0.00	0.00	0.00	0.00	0.00	0.00	0.00
P	0.00	0.00	0.00	0.00	0.00	0.00	0.00	0.00	0.00	0.00	0.00	0.00	0.00	0.00	0.00	0.00
Total Cations	3.0	3.0	3.0	3.0	3.0	3.0	3.0	3.0	3.0	3.0	3.0	3.0	3.0	3.0	3.0	3.0
Oxygen	4.0	4.0	4.0	4.0	4.0	4.0	4.0	4.0	4.0	4.0	4.0	4.0	4.0	4.0	4.0	4.0
Mg#	93.2	93.4	93.5	93.2	92.0	93.3	92.1	91.5	91.6	92.3	93.2	93.3	92.5	92.2	92.1	92.1

Mineral	Olivine			Chromite												
Sample	SN146B	SN146C	SN147A	SN004A	SN004B	SN010C	SN010D	SN010E	SN045A	SN045C	SN046B	SN047A	SN048C	SN048D	SN134A	SN134B
Paragenesis	P	P	P	P	P	P	P	P	P	P	P	P	P	P	P	P
Assemblage	Ol	Ol	Ol	Chr	Chr	Chr	Chr	Chr	Chr	Chr	Chr	Chr	Chr	Chr	Chr	Chr
SiO_2	41.28	40.86	41.02	0.03	0.02	0.22	0.22	0.23	0.07	0.26	0.14	0.09	0.07	0.06	0.12	0.11
TiO_2	0.00	0.00	0.00	0.32	0.28	0.08	0.08	0.07	0.22	0.21	0.13	0.00	0.22	0.23	0.01	0.01
Al_2O_3	0.00	0.00	0.00	7.40	8.22	6.49	6.37	6.45	5.06	5.20	5.80	8.19	5.76	5.55	10.65	11.28
V_2O_3	0.00	0.00	0.00	0.23	0.24	0.24	0.23	0.22	0.23	0.22	0.21	0.23	0.22	0.23	0.16	0.16
Cr_2O_3	0.02	0.01	0.02	63.29	62.88	64.55	64.49	64.39	65.24	64.45	62.88	63.65	64.03	65.05	60.74	59.87
FeO	7.76	7.70	7.79	14.55	14.59	14.59	14.66	14.54	15.51	15.51	14.94	14.05	15.45	15.64	13.80	13.77
NiO	0.41	0.41	0.41	0.11	0.11	0.12	0.12	0.12	0.12	0.12	0.12	0.08	0.12	0.12	0.12	0.12
MnO	0.10	0.10	0.11	0.21	0.19	0.18	0.19	0.19	0.20	0.20	0.20	0.20	0.20	0.21	0.17	0.18
MgO	50.74	50.37	50.47	13.66	13.64	13.78	13.78	13.94	13.12	13.26	15.05	13.67	13.44	13.08	14.28	14.09
CaO	0.01	0.02	0.01	0.00	0.00	0.00	0.00	0.00	0.00	0.00	0.00	0.00	0.00	0.00	0.00	0.00
Na_2O	0.00	0.00	0.00	0.00	0.01	0.00	0.02	0.02	0.02	0.00	0.01	0.01	0.01	0.00	0.01	0.00
K_2O	0.00	0.00	0.00	0.00	0.00	0.00	0.00	0.00	0.00	0.00	0.00	0.00	0.00	0.00	0.00	0.00
P_2O_5	0.01	0.00	0.00	0.00	0.00	0.00	0.00	0.00	0.00	0.00	0.00	0.00	0.00	0.01	0.00	0.00
Total	100.32	99.46	99.82	99.79	100.17	100.23	100.15	100.18	99.79	99.43	99.48	100.17	99.54	100.17	100.07	99.59
Si	1.00	1.00	1.00	0.00	0.00	0.01	0.01	0.01	0.00	0.01	0.00	0.00	0.00	0.00	0.00	0.00
Ti	0.00	0.00	0.00	0.01	0.01	0.00	0.00	0.00	0.01	0.01	0.00	0.00	0.01	0.01	0.00	0.00
Al	0.00	0.00	0.00	0.28	0.31	0.25	0.24	0.25	0.20	0.20	0.22	0.31	0.22	0.21	0.40	0.43
V	0.00	0.00	0.00	0.01	0.01	0.01	0.01	0.01	0.01	0.01	0.01	0.01	0.01	0.01	0.00	0.00
Cr	0.00	0.00	0.00	1.63	1.61	1.66	1.66	1.66	1.70	1.69	1.62	1.63	1.67	1.69	1.53	1.52
Fe2+	0.16	0.16	0.16	0.40	0.40	0.40	0.40	0.40	0.43	0.43	0.41	0.38	0.43	0.43	0.37	0.37
Ni	0.01	0.01	0.01	0.00	0.00	0.00	0.00	0.00	0.00	0.00	0.00	0.00	0.00	0.00	0.00	0.00
Mn	0.00	0.00	0.00	0.01	0.01	0.01	0.01	0.01	0.01	0.01	0.01	0.01	0.01	0.01	0.00	0.01
Mg	1.83	1.83	1.83	0.66	0.66	0.67	0.67	0.68	0.65	0.65	0.73	0.66	0.66	0.64	0.68	0.67
Ca	0.00	0.00	0.00	0.00	0.00	0.00	0.00	0.00	0.00	0.00	0.00	0.00	0.00	0.00	0.00	0.00
Na	0.00	0.00	0.00	0.00	0.00	0.00	0.00	0.00	0.00	0.00	0.00	0.00	0.00	0.00	0.00	0.00
K	0.00	0.00	0.00	0.00	0.00	0.00	0.00	0.00	0.00	0.00	0.00	0.00	0.00	0.00	0.00	0.00
P	0.00	0.00	0.00	0.00	0.00	0.00	0.00	0.00	0.00	0.00	0.00	0.00	0.00	0.00	0.00	0.00
Total Cations	3.0	3.0	3.0	3.0	3.0	3.0	3.0	3.0	3.0	3.0	3.0	3.0	3.0	3.0	3.0	3.0
Oxygen	4.0	4.0	4.0	4.0	4.0	4.0	4.0	4.0	4.0	4.0	3.9	4.0	4.0	4.0	4.0	4.0
Mg#	92.1	92.1	92.0	62.6	62.5	62.7	62.6	63.1	60.0	60.3	64.2	63.4	60.8	59.9	64.9	64.6

Mineral	Chromite		Clinopyroxene			Orthopyroxene			K-Spar	Coesite	
Sample	SN134C	SN134D	SN030A	SN030B	SN041B	SN064A	SN100A	SN132C	SN056A	SN097C	SN128A
Paragenesis	P	P	L	L	L	P	P	H	E	E	E
Assemblage	Chr	Chr	Cpx	Cpx	Cpx, Grt	Opx	Opx	Opx, Grt	K-spar	Sul, Grt, Co	Co
SiO_2	0.18	0.18	55.31	54.76	55.77	58.45	58.19	58.29	63.39	99.99	100.49
TiO_2	0.01	0.01	0.01	0.01	0.00	0.01	0.00	0.01	0.00	0.00	0.00
Al_2O_3	10.96	11.13	1.07	1.07	0.75	0.55	0.52	0.47	19.25	0.57	0.00
V_2O_3	0.17	0.18	0.03	0.02	0.00	0.01	0.00	0.01	0.00	0.00	0.00
Cr_2O_3	60.45	60.32	1.23	1.22	0.68	0.43	0.34	0.33	0.00	0.00	0.00
FeO	13.52	13.55	2.20	2.24	2.24	4.08	4.20	4.46	0.00	0.02	0.01
NiO	0.11	0.12	0.06	0.06	0.06	0.12	0.12	0.13	0.00	0.00	0.00
MnO	0.19	0.19	0.09	0.09	0.10	0.10	0.10	0.11	0.00	0.00	0.00
MgO	14.41	14.47	17.73	17.80	18.29	36.56	36.18	36.14	0.00	0.00	0.00
CaO	0.00	0.00	21.00	20.81	21.92	0.34	0.34	0.36	0.01	0.01	0.00
Na_2O	0.00	0.00	0.97	0.95	0.51	0.00	0.00	0.00	0.52	0.01	0.00
K_2O	0.00	0.00	0.09	0.09	0.11	0.00	0.00	0.00	16.24	0.09	0.01
P_2O_5	0.00	0.00	0.02	0.02	0.03	0.00	0.00	0.00	0.00	0.00	0.00
Total	99.98	100.12	99.80	99.12	100.46	100.63	99.99	100.31	99.41	100.69	100.51
Si	0.01	0.01	2.00	2.00	2.01	1.98	1.99	1.99	2.94	2.98	3.00
Ti	0.00	0.00	0.00	0.00	0.00	0.00	0.00	0.00	0.00	0.00	0.00
Al	0.41	0.42	0.05	0.05	0.03	0.02	0.00	0.02	1.05	0.02	0.00
V	0.00	0.00	0.00	0.00	0.00	0.00	0.00	0.00	0.00	0.00	0.00
Cr	1.52	1.52	0.04	0.03	0.02	0.01	0.01	0.01	0.00	0.00	0.00
Fe2+	0.36	0.36	0.07	0.07	0.07	0.12	0.12	0.13	0.00	0.00	0.00
Ni	0.00	0.00	0.00	0.00	0.00	0.00	0.00	0.00	0.00	0.00	0.00
Mn	0.01	0.01	0.00	0.00	0.00	0.00	0.00	0.00	0.00	0.00	0.00
Mg	0.69	0.69	0.96	0.97	0.98	1.85	1.84	1.84	0.00	0.00	0.00
Ca	0.00	0.00	0.81	0.81	0.85	0.01	0.01	0.01	0.00	0.00	0.00
Na	0.00	0.00	0.07	0.07	0.04	0.00	0.00	0.00	0.05	0.00	0.00
K	0.00	0.00	0.00	0.00	0.01	0.00	0.00	0.00	0.96	0.00	0.00
P	0.00	0.00	0.00	0.00	0.00	0.00	0.00	0.00	0.00	0.00	0.00
Total Cations	3.0	3.0	4.0	4.0	4.0	4.0	4.0	4.0	5.0	3.0	3.0
Oxygen	4.0	4.0	6.0	6.0	6.0	6.0	6.0	6.0	8.0	6.0	6.0
Mg#	65.5	65.6	93.5	93.4	93.6	0.9	0.9	0.9	-	-	-

Mineral	Sulphide					Native Iron	Native Iron
Sample	SN008A	SN019A	SN033B	SN086A	SN097B	SN088C	SN088D3
Paragenesis	P	P	P	E	E	P	P
Assemblage	Sul	Sul	Sul, Ol	Sul	Sul, Grt, Co	W-NI, Ol	W-NI, Ol
Si	0.00	0.00	0.00	0.00	0.00	0.01	0.05
Zn	0.01	0.00	0.00	0.00	0.00	0.00	0.00
Cr	0.00	0.18	0.47	0.00	0.00	0.06	0.08
Fe	0.90	39.13	39.74	54.84	54.62	94.98	98.63
Co	4.08	0.42	0.46	0.44	0.46	0.09	0.08
Ni	58.74	20.28	20.56	4.10	4.17	0.30	0.18
Cu	0.00	0.72	0.42	0.76	1.12	0.39	0.33
Mn	0.00	0.00	0.02	0.00	0.00	0.01	0.05
Mg	0.02	0.01	0.00	0.01	0.00	0.00	0.01
S	36.20	37.27	37.58	39.78	39.52	0.00	0.00
As	0.00	0.00	0.00	0.00	0.00	0.00	0.00
Total	99.94	98.01	99.25	99.94	99.89	95.82	99.41

Mineral	Wustite	Wustite
Sample	SN088C	SN088D
Paragenesis	P	P
Assemblage	W-NI, Ol	W-NI, Ol
SiO_2	2.11	0.68
ZnO	0.01	0.02
Cr_2O_3	0.55	0.99
FeO	93.49	95.30
CoO	0.07	0.08
NiO	0.01	0.01
Cu_2O	0.06	0.09
MnO	0.91	0.67
MgO	0.00	0.00
SO_3	0.02	0.01
As_2O_3	0.00	0.01
Total	97.22	97.85

Appendix E

Trace element result of garnet and clinopyroxene inclusions recovered from Snap Lake diamonds

Sample	**SN001**				**SN005**	**SN012**		**SN024**		**SN025**
	A	**B**	**C**	**D**	**A**	**A**	**B**	**A**	**B**	**A**
Mineral	Garnet	Garnet	Garnet	Garnet	Garnet	Garnet	Garnet	Garnet	Garnet	Garnet
Assemblage	gt	gt	gt	gt	gt	gt	gt	gt	gt	gt
Ti (ppm)	3767	3849	4241	3618	1939	1019	983.0	493.1	458.9	165.0
Sr (ppm)	0.79	0.78	0.76	0.74	0.63	0.43	0.23	4.26	4.06	1.24
Y (ppm)	39.90	39.94	38.93	37.18	8.87	1.42	1.78	1.10	1.13	1.18
Zr (ppm)	15.09	14.00	14.45	13.20	5.92	21.21	24.35	3.53	3.45	20.04
Nb (ppm)	0.46	0.73	0.79	0.71	0.01	0.27	0.53	1.12	0.90	0.32
Ba (ppm)	<LOD	<LOD	<LOD	<LOD	<LOD	<LOD	<LOD	<LOD	<LOD	<LOD
La (ppm)	0.06	0.06	0.07	0.06	0.00	0.04	0.00	0.49	0.42	0.04
Ce (ppm)	0.58	0.59	0.59	0.56	0.03	0.21	0.12	2.74	2.54	0.85
Pr (ppm)	0.19	0.19	0.19	0.18	0.02	0.08	0.08	0.44	0.41	0.53
Nd (ppm)	1.76	1.64	1.66	1.59	0.18	0.79	0.99	1.88	1.80	5.02
Sm (ppm)	1.27	1.20	1.26	1.19	0.20	0.36	0.41	0.44	0.41	1.21
Eu (ppm)	0.62	0.61	0.64	0.59	0.16	0.13	0.15	0.13	0.12	0.25
Gd (ppm)	3.17	3.07	3.13	2.99	0.59	0.34	0.49	0.35	0.35	0.61
Tb (ppm)	0.76	0.73	0.75	0.70	0.16	0.06	0.07	0.04	0.04	0.06
Dy (ppm)	5.90	5.91	6.17	5.76	1.41	0.29	0.37	0.22	0.24	0.25
Ho (ppm)	1.48	1.51	1.57	1.44	0.36	0.05	0.07	0.04	0.04	0.05
Er (ppm)	4.79	4.88	5.01	4.71	1.17	0.15	0.19	0.14	0.15	0.14
Tm (ppm)	0.76	0.77	0.80	0.73	0.18	0.01	0.03	0.03	0.03	0.02
Yb (ppm)	5.52	5.53	5.88	5.25	1.28	0.17	0.19	0.29	0.28	0.24
Lu (ppm)	0.88	0.87	0.89	0.83	0.19	0.03	0.03	0.06	0.06	0.06
Hf (ppm)	0.53	0.48	0.48	0.46	0.16	0.65	0.91	0.09	0.06	0.47

Sample	**SN026**			**SN027**			**SN036**	**SN041**		**SN049**
	A	**A2**	**B**	**A**	**A2**	**B**	**A**	**A**	**C**	**A**
Mineral	Garnet	Garnet	Garnet	Garnet	Garnet	Garnet	Garnet	Garnet	Garnet	Garnet
Assemblage	gt, ol	gt, opx	gt, ol	gt, ol	gt, ol	gt, ol	gt, ol	gt, cpx	gt, cpx	gt
Ti (ppm)	327.0	324.0	290.7	471.4	471.1	77.90	1725	11.70	24.10	264.0
Sr (ppm)	1.75	1.21	1.05	4.29	4.17	1.32	0.40	0.20	0.27	1.38
Y (ppm)	0.90	0.81	0.81	1.19	1.07	0.30	3.93	0.23	0.25	0.44
Zr (ppm)	1.24	1.13	1.09	3.41	3.28	0.53	22.69	0.03	0.31	1.72
Nb (ppm)	1.19	0.76	0.58	0.86	0.92	0.55	0.27	0.71	1.09	0.64
Ba (ppm)	0.96	0.10	<LOD	<LOD	<LOD	<LOD	<LOD	<LOD	<LOD	<LOD
La (ppm)	0.29	0.15	0.13	0.45	0.42	0.33	0.01	0.08	0.10	0.14
Ce (ppm)	1.24	1.10	0.91	2.61	2.61	1.08	0.15	0.62	0.65	1.04
Pr (ppm)	0.25	0.22	0.19	0.42	0.41	0.18	0.13	0.11	0.11	0.18
Nd (ppm)	1.11	1.08	0.91	1.90	1.75	0.84	1.92	0.31	0.39	0.85
Sm (ppm)	0.22	0.19	0.18	0.40	0.39	0.09	1.22	0.03	0.03	0.14
Eu (ppm)	0.06	0.05	0.06	0.13	0.12	0.02	0.43	0.01	<LOD	0.03
Gd (ppm)	0.16	0.17	0.18	0.29	0.33	0.05	1.30	0.00	<LOD	0.08
Tb (ppm)	0.02	0.02	0.02	0.04	0.04	0.01	0.18	0.00	<LOD	0.01
Dy (ppm)	0.13	0.12	0.11	0.21	0.21	0.04	0.94	0.01	<LOD	0.06
Ho (ppm)	0.03	0.03	0.03	0.04	0.04	0.01	0.15	0.01	0.01	0.02
Er (ppm)	0.12	0.11	0.12	0.15	0.13	0.06	0.34	0.05	0.05	0.07
Tm (ppm)	0.03	0.02	0.02	0.03	0.02	0.02	0.04	0.01	0.01	0.02
Yb (ppm)	0.32	0.30	0.29	0.29	0.26	0.25	0.25	0.18	0.24	0.28
Lu (ppm)	0.08	0.07	0.06	0.06	0.06	0.07	0.04	0.04	0.05	0.08
Hf (ppm)	0.05	0.03	<LOD	0.09	0.09	0.01	0.58	<LOD	<LOD	0.04

Sample	SN050	SN052		SN053		SN054		SN096		SN097
	A	A	B	A	A2	D	D2	A	A2	A
Mineral	Garnet	Garnet	Garnet	Garnet	Garnet	Garnet	Garnet	Garnet	Garnet	Garnet
Assemblage	gt	gt, ol	gt, ol	gt	gt	gt, ol	gt, ol	gt, ol	gt, ol	gt, co, sul
Ti (ppm)	1788	34.39	35.60	170.1	177.0	328.2	323.1	869.0	867.0	449.9
Sr (ppm)	2.20	0.60	0.39	2.48	2.54	0.92	0.89	2.21	2.08	0.41
Y (ppm)	3.14	0.19	0.20	0.33	0.37	1.22	1.11	2.07	1.91	1.52
Zr (ppm)	22.39	1.24	1.24	2.06	2.49	2.77	2.64	9.95	8.84	8.77
Nb (ppm)	1.46	0.61	0.58	0.90	0.95	0.78	0.79	0.97	0.92	0.19
Ba (ppm)	<LOD	<LOD	<LOD	<LOD	<LOD	<LOD	<LOD	<LOD	<LOD	<LOD
La (ppm)	0.64	0.01	0.00	0.34	0.32	0.07	0.08	0.39	0.35	0.00
Ce (ppm)	2.97	0.26	0.19	1.99	2.12	0.81	0.83	1.66	1.63	0.19
Pr (ppm)	0.52	0.11	0.10	0.35	0.37	0.19	0.20	0.31	0.29	0.12
Nd (ppm)	2.80	1.64	1.61	1.56	1.49	1.30	1.29	1.81	1.59	1.09
Sm (ppm)	0.87	0.64	0.61	0.15	0.21	0.34	0.33	0.35	0.30	0.36
Eu (ppm)	0.30	0.09	0.10	0.04	0.01	0.10	0.09	0.10	0.09	0.11
Gd (ppm)	0.84	0.14	0.14	0.08	<LOD	0.25	0.25	0.30	0.27	0.36
Tb (ppm)	0.12	0.01	0.01	0.01	<LOD	0.04	0.03	0.05	0.05	0.06
Dy (ppm)	0.67	0.05	0.04	0.07	0.03	0.23	0.21	0.37	0.35	0.33
Ho (ppm)	0.13	0.01	0.01	0.01	0.01	0.05	0.05	0.08	0.08	0.06
Er (ppm)	0.36	0.02	0.02	0.05	0.06	0.14	0.15	0.27	0.26	0.15
Tm (ppm)	0.05	0.01	0.01	0.01	<LOD	0.02	0.02	0.04	0.04	0.02
Yb (ppm)	0.45	0.12	0.11	0.21	0.34	0.22	0.27	0.40	0.37	0.30
Lu (ppm)	0.09	0.04	0.03	0.05	0.05	0.06	0.06	0.08	0.07	0.10
Hf (ppm)	0.55	0.02	0.02	0.04	<LOD	<LOD	0.09	0.34	0.32	0.22

Sample	**SN108**	**SN116**	**SN118**		**SN130**	**SN132**		**SN030**	
	A	**C**	**A**	**A2**	**A**	**A**	**B**	**A**	**B**
Mineral	Garnet	Garnet	Garnet	Garnet	Garnet	Garnet	Garnet	Clinopyroxene	Clinopyroxene
Assemblage	gt	gt, ol	gt, ol	gt, ol	gt	gt, opx	gt, opx	cpx	cpx
Ti (ppm)	61.30	101.9	474.0	476.0	285.1	361.7	385.2	85.30	90.60
Sr (ppm)	5.54	1.02	1.37	1.39	1.71	1.18	1.53	79.21	80.01
Y (ppm)	0.58	0.72	1.36	1.37	0.63	0.85	0.91	0.16	0.17
Zr (ppm)	0.96	2.15	2.99	2.81	3.02	3.09	3.30	0.08	0.06
Nb (ppm)	0.23	0.76	0.60	0.56	0.96	0.74	0.87	0.17	0.22
Ba (ppm)	0.07	<LOD	<LOD	<LOD	<LOD	<LOD	<LOD	4.70	4.99
La (ppm)	0.38	0.05	0.09	0.09	0.39	0.06	0.13	2.86	2.89
Ce (ppm)	2.36	0.86	0.72	0.71	1.80	0.78	0.96	5.96	6.05
Pr (ppm)	0.64	0.31	0.20	0.20	0.29	0.19	0.21	0.69	0.71
Nd (ppm)	3.38	1.96	1.32	1.38	1.41	1.12	1.15	2.59	2.59
Sm (ppm)	0.38	0.43	0.36	0.36	0.26	0.29	0.33	0.26	0.27
Eu (ppm)	0.06	0.11	0.14	0.13	0.07	0.09	0.10	0.05	0.06
Gd (ppm)	0.08	0.28	0.34	0.37	0.16	0.24	0.25	0.11	0.11
Tb (ppm)	0.01	0.03	0.04	0.06	0.02	0.03	0.03	0.01	0.01
Dy (ppm)	0.08	0.13	0.33	0.27	0.13	0.17	0.19	0.04	0.05
Ho (ppm)	0.02	0.03	0.06	0.05	0.03	0.03	0.04	0.01	0.01
Er (ppm)	0.08	0.07	0.17	0.16	0.08	0.10	0.08	0.02	0.01
Tm (ppm)	0.02	0.01	0.03	0.02	0.02	0.02	0.01	0.00	0.00
Yb (ppm)	0.18	0.14	0.16	0.19	0.17	0.13	0.17	0.01	0.01
Lu (ppm)	0.04	0.04	0.04	0.05	0.04	0.03	0.04	0.00	0.00
Hf (ppm)	0.02	<LOD	0.09	0.11	0.08	0.09	0.11	<LOD	0.00